UNIVERSITY OF SOUTHAMPTON

FACULTY OF SCIENCE

School of Chemistry

Directed Assembly of Functional Patterns

by

Francesco Giustiniano

Thesis for the degree of Doctor of Philosophy

March 2010

UNIVERSITY OF SOUTHAMPTON

ABSTRACT

FACULTY OF ENGINEERING, SCIENCE & MATHEMATICS

SCHOOL OF CHEMISTRY

Doctor of Philosophy

DIRECTED ASSEMBLY OF FUCNTIONAL PATTERNS

by Francesco Giustiniano

A multidisciplinary research network, namely CHELLnet, was founded with the aim of investigating novel research approaches to chemical cellularity and complexity. The synthesis of artificial chemical systems (i.e. not based on biological components) showing life-like behaviour represented the unifying target for the various subprojects.

The BrainCHELL project (or Directed Assembly of Functional Patterns, DAFP) aimed at developing multichannel, high sensitivity, electrical testing apparatus for the study of micro-scale, network-like, assemblies of various organic and hybrid materials. A multiple microelectrode array (MMEA) specifically designed for in-plane conductivity studies was used as the physical substrate for assembly, characterization, and reconfiguration experiments. Various nanomaterials were employed as the building blocks in the assembly procedures, with a focus on nanowires: 1) molecular wires (MWs) with oligophenyleneethynylenic (OPE) backbone and thiol (or cyanide) alligator clips were produced by organic synthesis methods, but were not largely employed in assembly experiments because of solvent compatibility issues; a set of experiments on MWs/NPs interfacial assembly has been reported, which uses an EtOH-soluble OPE MW (G. Rance); 2) conducting polymer (CP) polyethylene-dioxythiophene (PEDOT) micro- and nanowires, electrochemically generated in-situ from a solution of monomer and electrolyte; 3) multiwalled (carbon) nanotubes (MWNTs) assemblies, produced both in-situ via dielectrophoretic assembly and ex-situ via the interfacial assembly method; 4) MWNTs /PEDOT hybrid assemblies, produced both in-situ and ex-situ; 5) MWNTs/NPs assemblies produced ex-situ at an earlier stage of this project (Dr. D. Marsh; only tested on commercial microband arrays).

The demonstration of the first **physical, non-biological, neural network** capable of computational tasks, the main point of interaction with the computational research group CHELLware, was not accomplished within the limits of this project. Nonetheless two multichannel systems for low-level electrical testing (nA and pA level current measurement) have been developed and provided of basic automation capability: these were used to demonstrate anisotropic conductivity and reconfigurability in networks of organic and hybrid nanomaterials, laying the basis for further development of the system. A versatile experimental platform for molecular and nanoelectronics research is presented.

LIST OF CONTENTS.

LIST OF FIGURES, TABLES AND SYNTHETIC SCHEMES.

Chapter 1: ***Introduction.***

Chapter 2: ***Organic Synthesis.***

DECLARATION OF AUTHORSHIP

I, Francesco Giustiniano, declare that the thesis entitled

'Directed Assembly of Functional Patterns'

and the work presented in the thesis are both my own, and have been generated by me as the result of my own original research. I confirm that:

- this work was done wholly or mainly while in candidature for a research degree at this University;
- where any part of this thesis has previously been submitted for a degree or any other qualification at this University or any other institution, this has been clearly stated;
- where I have consulted the published work of others, this is always clearly attributed;
- where I have quoted from the work of others, the source is always given; with the exception of such quotations, this thesis is entirely my own work;
- I have acknowledged all main sources of help;
- where the thesis is based on work done by myself jointly with others, I have made clear exactly what was done by others and what I have contributed myself;
- parts of this work have been published as:

  'Assembly, structure and electrical conductance of carbon nanotube-gold nanoparticle 2D heterostructures.' Marsh, D. H.; Rance, G. A.; Whitby, R. J.; Giustiniano, F.; Khlobystov, A. N. *J. Mat. Chem.* **2008**, 18, 2249-2256.

  'Influence of Conformational Flexibility on Single-Molecule Conductance in Nano-Electrical Junctions.' Santiago, M.; Giustiniano, F.; Haiss, W.; Higgins, S. J.; Whitby, R. J.; Nichols, R. J. *J. Phys. Chem. C* **2009**, 113, 18884-18890.

Signed:……. **Date:**……

ACKNOWLEDGMENTS.

Due to the complexity of the proposed task, and the multidisciplinary nature of such project, many people were involved in several aspects of the design, testing and application of the apparatus and methods described. The author would like to thank first of all his supervisor Prof. Richard Whitby, without whose dedication during the design and production phases of the MMEA and the MMA, and whose support and advice in many of the practical and theoretical aspects of this study, most of this work would not have been realized. Thanks to Dr. Martin Grossel for his advise, and to Dr. Sally Dixon for the invaluable help and support in the laboratory. The author wishes to express gratitude also to several past and present members of the research community and staff of the University of Southampton, particularly from the Schools of Chemistry and Physics, all very helpful anytime it was needed. A special thanks to all the CHELLnet members, particularly to Prof. B. Whitaker and P. Kapetanopoulos for the time and competence dedicated to the design and prototyping of the MMA, and to Prof. A. Khlobystov, Dr. D. Marsh, Dr. N. Robertson and G. Rance for the help in designing and performing some of the experiments, and for the interesting collaborations undertaken. Among the collaborators not directly involved in the CHELLnet project the author wishes to thank particularly Dr. W. Haiss and Dr. I. Nandhakumar for introducing him to the STM technique. He also wishes to thank the Engineering and Physical Sciences Research Council for sponsoring the IDEAS Factory – Chemical Craftwork: 'ChellNet: Unifying Investigation in Artificial Cellularity and Complexity' (EPSRC Grant EP/D023645/1) and for granting the financial support that made this work possible. He will always be immensely grateful to his beloved family and friends, constantly close despite of physical distance, and ready with advice and moral support when it was needed the most.

ACRONYMS, SYMBOLS AND ABBREVIATIONS.

°C: degree Celsius.

0D: zero-dimensional.

1D: one-dimensional.

2D: two-dimensional.

3D: three-dimensional.

AC: Alternated Current.

AFM: Atomic Force Microscopy.

AI: Artificial Intelligence.

aq.: aqueous.

BET: Back-electron Transfer.

CE: Counter Electrode.

CHELL: CHemical cELL.

CMOS: Complementary Metal-oxide Semiconductor.

CNT: Carbon Nanotube.

CP : Conducting Polymer.

CT: Charge Transfer.

CV: Cyclic Voltammetry.

D/A: Digital-to-analog.

DABCO: 1,4-Diazabicyclo[2.2.2]octane.

DAFP: Directed Assembly of Functional Patterns (the title of this work).

DAQ: Data Acquisition.

DBU: 1,8-Diazabicycloundec-7-ene.

DC: Directed Current.

DCM: Dichloromethane.

DDT: Decanedithiol.

dec.: decomposition.

DEP: Dielectrophoresis.

DEPT: Distortionless Enhancement by Polarization Transfer.

DIPA: Diisopropylamine.

DMAP: Dimethylaminopyridine.

DMF: Dimethylformamide.

DPDA: Diphenyldiacetylene.

dppp: Diphenylphosphopropane.

DUT: Device Under Test.

ε: optical extinction coefficient.

EDIA: Ethyldiisopropylamine.

EDOT: (3,4)-Ethylenedioxythiophene.

EM: Electron Microscopy.

EMI: Electro-magnetic Interference.

ET: Electron Transfer.

FOV: Field of View.

fps: frames per second.

GC: Gas Chromatography.

GPIB: General Purpose Interface Bus (IEEE-488).

H-bond: Hydrogen-bond.

HDT: Hexanedithiol.

HeNe: Helium-Neon (laser source).

HRMS: High-resolution Mass Spectrometry.

I: Current.

ID: Inner Diameter.

IR: Infrared.

IV: current-voltage.

λ_{max}: maximum optical absorption.

LED: Light-emitting Diode.

logA: $\log_{10}$ Ampere.

LRMS : Low-resolution Mass Spectrometry.

MMA: Multi-channel Microelectrode Analyzer.

(M)MEA: (Multiple) Microelectrode Array.

MNEA: Multiple Nanoelectrode Array.

M_p: Melting Point.

MP: Megapixel.

MS: Mass Spectrometry.

MW: Molecular Wire.

MWNT: Multi-walled Nanotube.

NA: Numerical Aperture.

NI: National Instruments.

NIR: Near-infrared.

NMR: Nuclear Magnetic Resonance.

NN: Neural Network.

NP: Nanoparticle.

NPLC: Number of Power Line Cycles.

NT: Nanotube.

OD: Outer Diameter.

ODT: Octanedithiol.

OPE: oligo-(Phenylene ethynylene).

ρ: resistivity (specific resistance).

p-p: peak-to-peak.

PC: Personal Computer.

PCB: Printed Circuit Board.

PET: Photo-induced Electron Transfer.

$Pd(DBA)_2$: Palladium bis-dibenzylideneacetone

PEDOT: Poly-(3,4)-ethylenedioxythiophene.

PLC: Power Line Cycle.

PMA: phosphomolybdic acid.

PMAG: Primary Magnification.

psi: pound per square inch.

PSS: Polystyrene sulfonate (polyanion).

R: Resistance.

R_c: contact Resistance.

rbf: round-bottom flask.

rcr: recrystallized.

RE: Reference Electrode.

RIE: Reactive-ion Etch.

R_M: Resistance of the Material.

r.t.: room temperature.

SEM: Scanning Electron Microscopy.

SHE: Standard Hydrogen Electrode.

SMB: Sub-miniature (version) B.

SMU: Source-monitor Unit.

S/N: Signal-to-noise ratio.

SPM: Surface Probe Microscopy.

STM: Scanning Tunnelling Microscopy.

TBAB: Tetrabutylammonium bromide.

TBAF: Tetrabutylammonium fluoride.

TBAP: Tetrabutylammonium perchlorate.

TEA: Triethylamine.

THF: Tetrahydrofuran.

TLC: Tin-layer Chromatography.

TMSA: Trimethylsylilacetylene.

TSP: Test Script Processor.

TTF: Tetrathiafulvalene.

TV: Television.

USB: Universal Serial Bus.

UV: Ultraviolet.

V: Voltage.

V_{off}: offset Voltage.

V_{pp}: peak-to-peak Voltage.

VdW: van der Waals (force).

WD: Working Distance.

XR: X-ray (crystallography).

Ω: Ohm.

ZRA: Zero-resistance Ammeter.

Chapter 1 – Introduction.

1.1 – Background: Nanotechnology and Molecular Electronics.

During the last 50 years ever increasing efforts have been made to lay and reinforce the basis of the novel field of nanotechnology. The concepts at the heart of the so called 'nanosciences' were initially advanced by Feynman in the 1959[1], who proposed the enormous advantages that would arise from the ability to assemble few-atoms / molecules structures in a controlled fashion. It was not until 15 years later (1974) however that the term 'nanotechnology' was introduced by Taniguchi[2]; after few years this novel yet well-established field of research was reviewed by Drexler[3]. Significantly, in the same year, the ground-breaking report on the possibility to use molecules in electronic applications was published by Aviram[4], opening the way to the functional area of 'molecular electronics'. The discovery of conductivity in polyacetylene and other polymers with extensive π-conjugated systems[5] further supported the concept of using molecules as electronic components, constituting another essential milestone in the development of this field.

Nanotechnology constitutes a multidisciplinary branch of research concerned with the production of materials with features smaller than 100 nm; the enormous interest in this kind of technology arises from the predominance of quantum mechanical effects on such small scale, which results in novel (and sometimes unexpected) properties[6] in the nanomaterials when compared to the bulk. The difference in properties arises from their size being comparable (at least in one dimension) to the characteristic wavelength of the physical phenomena of interest: examples of such phenomenon are the nearly ballistic electronic conduction observed in carbon nanotubes (CNTs) and the size-dependant optical absorption and Coulomb-blockade in metal nanoparticles (NPs).

The use of single or few molecules as electronic components in a circuit (resistors, capacitors, transistors, etc.) represents the main focus of research in the area of molecular electronics. This area belongs to the sub-field of nanoelectronics (concerned not only with organic and molecular but also inorganic and hybrid materials), whose main goal is the miniaturization of electronic circuits past the physical limits of the current silicon-based technology; the other sub-fields of nanotechnology, namely 'nanomechanics' and 'nanophotonics', are of minor interest in the molecular electronics scenario, nonetheless many points of overlap exist as the result of the complex phenomena arising in the nano-scale regime.

An important distinction has to be made between technologies that use molecular materials in silicon based electronics and molecular electronics as such.

The use of organic materials, typically in the form of films[7], in combination with the present silicon-based technology[8], arises from the significant advantages attainable by combining the two without in fact aiming at miniaturization: as an example, logic gates were implemented using a SAM of rotaxane derivatives[9]; devices could be produced simply using ink-jet printing instead of photolithographic processes[10]. This kind of approaches, aiming principally at extending the functional ranges / improve the performance of the devices, are however often limited by the low production yield, a consequence of the holes and imperfections abundant in large area films/SAMs.

Molecular electronics refers to the study of the electrical properties of a limited number of molecular conductors, ideally aiming at performing single molecule measurements. The molecular wires are often assembled exploiting the self-assembly of thiol-groups onto gold to form the contacts. Two main electrodes configurations have been often employed: fixed electrodes with nm-scale gaps (nanogaps), produced by various lithographic and hybrid techniques, and then exposed to the MWs for assembly; one electrode fixed and allocating the MWs (pre-assembled onto it) that are tested in a dynamic fashion using an STM probe as the second electrode. While the former configuration generally result in many molecules (up to a few thousands) being simultaneously addressed, the STM methods typically allow for the detection of single molecule conductance events.

Despite nanogaps being successfully produced by optical ('nano-mushroom' approach)[11] and electron-beam lithography[12], fabrication procedures forming nanogaps by non-lithographic methods are of interest due to the higher scalability achievable in the fabrication process (with the initial devices produced in high yield by standard microlithography). Nanogaps were produced from the deposited metal structures in various ways: electroplating onto electrodes with micro-scale separation successfully reduced the gap to the sub-10 nm regime[13]; electromigration, induced by a forcing DC current (or electron-induced break junction, EIBJ, method), was used to generate a nm-scale disconnection in wires produced by various means, such as standard lithography[14], electron-beam nanolithography[15] or dielectrophoretic trapping of NPs[16]. In another interesting approach the nanowires are produced by template-assisted electrodeposition and contain a SAM junction, which is opportunely removed

after mounting the wire with lithographically defined contacts, forming a gap with the thickness of the SAM employed[17]: this kind of template-assisted method for the production of nanogaps (the SAM is the template in this case) results in higher reproducibility in defining the gap size, when compared to the previously described methods on fixed electrodes.

In order to address the problem of having to define gaps with sub-nm accuracy for molecular conductivity studies, several 'mobile electrodes' methods were devised.

A cantilever with ferromagnetic control could be used to tune the gap between a gold wire and a SAM on a fixed electrode[11]; alternatively a bridge between electrodes on a flexible substrate could be broken using a three-point bending mechanism, resulting in a gap with size dependant on the amount of bending, such as in the mechanical-control break junction technique[18] (MCBJ).

In several occasions a metal cluster (i.e. a NP) was allowed to assemble onto SAMs pre-assembled on the electrodes, with the molecules in the layer defining the gap-size such as in the nanowire-with-gap method[17]. Structures of this kind (metal-molecule-metal assemblies) were produced and investigated using both configurations. Fixed electrodes with a preassembled SAM could be exposed to the NP colloid and an AC potential field used to attract the NPs toward the gap[19]; for gap sizes larger than the NPs diameter an iterative process allowed multiple SAM and NP layers to be assembled until a connection was formed[20]. Alternatively a single electrode could be used for the SAM formation and NP assembly: by using the matrix isolation method (MI) individual NPs could be located and electrically contacted with a CAFM[21] or a STM[22] probe. These SPM methods present the significant advantage of probing a single molecular layer, whereas in the fixed electrode methods the collective response of two or more SAMs is measured.

Recently developed methods employing STM also allowed for the detection of single molecule conductance events[23, 24, 25], laying the basis for the electrical characterization of molecules of any length and shape, provided that self-assembling moieties are incorporated into the molecule. The understanding of the basic conduction properties of single molecules constitutes an essential preliminary step toward the production of 'all-nano' electronic circuits which would represent the theoretical bottom limit of miniaturization for molecule-based devices. Methods for single- / few- molecule conductance measurement were reviewed by James and Tour[26].

Some striking examples of molecular devices, and the future challenges in this field, have also been reviewed[27].

Three main nanodevice types can be identified according to the dimensionality of the cluster / molecule, the 'quantum-dot' (0D), the 'quantum-wire' (1D) and the 'quantum-well' (2D), each with respectively 3, 2 and 1 dimensions in the nano-regime; molecular or nano- electronics applications typically involve the use of one or more of such structures; the prefix 'quantum', used to underline the quantum mechanical nature of the conductivity, can be replaced by 'nano-' while still referring to the same kind of structures. Although Au nanoparticles (0D) are mentioned here, their production and assembly was of minor interest during this work: several works have been previously reported, both on their synthesis[28] and their self-assembly in 2D[29] and 3D[30] super-structures. Within this project, particular attention was put on the study of methods for the production of conductive nanowires, preferentially of organic nature, by entirely bottom-up procedures.

1.2 – Self- and Directed Assembly of Conductive Nanowires.

Nanowires of metallic or organic nature are essentially 1D conductors as the result of quantum confinement of the electrons across the main axis of the wire. The importance of identifying reliable methods for the production and the assembly of nanowires lies in the fact that the size of the connections in the circuit must scale down with that of the other components if true miniaturization has to be achieved; organic materials are preferred because of the high purity and monodispersity attainable via the organic synthesis methods, with sub-nm level control on the length (and shape) of the products; bottom-up procedures, particularly the self-assembly[31] of components driven by weak chemical interactions (VdW, H-bond, π-stack, etc.), are preferred mainly for the ease of scalability in the production (based on the parallelism characteristic of the assembly process).

The current methods of fabrication of electronic components are instead prevalently top-down in nature, which constitutes the main technological limit to miniaturization: although nanolithography and other methods were developed for the top-down production of nano-sized features, the intrinsic cost of the processes and the low parallelization achievable render them unsuitable for the commercial exploitation in the electronics industry.

It should be noticed that self-assembly, a bottom-up process, constitutes the most antique and powerful means by which biological systems are produced in nature. A thorough understanding of the range of weak interactions between molecules, the object of supramolecular chemistry research, might enable us to encode the dynamics of the assembly process in the molecular structure by rational design of the molecules involved.

Many different materials have been successfully shaped into wires by template-assisted assembly[32] and self-assembly methods[33]; most of these needed however post-assembly manipulation in order to be interfaced with silicon-based array of microelectrodes and tested[34]. A more rational solution that would minimize the use of top-down fabrication steps lies in the ability to produce the wires in-situ (i.e. between microelectrodes) by means of electrical and/or electrochemical methods. To date such approach, namely 'directed assembly', has been applied to the synthesis of conducting polymer (CP) wires by anodic electropolymerization[35, 36, 37, 38, 39], to the cathodic electrodeposition of metal structures[40, 41, 42], to the synthesis of carbon nanotubes[43] (by chemical vapor deposition), and to the assembly of colloidal particles under AC conditions (DEP, dielectrophoresis) [44, 45]. Mixed approaches, involving self-assembly of the base structures and directed assembly methods for the manipulation of the molecular- / nano-elements, have also been proposed[46]. During this project, as already mentioned, organic materials were preferred, specifically the conducting polymer PEDOT, MWNTs and OPE MWs: examples of directed and mixed-assembly experiments are reported in Chapter 4.

1.3 – Experimental Platform, the Nanocell device type and Neural Networks.

While preliminary experiments on the directed assembly of CP connections were run on a MMEA with mm-scale interelectrode gap (sub-Section 4.2.1), a MMEA with μm-scale gaps was designed and produced. The design derived from that introduced by Tour for the Nanocell device type[47] (Figure 1a), which constitutes an innovative approach toward the production of functional assemblies of nanomaterials.
The initial idea proposed in Tour's book was to let ligand-stabilized nanoparticles (NPs) assemble randomly onto the interelectrode SiO_2 surface of a MMEA, and successively allow molecular wires (MWs), synthesized by conventional methods, to self-assemble onto the NPs. Self-assembly resulted from the presence in the MWs of electron-rich groups (such as thiol-, isonitril-) amenable to assemble onto gold, the

metal the NPs and the electrodes were made of. In later works the random ensemble of NPs was replaced by discontinuous gold films as a mean to bridge larger interelectrode gaps, while keeping low the number of isolated metal clusters across the gap; this could be done on μm-scale MMEAs produced by conventional optical lithography, therefore simplyfing significantly the fabrication process. The resulting Nanocell device, based on a hybrid material, would present electronic properties confirming the presence of the organic conductor. The aggregates produced using 'switchable' MWs could be subsequently 'trained' or 'programmed' by using an electric potential to switch selected wires between different states of conductivity. If resistive-only MWs were to be used, the ability to reposition them under electric field control would surely enable superior reconfiguration capability, and the access to truly 'evolvable' circuitry.

This kind of approach constitutes in effect an inversion of the typical circuit design, whereas the functionality is endowed in the MWs, and the NPs / metal islands serve as the nodes of the system; alternatively the nodes could be resistive-only organic conductors (such as CNTs, Figure 1b) with the functional molecules assembled at their cross-junctions.

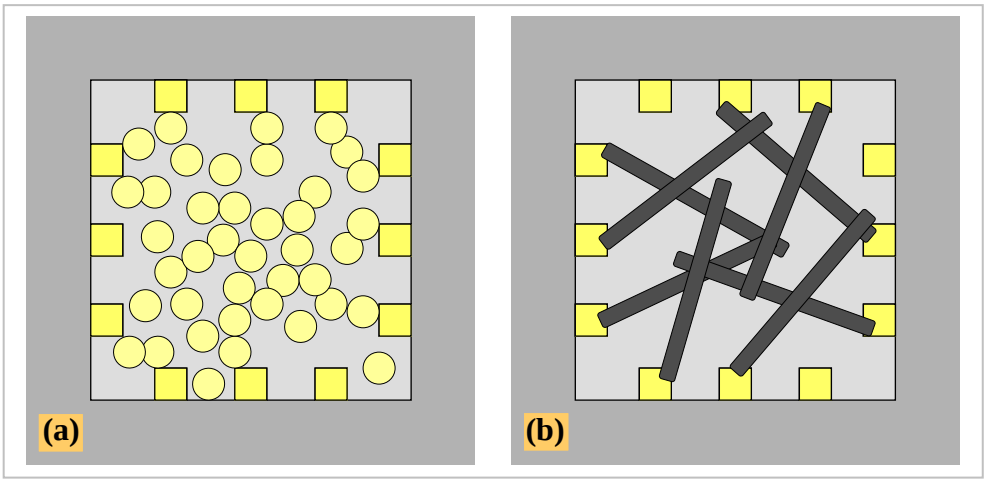

Figure 1. Schematic representation of conductive micro-networks assembled on multiple electrode arrays for electrical testing / training: (a) The Nanocell device type (see main text), employing NPs (diameter ~ 100 nm) interlinked with MWs (not shown in Figure, length ~ 1 nm); (b) an alternative assembly using NTs (length ~ 1 μm in Figure; longer NTs may be used on larger arrays).

Following this lead, several conductive MWs with different lengths and substituents were synthesized during this project (Chapter 2): according to established precedents[48], the MWs were thiol-terminated at both ends so to ensure their assembly

on / between gold NPs; to contrast the very low solubility of the OPE backbone and facilitate the synthetic procedures, the wires were functionalized with lipophilic moieties, which resulted in a useful solubility in DCM and aromatic solvents. However during later stages of the project it was found generally impossible to produce patterns of NPs stable to the treatment with aggressive organic solvents, and the multi-step assembly approach was dismissed. Alternatively, the directed assembly of MWs-NPs connections from solution was investigated: however the poor resistance of the solvent chamber system to the solvents employed made this approach impractical. Only one implementation of the Nanocell concept was reported, using instead EtOH-soluble MWs and charge-stabilized NPs, synthesized and assembled into hybrid films by G. Rance (Dept. of Chemistry, University of Nottingham; see sub-Section 4.4.3).

It should be recognized that such a system, with many more internal nodes / connections than the electrodes directly addressed and variable strength (or state) connections, constitutes in effect a 'physical' neural network (NN) not based on biological components. The importance of understanding and eventually exploiting the computational capabilities of biological neural networks was first recognized by Turing ('Intelligent Machinery', 1948), posing the basis for the study of artificial intelligence (AI) approaches to computation. Artificial neural networks, typically in the form of computer programs simulating a large number of simple computational elements ('neurons') with tunable interconnectivity (variable 'synaptic weight'), have been demonstrated capable to perform many non-trivial computational tasks, such as classification, pattern recognition (based on associative memory), sequence recognition (time-sequential memory), problem-solving and decision-making, and last but not least a variety of data analysis procedures (mining, clustering, filtering, etc.).

The computational power and diversity of the NN model arises in first instance from the massive parallelization of the connectivity which results in the emergence of collective responses sustaining the largest deal of computation in these systems. Such massive parallelization is possible because the computing nodes or 'neurons' do not need to be directly addressed (are therefore referred to as 'hidden' layers) and can be in much larger number than the nodes used to operate the network. The addressable nodes in the system are used to feed-in information or provide training (input nodes), and to 'read' the processed information (output nodes) (Figure 2). Training is provided by modulating the strength of inter-neuron coupling that is the 'synaptic

weight' of the connections (represented with arrows of different thickness in the Figure): in this way specific stable 'minima' are encoded in the state space flow of the system and specific input/output correlations result.

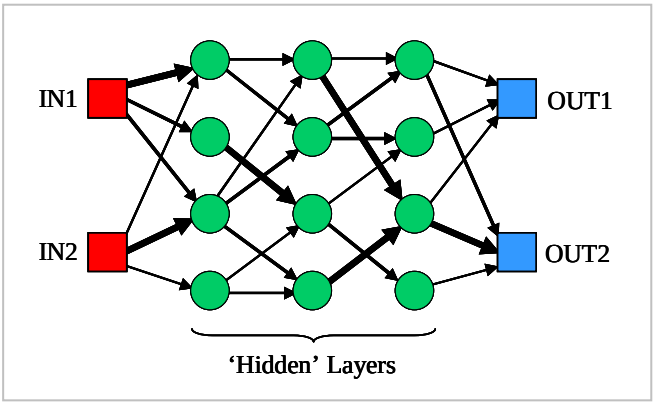

Figure 2. Schematic representation of the structure of a Neural Network (NN). In the feed-forward type shown here the information enters the network through the input nodes (IN1 and 2), is processed by the hidden layers (the 'neurons' of the system), and read via the output nodes (OUT1 and 2).

Important work by Hopfield[49] analyzed in detail the feasibility and the processing capability of computation using NNs, highlighting the need for backward coupling between the neurons as a requisite for the emergence of collective computational properties. Several hypothetical approaches to the implementation of 'physical' NN not based on neurons or other biological constituents were anticipated by Haddon[50]. To date, although many molecular electronics devices[51] and procedures for the assembly of conductive molecular materials (particularly CNTs[52]) have been demonstrated, vague work has been reported on the exploitation of the collective properties of 'physical' NNs[53].

1.4 – The CHELLnet consortium.

The DAFP project is part of a collective and multidisciplinary investigation of approaches to '**ch**emical c**ell**ularity' (CHELL) and artificial life[54] conducted by the CHELLnet research network (www.chellnet.org), and sponsored by the Engineering and Physical Sciences Research Council (EPSRC). Within the network, four main areas of expertise were identified and investigated by different research groups (Figure 3).

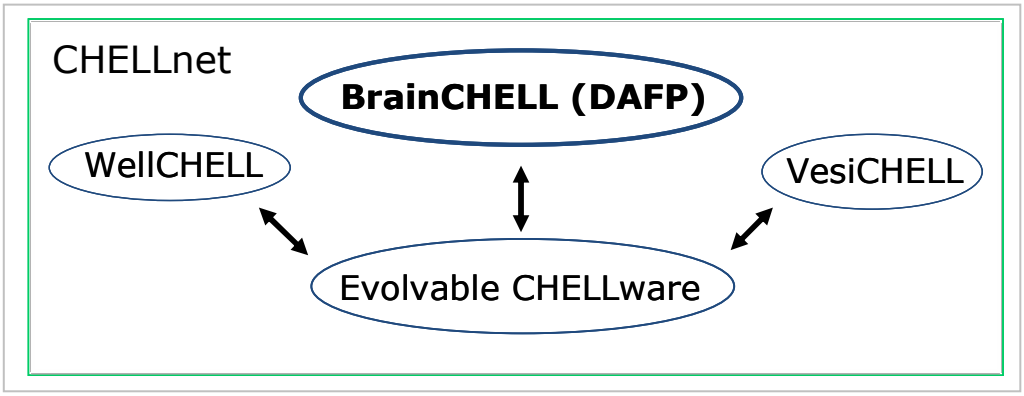

Figure 3. Scheme of the collaborations within the CHELLnet group, a research network founded to investigate approaches to the realization of artificial chemical systems capable of life-like behaviour (see main text and visit www.chellnet.org for more informations on the various sub-projects).

The work reported here (Directed Assembly of Functional Patterns, DAFP, or BrainCHELL within the CHELLnet) was mainly done in collaboration with research groups in Leeds (Prof. B. J. Whitaker) and Nottingham (Prof. A. N. Khlobystov), and focused on the development of materials and methods for the production of physical, non-biological, neural networks on 2D Multiple Micro-Electrode Arrays (MMEA). Various materials were produced at different stages of this project, particularly MWs in Southampton (within DAFP, Chapter 2) and MWs, NPs (G. Rance, sub-Section 4.4.3) and CNTs (Dr. D. H. Marsh, sub-Sections 4.4.1-.2) at the University of Nottingham. The development of the MMEA needed for connecting the micro-network to the macro-world, the implementation of the electrical testing apparatus for measuring current in the low pA range, and the production and screening of various organic and hybrid networks, all constitute parts of the DAFP project (Chapters 3 and 4). The dedicated electrical analyzer (MMA, sub-Section 3.4.2) was produced mainly by P. Kapetanopoulos (University of Leeds), testing of the instrument and optimization of the software interface were accomplished mostly by us.

The Multi-channel Microelectrode Analyzer (MMA) was specifically designed to simultaneously address all the electrodes (input/output nodes) and attempt the evolutionary training of reconfigurable networks: such work, aimed at using potential fields to produce specific patterns of conductivity, was intended as the main point of interaction with the CHELLware branch of CHELLnet (Dr. N. Krasnogor, P. Siepmann, J. Smaldon; University of Nottingham), focused on the simulation of physical micro- and nano-systems by computational techniques[55]. Unfortunately, as a

consequence of the novelty and complexity of such study, and of the short amount of time available, this part of the project halted at the speculative stage.

Chapter 2 – Organic Synthesis.

2.1 – Molecular Wires (1): oligo(Phenylene Ethynylene)s.

An oligo(phenylene ethynylene) backbone (OPE) was chosen as the basic structural requirement to obtain rigid 1D molecules (molecular wires, MWs) with an extended π-system; in principle the oligo(phenylene vinylene) (OPV) system would have yielded analogue MWs, but the OPE structure was preferred because more easily synthesized by iterative Sonogashira coupling[56]. To ensure the assembly on metallic NPs and electrodes, the MWs were terminated with functional groups amenable to chemical and electrochemical interaction with metal substrates. OPE MWs with various lengths, shapes and functionalization have been repeatedly reported by Tour[57, 58].

The synthesis of a protected sulfur-clip for the self-assembly of the wires onto gold surfaces has been previously described by Wang[59] (Scheme 1). The presence of a protecting group was found necessary to prevent the oxidative formation of disulfide bridges between molecules (polymerization in the case of bisfunctionalized compounds).

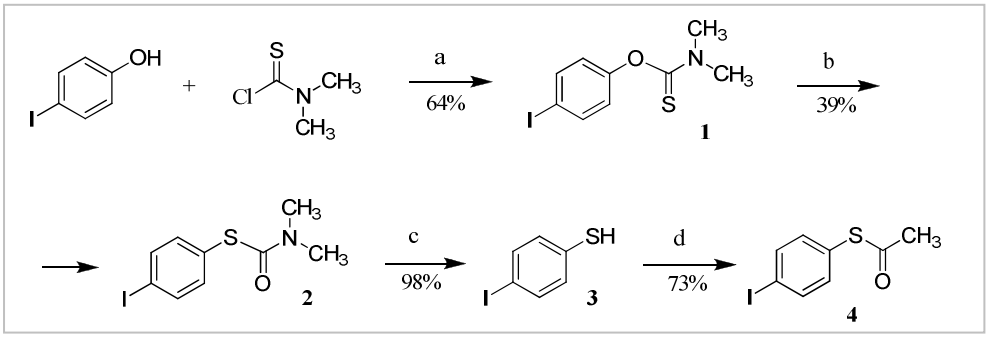

Scheme 1. (a): NaH, DMF, r.t., 20 h; (b): 235 °C, 2 h; (c): KOH, MeOH, 80 °C, 1 h; (d): AcCl, pyridine, r.t., 15 min.

As the starting material, an aryliodide was preferred to a bromide because of its enhanced reactivity under Sonogashira conditions: as described by Mio[60], using the aryliodide the coupling takes place at r.t., while higher temperature is needed with bromides. The r.t. conditions, together with the use of a hindered base (EDIA, Hunig's base) in the final coupling step between the clip-fragment and the OPE backbone, resulted in a lower degree of deprotection to unstable thiol byproducts. The β-cyanoethyl protecting group was considered as an alternative[61] but, although more stable, was discarded because of the generally poor yields obtained (~ 30%).

The arylbisiodide **6** (Scheme 2) was used as the starting fragment in the iterative bidirectional[57] Sonogashira coupling leading to bisacetylene **10**, the alkyl chains on **6** serving the purpose of maintaining the intermediates reasonably soluble as the size of the OPE backbone increased. The unprotected bisacetylene **10** was successfully coupled with two different terminal clip fragments (4-bromobenzonitrile or 1-acetylthio-4-iodobenzene), yielding 5-ring MW with different affinity for gold and with an approximative length of 3.5 nm. Compounds **11** and **12** have been previously reported by Dixon[62].

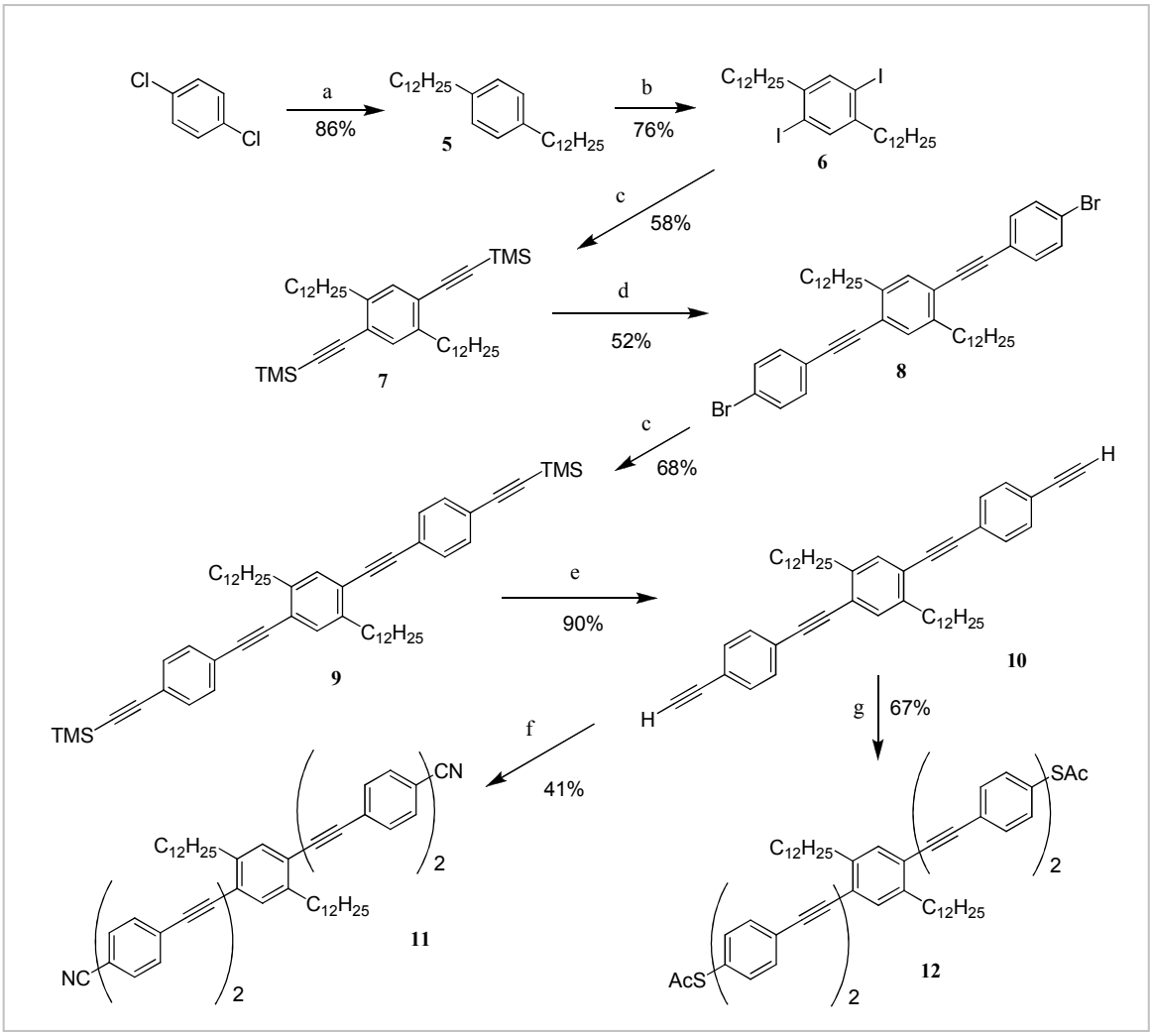

Scheme 2. (a): $C_{12}H_{25}MgBr$, $NiCl_2$-dppp, Et_2O, r.t. for 4 h, then 50 °C overnight; (b): I_2, H_5IO_6, CH_3COOH, H_2SO_4c, DCM, 95 °C, 20 h; (c): TMSA, $Pd(PPh_3)_2Cl_2$, CuI, TEA, benzene, 70 °C, 20 h; (d): 1-bromo-4-iodobenzene, $Pd(PPh_3)_2Cl_2$, CuI, DBU, H_2O, benzene, 70 °C, 17 h; (e): K_2CO_3, (3/1) DCM/MeOH, r.t., 1.5 h; (f): 4-Br-benzonitrile, $Pd(PPh_3)_2Cl_2$, CuI, TEA, THF, r.t., 22 h; (g): **4**, $Pd(PPh_3)_2Cl_2$, CuI, EDIA, THF, r.t., 4 h.

To overcome the deleterious effect of the steric hindrance of the alkyl- chains, the halogenation to iodide **6** was preferred. Although the reaction proceeded with good yield, a fraction of the material was found to be the tris-iodination byproduct (16 % as estimated by ^{1}H NMR): after repeated failures in separating the two, the impure material was used in the following steps. The purification of compound **7** was found effective so no more attention was dedicated to the optimization of the iodination reaction. This was later revised and optimized by C. Pearson ('Molecular Wires', MChem 3rd year project 2006-07): the same reaction conditions, but the use of ambient temperature and short reaction time (about 1 h), successfully yielded the bis-iodide without significant formation of byproduct.

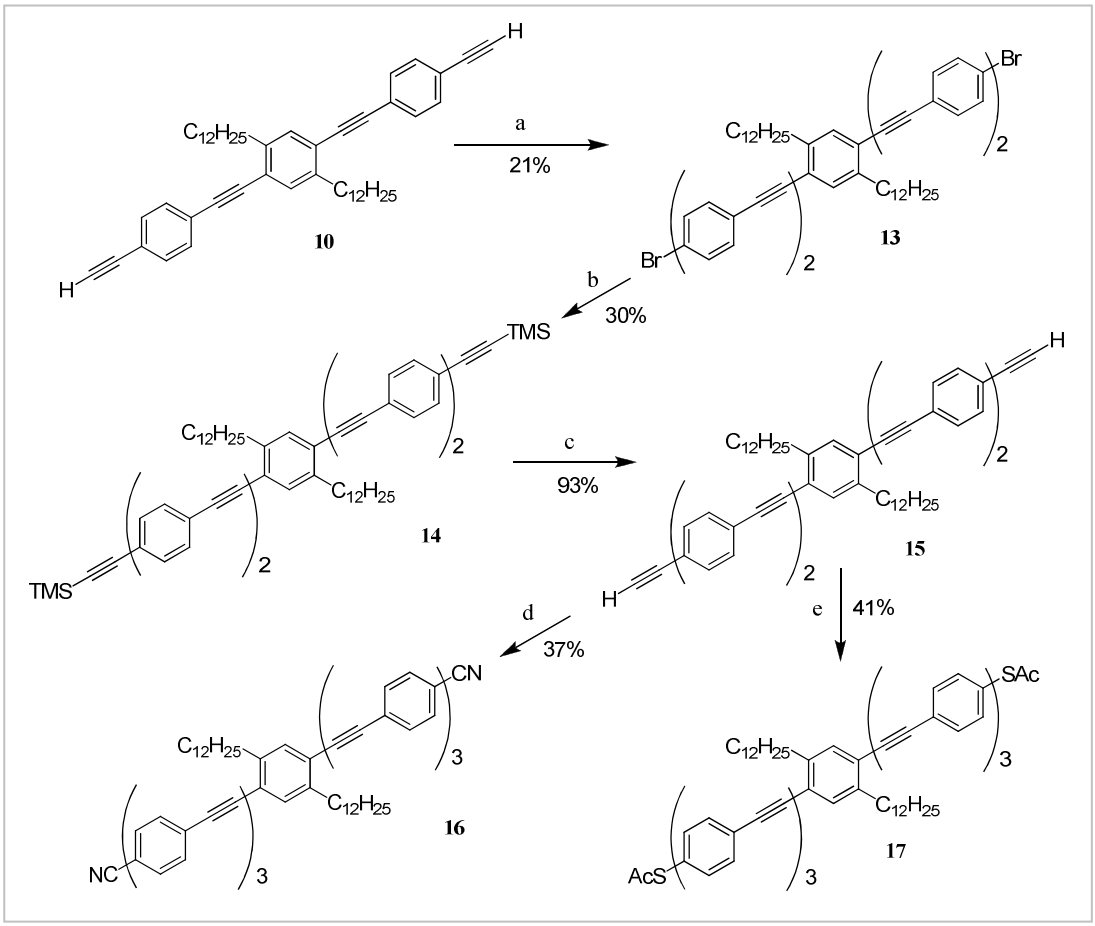

Scheme 3. (a): 1-Br-4-I-benzene, $Pd(PPh_3)_2Cl_2$, CuI, TEA, benzene, 70 °C, 12 h; (b): TMSA, $Pd(PPh_3)_2Cl_2$, CuI, TEA, benzene, 70 °C, 17 h; (c): TBAF, THF, r.t., 15 min; (d): 4-bromobenzonitrile, $PdCl_2$, PPh_3, CuI, TEA, benzene, 70 °C, 22 h; (e): **4**, $Pd(PPh_3)_2Cl_2$, CuI, DIPEA, THF, r.t., 14 h.

Further iterative coupling on the intermediate **10** (Scheme 3), to obtain the bisacetylene **15**, proceeded with low and modest yields, principally because of the poor solubility of the 5-ring OPE intermediates. From intermediate **15** were obtained the 7-ring MWs **16** and **17** (length ~ 5 nm), with overall yields lower than 1%.

The bidirectional approach shown here represents the only way to couple an OPE wire with a poorly stable terminal clip under Sonogashira conditions. Its main limits are the non-trivial chromatographic purification, due to the low yet similar solubility of starting material, product and byproducts (mainly from mono-coupling), the low efficiency of the final coupling step, and the very poor overall yields.

MWs with a CN-clip were obtained alternatively by a divergent-convergent approach (Scheme 4). This is generally possible when the terminal clip is stable to the coupling conditions (particularly base and high temperature). The synthesis of **19** has been described by McIlroy[63]; the 3-ring MW **20** (length ~ 2 nm) has been reported by Dixon[62].

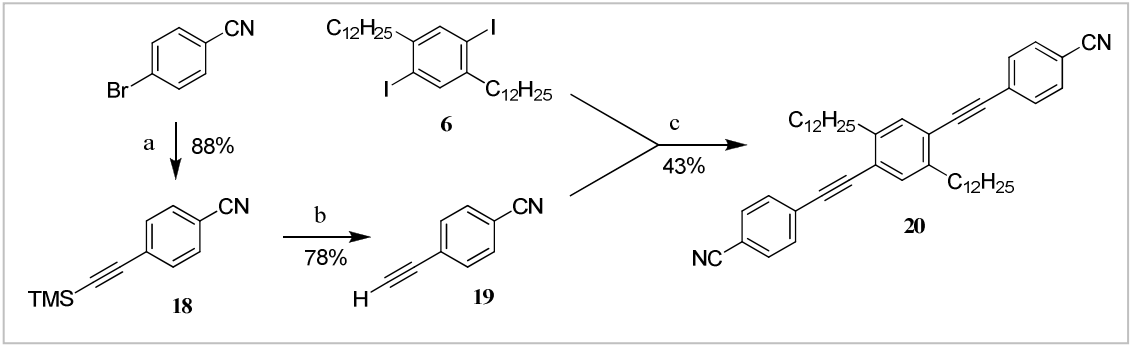

Scheme 4. (a): TMSA, $Pd(PPh_3)_2Cl_2$, CuI, TEA, THF, r.t., 3 h; (b): K_2CO_3, MeOH, r.t., 3 h; (c): $Pd(PPh_3)_2Cl_2$, CuI, TEA, benzene, 80 °C, 4.5 h.

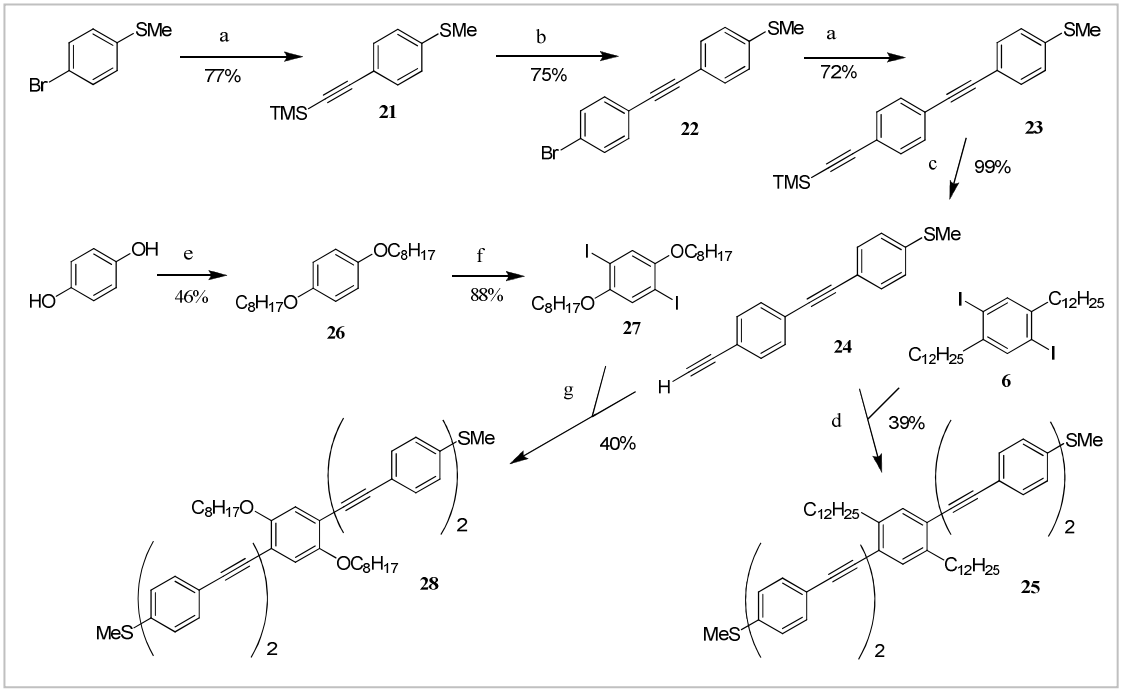

Scheme 5. (a) 4-bromothioanisole, TMSA, $Pd(PPh_3)_2Cl_2$, CuI, iPr_2NH, MeCN, 25 h, 70 °C; (b): 1-Br-4-I-benzene, $Pd(PPh_3)_2Cl_2$, CuI, DBU, benzene, 70 °C, 1 d; (c): K_2CO_3, MeOH/DCM, r.t., 1.5 h; (d): **6**, $Pd(PPh_3)_2Cl_2$, CuI, TEA, benzene, 70 °C, 16 h; (e): octylbromide, TBAB, KOH, 80 °C, 17 h; (f): $Hg(OAc)_2$, I_2, DCM, r.t., 19 h; (g): $Pd(PPh_3)_2Cl_2$, CuI, TEA, benzene, 70 °C, 13 h.

The same strategy was applied to the synthesis of the thioether-protected MWs **25** and **28** (Scheme 5). An alternative synthesis of **22** has been previously reported by Hsung[64]. The solubilizing fragment **27** was synthesized according to Shirai[65]. The presence of the alkyloxy- groups in **28** is expected to confer the molecule different electronic characteristics than the simpler alkyl- OPE wires.

The Sonogashira conditions to compound **21** (Scheme 5) were defined by parallel screening, using the commercially available bromothioanisole: using the conditions as in reaction 6 (Table 1; TMSA, $Pd(PPh_3)_2Cl_2$, CuI, DIPA, acetonitrile, 70 °C) and increasing the amount of catalytic system to the usual 5/10/10 ratio (mol% of starting material) it was possible to synthesize **21** with a 77% yield. In fact, the standard Sonogashira conditions (i.e. benzene, TEA) were found less effective when applied to the electron-rich bromothioanisole (yield 47%, 5 mmol scale).

Reaction	Catalyst	Cat/Lig/Cocat	Base	Solvent	% Yield[a]
1	$PdCl_2$	1/2/2	$CsCO_3$	Benzene	Product + By-products
2		2/4/4			
3	$Pd(DBA)_2$	1/2/2			
4		2/4/4			N/A
5	$PdCl_2$	1/2/2	DIPA	MeCN	40
6		2/4/4			46
7	$Pd(DBA)_2$	1/2/2			8
8		2/4/4			38

Table 1. Screening of two Pd sources and two solvent/base systems in the Sonogashira coupling to compound **21** ([a] yields based on calibrated GC peak areas).

The MW **29** (Scheme 6, also reported by Hsung[64]) was synthesized in order to test the conditions reported by Pinchart[66] for the deprotection to free thiol. However the presence of the triple bond resulted in the formation of byproducts when the compound was exposed to a strong nucleophile such as the tertbutylthiolate anion (even though lower temperature was employed). Since MWs with –SMe clip have been reported to form SAMs under conditions of potential-assisted assembly[67], this group is still considered a valid alternative to the more labile -SAc.

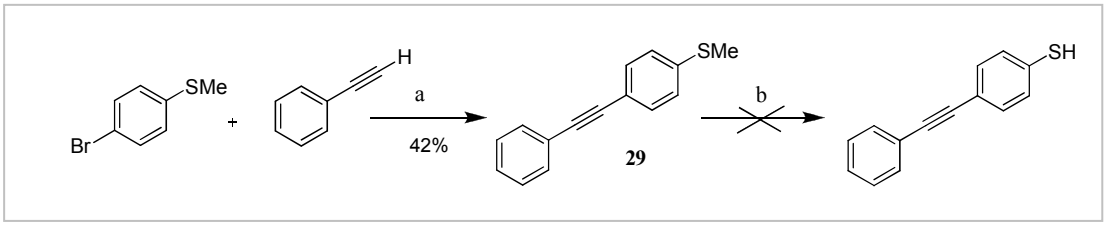

Scheme 6. (a): $PdCl_2$, PPh_3, CuI, TEA, benzene, 70 °C, 23 h; (b): tBuSNa, DMF, 100 °C.

The divergent-convergent approach also represents a useful strategy to obtain MWs with different central electroactive moieties (Scheme 7). The 2-(TMS)-ethyl-protecting group, first described by Yu[68] in the synthesis of OPEs, was used in the synthesis of the 3-ring NO_2-MW **33** (Scheme 7). Several nitro-substituted MWs have been reported by Tour (see [58] for an example).

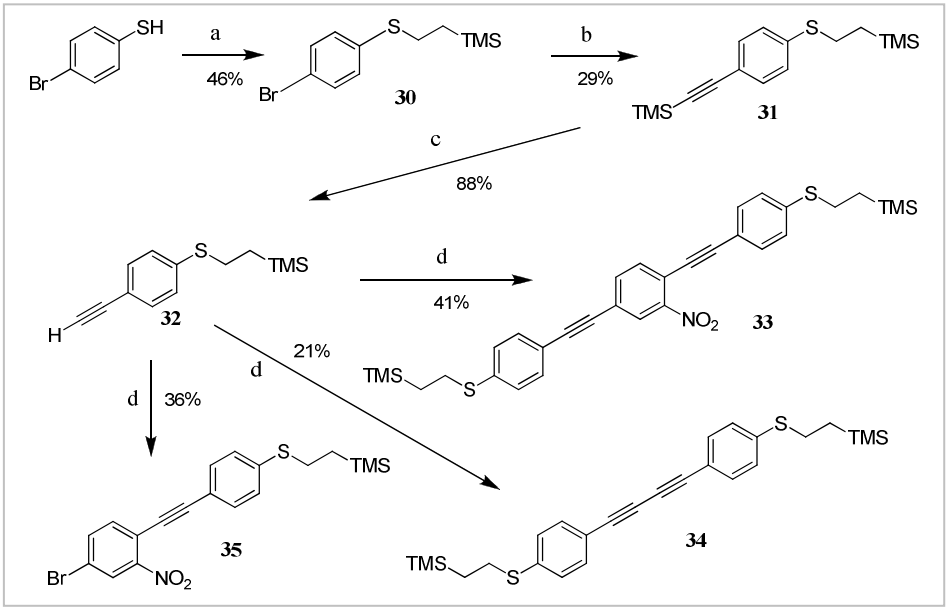

Scheme 7. (a): vinyltrimethylsilane, $(tBuO)_2$, 100 °C, 3 h; (b): TMSA, $PdCl_2$, PPh_3, CuI, TEA, benzene, 70 °C, 22 h; (c): K_2CO_3, (5/1) MeOH/DCM, r.t., 3 h; (d): 1,4-dibromo-2-nitrobenzene, $PdCl_2$, PPh_3, CuI, TEA, benzene, 70 °C, 5 h.

The number of OPE MWs produced was considered sufficient for the preliminary study of their electrical properties. To extend further the range of functional groups attached to OPE wires we moved onto the synthesis of a photo-switchable C_{60}-OPE dyad.

2.2 – Fulleroids.

In order to produce organic conductors with new electronic properties, the fullerene molecule was chosen as an interesting candidate for the covalent attachment to the OPE backbone. The family of fullerenes has been subject of intense research in materials science because of the peculiar electron affinity of these macromolecules. The most studied member of such family, [60]fullerene, can accept up to 6 electrons, as shown by CV experiments[69, 70]. Such properties have led to the design and synthesis of donor-bridge-acceptor dyads[71, 72, 73, 74 75] in which the fullerene cage, upon

irradiation with UV or visible light, can accept an electron from an electron rich moiety covalently attached to it (Photo-induced Electron Transfer, PET; Figure 4).

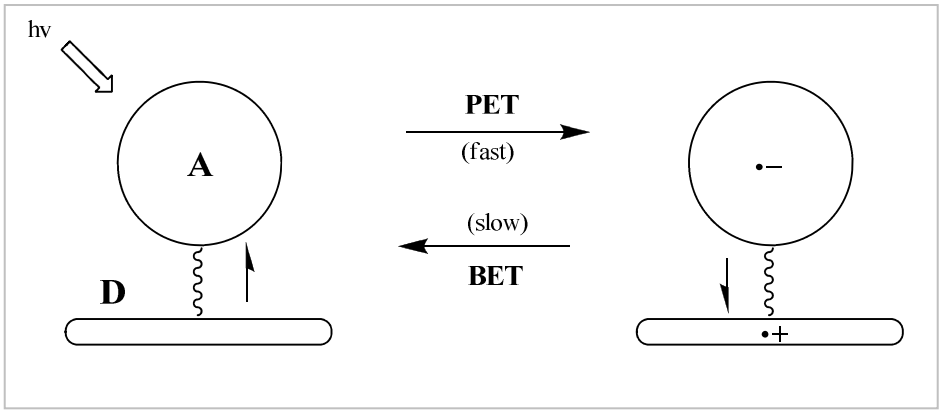

Figure 4. Photo-induced Electron Transfer (PET) and Back-electron Transfer (BET) in a Donor - bridge - Acceptor dyad.

Formally the electron transfer (ET)[76] follows the excitation of an electron in the C_{60} molecule to a singlet excited state, with short lifetime, and consequently to a triplet excited state, with lower energy and longer lifetime. Depending on the degree of conjugation of the bridge fragment the ET can follow two different mechanisms: a through-bond transfer in the case of a rigid and conjugated bridge; a 'through-space' transfer, following the formation of a transient intra-molecular exciplex, in the case of a 'floppy' non-conjugated bridge. The resulting charge-transfer (CT) complex, to be useful in optoelectronics and molecular electronics applications, has to be stable as long as possible: a half-life time in the millisecond, or even in the microsecond range, is a reasonable long time for charge storage and electron relay devices. The lifetime of the CT complex will depend on factors such as solvent, concentration and degree of conformational freedom of the molecule. Generally a slower back-electron transfer (BET) takes place in polar solvents and dilute solutions (lower probability of inter-molecular quenching); a non-conjugated bridge yields as well a slower BET, but a too high conformational freedom can make it faster by intra-molecular ('through-space') quenching. To achieve a low conformational freedom, without using a π-conjugated system, we decided to use a steroidic fragment as the bridge. The use of a similar fragment has been previously reported by Maggini[77].

The fulleropyrrolidine **36** (Scheme 8) was synthesized as a model system to test the conditions for covalently linking the C_{60} to a saturated hydrocarbon moiety. The reaction proceeded with poor yield, likely because of the low solubility of N-

methylglycine in toluene. The dipolar cycloaddition conditions for this reaction have been previously described by Maggini[78].

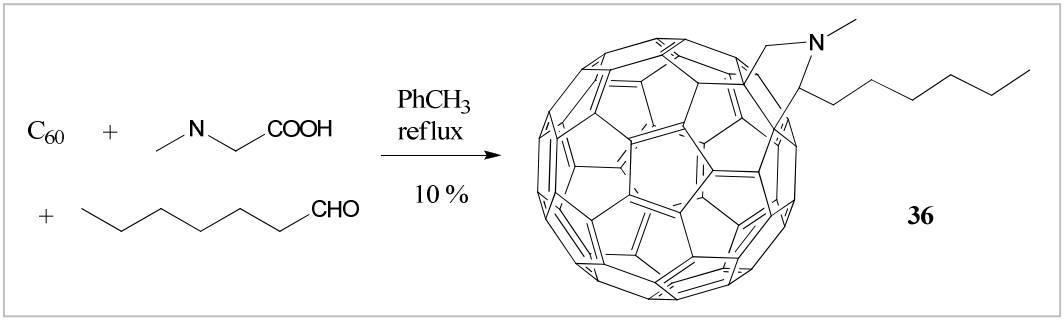

Scheme 8. Covalent functionalization of [60]fullerene (sarcosine, heptanale, toluene, 120°C, 2 h).

To synthesize a fulleroid with a polycyclic hydrocarbon bridge, lithocholic acid was reduced to aldehyde **37** and used to synthesize the fulleropyrrolidine intermediate **38** (Scheme 9). The procedure leading to **37**, previously described by Sato[79], has been modified in order to deal with the very low solubility of the steroid starting material in the reaction solvent. The conditions to fulleroid **38** consist in a modification of those used in the synthesis of compound **36**.

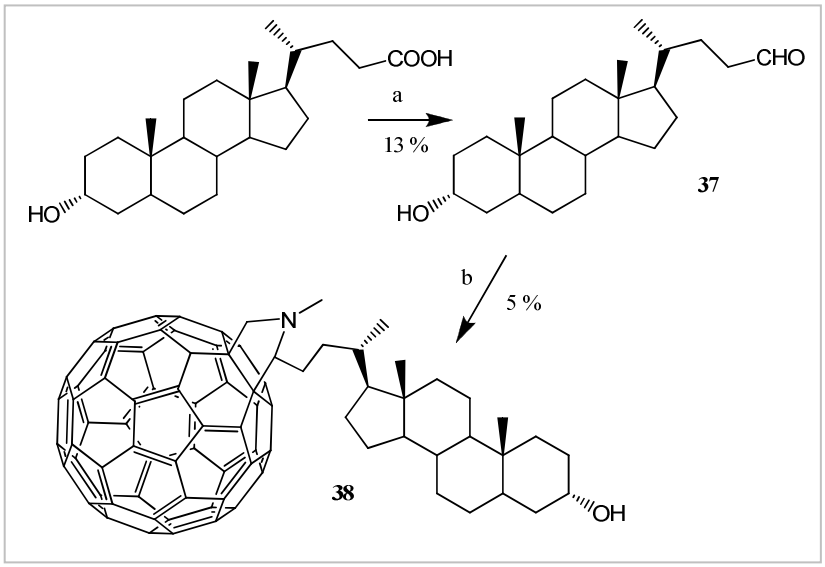

Scheme 9. Covalent functionalization of [60]fullerene: (a) lithocholic acid, iPrMgBr in Et_2O, Cp_2TiCl_2, 5 h, r.t.; (b) C_{60}, sarcosine, **37**, toluene, 2.5 h, 120 °C.

The methylthioether group was chosen as termination for the MW so to exclude the variable of the protecting group stability, and concentrate on solubility issues and the stability of the fullerene cage. The 3-ring MW **42** was synthesized, although with poor yield, according to Scheme 10.

The deprotection to **39** is a standard procedure; the acetylene product has been previously reported by Stiegman[80]. The Friedel-Crafts acylation and the oxidation

leading to compound **41** are standard procedures[81]. The only procedure reported in literature for the Sonogashira coupling on benzoic acid derivatives[82] (electron-poor) uses DMF as solvent but no experimental data were reported. The coupling conditions to MW **42** have been adapted from a procedure, defined by parallel screening, for the coupling in DMF solvent (Table 2, reaction 8) to produce compound **21**. Under the modified conditions (catalytic system increased to 10/20/20 ratio, temperature 60 °C) the poor yield obtained was mainly ascribed to the instability of the compound to the purification procedure: this was found to decompose on silica (in air) even when light was excluded. The process was not repeated with the complete exclusion of light/air as a sufficient amount of product was obtained for characterization and testing purpose. The use of a protecting group for the carboxyl- moiety would probably be the most effective way to improve the coupling on such fragment.

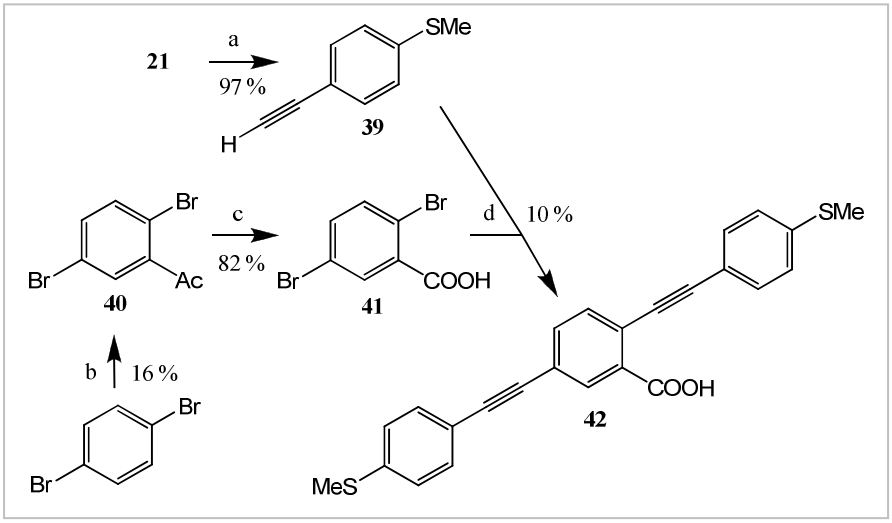

Scheme 10. Synthesis of a carboxyl-functionalized OPE: (a) **21**, K_2CO_3, MeOH, r.t., 0.5 h; (b) AcCl, $AlCl_3$, 120 °C, 2 h; (c) **40**, NaClO (aq.), dioxane, 75 °C; (d) **39**, **41**, $Pd(PPh_3)_2Cl_2$, CuI, DABCO, DMF, 60 °C, 2 h.

Reaction	Solvent	Base	% Yield[a]
1	Toluene	TEA	4
2		EDIA	Product + Byproducts
3		DIPA	
4		DABCO	26
5	DMF	TEA	Product + Byproducts
6		EDIA	
7		DIPA	
8		DABCO	46

Table 2. Screening of two solvents and four bases in the Sonogashira coupling to compound **21** ([a] yields based on calibrated GC peak areas). Other reagents and conditions: 4-bromothioanisole, TMSA, $PdCl_2$ / PPh_3 / CuI (2/4/4 mol% of starting material), 90 °C.

Because of the instability of MW **42**, we synthesized compound **43** in order to test the esterification of a phenylcarboxylate with fulleroid **38** (Scheme 11). The use of a rigid aliphatic spacer and an ester linkage between the donor and acceptor fragments is expected to extend the half-life of charge separation in the resulting photo-dyads[77]. Compound **43** constitutes therefore a potential candidate for the synthesis of donor-bridge-acceptor dyads with different donor moieties.

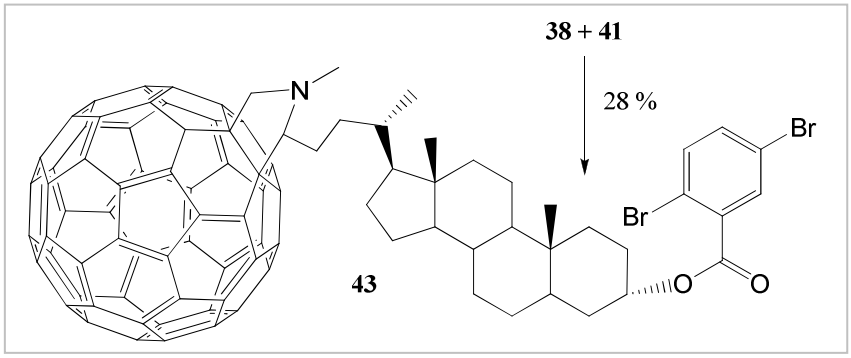

Scheme 11. Bis-bromide fulleroid **43**, a precursor for the synthesis of different donor-bridge-acceptor dyads: **41**, $SOCl_2$, 90 °C, 1.5 h; **38**, DMAP, TEA, DCM, r.t., 22 h.

The esterification of MW **42** with fulleroid **38**, or alternatively the Sonogashira coupling on the dibromo-fulleroid **43**, were not accomplished because of the small amount of starting material available, the instability of MW **42** and the lack of literature on the use of Sonogashira conditions in presence of the C_{60} moiety. The compounds were not synthesized again principally because no way of testing the MWs under electric control had been implemented to date. Although the proposed model molecule (Figure 5; X = SMe, n = 1) has not been obtained, C_{60}-bridge-OPE systems are still of interest. Upon illumination, quenching of the strong fluorescence of the OPE wire is expected as result of the electron transfer to the fullerene fragment, as well as the induction of hole-doped conductivity in the OPE MW. A new kind of photo-switchable molecular conductor is here proposed.

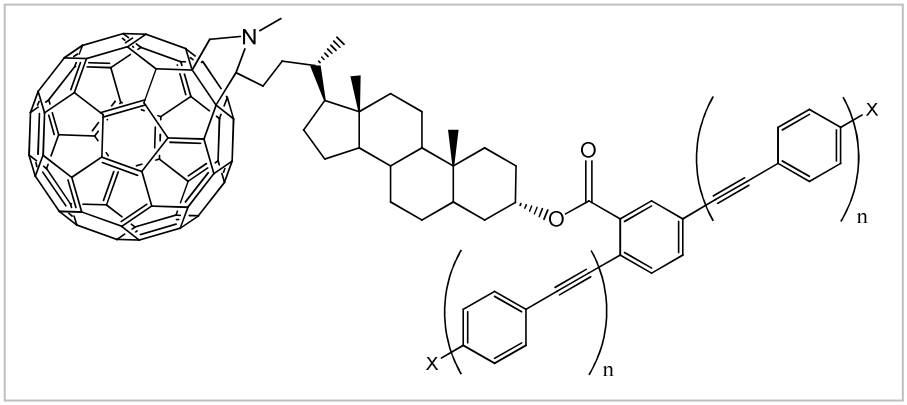

Figure 5. Photo-switchable [60]Fullerene-bridge-OPE MW.

2.3 – UV Spectroscopy.

UV spectra have been acquired for several of the OPE MWs produced (Figure 6). By comparing MWs of different lengths (CN-series: **20**, **11**, **16**; Figure 7) bathochromic effect could be easily observed, consistently with data previously reported[57] for similar MWs: this arises from the extension of conjugation of the π-orbitals with increasing length of the OPE fragment, which in turn results in higher absorbance at lower energies (higher wavelength).

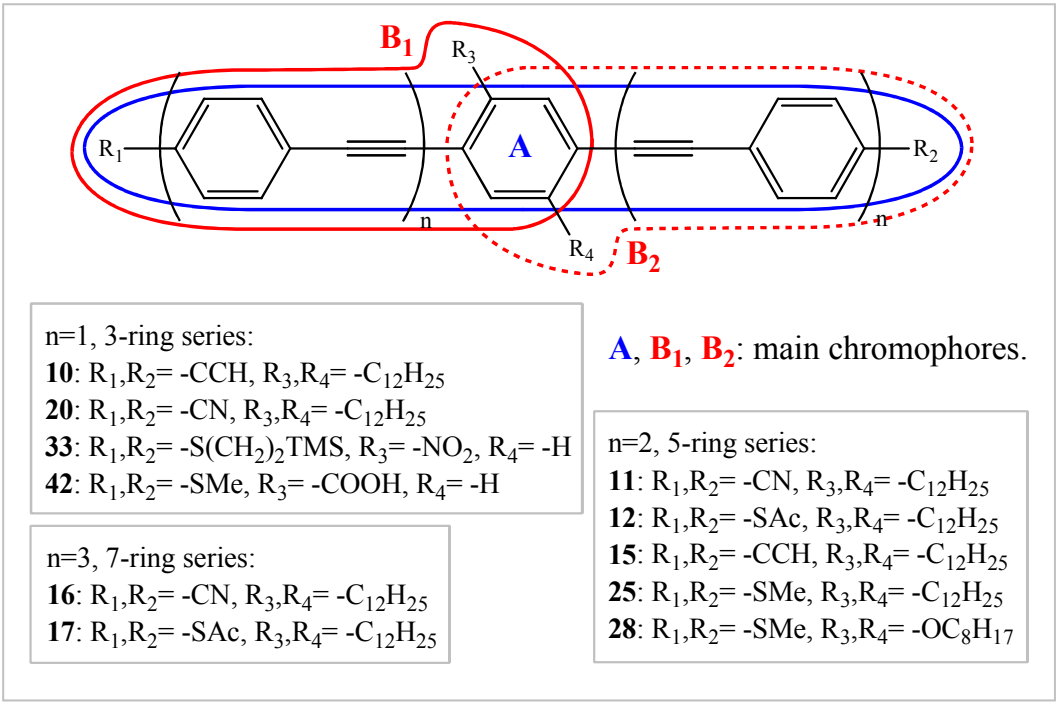

Figure 6: List of OPE MWs analyzed by UV-vis spectrophotometry. The main chromophores have been highlighted in the structure (see main text for discussion).

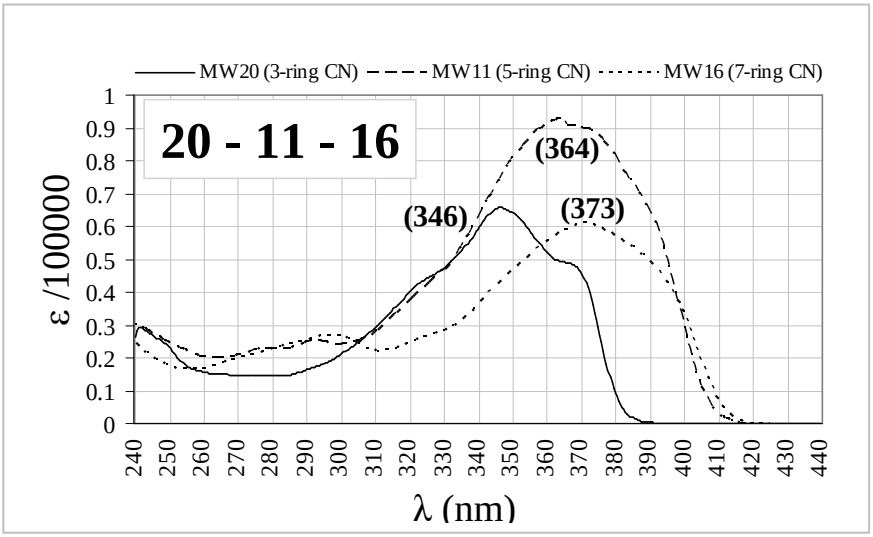

Figure 7: UV absorption spectra of CN-terminated OPE MWs **20** (λ 346 nm, ε 0.66x10^5), **11** (λ_{max} 364 nm, ε 0.93x10^5) and **16** (λ_{max} 373 nm, ε 0.61x10^5). [All spectra recorded in $CHCl_3$.]

All the compounds characterized by one main absorption feature were found to have λ_{max}s mainly dependent on the length of the OPE fragment (main cromophore A in Figure 6) and irrespective of the terminal functionality (alkyne, cyanide, alkylthiol or acetylthiol, compounds **10**,**20**,**33**, **11**,**12**,**15**,**25**, **16**,**17**; Figures 8, 9 and 10, 3-ring, 5-ring and 7-ring OPE series respectively); approximative wavelengths of 345, 360 and 370 nm were characteristics of the three respective length series.

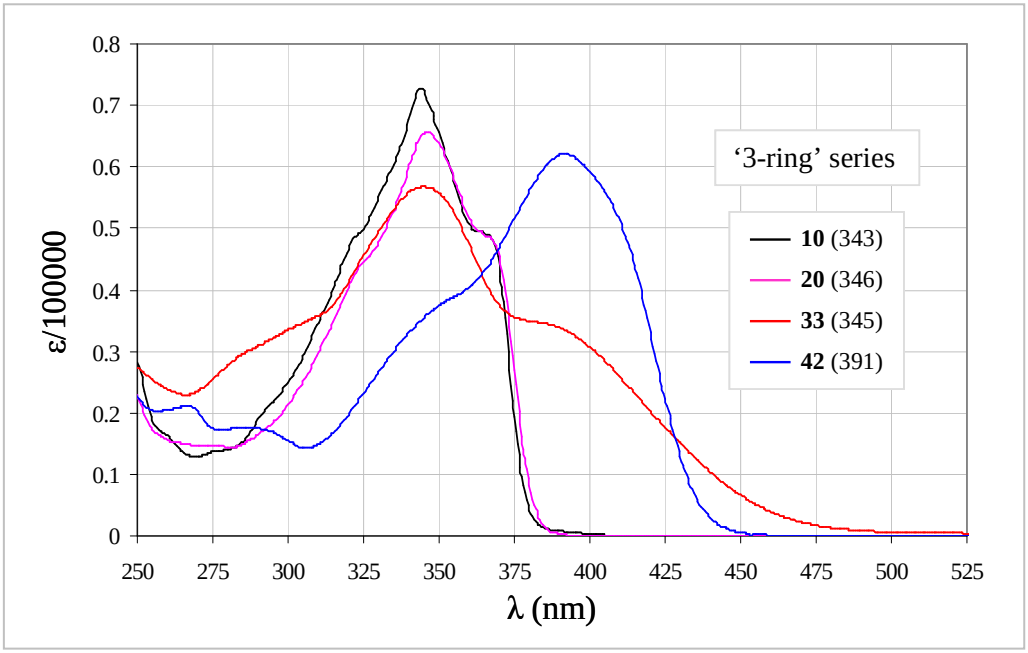

Figure 8: UV absorption spectra of 3-ring OPE MWs **10** (λ_{max} 343 nm, ε 0.75 x 10^5), **20** (λ_{max} 346 nm, ε 0.66x10^5), **33** (nitro-substituted; λ_{max} 345 nm, ε 5.67 x 10^5) and **42** (carboxyl-substituted; λ_{max} 391 nm, ε 0.62 x 10^5).

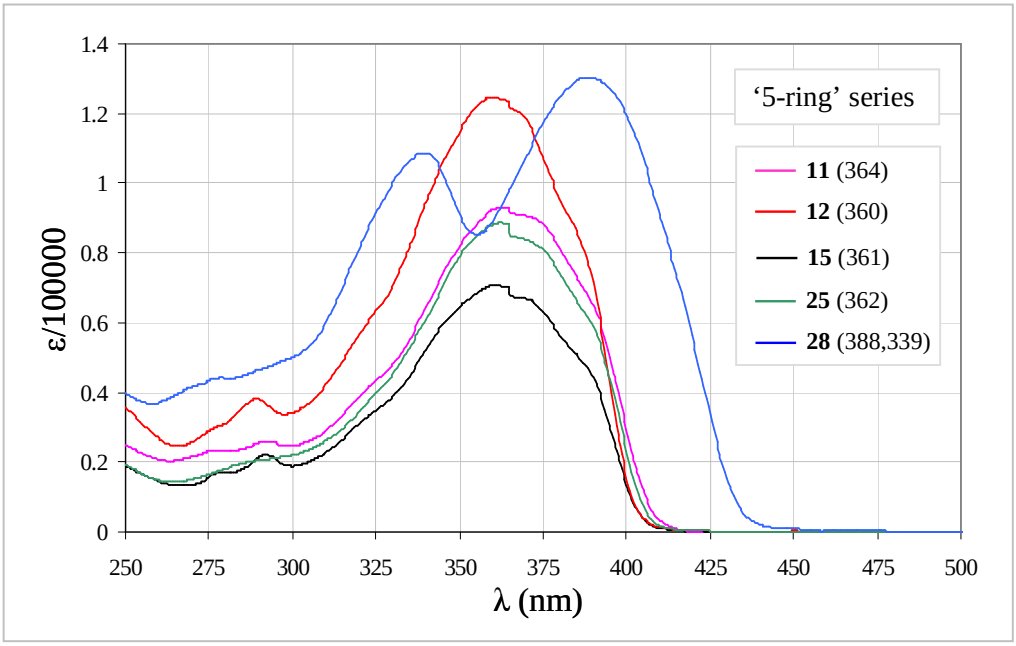

Figure 9: UV absorption spectra of 5-ring OPE MWs **11** (λ_{max} 364 nm, ε 0.93x10^5), **12** (λ_{max} 360 nm, ε 1.25x10^5), **15** (λ_{max} 361 nm, ε 0.71 x 10^5), **25** (λ_{max} 362 nm, ε 0.89 x 10^5) and **28** (bisalkyloxy-substituted; λ_{max1} 388 nm, ε 1.30 x 10^5; λ_{max2} 339 nm, ε 1.09 x 10^5).

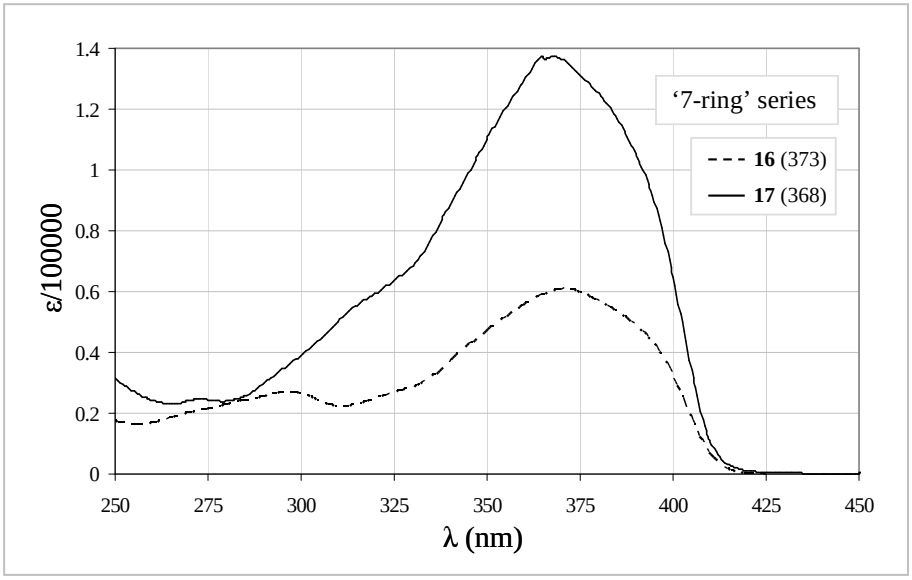

Figure 10: UV absorption spectra of 7-ring OPE MWs **16** (λ_{max} 373 nm, ε 0.61x10^5) and **17** (λ_{max} 368 nm, ε 1.37x10^5).

The extension of conjugation on the substituent in position 2 of the central benzene ring produced an additional chromophore B_1 (Figure 6), with the electrons mainly delocalized over the ethynylphenyl fragment in orto to the substituent; this resulted in a pronounced shift in the λ_{max} (of ~ 45 nm) measured for the carboxy-substituted **42**, and in a shoulder appearing in the absorption region typical of cromophore A. Interestingly the opposite trend was observed for the respective absorbances in the spectrum of the nitro-substituted **33** (Figure 8), also characterized by the presence of chromophore B_1. In the centrosymmetrical alkyloxy-substituted **28** (Figure 9) an additional chromophore B_2 (Figure 6) contributes to the absorption resulting in a bathochromic shift of λ_{max} similar to that observed for MW **42**; the absorption feature of the 5-ring chromophore A (at ~ 360 nm) was mainly obscured by the strong (additive) B_1,B_2 absorption and a new feature appeared at ~ 340 nm, strongly suggesting the presence of a further chromophore in MW **28**: this could possibly be the terminal 3-ring OPE fragment, which would explain the high absorbance observed by symmetry reasons.

Since a detailed mathematical analysis of these molecules was not part of this project, the UV-vis data reported result hard to interpret and discuss further: nonetheless evidence for electronic delocalization along the whole OPE backbone was found for most of the wires in the photoexcited state; this, together with the observed effect of different central substituents on the λ_{max}, and the possibility of multiple maxima, suggests the conductivity in these MWs as being significantly influenced by

the illumination conditions. Further investigation is needed to better characterize the compounds produced and assess their potential as molecular conductors.

UV-vis spectra were also recorded for the fulleroid intermediates **38** and **43**, and found consistent with the data previously reported for the fulleropyrrolidine fragment[76] (Figure 11).

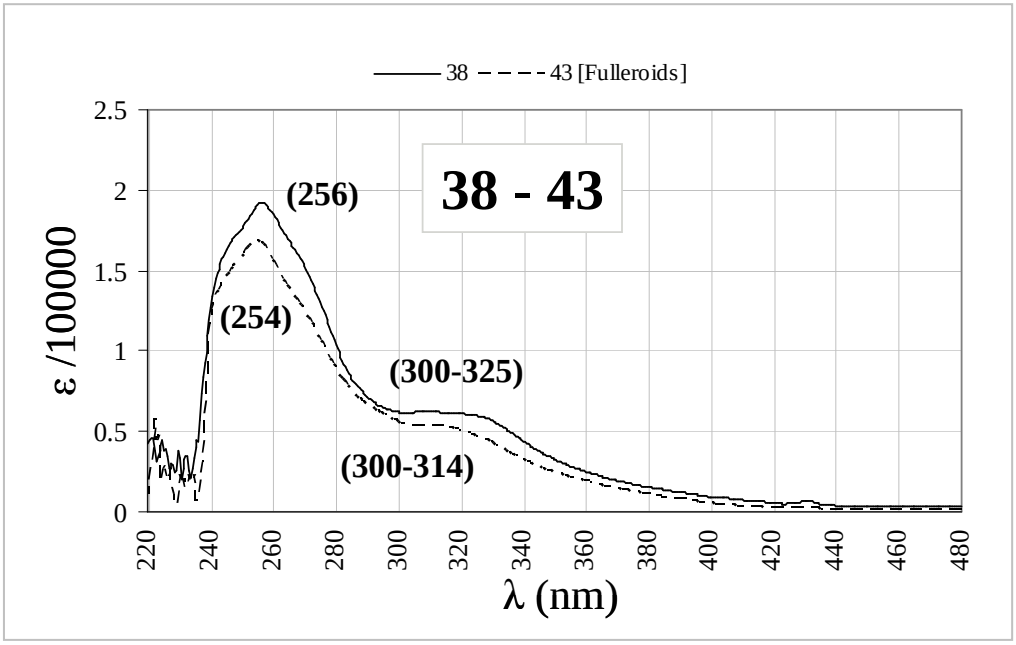

Figure 11: UV absorption spectra of fulleroids **38** (λ_{max} 256 nm, ε 1.92 x 10^5, shoulder ε 0.62 x 10^5) and **43** (λ_{max} 254 nm, ε 1.69 x 10^5, shoulder ε 0.55 x 10^5).

2.4 – Molecular Wires (2): rigid analogues of hexane- and decane-dithiol.

Part of the synthetic work involved the synthesis of two alkanedithiol MWs (Schemes 12 and 13) for the group of Prof. R. Nichols and Dr. W. Haiss (University of Liverpool, Chemistry), that has recently developed techniques for the measurement of single-molecule conductivity using STM[23]. The two MWs produced were designed as cyclo-alkyl analogues, with limited conformational freedom, respectively of the hexanedithiol (HDT) and decanedithiol (DDT) MWs. During STM studies on the conductivity of linear chain dithiols it was observed temperature dependence in the statistical distribution of 'current jump' events (Haiss et al.[24]): this suggested a possible correlation with the temperature-dependent distribution of gauche conformers in this kind of molecules. This idea was supported by the lack of T dependence with the tip set at such a height that only the fully stretched all-trans conformer could

bridge the tip-substrate gap, and lead to the synthesis of the cyclic analogue closely matching (in S-S distance and σ-bonds orientation) such all-trans conformer.

The hexanedithiol analogue **46** was synthesized following previously reported procedures (Scheme 12). However the bistosylation reported by Swepston[83] involved an unclear purification procedure and lacked of characterization data. The conformations of the two isomers have been assigned by comparison of the M_ps of the isolated compounds (trans-, 164-168 °C, purity > 95% as estimated by ^{1}H NMR; cis-, 81-86 °C, purity 90%) with those reported by Haggis (part X; trans-, 162-163 °C; cis-, 95 °C)[84]. After separation, the two isomers underwent the same reaction to form the thioacetyl- target compounds, of which only the trans- isomer was then used in the STM study; the reaction conditions for the displacement of the tosyl- group using a thioacetate have been previously described by Whistler[85].

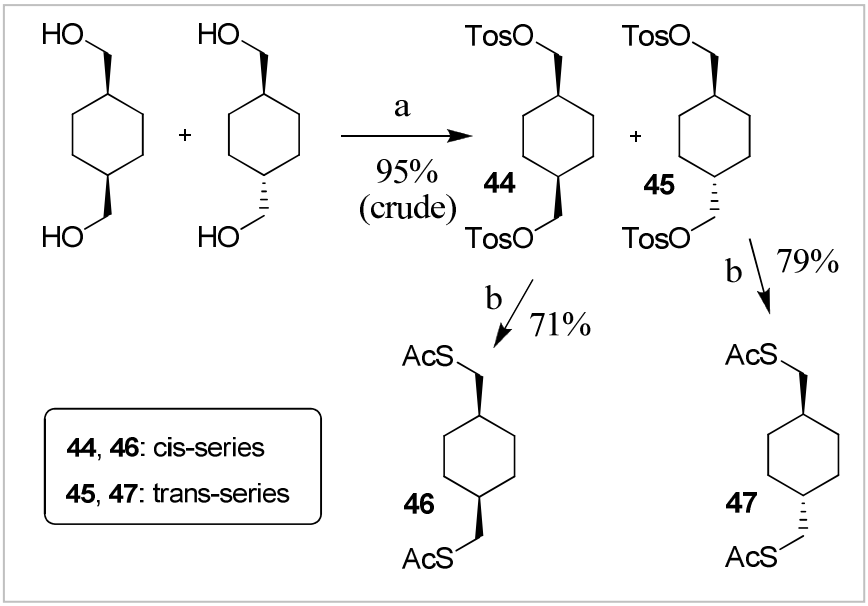

Scheme 12. Synthesis of ring-analogues of the hexanedithiol MW. Conditions: (a) 1,4-cyclohexanedimethanol, tosyl chloride, pyridine, 1 °C, 65 h; (b) **44** or **45**, potassium thiolacetate, acetone, 65 °C, 20 h.

Following the procedure reported by Cannon[86], the biscarboxylic acid **49** (Scheme 13) was obtained with good isomeric purity (M_p 351-353 °C, consistent with that reported). The target compound **52** was then obtained using conditions similar to those employed to synthesize **46** and **47**.

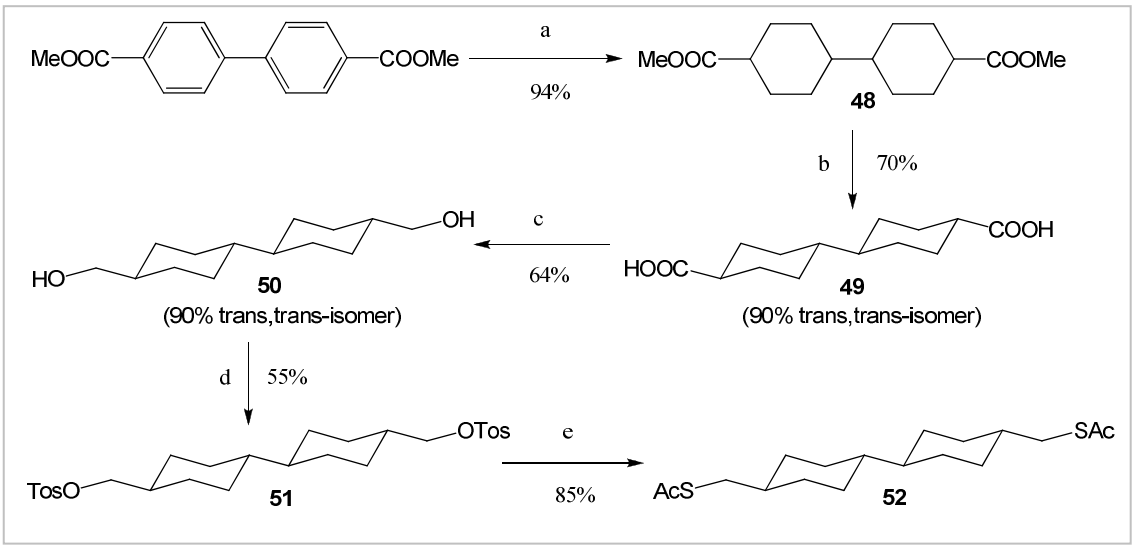

Scheme 13: (a) H_2, PtO_2, Pd/C, AcOH, 50° C, 350 psi; (b): 1] NaOH, EtOH/H_2O, 75° C; 2] dry, 275° C, 3 h; (c) $LiAlH_4$, THF, 60° C; (d) TosCl, pyridine, 1° C, 20 h; (e) AcSK, acetone, 70° C, 20 h.

Confirmation of the assignments has been provided by X-ray diffraction analyses[87] of the trans-bistosylate **45** (Figure 12a; white needles from EtOH, $\mathbf{M_p}$ 164-168 °C) and of the target compound **52**, found to be the trans,trans-isomer (Figure 12b; white needles from EtOH, $\mathbf{M_p}$ 110-112 °C).

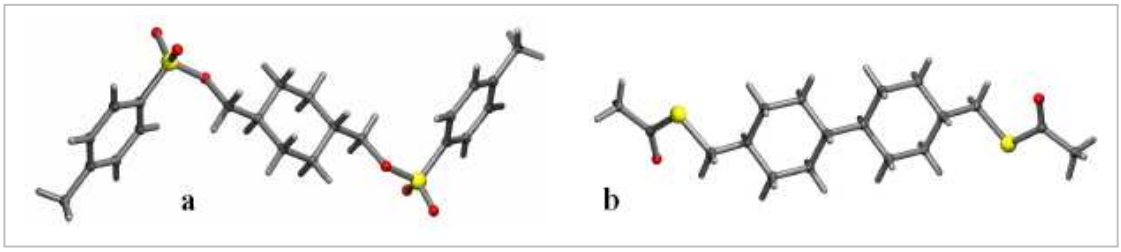

Figure 12. X-Ray diffraction analysis of compounds **45** (**a**) and **52** (**b**), both recrystallized from EtOH.

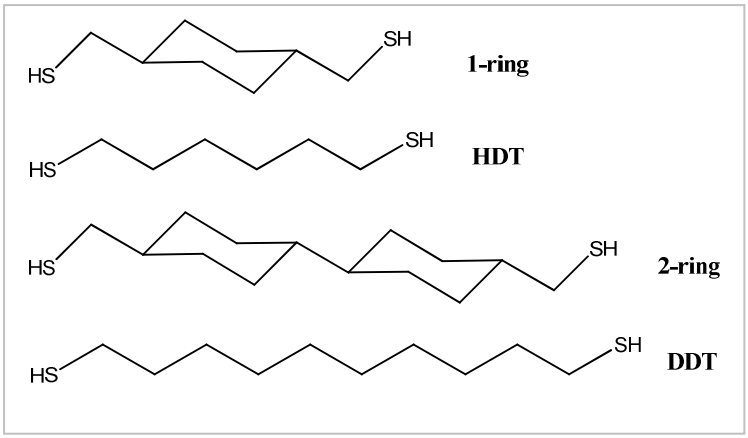

Figure 13. Insulating MWs synthesized for the STM study of the T dependence in single molecule conductivity, and their linear chain analogues (note that the free thiol is shown here but the compounds were synthesized as acetyl-protected thiols for increased stability).

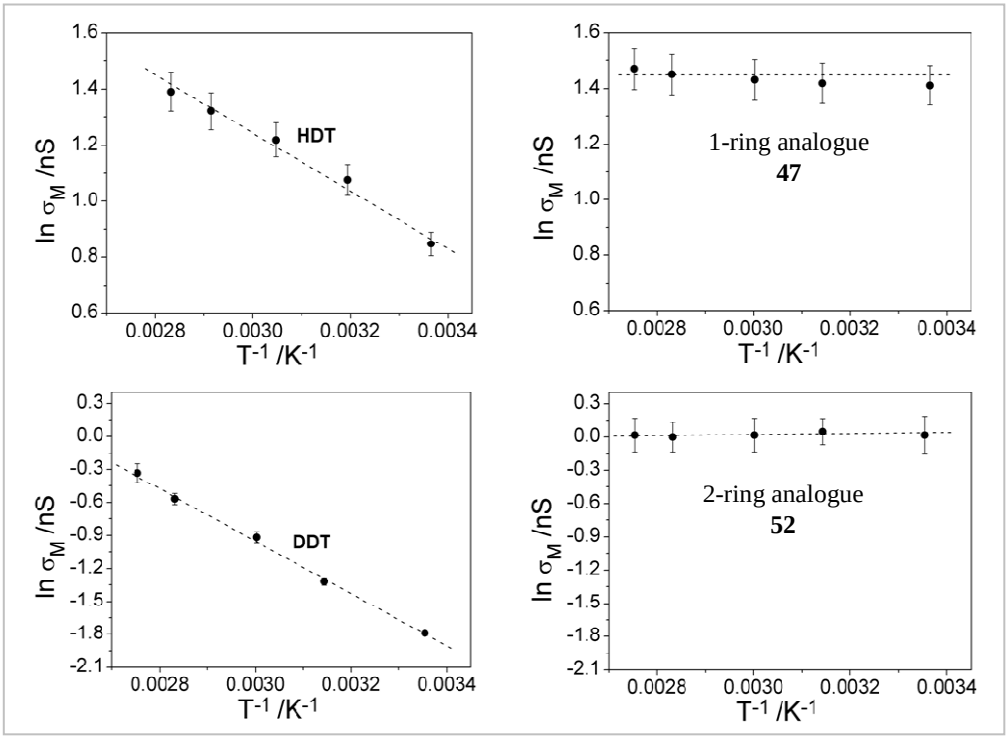

Figure 14. Plots of the logarithm of the single-molecule conductivity (ln σ_M) versus reciprocal temperature (T^{-1}) for the compounds shown in Figure 10 (STM in I(t) mode: I_0 = 20 nA for HDT and 1-ring, 6 nA for DDT and 2-ring, U_t = 0.6 V). T range 25-90 °C. Dashed lines are linear fits.

The two MWs and the model compounds HDT and DDT (Figure 13) were tested by Nichols et al. using STM in I(t) mode (constant height, feedback disabled): the chosen tip-substrate separation allowed for multiple HDT and DDT conformers to bridge the gap, and the previously reported T dependence was observed. When the measurements were repeated on the cyclic analogues the T dependence was absent (within error), supporting the hypothesis that the multiple conductivity states arise from a distribution of conformers with different conformational energy and conductivity (Figure 14). More details on this study can be found in the reported document[88].

2.5 – Conclusions.

Several MWs were produced as pure compounds during this project; seven of these were NCEs (Figure 15; novel compounds underlined). Most of them featured an OPE backbone, providing a 1D π-conjugated system, and terminal groups for the attachment onto Au or other metals; other groups were attached to the middle phenyl-ring, such as aliphatic chains (to aid solubility) or electron-withdrawing moieties.

Two of these (MWs **12** and **33**) were used to produce conductive MWs/NPs interfacial films that were electrically tested using commercial multiband MEAs (not reported here) and a Parameter Analyzer (Agilent 4155C); all of the wires produced during this project are expected to support electrical conductivity, and could therefore be employed in molecular electronics applications. As reported later (sub-Section 4.4.3), an analogue MW was produced by G. Rance and assembled into conductive MWs/NPs networks via the interfacial technique; these assemblies were produced during the final stage of this project when the 20-electrode MEA was available, and could be electrically characterized using the automated testing routine (see Chapter 3). The same technique could be applied to the production of NPs fims incorporating any of the MWs produced here: of course, due to the preferential solubility in organic solvent, the MWs should be supplied as a very dilute solution in the organic super-phase (aromatic hydrocarbons preferred; high dilution is necessary to avoid the formation of MW crystals and microdomains within the film).

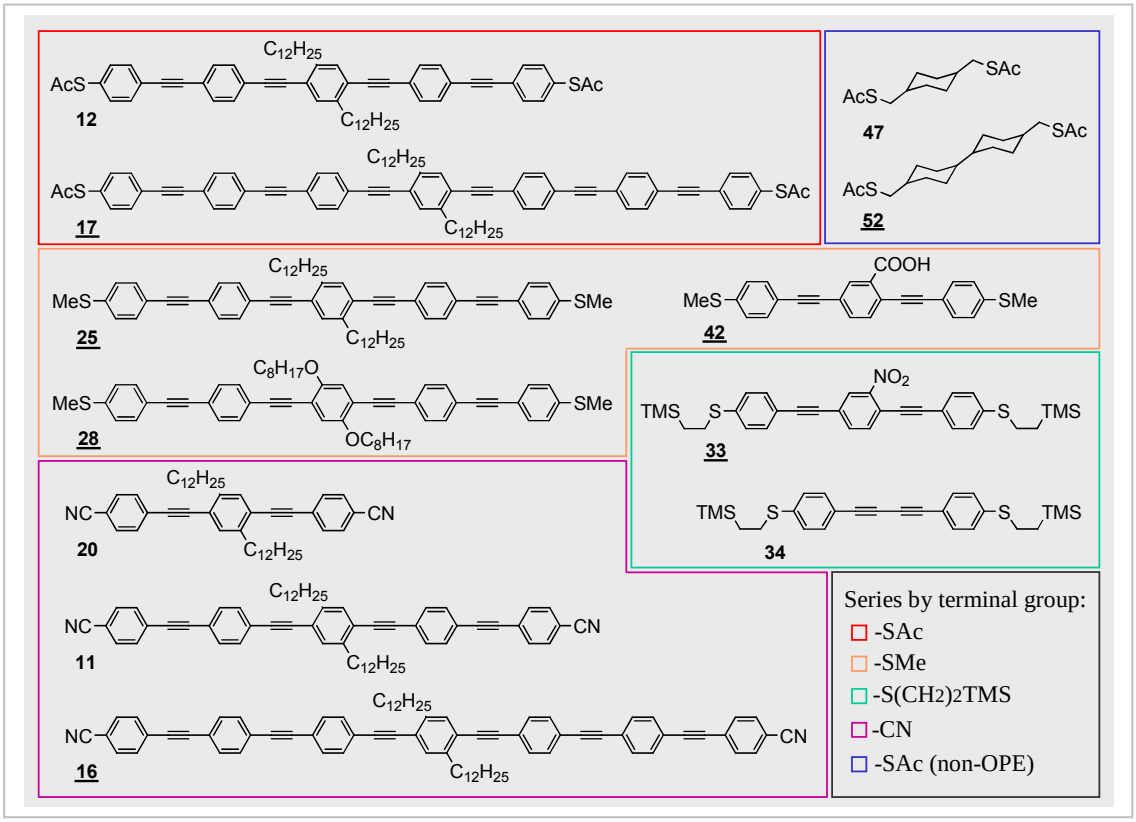

Figure 15. Small library of OPE MWs synthesized during this project. Twelve final compounds were produced, seven of which were NCEs (underlined numbers). The wires can be classified according to the terminal binding moieties (as in the Figure) or according to the length (i.e. 3-, 5-, 7-ring OPEs). Two of the wires were specifically designed for single molecule conductivity studies using STM (blue frame in the Figure and Section 2.4).

While it was found reasonably straightforward to produce hybrid MWs/NPs systems, MWs-only systems were not feasible: a significant piece of complementary information was thought to be the electrical characterization of the wires using single- or few-molecule techniques, reason for which preliminary work using STM and the I(s) technique[23a] was carried out. By using the reference molecule ODT adsorbed onto flame annealed Au substrates, typical current jumps could be observed (Figure 16), which were attributed to the attachment / detachment of ODT molecules between the STM tip and the substrate. Although a statistical analysis of the jumps was not carried out, differently sized jumps could be appreciated, accordingly with the results reported by Haiss[89]. An automated software routine for the characterization of the current jumps should be developed in order to standardize the jump picking criteria; matching of the results from reference compounds with those reported in literature would justify the application of the same testing method to the determination of the single molecule conductivity for the MWs reported here. The data accessible via the STM method are considered essential to the understanding of the conductivity properties of hybrid MWs/NPs networks in which each electrical path is composed of many conductive elements assembled both in series and parallel connections.

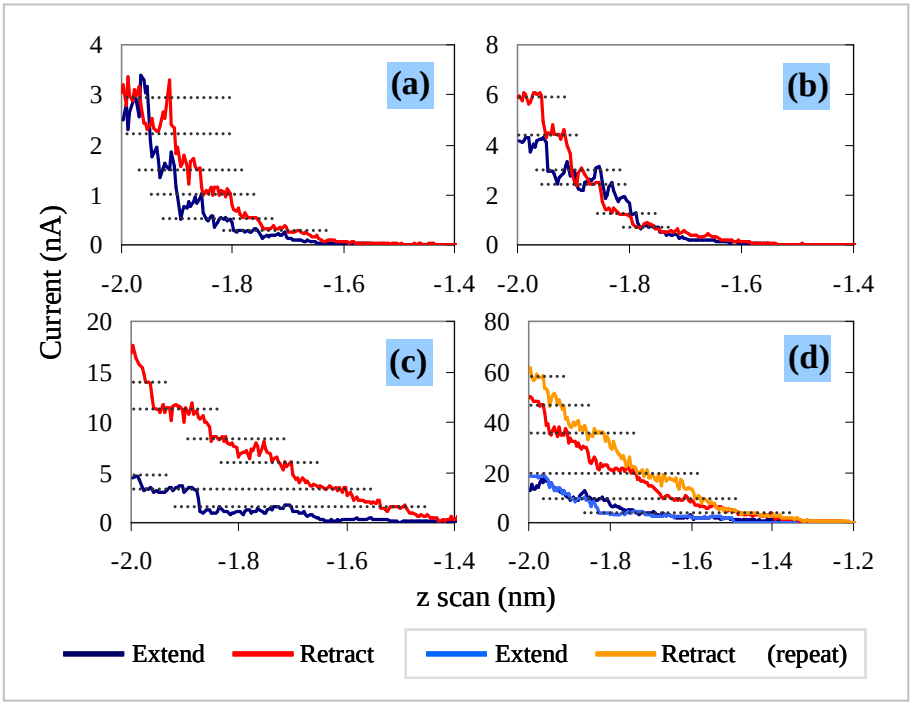

Figure 16. Current jumps obtained from ODT using STM and the I(s) technique. Dotted lines have been arbitrarily used to mark plateaux and current steps: (a)-(d) measurements at different locations on the substrate; in (d) repetition of the measurement yielded similar responses. Conditions: flame annealed Au substrate and tip; the substrate was soaked for 10 s in ODT 50 µM (MeOH); bias voltage (U_0) and setpoint current (I_0): 300 mV, 2 nA ((a), (b)); 150 mV, 10 nA ((c), (d)). Acquired on a Veeco Nanoscope III STM.

Chapter 3 – Electrical characterization: Methods and Apparatus.

3.1 – Basic theory and outline.

A silicon based Multiple Micro-Electrode Array (MMEA) device, fabricated by conventional optical lithography methods, was chosen as the physical substrate for the study of the assembly and electrical properties of the materials of interest.

The micro-scale conductive assemblies were produced / deposited on the array by various means, and electrically characterized by DC current measurement under a constant applied voltage (typically 1 V or 0.1 V). Occasionally voltage sweep methods were employed. The square geometry of the array (electrodes along the sides) allowed for measurement over different interelectrode gaps. According to Ohm's law, knowing the current (I) and the applied voltage (V), the resistance (R) can be derived from:

$$R = V / I$$

Two-electrode sets were employed for characterization purpose (2-probe method), and therefore the measured R equals the sum of the material resistance (R_M) and the two contact resistances (R_c):

$$R = R_M + 2\ R_c$$

In the ideal case of the conductor being ohmic and the contact resistances being identical, the proposed set-up would allow for the determination of the contact resistance and the sample resistivity (ρ). Briefly, R is measured at different inter-electrode gaps and plotted against the gap size; if a linear correlation is found, the slope (a) of the fitting equation represent the resistivity, and the intercept (b) with the y-axis twice the contact resistance (R_c):

$$y = a\ x + b$$

$$y = \rho\ x + 2\ R_c$$

This method, suitable for the characterization of homogeneous ohmic conductors, could not be applied in the context of this study. It was not possible to find such linear relationship in any of the assemblies characterized, the main reason being the inhomogeneous conduction intrinsic in the films / assemblies produced. Indeed some evidence for a large variability in the contact resistances within the same assembly

was found (preliminary data, not reported). Test experiments using Ferrocene (sub-Section 3.4.2) suggested differences in electroactive surface among the electrodes.

Averaging was employed at two different levels: for each potential input applied, a number of raw samples (n_1) were automatically integrated in the software in order to reduce the output file size; this produced a (n_2) number of output samples that were averaged again to provide a value representative of the current at that determinate input. The (n_2) data set was used as a whole only when the measurement produced a quick and steady response; when large capacitive settling was observed, only the second half (or the last quarter) of the set was averaged, so to provide a current value as close as possible to the I_{ss}. When current / voltage or current / distance data are presented, each current point represents the average of (n_2) samples acquired at a specific channel and applied voltage (see Section 3.4 for further details).

Because of the complexity of the system under study, and since a more detailed analysis of the particular mechanisms of conduction was not the primary aim of this project, most of the data presented in the next chapter have been discussed mainly in a qualitative form; except than in few cases, no theoretical model was found to explain the distribution of data. Where data relative to the characterization of the measurement system have been presented the simple equation R = V / I was sufficient as no contact resistances had to be taken into account.

3.2 – Microelectrode Arrays.

A silicon-based Multiple Micro-electrode Array (MMEA) was used as the physical substrate for the assembly studies. The device, fabricated by conventional optical lithography methods, featured a square array of microelectrodes continuing into tracks and mm-scale contacting pads. Despite Innos Ltd. being the initial contractor, the devices used for the majority of the experiments were produced by J. Gardner (Warwick). The change of contractor came as a result of the slow delivery times encountered, themselves a consequence of a series of procedural mistakes on behalf of Innos Ltd. During the period of about 1 year under the first contract three batches of the MMEA were produced, all of which turned out unsuitable for the proposed application. The first version, as originally conceived, featured 40 micro-electrodes disposed around a square platform 50 x 50 μm^2 in size; a large square back-electrode at the center of the platform provided a mean for ‘gating’ the device (Figure 17).

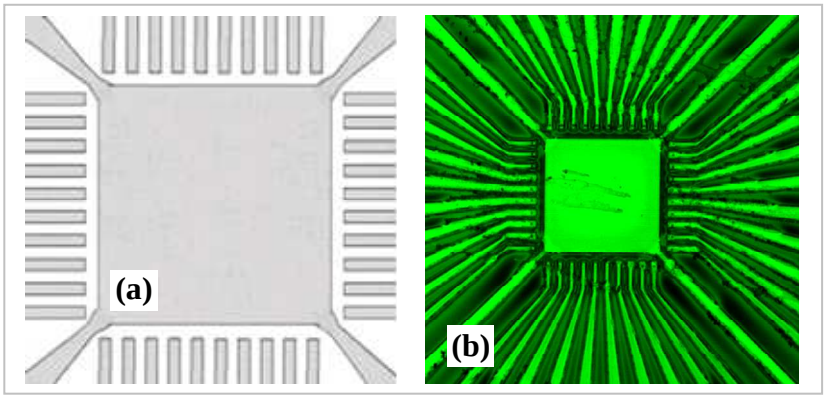

Figure 17. MMEA design, Innos, version 1. a) Schematic of the array, 40 microelectrodes and one central back-gate electrode; b) Confocal microscopy picture of the array (HeNe source): the via-holes for electroplating the electrodes can be spotted at the end of the tracks. The square array measures approx. 50 x 50 μm^2.

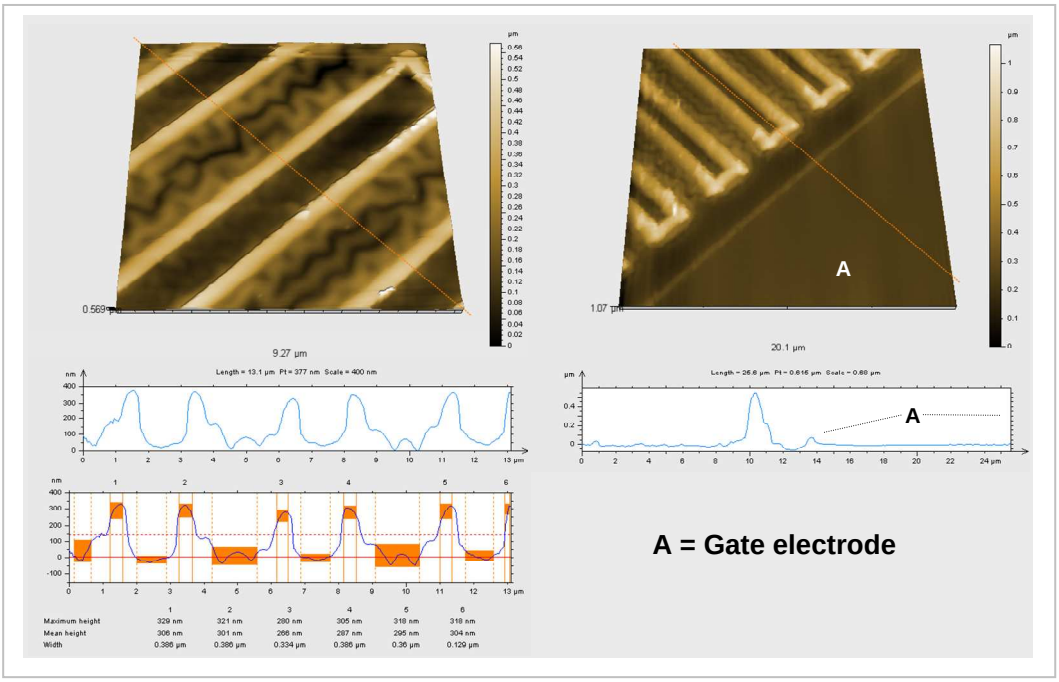

Figure 18. AFM images[90] of the MMEA surface: the resist coating the gold structures aimed at producing a flat surface; disc microelectrodes were later to be electroplated at the tip of the gold tracks (through holes appositely etched in the resist). Notice the presence of 'horns' at the edges of the tracks and of the central gate electrode.

When the device was released for testing it was not yet completed, requiring the final electroplating step to form disc (or hemispherical) microelectrodes. For this purpose via-holes were etched through the resist at the end of the tracks (such holes are barely visible in Figure 17b), and an additional track connecting all the devices on the wafer was included in the design (so that they could all be electroplated with a single connection). When it was characterized by AFM (D. Marsh[90], BrainCHELL Nottingham), the analysis of the surface geometry highlighted some unexpected

features: the side and tip edges of the tracks were decorated with characteristic horn-shaped features (see the height profile plots in Figure 18). These were the direct result of the reactive ion etch process (RIE) used to define the metal structures, contrarily to the requested chemical etch. Such geometry made the device unsuitable for the study of two-dimensional assemblies; because of the complications encountered with the proposed fabrication route this design was discarded.

The second design of the device involved dropping the central gate, increasing the central area (to 100 x 100 μm^2) and forming square-shaped microelectrodes simply by leaving exposed the tips of the tracks (Figure 19b). Although the fabrication consisted only of well established procedures, the first batch of the new design was found to have all the gold tracks electrically connected through the (doped) Si base. The origin of this anomaly was traced back to the very first step of the production, when the oven for the thermal growth of the SiO_2 dielectric had been mistakenly filled with N_2; this resulted in the successive deposition of Ti and Au straight onto the Si substrate. Apart for this, the device geometry was found to comply with the design, and therefore a new batch was produced.

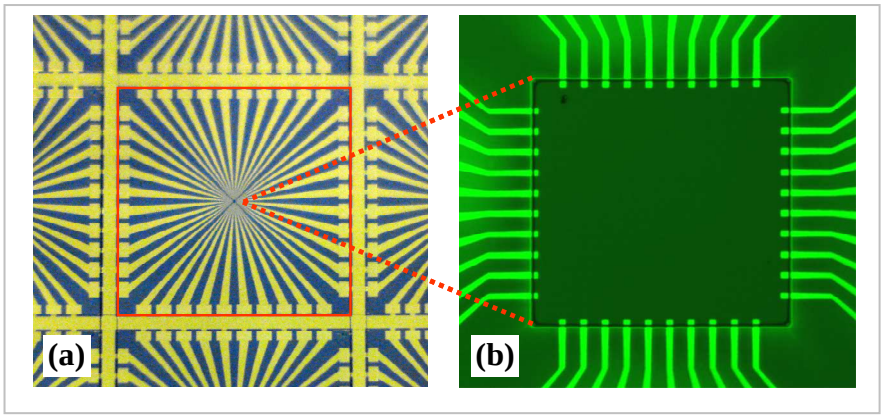

Figure 19. MMEA design, Innos, version 2 (3rd batch): a) Picture of part of the wafer showing one device (red frame) and the electroplating track connecting it to the neighbour devices; b) Confocal microscopy picture of the array (HeNe source). Materials: central platform, SiO_2; bright features, Au tracks; top insulating layer, SU8 resist. The square array measures approx. 100 x 100 μm^2; the dotted lines show its location on the device.

However the electroplating track, introduced in the first version and with no practical use in the second, was still present when the wafers from the new batch were diced (Figure 19a). This resulted again in short circuits being formed between the individual gold tracks and the underlying silicon substrate. The leaking pads on the devices could be mapped by connecting the drain (0 V) to each of the 40 pads consecutively (Figure

20), with the device lying on a flat aluminium base addressed as the source electrode (+ 3 V): since the bottom face of the device is also coated with the dielectric SiO_2, the electrical continuity in this pad-to-base configuration derives from the same kind of mechanical damage responsible for the Au-to-Si leaking.

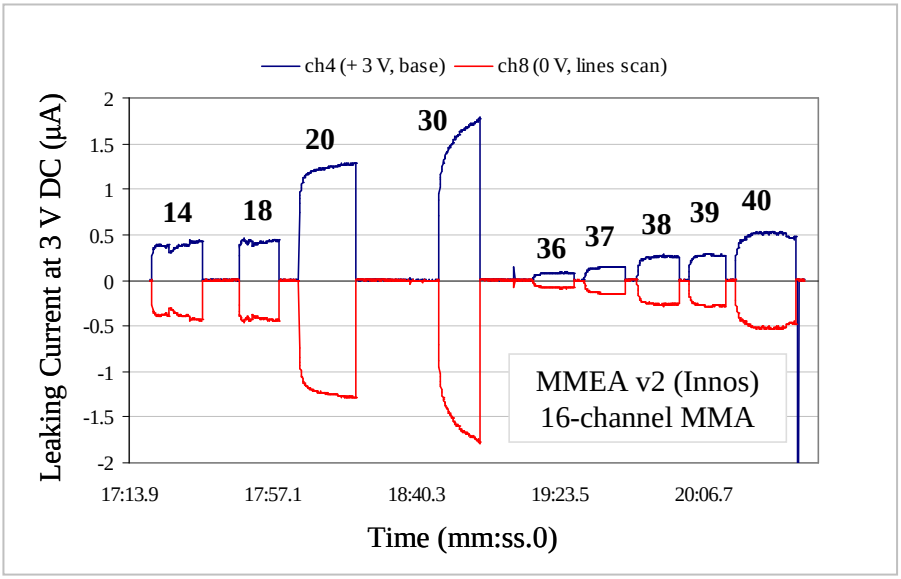

Figure 20. Typical line scan to identify leaking pads, recorded using the Multichannel Microelectrode Analyzer (16-channel MMA, discussed in a later section) and the MMEA v.2 (Innos). Connections: channel 4 (+ 3 V, source) to base (back-electrode), channel 8 (0 V, drain) is used to address the pads sequentially. This test shows 9 leaking pads out of 40 (numbers in bold are electrode assignments).

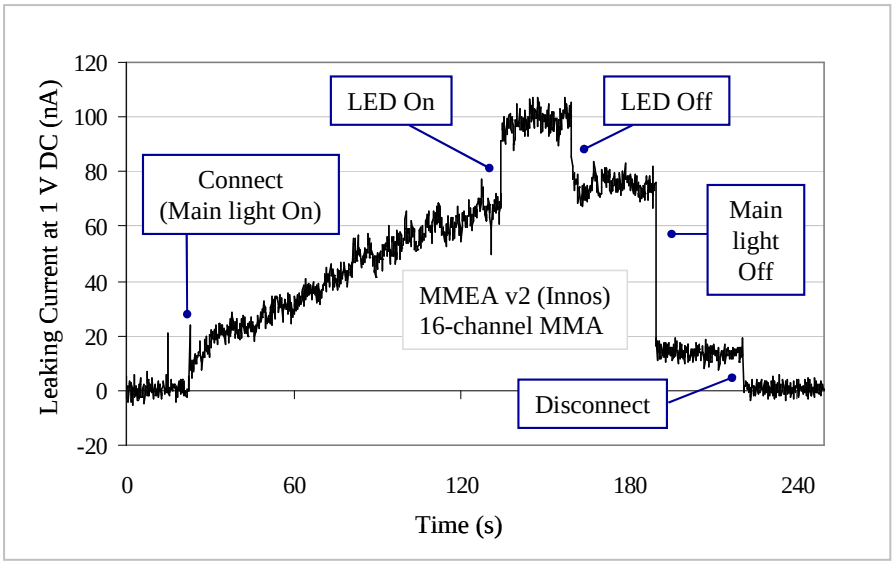

Figure 21. Light-dependence of the leaking current recorded using the Multichannel Microelectrode Analyzer (16-channel MMA, discussed later) and the MMEA v.2 (Innos). Connections: channel 4 (+ 1 V, source) to pad 3, channel 8 (0 V, drain) to pad 10 (cross-platform leaking path, insulating base). Notice a residual current of about 15 nA after the lights were switched off.

The proposed leaking path was confirmed when it was possible to record a light-dependant increase in the leaking current (Figure 21); light-dependant conductivity is a well-known property of semiconductor materials (p-doped Si in this case).

Irreproducibility in the leaking current was often found: some non-leaking pads could start leaking after testing or vice-versa, complicating any attempt towards pre-characterizing the devices. The use of a relatively high test voltage such as + 3 V DC, aimed at either 'stabilizing' or resistively burning the leaking paths, did yield a few consistent results. However the 'mapped' devices still presented a number of pads amenable to leak current up to the μA-range; the devices found to be 'non-leaking' could possibly leak current below 1 nA, the resolution of the test system at the time (see later Section). Although the devices have been used for the first experiments with CP (Conducting Polymer) on a micro-scale electrode array (see sub-Section 4.2.2), there was no point in using them for the electrical characterization of the assembly produced. The already quite complex problem of identifying the contribution of the various contact and network resistances would have become impossible to deal with in presence of leaking paths in parallel with such resistances (and through a semiconductor). A new contractor was found, and the design was further minimized in order to increase the dies/wafer yield and compensate for the loss of resources occurred in the previous contract.

The third version of the MMEA (Figure 22; produced by J. Gardner, Warwick) repeats the design of the previous version, with some differences. It features a 4x5 electrode array (instead of 4x10) with a platform area of 50x50 μm^2 (as in the original design); the device measures about 0.5 x 0.5 cm^2 (a quarter than the previous, with a 4-fold increase in the production yield); Si_3N_4 was used as the top insulating resist, making the device suitable for cleaning with strong oxidizing agents (not possible with the organic SU8).

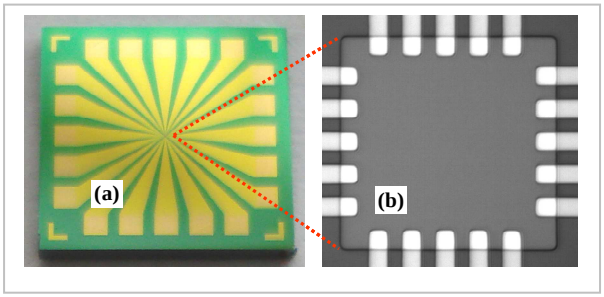

Figure 22. MMEA design, J. Gardner, version 3: a) picture of the device, size ~ 0.25 cm^2; b) optical microscopy image of the array (dotted lines show its position on the device), size approx. ~ 50 x 50 μm^2 (the exposed window measures exactly 67 x 67 μm^2, the electrodes 6 x 6 μm^2 , SEM data[90]). Materials: central platform, SiO_2; bright features, Au tracks / micro-electrodes; top insulating layer, Si_3N_4.

The devices were produced using either gold or platinum as the electrode material, with the intention of studying the assembly of MWs (see Chapter 2) on two different metals. As already mentioned (Section 1.3) we could not use this array to test the MWs produced, exception made for the testing of MWs/NPs films produced by G. Rance in Nottingham (sub-Section 4.4.3). It was indeed used to study the assembly of other conducting materials, particularly CPs and NTs (Chapter 4). Despite the difference in standard potential between the two metals (+ 1.52 V for Au, + 1.19 V for Pt; vs SHE), the differential measurement method resulted in no significant differences being noticed for the two metals. The devices have therefore been used interchangeably, noting the electrode material.

In order to fix the electrode assignment all the dies were routinely marked before use (in one corner on the back, using a diamond tip): consistency in the orientation of the die when this was connected for measurement / imaged enabled the correlation of the visual information with the electrical characterization data (see next Chapter).

3.3 – Probe Station.

The microelectrodes on the device were addressed by simultaneously connecting all of the pads on the die: commercial probe cards (Figure 23; Probe Technologies), mounted on a home-built probe station, or a commercial spring-socket connector (Figure 24; Aries Inc.), served this purpose.

The 20-pin connectors (Figures 23b and 24), acquired when the final MMEA device became available, mounted coaxially shielded cables. Further reduction of the EMI noise was achieved by limiting the length of the cables (maximum ~ 1 m) and by placing the probe station inside a Faraday cage (Figure 25). Such expedients allowed for the use of the lowest measurement ranges when using the electrical apparatus described in the next section; leaking currents < 1 pA at 1 V were typical for the devices and consistent with the reported PCB and cable resistances (> 1 TΩ).

Optical microscopy images and videos of the array while connected to the system could be obtained by using a confocal microscope with a long working distance objective (13 mm WD; Figure 26 A). A digital camera (monochrome, 1.3 MP) was used for video acquisition. A vibration-free environment for the microscope (Figure 25 B) and the probe card (Figures 23 and 26 B) could be attained by placing

the whole probe station (weight ~ 13 Kg) on a vibration-insulation platform (Figure 25 D).

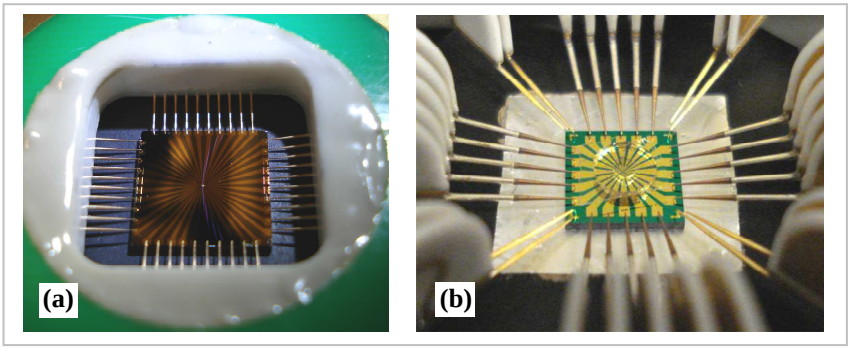

Figure 23. Probe Cards, close-up view of the probe area with connected device: a) non-coaxial, with MMEA v.2 (40 electrodes, array size 100 x 100 μm^2, device size ~ 1 cm^2); b) coaxial, with MMEA v.3 (20 electrodes, array size 50 x 50 μm^2, device size ~ 0.25 cm^2; the circular structure at the centre of the device is a removable solvent chamber).

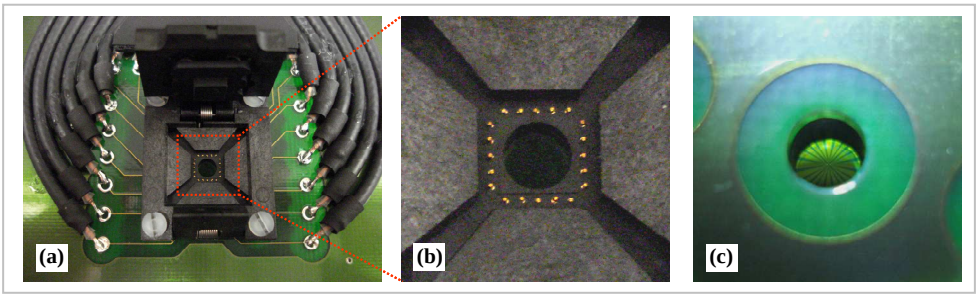

Figure 24. Spring-socket Connector: a) whole socket (open, without MMEA) mounted on custom-made PCB, coaxial connections start a few centimeters away from the device; b) close-up view of the device slot; c) socket in use with MMEA v.3 (20 electrodes, array size 50 x 50 μm^2, device size ~ 0.25 cm^2), top view. The device is placed face-down in the socket that is clamped and then reversed. The circular window for accessing the device measures ~ 3 mm in diameter.

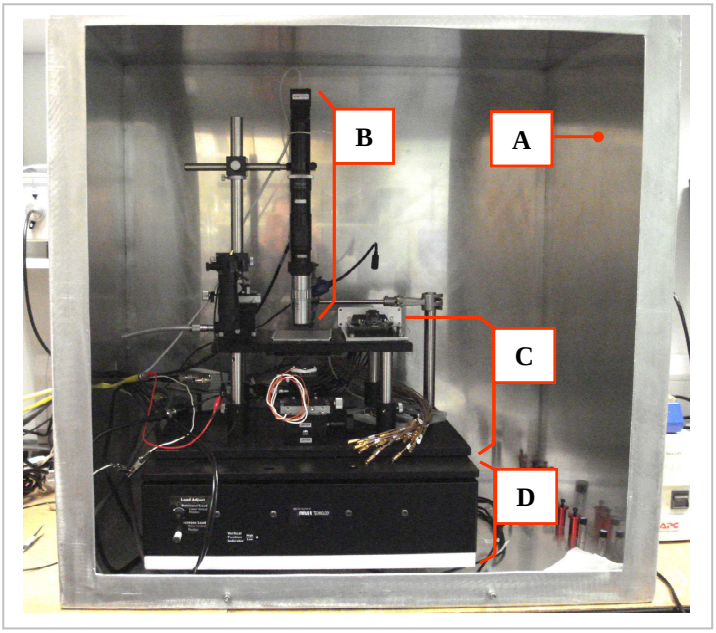

Figure 25. Apparatus for the electrical connection of the MMEA devices and the microscopic monitoring of the array: **A**. Aluminium Faraday cage (lid not shown); **B**. Confocal Microscope (halogen source); **C**. Probe Station; **D**. Vibration-insulation Platform.

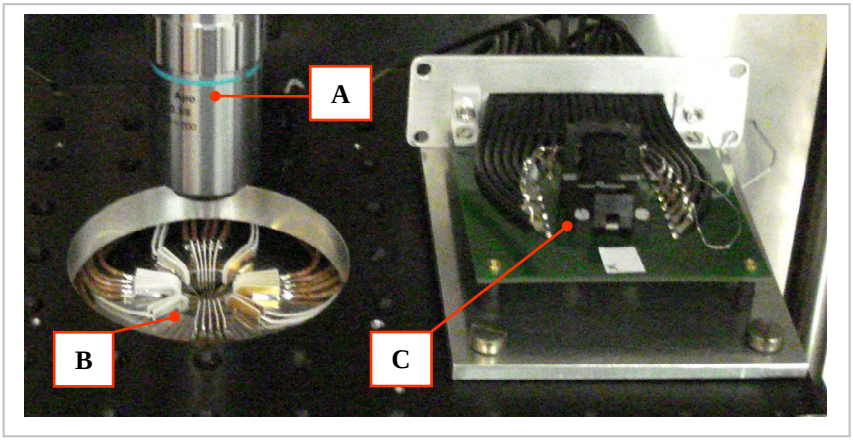

Figure 26. Close-up view of the Probe Station (see also Figure 25): **A**. Long Working Distance microscope objective (13 mm WD) for imaging the array while the device is connected (microscope retracted in the Figure); **B**. Low-noise Probe Card (see also Figure 23b; only one probe card at a time can be fitted on this probe station); **C**. Spring-Socket Connector (see also Figure 24), it can be fixed or free standing (by unfitting the aluminium slab).

Experiments in solution could only be video-recorded when the device was connected via the probe card. The larger accessibility to the device allowed for the use of a micro-volume solvent chamber (Figure 23b): this was assembled by positioning a silicone gasket (square-ring) onto the die, filling its bore with a micro-pipette and sealing the top with a portion of glass cover slip. It was found that images of reasonable quality could be obtained only by using cover slips (thickness ~ 0.1 mm) and gaskets not thicker than 0.5 mm: the use of a higher column of solvent and/or a thicker glass slide resulted in the build-up of optical interference and consequent loss of optical resolution (cloudiness). The volume of the chamber was therefore limited by both the maximum allowable height of the chamber (0.5 mm) and the dimensions of the die: on the 0.25 cm^2 devices a gasket with 3 mm OD, 1 mm ID and 0.5 mm thickness was used, resulting in a volume of ~ 0.4 µL. An additional limitation of this solvent chamber system was the onset of swelling even with non-aggressive solvent such as MeCN. The swelling determined loss of seal and intake of air: when the forming bubble reached the field of view the experiments were generally stopped. With the MeCN / silicone gasket system experimental times as long as half an hour could be obtained, although with poor reproducibility in the solvent chamber performance (even a tiny dust particle would cause the seal to fail within the first few minutes). Swelling was obviously more severe with solvents such as benzene, toluene or DCM, required to solubilise the MWs produced in the synthetic part of the project (Chapter 2). Since microscopic observation was not required for the MW systems,

fluorosilicone gaskets were produced for use with the spring-socket connector: these were meant to provide a seal between the device and a section of Teflon tubing (length ~ 15 mm) fitted into the bore of the socket (diameter ~ 3 mm). Despite the specifications for the fluorosilicone elastomer reporting a maximum swelling of only 20% after one week (soaking in jet fuel), swelling was found to occur within the first few minutes of soaking (in toluene or DCM), making such approach unpractical. The limits imposed on the volume of solution, the experimental time, and the choice of solvents available for the experiments could be overcome by appropriate design of a microfluidic solvent chamber with high chemical tolerance.

3.4 – Instrumentation.

3.4.1 – Electrical testing of low-dimensional materials in air.

Commercial instruments for the low-level electrical characterization of the materials object of study were acquired from Keithley. The model 2636 dual Source Monitor Unit (SMU) can apply DC voltage down to a resolution of 5 μV (effectively ~ 500 μV when considering the accuracy and the noise), while measuring the current with a digital resolution of 1 fA and accuracy of +/- (0.15 % reading + 120 fA). In order to automate the measurement, and scan different electrode sets without having to interfere with the apparatus, a System Switch Multimeter was acquired, again from Keithley. The model 3706, mounting a 3721 dual 1 x 20 multiplexer card, allowed for any set of the 20 electrodes to be addressed in a 2-point configuration, using one SMU channel on the 2636. An alternative configuration, such as the 4-point method, was not implemented: the anisotropy in the conductivity at the micro-scale makes this method more suitable for (relatively) large area band-microelectrode arrays, on which many parallel conducting paths can short the two electrodes. In the context of this study (2D conductive organic networks), and with the 20 electrode array used as platform, a 2-point scan of all possible conductive paths between the electrodes (190, avoiding repetitions) provided sufficient information about the degree of homogeneity of the conductive network, the stability of the connections, and the possibility of reconfiguration.

Automation of the scanning routines was implemented using the built-in processing capability of the instruments: user-defined scripts (.tsp) can be uploaded into the machine, where they are compiled by an internal processor and executed. The 2636 is connected to the computer via a GPIB interface, and to the 3706 via TSP-link.

With this configuration a script is loaded into the 2636 that functions as the ‘master’; when the test routine starts the 2636 addresses the 3706 (the ‘slave’) with switching instructions, and records the data without any need for communicating with the computer; when the routine ends the data are printed to the computer screen and saved. Because of the large amount of data collected during each test, the routines were configured as to print to screen after each switch-measure operation. As an alternative LabVIEW could be used to control the instruments and automatically save the data; however this option was not exhaustively explored.

The values obtained from the instrument are the result of hardware-based integration of the acquired signal: the power line frequency (50 Hz) is automatically detected, and the instrument samples over time windows that are multiples (or fractions) of a power line cycle (PLC); the hardware sampling frequency is not clearly stated in the specifications but is assumed to be ~ 5 KHz, the sampling rate at the minimum PLC setting (0.001 PLC) when in source/measure mode. The most commonly used setting is 1 PLC, delivering an apparent sampling rate of 50 Hz: this means that the instrument integrates ~ 100 raw samples (n_1) and outputs an average sample (n_2) each ~ 20 ms [NPLC x (1 s / 50 cycles)]; higher PLC values were not used because they were not found to significantly improve the S/N ratio. In order to obtain a single representative current value per measurement a number of (n_2) samples (typically in the range 50-200) was acquired and averaged; when capacitive settling predominated only the second half of the data set was averaged, so to have a value as close as possible to the steady-state current. Standard deviation was not reported for the (n_2) samples because the accuracies with which the voltage is applied and the current read (n_1 samples) are characteristic of the instrument, reported in the specifications. In many experiments the measurement (n_2 data) did not yield a stationary reading but multiple conductive states close together, in which case the average constitutes a value representative of the overall conductivity across the path. Standard deviations for the so generated (n_3) samples have also not been reported because of equivocal interpretation.

Since the duration of each measurement is approximately the same (once set the number of PLC and the number of (n_2) samples), and since each (n_2) data set is averaged to obtain a single value, no timing information was generally acquired. Timestamps were only used to elucidate the operational control of the Keithley instruments, and occasionally for frequency analysis of EMI affecting the signal. Time

overheads were always associated with range switching (meant to let the system settle), and had to be taken into account when plotting the current traces: the overheads were appearing in the single variable plot as spurious current jumps, typically observed in correspondence of the range switch thresholds (100 pA, 1 nA, 10 nA, 100 nA, 1 μA). While these were generally ignored, all the jumps taking place within the same current range (and above the noise background) were instead attributed to physical modifications in the conductive path subject to measurement.

The main limitation of the characterization system just described is the switch board (Keithley 3721 mounted in the 3706), not designed for delivering currents in the lower pA and sub-pA range: still, when the system (2636-3706-3721-probe card / Aries socket) was tested in open circuit configuration, the background current (due to noise and characteristic leaking) was found typically lower than 0.5 pA (with ~ 0.5 pA standard deviation). Slightly improved resolution could be attained by replacing the 3706 with a custom-made switch board[91]: the use of high quality / low leaking relays reduced the typical background current to less than 1/3 pA. The switch board was specifically designed for the testing of 'nanogap' devices (not reported here), and allowed for 10 electrodes to be addressed as source, with the other ten working as drain (at ground potential; 10 nanogaps / device). Since it could not address the whole MMEA, it was not used for the characterization of conductive assemblies: nonetheless it represents a valuable alternative (to more sophisticated switch cards) for the measurement at the sub-pA level on multiple micro- and nano-electrode arrays (MMEAs and MNEAs).

The resolution of the 2636-3706 system was considered adequate for the characterization of the materials object of study, and extensively used for the electrical test of conductive networks (in air, at r.t.). The source-measure instrument described in the next section (MMA), needed principally to address all the electrodes simultaneously, also aimed at achieving similar or better resolution in the low pA range.

3.4.2 – Multi-channel Microelectrode Analyzer[92] (MMA).

Achieving independent control of the potential applied to the electrodes, so to coherently drive/direct the assembly of conducting connections, turned out to be a significantly harder challenge. In order to continuously address all the electrodes in the array with a determinate potential pattern, while monitoring the current flow

through the system, a multi-channel potentiostat - amperometer was needed. The available commercial solutions were deemed unsuitable, mainly because of the low number of independent channels, a limited operational flexibility, and the cost (expensive multi-channel systems analogous to the one employed here are commonly employed for medium/high-throughput testing applications in the semiconductor industry). To overcome the lack of easily accessible instruments, the design and production of an application-specific Multi-channel Microelectrode Analyzer was undertaken: the work was done in collaboration with Prof. B. Whitaker and P. Kapetanopoulos (University of Leeds; part of the CHELLnet project), that took charge of most of the practical aspects related to prototyping, basic testing and software implementation.

In order to identify circuit configurations and electronic components suitable for the application, several multi-channel electronic circuit boards were produced at intermediate stages of this project. Only the final 20-channel MMA and the first 16-channel prototype are discussed here; testing of the intermediate prototypes and the complete design process have been omitted because of minor relevance for this discussion. In all cases the MMA featured multiple independently addressable potentiostats, each configured as a zero resistance ammeter (ZRA), and was PC-controlled. Additional details about the circuit design, fabrication, and prototype testing can be found in P. Kapetanopoulos's PhD Thesis[92].

The first version of the MMA (16-channel) was operated using a single DAQ card (NI PCI-6229) with 4 D/A channels. In this version each D/A channel addressed a set of 4 lines, for a total count of 16. Each line could be independently addressed by mean of relays (controlled by the same 6229 card), so that any number of lines could be switched on/off; the number of different voltage inputs was limited to 4 as the number of D/A channels on the card. In the latest design (20-channel, 20 voltage inputs), to extend the capability of the system and apply voltage independently to each electrode, an additional DAQ card (NI PCI-6703) with 16 D/A lines was introduced. The NI cards were PC-operated using LabVIEW and controlled the hardware, composed by 2 motherboards each mounting 5 x 2-channel plug-in PCBs (Figure 27). The digital resolution and input/output range, respectively 16 bit and +/- 10 V, were identical on both cards. The LabVIEW code, initially developed by P. Kapetanopoulos[91], became later object of this study in the attempt to solve some operational problems accompanying the MMA in its latest release (principally random

failures and delays in applying the signal; these were caused by race conditions between drivers addressing the same card).

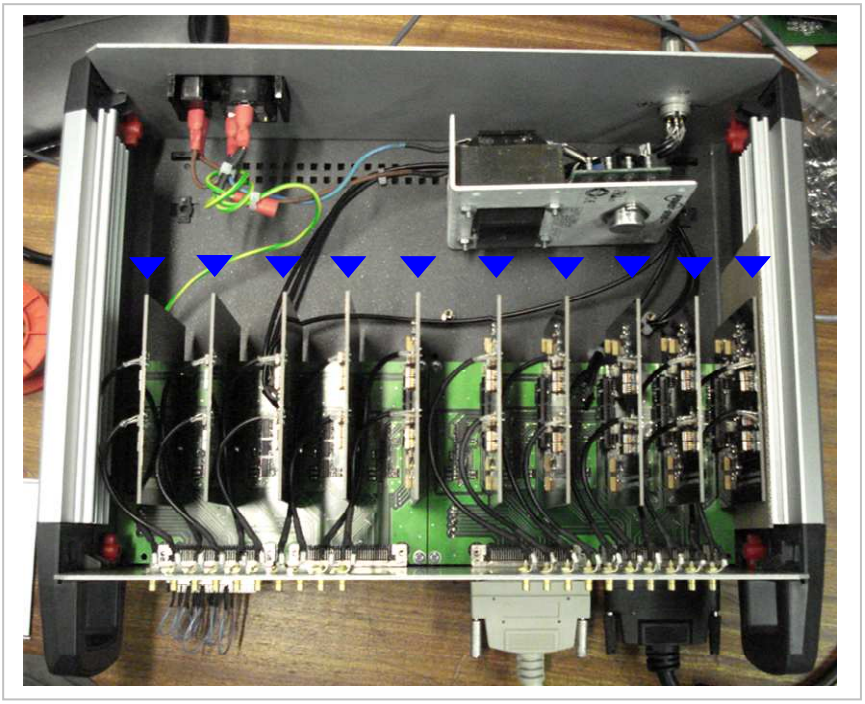

Figure 27. MMA (20-channel, 3 ranges): modular assembly from pluggable 2-channel PCBs (arrows). The top panel was removed to show the internal assembly.

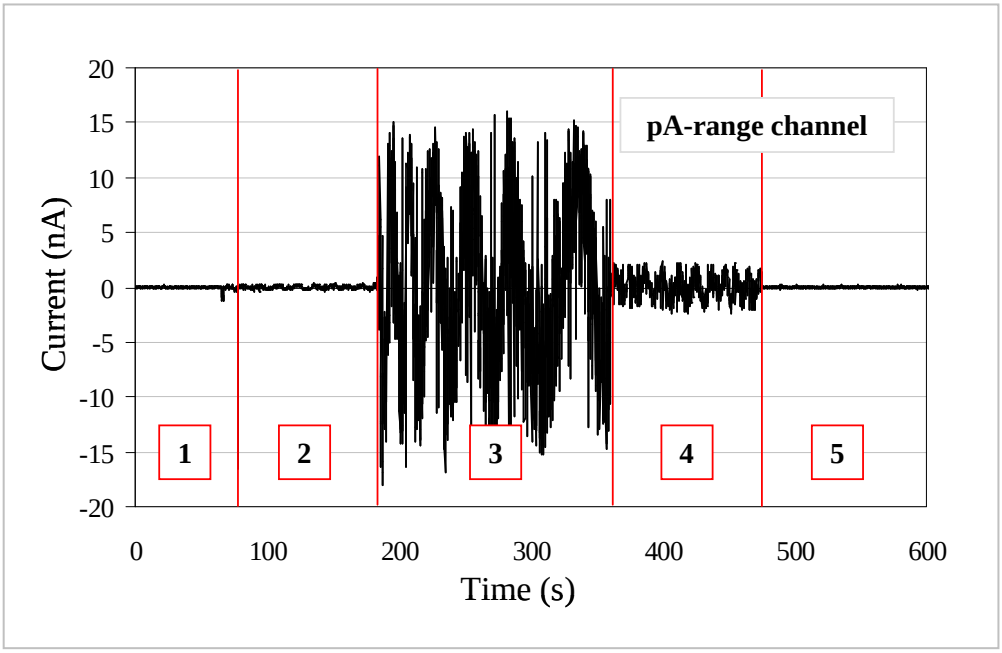

Figure 28. Effect of cabling and shielding on the EMI pick-up of a medium gain channel (open circuit; 16-channel MMA, 3 range / gain settings): (**1**) 20 cm long cables, noise +/- 100 pA; (**2**) additional 10 cm cables on breadboard, +/- 300 pA; (**3**) additional 60 cm cables to probe card, +/- 15 nA; (**4**) shield cables (tin foil) and ground, +/- 2 nA; (**5**) ground also the microscope / probe station, +/- 120 pA (p-p noise).

Using the ZRA design all the electrodes could be operated in differential mode, with the sum of the current flowing into the system through the input electrodes equaling the total current exiting at the output electrodes. The direction and the amount of current at each electrode would be determined by the absolute potential difference between the active electrodes and by the resistance of the conductive path. Since a positive test voltage was usually applied to the (source) electrodes it made sense to define as inputs the anodes, and as current the flow of positive charges, therefore adopting the classical convention for the direction of the current flow. A positive voltage produced a positive current when electrons were extracted out of the system and into the source electrode. Although such a system is conservative, and the amount of current flowing should only depend on the applied voltages, parasitic currents up to hundreds of pA could be observed during system testing. These could be attributed principally to EMI induced noise, and minimized by shielding (Figure 28).

Efficient shielding of the cabling and the connectors was found to be a basic requirement for the proposed application: coaxial cables and connectors were routinely employed in the later versions (for testing and for all the experiments with the final MMEA, v.3). A Faraday cage was used to house the probe station and to provide basic EMI shielding; when needed, further shielding was attained by closing the working access with a removable door. Further expedients were needed in order to avoid spurious current, such as avoiding handling the cables before the measurement (tribo- and piezo-electric effects) and use a common earth point for the instruments and the shielding (to avoid ground loops). Nonetheless the source switching operation generally produced a higher response as consequence of the circuit and cables capacitances, both in the commercial instruments and in the MMA.

In order to produce a flexible instrument, one of the main objectives was to widen the dynamical range as much as possible. This was achieved by switching the current entering each ZRA through different feedback resistors, each providing different scaling of the signal; a number of four was deemed appropriate to test the concept. The resistors employed measured approximately 316 Ω (R1), 82 KΩ (R2), 22 MΩ (R3) and 5 GΩ (R4) (R abbreviations also used as assignment for the ranges). By using different combinations of resistors ‘low gain’ and ‘high gain’ versions of the boards could be produced. Two 20-channel MMAs were produced simultaneously toward the end of this project, and they mounted respectively low gain (R1, R2, R3) or

high gain PCBs (R2, R3, R4) only; nonetheless any combination of useful ranges could be easily implemented within the same device.

Since the NI cards measure voltage, a calibration procedure was needed to convert the acquired signal into current data. Calibration of the device was accomplished by measuring the IV response at each channel and range through an appropriate known resistor (tested with the Keithley 2636; forcing current method with the current chosen as to produce similar measured V drops across the different resistors; the average of three runs was used as the R value). Only the calibration of the high gain MMA is reported here; a similar method was also used for the low gain version. Resistors with values (nominal value, tolerance) of 999,413 Ω (1 MΩ, 5 %), 49,505,027 Ω (50 MΩ, 10 %) and 7,086,652,200 Ω (10 GΩ, 30 %) were employed as the load, respectively, for ranges R2, R3, R4. Scanning the V between +/- 5 V (starting and finishing at zero) produced a current (measured by the NI cards as a voltage drop across the feedback resistor, in mV) that was averaged and plotted against the calculated current response (in μA); linear fitting of the data produced 'slope' and 'offset' values per each channel and range (essentially for each of the 60 feedback resistors in the instrument). These values were stored as a text file and used in the software to automatically convert the signal so to output current data (in μA: the output unit can be changed by appropriately scaling the values in the calibration file). The average slopes (one per range) derived by this method were used to estimate the dynamic range of the device. Setting the DAQ cards input range to +/- 10 V resulted in a digital resolution of 0.3 mV / bit, having both cards 16-bit resolution. The resolution of the device was found acceptable on ranges R2 and R3 (standard deviation ~ digital resolution, [92]), but partially limited by electrical noise on range R4 (standard deviation ~ 5 mV, [92]). The theoretical bottom limits for the three ranges were calculated (in μA) by multiplying the average slopes from the calibration for the 1-bit value (0.3 mV), and found to be 3.66 nA (R2), 13.6 pA (R3) and 78 fA (R4). The theoretical top limits are then derived by multiplying the bottom limit for the digital resolution (that is 65536 for a 16-bit converter; Table 3).

Range (feedback R, Ω)	**R2** (82K)	**R3** (22M)	**R4** (5G)
Max. measurable I (theoretical, 16 bit ~)	240 μA	890 nA	5.13 nA
Min. measurable I (theoretical, 1 bit ~)	3.7 nA	14 pA	80 fA

Table 3. Allowable measurement ranges on the MMA (20-channel, high gain version). Electrical noise limited the actual resolution to ~ 1.5 pA (best case).

To avoid repeated switching between two adjacent ranges (i.e. because of noise or unstable conductivity) a virtual 'Schmitt trigger' was implemented in the software and used for auto-ranging. By partially overlapping the ranges, two regions could be defined in which a varying signal would not induce range switching; the measurement continued using the set range until the signal exceeded its high or low threshold. In order to protect the op-amps from saturation (i.e. during 'spike' events and range switching), the maximum input voltage the card would read, before switching to a less sensitive range, was set to 3.5 V. To avoid measuring in the least sensitive region of the range, the bottom threshold for range switch was set to 10 mV, about 30 times the digital resolution (~ 5 bit). As a result of these constraints the dynamical range of the device was reduced with respect to the theoretical range; Figure 29 shows the ranges (converted to current) and the overlap regions. Although the use of the 'Schmitt trigger' routine did produce the expected response, anomalous range switching was sometimes observed; this could be possibly caused by EMI interference with p-p values in the nA-range.

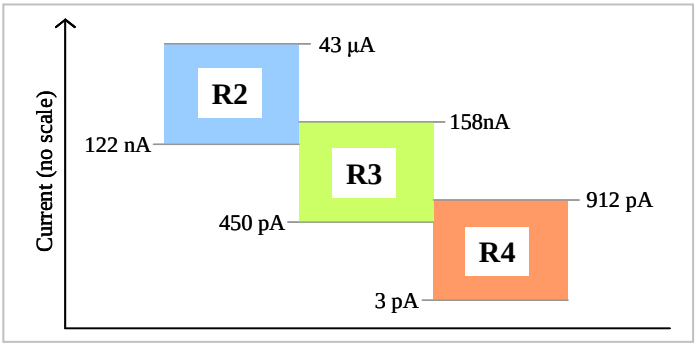

Figure 29. Dynamical range when the MMA (20-channel, high gain version) is operated using a 2-threshold auto-ranging routine. Ranges R2 and R3 (low gain end) overlap by ~ 35 nA, R3 and R4 (high gain end) by ~ 450 pA. The working range is used until the signal exceeds its high or low threshold.

A cut-off threshold was set at 43 µA (3.5 V input on R2), and any channel saturating R2 was automatically switched off and kept in this state. At the low end of the dynamic range no threshold was set, and the measurement continued when the input was below 10 mV. This allowed us to characterize the background current of the device using a typical scan protocol. A typical 2-point scanning routine (+1 V DC, 190 measurements, 200 (n_2) samples/measurement) was executed in open circuit configuration, with nothing connected to the MMA. In order to check for internal leaking also the data from the drain channels were analyzed. Most averages lied

within +/- 2 pA, consistently with the reported accuracy; the slightly larger standard deviation observed on the source signals was interpreted as instability caused by the voltage being applied in absence of a load (i.e. through the > 1 TΩ load characteristic of the internal circuitry). Drifts in the order of tens of pA were sometimes observed and attributed to switching and electrical noise (source switching typically resulted in 'spikes', suggesting the need for longer settling times at some specific switching points in the scan).

In order to test the instrument in a real application it was decided to perform cyclic voltammetry analysis of the oxidation of ferrocene in MeOH, using TBAP as supporting electrolyte. Although appropriate reference electrodes were not included in the design, mainly because of constraints related to the solvent systems of interest (non aqueous-based), the use of a large CE (Pt wire) yielded data consistent with the literature. A 250 μm diameter Pt wire was connected to one of the channels and used as common drain (or CE/RE in a 2-point electrochemical set-up). To avoid field-induced distortions the non-addressed electrode was connected to the adjacent electrode-channel: this resulted in 18 channels addressing single microelectrodes, 1 channel addressing a 2-electrode array, and 1 channel balancing the current flow through the Pt wire CE; according to this set-up the current recorded at the 2-electrode channel was halved when the data were analyzed. The potential on the 20 microelectrodes was scanned simultaneously from 0 to 1 V and return (5 mV increment, scan rate 52 mV/s) while recording the current. The scan was executed four times, and settling between runs was observed for all channels (Figure 30 shows one representative channel). The current at 0.4 V in the last forward scan (oxidation of ferrocene to ferrocenium, Cp_2Fe^+) was then used to compare the electrode responses.

Analyzing the data two observations could be made: similar currents were obtained at the electrodes situated on the same side of the array (Figure 31); such electrodes presented significantly different areas, dividable into four groups (Figure 32).

According to Figure 32 the representative electrode width x was measured and its square taken as the unit area for an ideal square microelectrode; the relative area of the electrodes in the groups A-D was then estimated with respect to x^2. A high fraction of the dies were affected by misalignment between the electrode array and the square window in the top resist layer; although the electrodes width (aimed 5 μm; found 6 μm, SEM data[90]) was found to comply with the accuracy of the photolithographic

process (+/- 1 μm), the misalignment resulted in a +/- 2 μm variability in the electrodes length (the dimension along the main axis of the track).

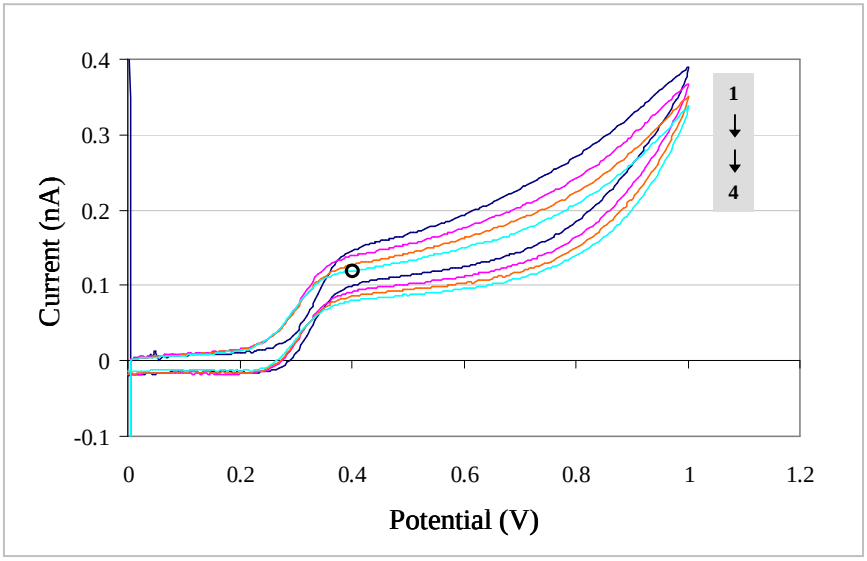

Figure 30. Cyclic voltammetry of Ferrocene (0.1 mM) in MeOH; supporting electrolyte TBAP (10 mM); scan rate ~ 50 mV/s, increment 5 mV. Four consecutive scans on the same electrode are shown; the current at 0.4 V in the last forward scan is used to compare the electro-activity of the microelectrodes.

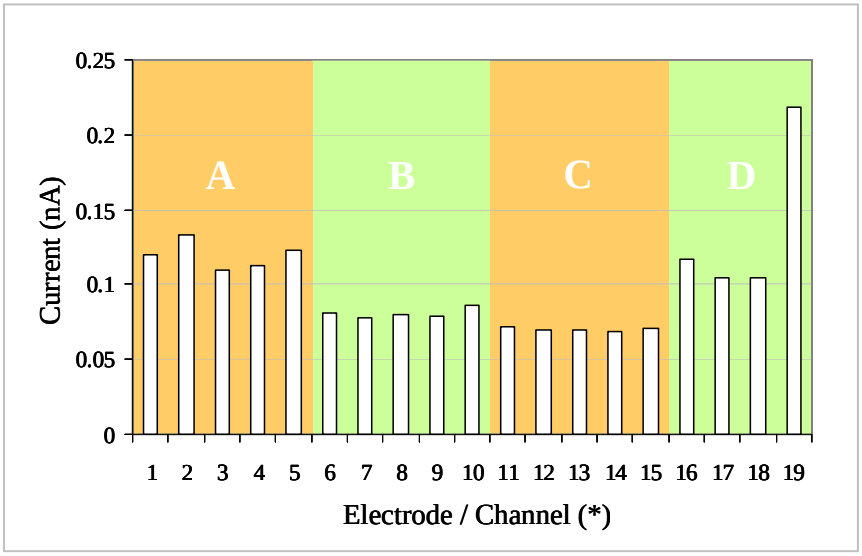

Figure 31. Cyclic voltammetry of Ferrocene (0.1 mM) in MeOH. The currents at 0.4 V in the last forward scan are shown for all the electrodes: four groups (A-D) can be identified and associated respectively to the 5-electrode arrays (sides of the square array, see next Figure). (*): channel 19 addressed 2 electrodes (19 and 20) simultaneously (recorded current double than at the electrodes in the same group).

When the average current was plotted against the relative area, for each group A-D, a linear correlation was found between the apparent surface area and the measured current (Figure 33). The fact that the standard deviation increased with the apparent

area suggests a larger difference in electroactive area on the larger microelectrodes. Attempts to clean the dies and improve the uniformity of the electrode surfaces were unsuccessful (Piranha, O_2 plasma), suggesting contamination of the microelectrodes with inorganic material (top resist Si_3N_4).

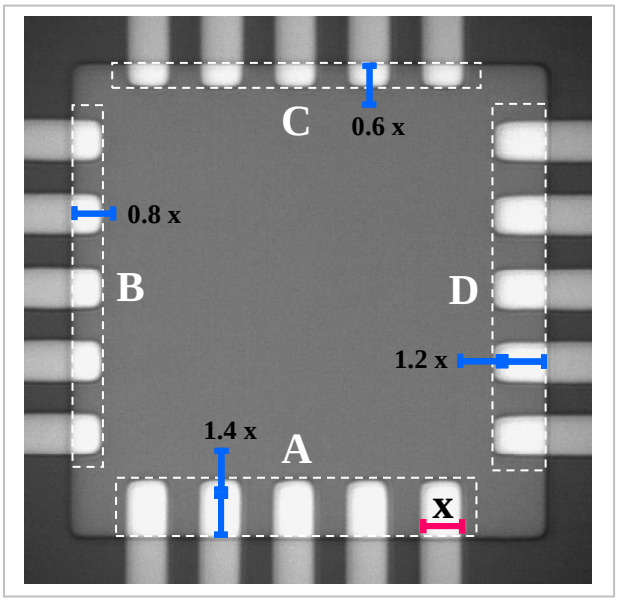

Figure 32. Optical microscopy image of the MMEA used for the cyclic voltammetry experiment with Ferrocene (see also Figures 30 and 31): electrodes with different surface area are divided in 4 groups (A-D) and their relative area is determined. Scale bar (x) 6 µm.

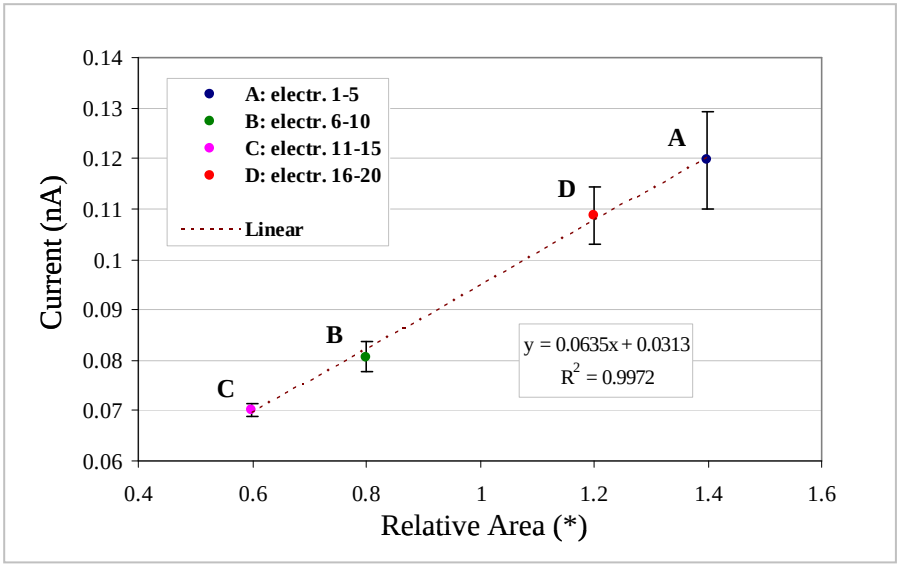

Figure 33. Averages of the current at 0.4 V (last forward scan) recorded during cyclic voltammetry of Ferrocene (0.1 mM) in MeOH. Each point represents the average current at the electrodes in each of the groups A-D (defined in Figures 31 and 32). (*): unit area 36 µm^2.

A direct comparison of the MMA and the Keithley system performance in the testing of conductive assemblies in air was also attempted, although with some limitations. The complexity of the task of designing, prototyping, testing and assembling the MMA resulted in the production only being complete toward the very end of this project. The network assemblies used for comparing the two instruments had been produced some time earlier, and were typically showing a general decrease of the overall conductivity, possibly attributed to oxidative degradation during testing and storage. As a result, no linear correlation between the data acquired on the two instruments could be found. A preliminary analysis of the data sets using statistical methods suggests the discrepancy between the two measurements being consistent with the accuracy of the MMA (Figure 34; most differences between the two measurements lying in the range +/- 20 pA and center of the Gaussian fit at 7 pA).

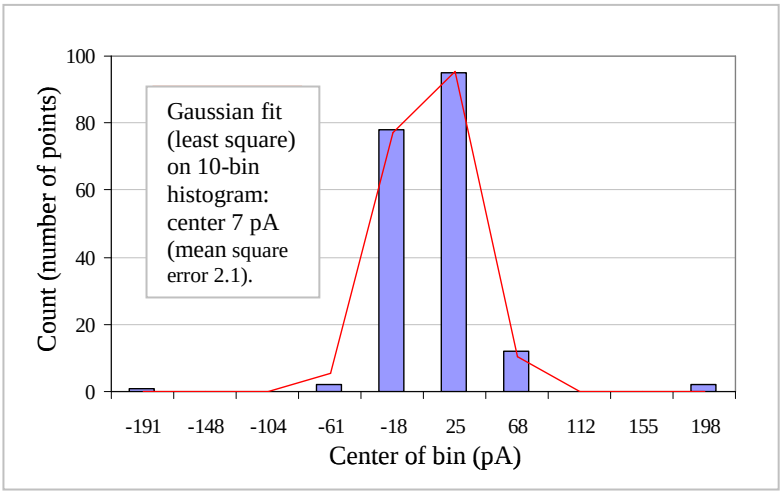

Figure 34. Histogram of the differences between the open-circuit current measured with the MMA and with the Keithley system (190 data points).

Although the instrument could have been used for the directed assembly and evolutionary training of NT/CP networks (see next chapter), conductive in the nA- and µA-range, the time constraints, and the impossibility to deal with large amounts of data within this project, precluded this approach. Further characterization, aiming to improve the S/N ratio, and the upgrade of the software interface, aiming to web-based data exchange with the CHELLware group in Nottingham, will be needed in order to enable the evolutionary study of the assembly of micro- and nano-structures on MMEAs.

Chapter 4 – Methods for the production of μm-scale 'physical' Neural Networks.

4.1 – Assembly of 2D conducting networks on MMEAs.

As mentioned in the Introduction, the principal aim of this project has been to produce and electrically characterize quasi-2D networks of organic conductors, setting the basis for the study of neural network-based computation using organic and hybrid materials. The dimensions of the network object of investigation were defined by those of the MMEA used to connect it to the electrical instrumentation: as previously described (Chapter 3.2) a MMEA with 20 microelectrodes along the sides of a 50 x 50 μm^2 square SiO_2 platform was used as the final test bed. Although the electrical testing simply involved the analysis of the conductivity pattern of the networks (when a capacitive response was evident this was deliberately omitted in the analysis), the proposed methodology can be virtually applied to any kind of molecular device (switches, diodes, capacitors, etc.), given the appropriate assembly procedure and test routine. It is worth to notice here that while testing the resistance of the paths in the network only requires one measuring channel (and at least two electrodes addressed at once), a thorough analysis of the network-like structure of these assemblies would only be possible when all the electrodes are addressed simultaneously: the production of the MMA (described in Chapter 3.4.2) and the automation of the testing routines / data analysis constituted the preliminary steps in such direction, but there was not enough time to use them significantly within this project.

Mainly 'bottom-up' fabrication procedures were employed, particularly the directed-assembly of conducting connections (micro- and nano-wires) under a DC or AC potential field, and the self-assembly of films of nano-components at the interface between immiscible liquids or at the air-water interface. Specifically, the principal constituents of the assemblies produced were one of the following:

a. PEDOT (poly-3,4-ethylenedioxithiophene), electrosynthesized via either AC or DC conditions, using Na PSS, $LiClO_4$ or TBAP as the supporting electrolyte (Section 4.2);
b. NTs assembled by dielectrophoresis (DEP) and in presence of EDOT monomer (without supporting electrolyte; Section 4.3);
c. NTs (produced by D. Marsh[93] and assembled into films by us); NTs and NTs/NPs hybrids (materials and films produced and transferred by D. Marsh[94]); NPs and MWs/NPs hybrids (materials and films produced and

transferred by G.Rance[95]); all assembled into films using the interfacial assembly technique and transferred to the MMEA post-assembly (Section 4.4).

In all cases the conductivity patterns were found to be fairly constant, although some variability could be observed. A general decrease in conductivity, characteristic of PEDOT assemblies, was mainly ascribed to oxidative degradation during storage / testing (in air). Multiple conductivity states were often observed in NTs assemblies: in this system repeated testing highlighted slight changes in the conductivity pattern mainly ascribable to reconfiguration of the connections in the network, and to a less extent to the degradation processes. The NTs assemblies were also found to reconfigure upon cyclically scanning the voltage applied to the paths, with a general increase in conductivity and a stabilizing effect on the connections.

4.2 – Directed Assembly of Conducting Polymer Networks by Electrosynthesis.

Among the variety of monomers[5c] that could be electrochemically polymerized to obtain highly conjugated conducting materials, we have chosen 3,4-ethylene-dioxythiophene (EDOT), a bicyclic thiophene derivative, mainly because of the high conductivity and excellent air stability of the polymerized product (PEDOT)[96, 97]. Both properties arise from the unavailability of the β heterocyclic positions to the attack on behalf of free radicals (polymerization mechanism shown in Scheme 14), leading on one side to increased regioregularity in the polymeric backbone (only α-α bonds and non-branched chains are possible), and on the other to increased stability of the product.

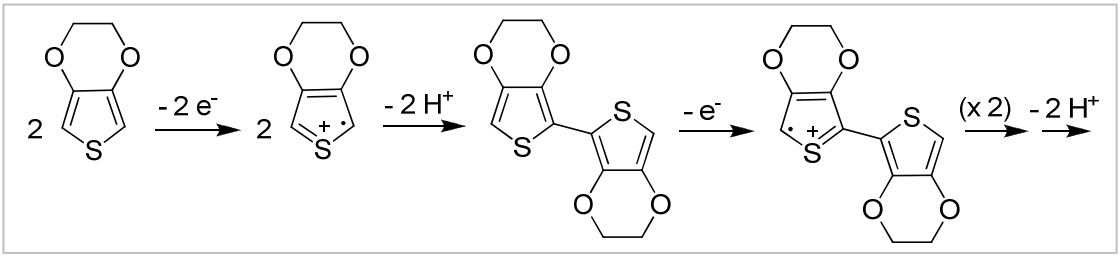

Scheme 14. General mechanism for the formation of PEDOT: the oxidation of EDOT monomer and soluble oligomers produces free radicals that propagate the polymerization reaction.

Other important properties of this polymer are its low band gap[97], resulting in electrochromism, and its poor solubility in many different solvents. The electro-chromism proved useful to interpret the video information from the polymerization process; the poor solubility was critical to obtain solid aggregates in the solvents used (mainly water/MeCN and neat MeCN). The fact that the insoluble polymer could be

doped[97], becoming itself the working electrode, allowed for off-electrode polymerization and enabled the fabrication of conducting connections between the electrodes.

The polymerization of conducting polymer aggregates in off-electrode fashion to produce functional networks has some precedent in literature. Most of the work on this concept was reported by Fujii[39], indeed there are both earlier[98] and later[99] reports using similar approaches; it should be pointed out that while in these works a ring-electrode cathode was used (as the CE), aiming principally at producing radial patterns with fractal morphology, in our case the focus was on producing directional polymerization patterns bridging the active electrodes. This has been recently accomplished by Thapa[100] using a methodology very similar to that employed here. Since none of the assembly procedures attempted by us was able to reliably reproduce the directional polymerization, such as in [100], few emphasis has been put on the assembly method. Most of the conditions employed, either DC or AC voltages, resulted in the formation of polymer interconnects, although not exclusively between the electrodes addressed; as explained later, AC voltages higher than 2 V were generally preferred. The use of AC potential has been employed to date mostly for the dielectrophoretic assembly of various polarisable materials (mostly nanoparticles[44], nanotubes[45] and nanowires[101]). Indeed some of the results of this work and the existing literature[100, 38] strongly suggest it may be the only useful approach for the directed assembly of conducting connections from ionic or monomeric solutions.

During preliminary studies both DC and AC electropolymerizing conditions were evaluated, and only the AC conditions turned out useful for the production of such interconnects. The use of DC potential was found capable of inducing off-electrode polymerization at the anode, but the connection was usually prevented by the vigorous gas evolution occurring at the cathode (electrolysis of water). When AC conditions (very low frequency) were employed, the off-electrode polymerization occurred at both electrodes and the final connection was usually established away from the electrodes (where the gas evolution took place). During the assembly the colour of the growing branches was observed undergoing the characteristic voltage-dependant cycling: a dark-brown / black colour was evident during the cathodic half-cycle, indicating electroneutrality in the polymer (absorbing in the centre of the visible spectrum); this turned to pale-blue (clearly discernable when over Pt electrodes) during the anodic half-cycle, consistently with the colour reported[97] for the p-doped

state (absorbing in the NIR region of the spectrum; formed at potential higher than 0.25 V *vs.* Ag/AgCl). Although the existence of the n-doped state (at potential lower than -1.9 V *vs.* Ag/AgCl) was also reported[97], no colour change was attributed to the polymer in this state. When AC signals of amplitude sufficient to induce p-doping at the anode and n-doping at the cathode were employed (i.e. larger than 2 V_{pp}), this always resulted in one electrode turning dark while the other turned to transparent blue.

It should be noticed that the gas evolution, depending upon the presence of a significant amount of water in the system, makes the water/MeCN solvent system non-ideal for the kind of experiments proposed. Although this issue was later resolved by using MeCN-only systems (in the μm-scale experiments, sub-Sections 4.2.2-.3 and Section 4.3), some experiments carried out on mm-scale with the water/MeCN system have been here reported to highlight some consistent features in the assembly process.

4.2.1 – Preliminary work: assembly of PEDOT connections on home-made MMEAs with mm-scale interelectrode gaps (2- and 4-electrode).

To preliminary test the electropolymerization approach on a larger and more accessible scale, some experiments with PEDOT were run on home-made arrays of disc microelectrodes (see Experimental Section for the fabrication procedure). Although electrical characterization data were not acquired for most of these experiments, the video information could be used to highlight some features crucial to the understanding of the assembly mechanism.

Two types of MMEAs were produced as single units and repeatedly employed for several experiments. The arrays, namely A and B, were composed of a base (Teflon, A; glass, B) embedding 2 (A) or 4 (B) Pt wires, respectively 250 and 127 μm in diameter; only the transverse section of the wires was left exposed and served as the disc microelectrodes. After each experiment the microelectrodes were reactivated by polishing the array surface until clean metal was exposed.

Using the array A, a commercial signal generator (Velleman PCG10/8016) and an inexpensive camera microscope (IntelQX3), it was possible to produce directional PEDOT connections spanning across a 2 mm gap, while video recording the process (Figure 35). AC conditions and relatively high voltage (up to 10 V_{pp}) were found necessary to produce visible aggregates at both electrodes, and to initiate the directional growth.

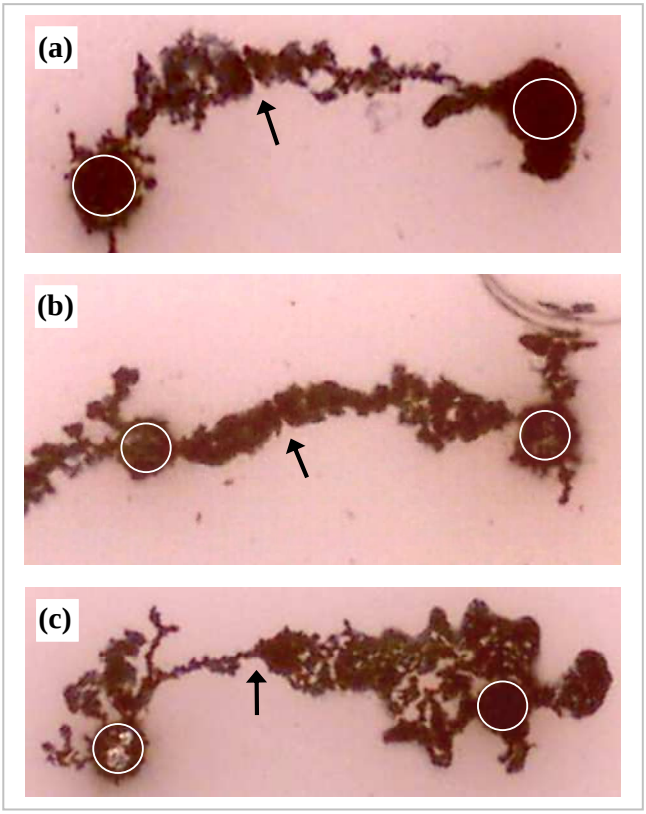

Figure 35. Conductive PEDOT connections between disc microelectrodes. **Conditions.** Solution: 3/2 EDOT 0.66 M (MeCN)/Na p-Tos 0.01 M (aq.). Assembly: square wave in all cases; 0.1-0.5 Hz, 4-8 V_{pp} **(a)**, 0.1-0.2 Hz, 8-9 V_{pp} **(b)**, 0.1 Hz, 8 V_{pp} **(c)**; in **(a)** and **(b)** the conditions were varied during the experiment. The arrows indicate the point at which short-circuit occurred, preventing further polymerization. Images **(a)** and **(c)** were taken after removal of the solution. The same array was used for the three experiments (shown at slightly different scales). Electrodes (white circles): Pt, diameter 250 μm, inter-electrode gap ~ 2 mm.

The successful fabrication of polymer interconnects shorting electrically the two electrodes was attributed to the influence of the applied electric field, capable to 'direct' the assembly preferentially in the area between the electrodes (that is also the region with the strongest electric gradient). Further evidence for the role of the electric field in directing the polymerization lies in the fact that the short-circuit point often assumed a synapsis-like morphology (see arrows in Figure 35 a, b): this was attributed to the sudden interruption of polymerization as the final connection formed, causing the electric potential to drop.

Although the experiments shown lasted about half an hour, the actual growth process (when successfully initiated) was found to be significantly quicker: the polymerization front typically moved away from the electrode at the approximate speed of 30 μm / wave cycle (forward speed at 0.1 Hz; at this speed the 2 mm gap would be bridged in about 10 minutes, under optimal conditions). Interestingly, in concurrence

with each anodic half-cycle, a dark-coloured polymerization wave could be observed being repelled by the forming aggregate; the fact that during the cathodic half-cycle the wave was bouncing back toward the polymer front led us to conclude it was composed by insoluble oligomeric cations (Figure 36). This would point out to a mixed assembly mechanism in which the aggregation of loose polymer chains plays a major role.

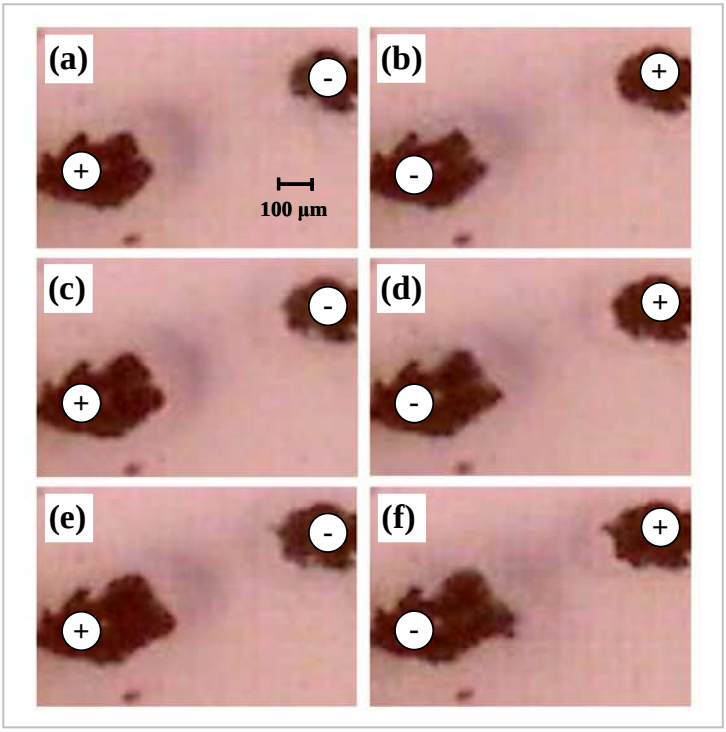

Figure 36. Directional off-electrode polymerization of PEDOT under an AC potential field. A magnified view of the centre of the aggregate in Figure 35 (b) is shown here. **Conditions.** Solution: 3/2 EDOT 0.66 M (MeCN)/Na p-Tos 0.01 M (aq.). Assembly: square wave 0.1 Hz, 9 V_{pp}. The sequence **(a)-(f)** shows the polymerization process during three consecutive cycles of the applied signal (images taken at each half-cycle): dark waves of insoluble, positively charged, oligomers are repelled by the polymerizing front during the anodic half-cycle, and attracted back during the cathodic half-cycle.

The effect of the polymerization/aggregation mechanism resulted more evident when a different kind of morphology, with evident 'wave front'-like aggregates, was also obtained under identical conditions (Figure 37); despite the difference in morphology, some consistent features could still be observed. Each anodic half-cycle produced bound polymer (doped and scarcely visible) and a dark polymerization wave, which was then attracted back during the cathodic half-cycle; the speed of growth was again about 30 µm / wave cycle (forward speed at 0.1 Hz); the polymerization occurred preferentially along the electric field gradient, and terminated as soon as the 'synapsis-like' connection formed (indicated by the arrows in Figure 37).

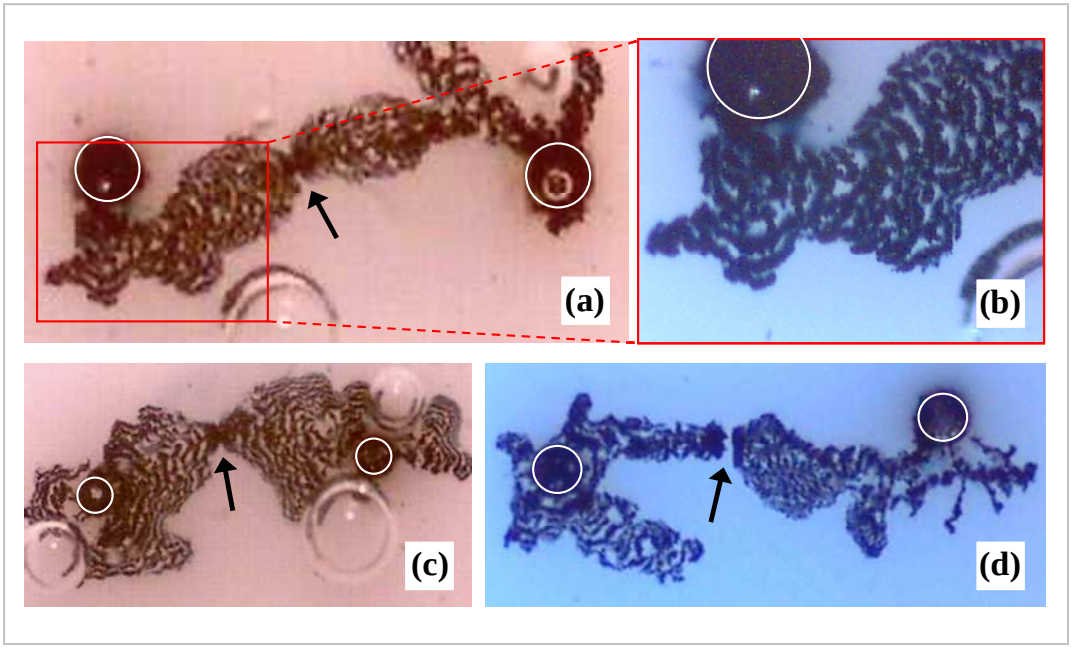

Figure 37. Conductive PEDOT connections between disc microelectrodes. **Conditions.** Solution: 3/2 EDOT 0.66 M (MeCN)/Na p-Tos 0.01 M (aq.). Assembly: square wave 0.1 Hz in all cases; 6-7 V_{pp} **(a)**, 8-9 V_{pp} **(c)**, 9 V_{pp} **(d)**; in **(a)** and **(c)** the conditions were varied during the experiment. In **(b)** the boxed area in **(a)** has been enlarged to highlight the 'wave front'-like morphology (the difference in colour arises from using a different source of light). The arrows indicate the point at which short-circuit occurred, preventing further polymerization: in **(d)** the final connection was evidently broken after removal of the solvent (still present in **(a)-(c)**). The same array was used for the three experiments (shown at different scales). Electrodes (white circles): Pt, diameter 250 µm, interelectrode gap ~ 2 mm.

Preliminary experiments on PEDOT electropolymerization in the presence of CNTs (MWNTs, Figure 38) were carried out using the same array (A). Only one experiment is reported here in order to illustrate some analogies with the PEDOT-only connections on the mm-scale: the reasons for using CNTs in this project are described in the Section dedicated to the µm-scale MWNTs networks (Section 4.3). Although some connections could be produced, the directional polymerization was harder to initiate, and the typical oxidation waves were less evident.

Directionality was retained, and the speed of the assembly process was unvaried (~ 30 µm / wave cycle, forward speed at 0.1 Hz), suggesting that not more than one layer of NTs (length ~ 30 µm) was incorporated at each cycle. Also the hybrid connection was subject to fracturing upon removal of the solvent, with the difference that multiple fracture sites were evident (while only the synapsis-like junction was typically interrupted in the PEDOT-only assemblies). This was attributed to the presence of bulk PEDOT-NT aggregates (not bound to the surface), that although able to provide conduction during the assembly, were not structurally strong enough to resist the

removal of the solvent. Since it did not provide any significant advantage in the assembly of mm-scale interconnects, the NTs/CP approach was temporarily discarded to be later applied to the fabrication of μm-scale interconnects (once the μm-scale MMEA became available).

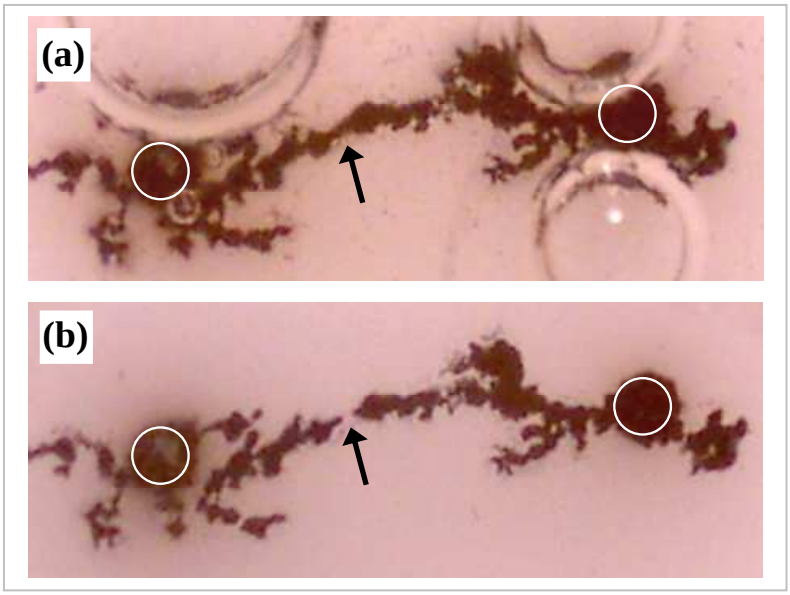

Figure 38. Conductive PEDOT/MWNTs connection between disc microelectrodes. **Conditions.** Solution: 4/1 [EDOT 0.25 M, MWNTs* 90 μg / mL (MeCN)]/Na p-Tos 0.01 M (aq.). Assembly: square wave 0.1 Hz, 4-10 V_{pp}. The arrows indicate the point at which short-circuit occurred, preventing further polymerization: in **(b)** other than the final connection, other fracture points resulted from removal of the solvent (still present in **(a)**). The same array shown in Figures 35-37 was used also for this experiment; electrodes (white circles): Pt, diameter 250 μm, interlectrode gap ~ 2 mm. CNTs* (source, product code, dimensions): MER, MRCMW: diam. 35+/-10 nm, length ~ 30 μm.

Using the array B (interelectrode gap ~ 1 mm) some PEDOT assembly experiments were repeated while measuring the current at one of the electrodes. In a typical experiment, an amperometer was connected in series with the signal generator and the microelectrode array. A square wave signal with very low frequency (0.1 Hz) was used as the source of potential, producing the expected oxidation and polymerization cycles at the two electrodes. This eventually resulted in the directional growth of polymer branches along the electric field gradient, and electrical connection at the contact point between the polymeric wires (Figure 39).

The use of electrolyte in μM concentration was found necessary to reduce capacitive currents at the electrode, and enable us to electrically detect the formation of the connection while in solution (graph in Figure 39). It should be noticed that upon connection the polymerization stopped: the large increase in current observed can only be ascribed to conduction through the polymeric wire (with an approximate resistance of

25 KΩ). When the solvent was removed and the aggregate rinsed, although no evident fracturing occurred, the resistance was found to increase (Figure 40; ~ 400 KΩ at + 3 V DC). It was also observed that testing in air under DC voltages higher than 3 V typically damaged the connection (Figure 40a), producing asymmetric IV response (Figure 40b: tested at negative voltage after than at positive voltage). According to these results the assemblies later produced were typically tested only in air (after drying and stabilizing for some days) and at a low DC voltage (1 or 0.1 V): as reported in Section 4.2.3, these expedients produced acceptably stable current readings.

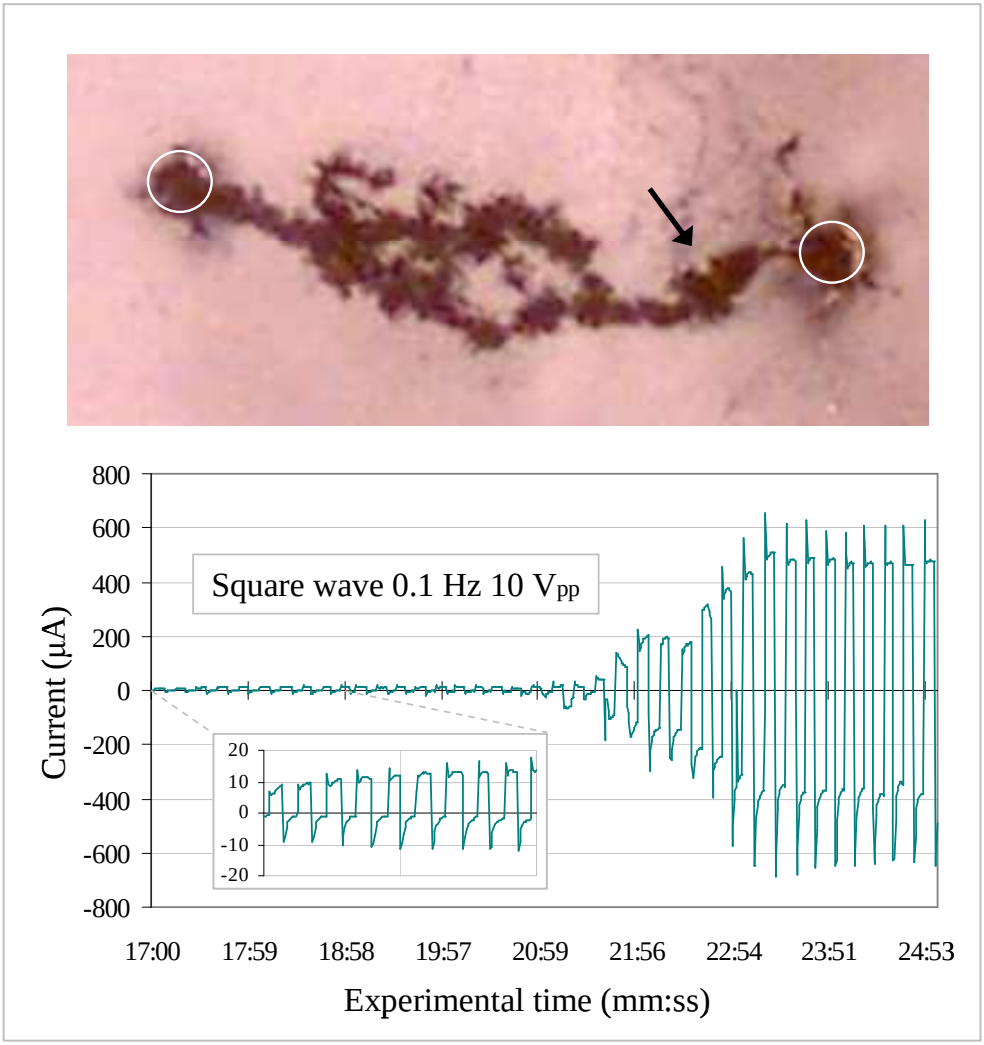

Figure 39. Conductive PEDOT connection between disc microelectrodes. **Conditions.** Solution: 3/2 EDOT 0.47 M (MeCN)/Na p-Tos 1 µM (aq.). Assembly: square wave 0.1 Hz, 8-10 V_{pp}. Most interconnect was grown at the left electrode, whose current trace during the experiment is shown: the inset shows the extent of the electropolymerizing current, the main plot shows the increase in current when the connection is formed. Two of the four electrodes of array B were used for this experiment; electrodes (white circles): Pt, diameter 127 µm, interelectrode gap ~ 1 mm.

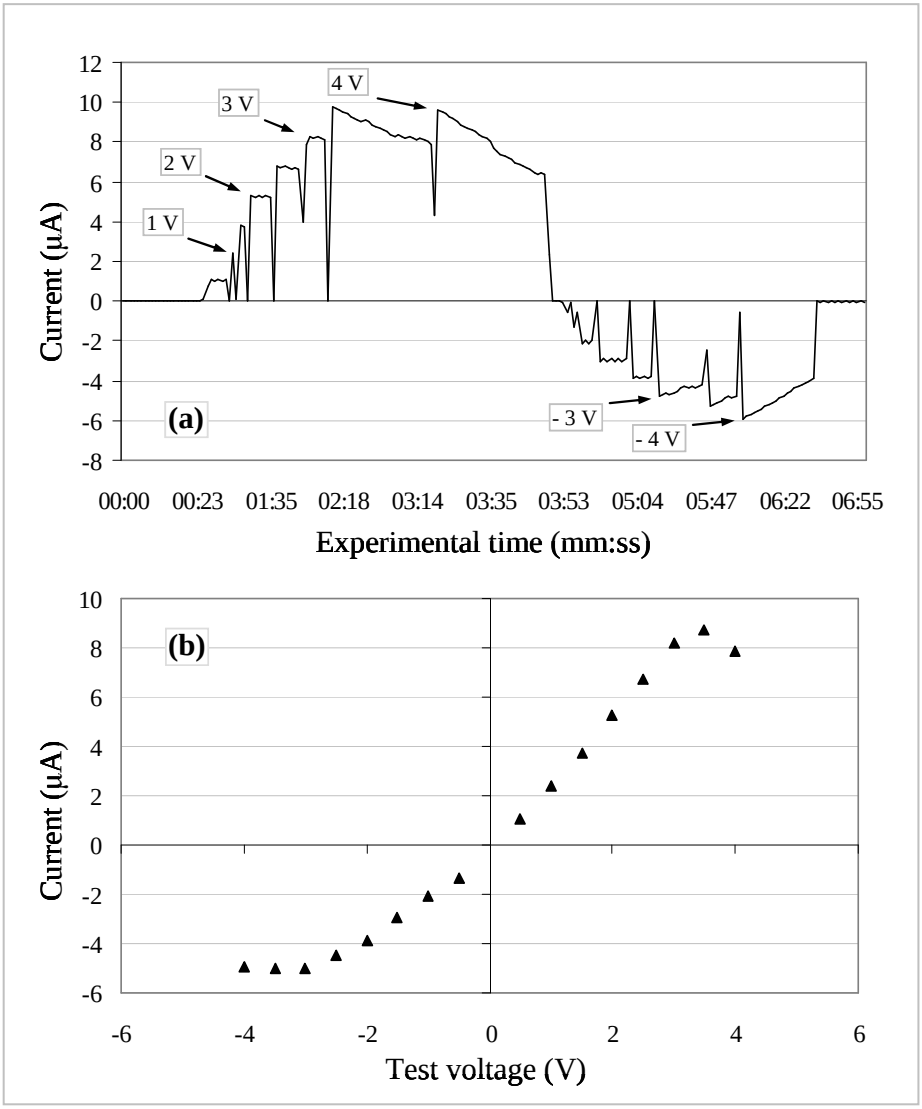

Figure 40. Electrical testing (in air) of the PEDOT connection shown in Figure 39. **Conditions**: DC voltages with 0.5 V increment. Notice the time-dependant decay of conductivity at voltages larger than +/- 3 V **(a)** and the asymmetry in the IV response (points in **(b)** are averages of the measurements at each applied V in **(a)**).

Extensive electrical characterization of such assemblies was not accomplished at the time as the MMA and the software were still in the prototyping phase. Nonetheless these experiments show that the directed assembly method can be extended to systems with more than two electrodes, and that more complex network structures result from increased complexity in the electric fields applied.

Analogous experiments were run on the array B using the 16-channel MMA (4 D/A channels, see Section 3.4.2). By using a 2-point set-up, it was possible to sequentially form two PEDOT interconnects and cross-link them in a three-step process (Figure 41a). By addressing the four electrodes simultaneously with various

potential patterns (and higher frequencies), a much more interconnected network, with fractal and thin-film structures, could also be produced (Figure 41b).

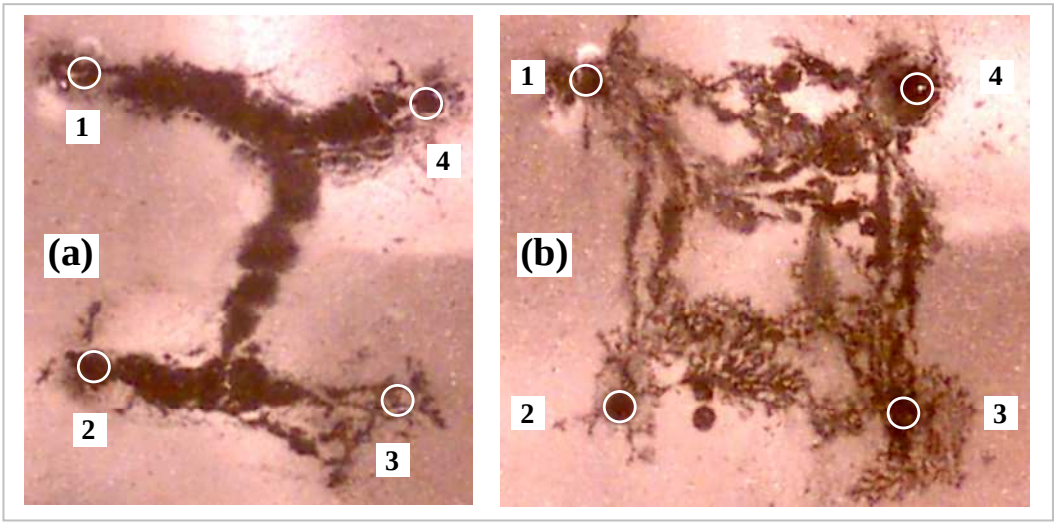

Figure 41. Conductive PEDOT networks assembled by AC electrochemical polymerization on a MMEA. **Conditions**: Solution: **(a)** 7/5 EDOT 0.47 M (MeCN)/Na p-Tos 1 μM (aq.); **(b)** 3/2 EDOT 0.33 M (MeCN)/Na p-Tos 1 μM (aq.). Assembly: **(a)** always square wave, 0.1 Hz: 20 V_{pp} on set 2-3; 8 V_{pp} on set 1-4; 8 V_{pp} on set 1-3 to cross-link the two pre-formed connections; **(b)** always square wave, 2-10 Hz range, maximum 12 V_{pp}. In **(b)** all the electrodes were addressed simultaneously with a variable potential pattern. Electrodes (white circles): Pt, diameter 127 μm, interelectrode gap ~ 1 mm.

Similar experiments were also performed using the same array (B) and a different conducting material, the organic ionic solid tetrathiafulvalene bromide (TTF Br). This material can be electrodeposited at the anode under potential control[102] (the mechanism is shown in Scheme 15), effectively resulting in long range 1D assembly (Figure 42). During the deposition, overlapping of the π-orbitals of adjacent molecules occurs, leading to preferential aggregation along the axis normal to the molecule plane and highly anisotropic conduction (major through the π-stack assembly) in the as-formed crystal.

The direction of growth had evidently no correlation with the electric field applied, and probably depended more on the orientation of the electrode-bound nuclei in the initial phase of the crystallization. Additionally, the as-formed wires were found to dissolve in proximity of the anode, while the electrodeposition continued at the tip closer to the cathode (phenomenon of the 'walking' crystal)[102]. Because of the peculiar assembly mechanism (lack of electric field-imposed directionality) and the instability observed in the salt form the use of this material for the production of conductive networks was dismissed.

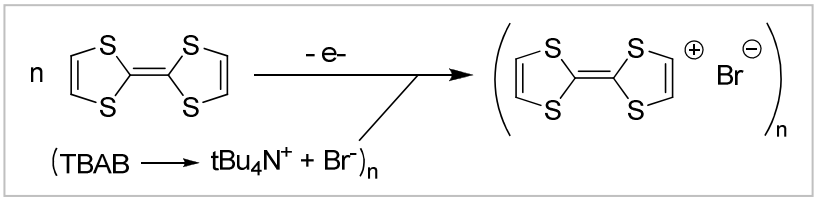

Scheme 15. General mechanism for the electrodeposition of TTF Br: no polymerization reaction occurs and the solid results from the crystalline packing of the salt sub-units.

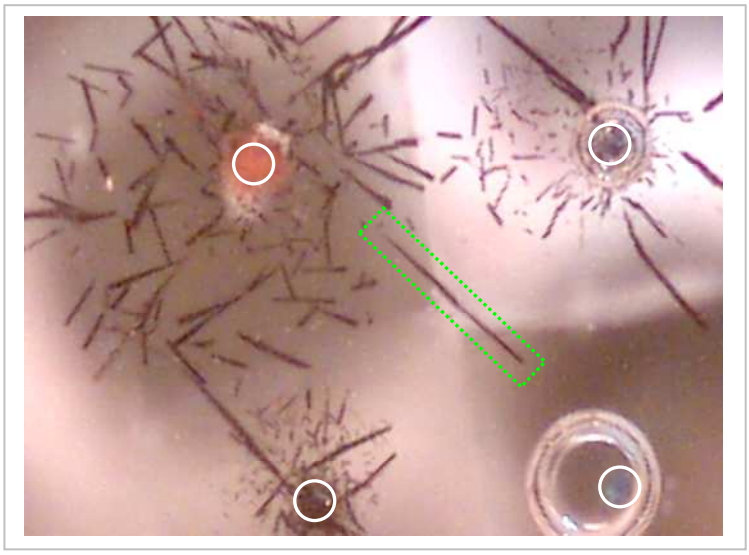

Figure 42. Conductive TTF Br micro-crystals electrodeposited on a MMEA. **Conditions**: Solution: TTF 2.5 mM and TBAB 50 mM (DMF, degassed). Assembly: square wave 0.1 Hz, 2 V_{pp}, + 3 Voff. Many crystals were found to loose connection with the anode during the experiment; some kept growing toward the cathode, while the tip close to the anode progressively dissolved: the dotted frame highlights one of such 'walking' crystals. Electrodes (white circles): Pt, diameter 127 µm, interelectrode gap ~ 1 mm.

4.2.2 – Assembly of µm-scale PEDOT connections on the 40-electrode MMEA (Innos v.2).

As previously described (Section 3.2), the MMEA devices commissioned to Innos Ltd. (3rd batch) were found to comply with the proposed design and passed the visual inspection. Although some of the electrode-track-pad structures were electrically shorted through the Si substrate, some of the devices were employed to test the AC method for off-electrode polymerization on a smaller scale (size of the array ~ 100 x 100 μm^2, electrodes in groups of ten along the sides of a SiO_2 square platform).

A commercial signal generator (Velleman PCG10/8016) was employed as the potential source. The use of higher frequency (10 Hz vs. the 0.1 Hz used on the mm-scale arrays) and of a MeCN-only solution allowed for the experiments to be carried out avoiding significant 'bubbling'. Since the devices had some electrodes shorted to

the Si base, this was addressed as the counter-electrode, while the signal was applied sequentially to one electrode at a time: by using this set-up, no polymerization would occur with the signal applied to an electrode that is shorted to the base, while a complex potential pattern would result by applying the signal to a well insulated electrode. Although the characteristic leaking resistance could not be determined for each electrode/device (see Section 3.2), the directionality observed was ascribed to the electric field between the active electrode (at which polymerization occurred) and the counter-electrode(s) (i.e. the electrodes more short-circuited to the base).

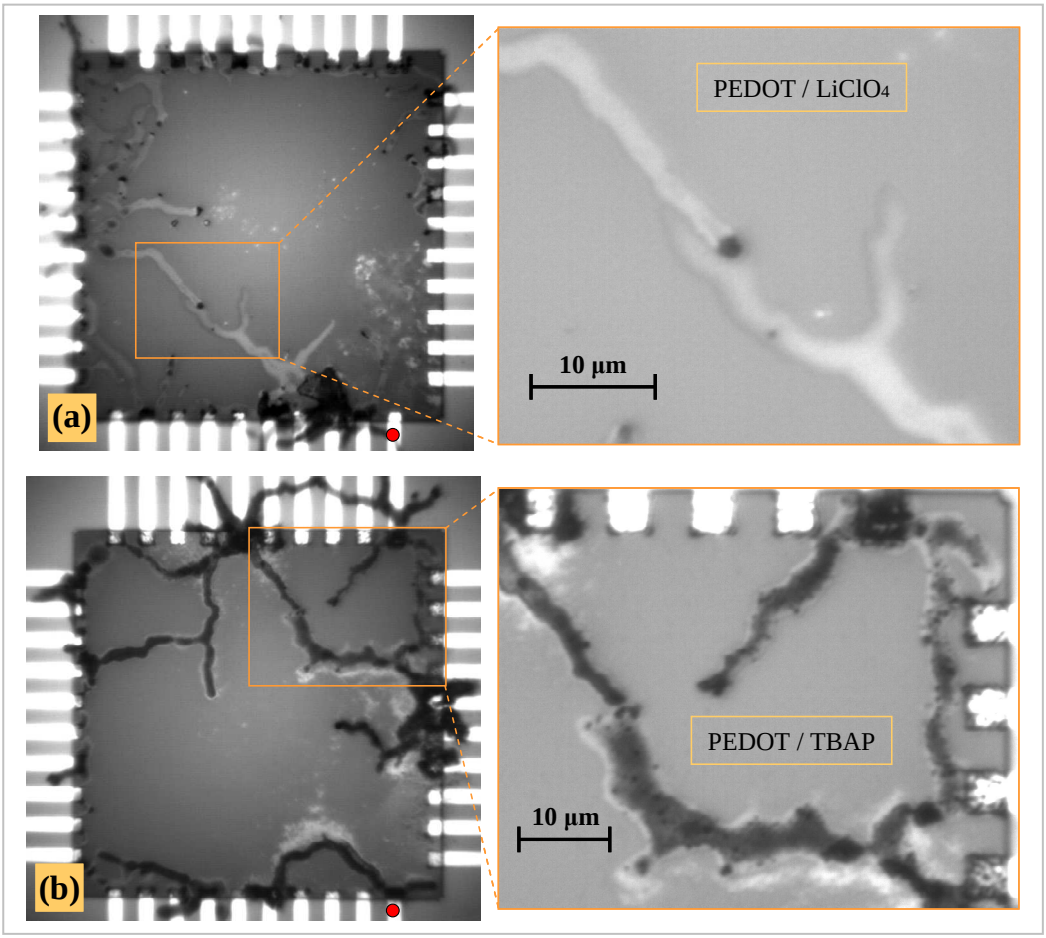

Figure 43. Conductive µm-scale PEDOT networks on MMEAs (Innos v.2). **Conditions**: Solution: EDOT 50 mM, electrolyte 0.5 µM (MeCN). Assembly: sine wave 10 Hz, 8 V_{pp}. The only significant difference between the two experiments shown was the electrolyte, $LiClO_4$ in **(a)**, TBAP in **(b)**, which resulted in polymer aggregates with different reflectance (in absence of solvent). The square platform (left hand side) measures about 100 x 100 μm^2, the electrodes (Au) are about 5 µm wide with 10 µm pitch (the red dot indicates electrode 1, numbering increases clockwise). A magnified view of the aggregates is shown on the right hand side.

Notice how some of the branches changed the direction of growth during the process, possibly following the (locally) highest electric gradient, and in many cases pointed

toward the tip of a pre-existent polymeric branch until connection occurred. Another interesting effect of the electric field on the polymerization, not appreciable on the mm-scale devices, can be observed in the magnified view of Figure 43b. Although lacking a polymer film, electrodes 27-29 present polymer aggregation at their corners; also when visible polymer branches were connecting the electrodes (as an example see electrodes 29-34) the highest density of polymerization occurred at the corners. These observations suggest the electrode geometry as having a major effect on the morphology and connectivity of the proposed networks.

During preliminary testing, the electrodes evidently connected by polymer aggregates were found to be also electrically shorted; it was however very difficult to differentiate the conduction through the polymer from the characteristic leaking of the devices. For this reason the MMEA presented in this sub-section was dismissed and further experiments delayed until a fully operational device became available. These experiments were indeed worth mentioning as they constitute the first attempts toward the directed assembly of conducting polymer interconnects on the μm-scale. Although height profiles of the aggregates were not obtained, the modality of growth and the optical information suggest they could be thin film structures with thickness in the hundreds of nm-range; if the thickness was to be found smaller than 100 nm, the as-produced polymer branches could be classified as a novel nanomaterial.

4.2.3 – Assembly of μm-scale PEDOT interconnects on the 20-electrode MMEA.

A fully operational MMEA device was produced and passed the visual inspection and electrical testing (Section 3.2). The device featured 20 square microelectrodes (area 6 x 6 μm^2), disposed in groups of five along the sides of a SiO_2 platform (area 67 x 67 μm^2). A System Switch Multimeter (Keithley 3706; mounting the 3721 plug-in card, a dual 1 x 20 multiplexer card) in series with a dual Source Monitor Unit (SMU; Keithley 2636) allowed for any combination of electrodes to be connected to one of the SMU channels. The typical test routine involved the measurement of DC current on all the combinations of two electrodes (190, avoiding repetitions); although some initial testing was carried out at 1 V DC, a lower voltage (0.1 V) was later employed to reduce thermal stressing of the connections. The device was electrically addressed using a low-noise connector, fitted with coaxial cables and placed in a Faraday cage for improved EMI shielding (Section 3.3); this allowed, using the instrumentation mentioned above, to record current down to the low pA-

range (standard deviation ~ 0.4 pA, typically lower than 1 pA on the lowest measurement range). Most of the data reported consist of the current averages (recorded at each set of two electrodes) plotted against the interelectrode gap: for this purpose a calibrated optical image of the MMEA was used for the determination of the electrode separation (Figure 44); for symmetry reasons the 190 combinations of two electrodes were divided in 24 groups of interelectrode gaps, in the range 4 - 67 μm. It should be pointed out that, although such method allows for a qualitative assessment of the degree of electrical anisotropy in the networks, the interelectrode gap assigned to each connection may not reflect the actual length of the electrical path. Since electrical anisotropy was often observed, the 4-point method could not be employed; electrical, visual and, possibly, topographic information should be correlated to derive the actual resistivity of the materials / interconnects object of this study.

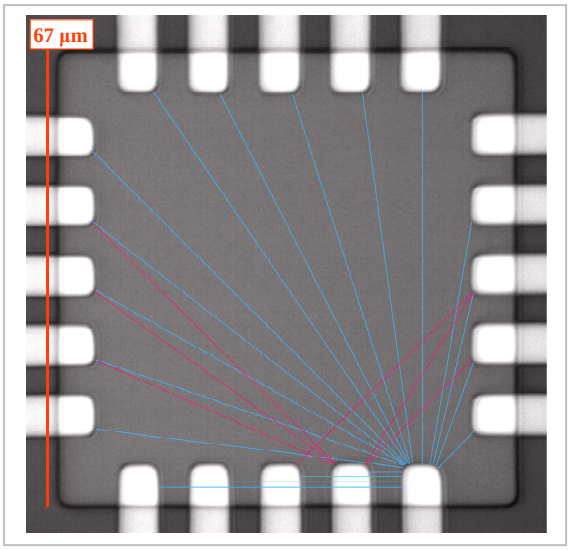

Figure 44. Optical image of the 20-electrode MMEA device. The microelectrodes (Pt or Au; area 6 x 6 μm^2) lie on the sides of a SiO_2 square platform; the insulating resist, defining the MMEA, is Si_3N_4. For symmetry reasons only 24 different inter-electrode gaps were assigned (and used in the 'current vs gap' plots).

A simple experiment was devised to test the concept of electrically monitoring the formation of interconnects during the assembly process (i.e. in solution). Since the use of AC (or pulsed DC) signals for the polymerization complicated the measurement, short measuring steps (at 1 V DC) were interposed between consecutive polymerizing signals. Using the Keithley system (2626-3706-3721, see sub-Section 3.4.1) and an automated test routine (in .tsp language), the formation of PEDOT interconnects between adjacent electrodes was implemented in a reproducible fashion (Figure 45). Each set of two electrodes underwent the same process in a serial fashion,

starting at set 1-2 and using the electrodes exclusively (i.e. after assembly on set 1-2 the next was set 3-4 and so on, for a total of 10 assembly experiments on the same device). The assembly-test routine involved, for each set of electrodes, an initial pre-assembly DC measurement followed by 6 iterations of assembly DC pulses (pulse at + 3 V, rest at – 3 V, duration 50 ms each, five cycles) and DC measurement (for a total of 7 DC measurements). All the DC measurements consisted of the acquisition of ten points, of which only the last five were used to produce averages (to account for capacitive discharge); only the averages so obtained were used in this analysis.

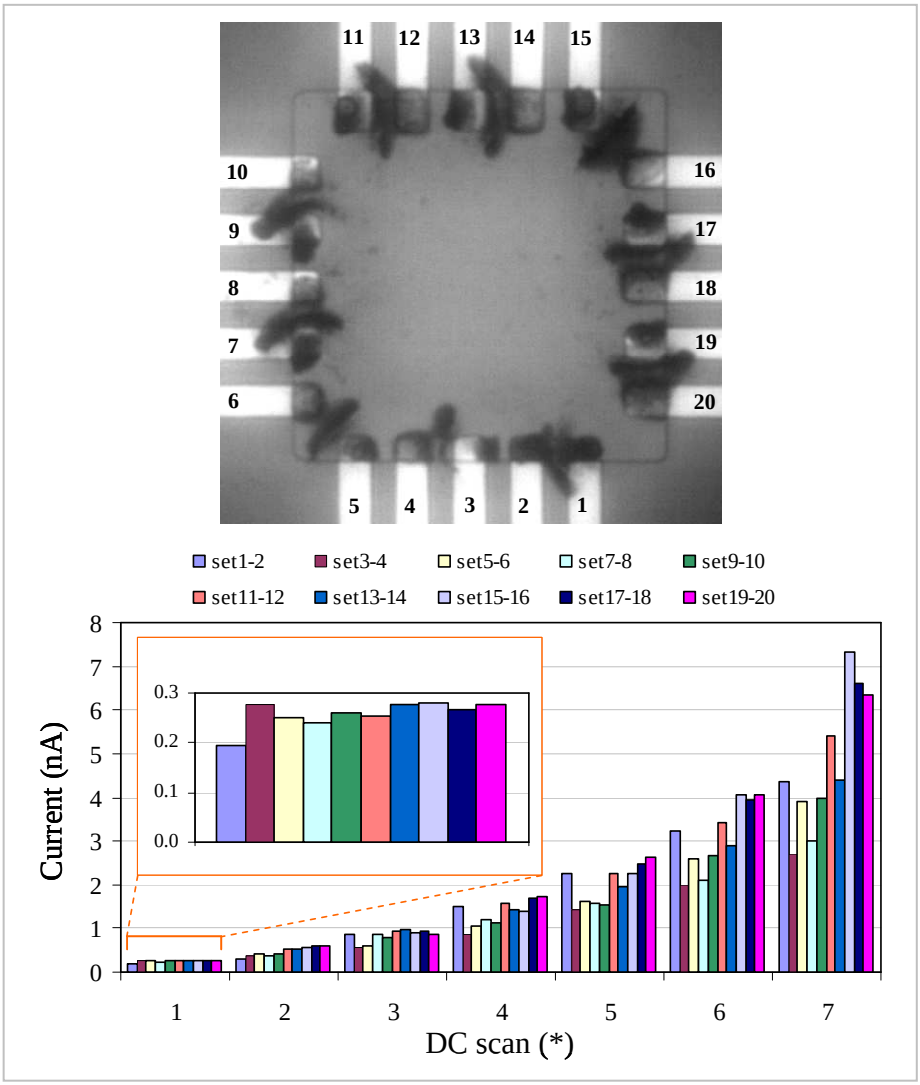

Figure 45. Formation of μm-scale PEDOT interconnects between adjacent electrodes using a pulsed DC method. **Conditions.** Solution: EDOT 50 mM, TBAP 0.5 μM (MeCN). Assembly: trains of square pulses, 10 Hz, 6 V_{pp}, - 3 V_{offset}. (*) The DC scans were not simultaneous, due to limitations with the system employed: the scans, consecutive on each of the 10 sets of electrodes, are shown together for comparative purpose. Notice that: 1) after each pulse sequence the DC measurement yielded higher values; 2) the sets of electrodes after set 1-2 (first to be addressed during the experiment) present consistently higher pre-pulse DC values (inset) due to parasitic polymerization (see main text for details). Electrodes: Pt, area 6 x 6 μm^2 ca.

As expected, the post-pulse DC measurements showed consistently higher values for the current, confirming the efficacy of the pulse trains in connecting the electrodes addressed during the experiment. Interestingly, however, the pre-pulse DC measurements taken after the assembly on the first set of electrodes (set 1-2) resulted in a higher initial current (see inset in Figure 45), suggesting that they could have been subject to polymerization during the assembly on the first set. This hypothesis was supported by the video information, as visible polymerization was typically observed on the electrode directly opposed to the source electrode with respect to the drain (i.e. 3 for set 1-2, 5 for set 3-4 and so on): doping-dedoping cycles also occurred, in phase with the pulsing electrode.

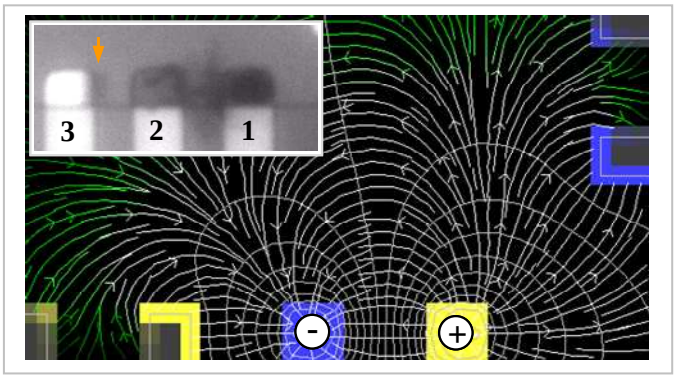

Figure 46. Electric field-induced polarization and electropolymerization on a non-addressed electrode (3 in the inset, the arrow points to the polymer aggregate). A simulation using a Java applet (by P. Falstad) is shown, and in the inset a snapshot taken at an intermediate stage during the assembly on set 1-2 (see main text for more details). Conduction through the active path (set 1-2) induces polarization of the adjacent electrodes / tracks that eventually results in parasitic polymerization / aggregation of oligomers. Electrodes (inset): Pt, area 6 x 6 μm^2 ca.

This phenomenon, to which we refer as 'parasitic polymerization', was ascribed to the effect of the electric field-induced charge on the non-addressed electrodes (Figure 46): the induced polarization was typically sufficient for the polymerization to occur (inset in Figure 46, arrow), indicating potential differences of the same scale as the polymerizing signal employed. Although non-addressed electrodes were electrically isolated (by mean of the 3721 switch card), the relatively large capacitance of the system (probes, cables, plugs and soldering points) evidently provided sufficient electron sink capability for the polymerization to take place; alternatively the charge could have been balanced by the electrons leaking through the resist (insulation resistance ~ 10 TΩ). As shown in later experiments, the occurrence of unwanted 'parasitic' polymerization was a constant with this experimental set-up, and was

generally ascribed to the very small interelectrode gap typical of the MMEA employed (gap / electrode width ratio ~ 1).

A similar experiment involved operating all the sets of electrodes simultaneously by means of the MMA (20-channel, sub-Section 3.4.2). The anode-cathode order was mirrored on adjacent sets of electrodes, so to have virtually zero potential difference between electrodes belonging to different sets (Figure 47b; yellow: positive charge; blue: negative charge). The polymerization method employed half-sine anodic pulses (15 pulses with + 3 V amplitude, ~ 4 Hz frequency), alternated with DC measurement steps (for a total of 16, including the pre-pulse measurement): the use of purely anodic pulses resulted in polymerization only on the desired electrodes (Figure 47a); off-electrode aggregates were observed half-way between the electrodes in each set (arrows in Figure 47), apparently aligned with the equipotential lines of the as-generated electric field (compare (a) and (b) in Figure 47).

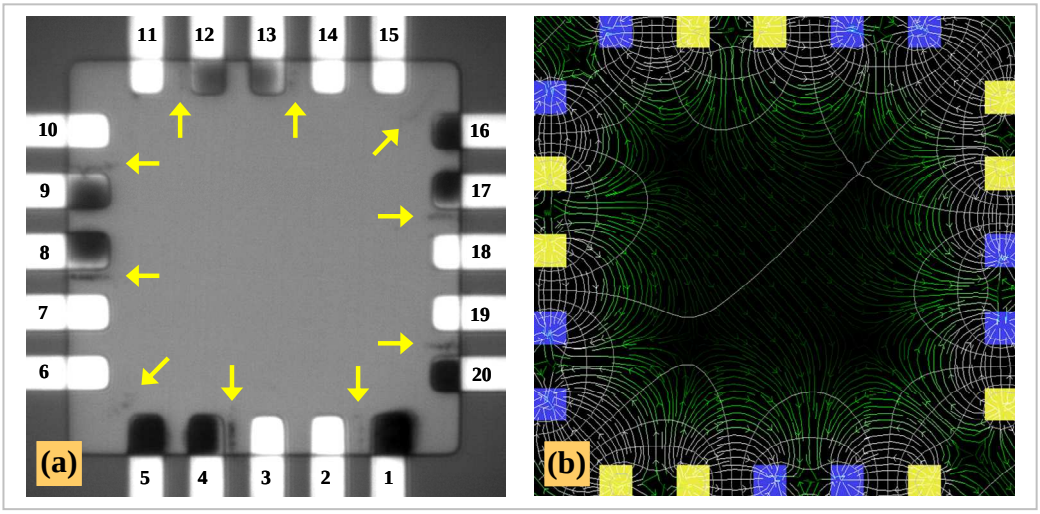

Figure 47. Simultaneous formation of sub-µm PEDOT connections. **Conditions.** Solution: EDOT 50 mM, TBAP 0.5 µM (MeCN). Assembly: 15 half-sine pulses (4 Hz, 3 V_{pp}, 0 V_{offset}) intercalated with DC measurements at + 1 V. **(a)** Optical image of the assembly (image taken in air); **(b)** A simulation (Java applet by P. Falstad) showing approximately anodes, cathodes and the electric potential field generated (i.e. static representation at the peak of the potential pulses). The arrows in **(a)** point to off-electrode aggregates aligned with the equipotential lines in the field. Electrodes: Au, area 6 x 6 μm^2 ca.

As in the previous experiment, the post-pulse DC measurements showed generally higher values for the current (Figure 48), confirming that each pulse had the effect of 'strengthening' the connection. To check for the occurrence of parasitic polymerization, a serial DC scan was performed (+ 1 V DC, in air). Surprisingly, the most conductive connections were found between the electrodes addressed as anodes during the assembly experiment (Figure 49, all above the level of current measured in

solution): no explanation could be given for this, unless assuming the time control on the electric potentials as inadequate for the electrochemical system employed.

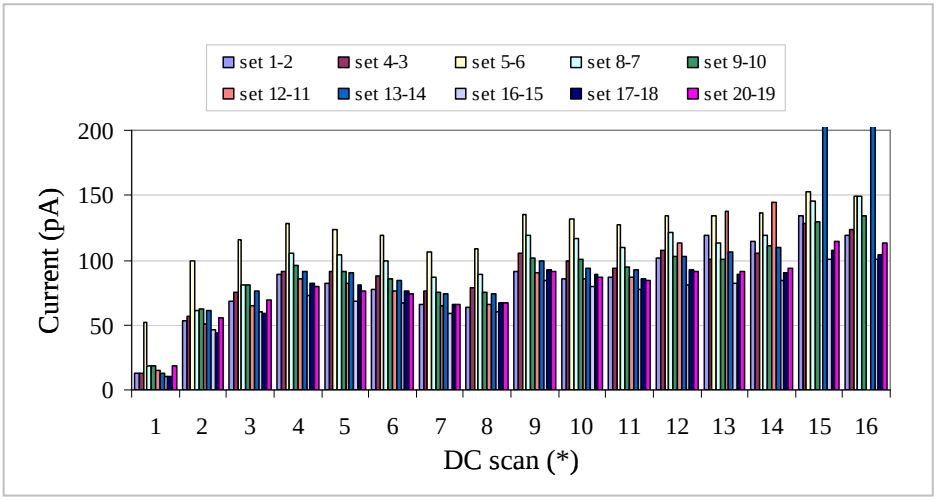

Figure 48. Formation of µm-scale PEDOT interconnects between adjacent electrodes using half-sine pulses. (*) The DC measurements were simultaneous, as well as the assembly pulses (see MMA, sub-Section 3.4.2). Note that in the legend the first electrode in the set is always the pulsing electrode.

Although it was noticed that connections detectable electrically could be obtained without any significant off-electrode polymerization (i.e. sub-µm scale aggregates, below the optical resolution limit), some attempts were made in order to reproduce the highly directional off-electrode polymerization observed on the previous MMEAs (sub-Sections 4.2.1 and 4.2.2). This was generally difficult to achieve: 'parasitic polymerization' usually predominated during the assembly; only the use of well-digitized AC signals was found able to initiate the desired growth mechanism.

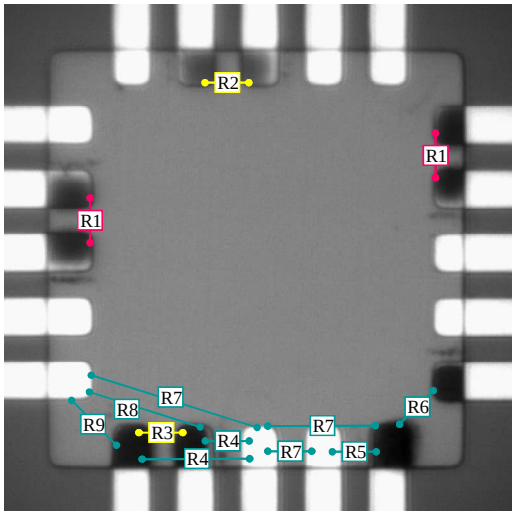

Resistor network assignment	Current at 1 V DC
R1	10 µA
R2	380 nA
R3	220 nA
R4	800 pA
R5	600 pA
R6	330 pA
R7	290 pA
R8	270 pA
R9	230 pA

Figure 49. Resistor network analogue of the polymeric assembly (same as in Figure 47). Counterintuitively, the lowest resistance connections occurred between the electrodes addressed (simultaneously) as the anodes (exception made for R6). Current values below 200 pA were discarded (digital resolution of 100 pA in this particular measurement, Keithley 2636-3706). Electrodes: Au, area 6 x 6 μm^2 ca.

In the next experiment the MMA was used in conjunction with the commercial signal generator (Velleman PCG10/8016), as the MMA in the latest stage of production was not able to produce AC signals with satisfactory accuracy. This expedient eventually resulted in a mixture of assembly morphologies, with most of the electrodes interconnected in series because of parasitic polymerization / aggregation, and a few parallel connections produced via the directional assembly mechanism (Figure 50).

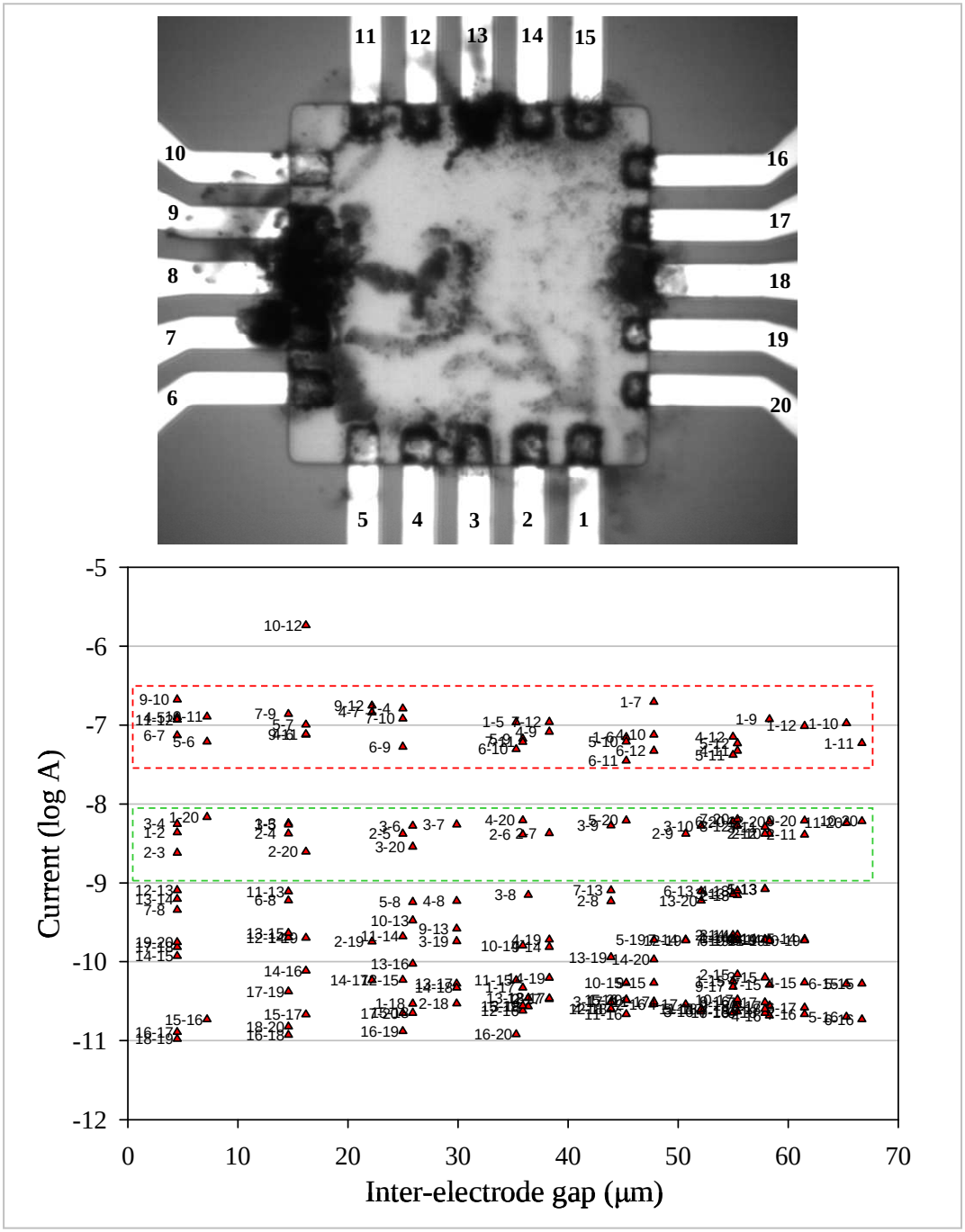

Figure 50. Conductive PEDOT network electrochemically generated on a MMEA. **Conditions.** Solution: EDOT 50 mM, $LiClO_4$ 0.5 μM (MeCN). Assembly (AC signal on electrode 8): sine wave 10 Hz, 4 V_{pp}, 0 V_{offset}. Testing: + 1 V DC (the first electrode in the sets always the source). Electrodes: Au, area 6 x 6 μm^2 ca.

Overlooking the non optimal assembly conditions, some considerations could be made by analyzing the network electrically and visually in the dry state: all electrodes where interconnected at some extent, with a range of resistances varying across more than five orders of magnitude (log_{10} of the current averages were used in the plot); the contribution to the conductivity of both serial and parallel connections resulted in the lack of evident trends in the current vs. interelectrode gap plot, exception made for some data points clustering in relatively small current ranges (i.e. 50-500 nA and 1-10 nA, broken frames in Figure 50).

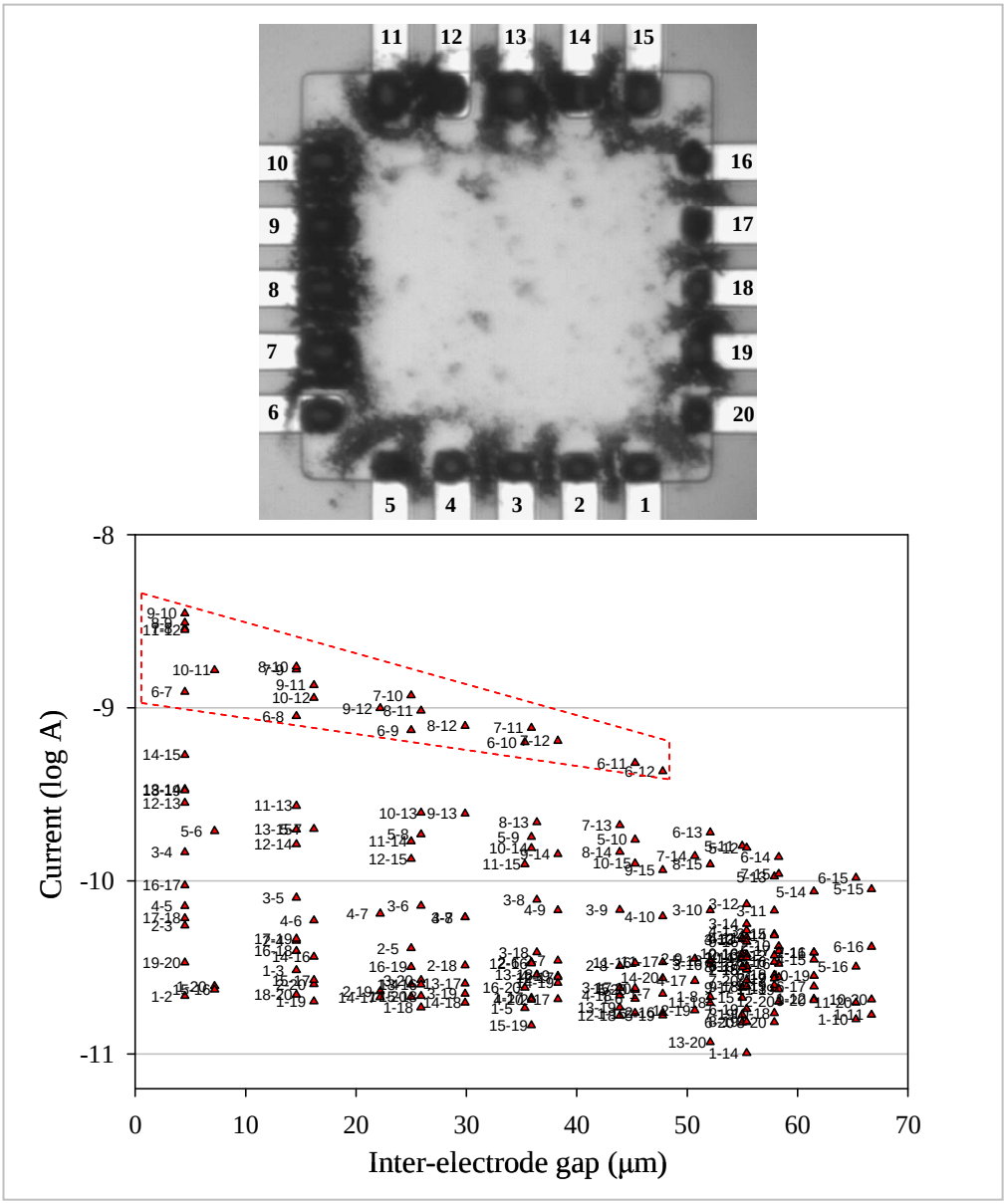

Figure 51. Conductive PEDOT network electrochemically generated on a MMEA. **Conditions.** Solution: EDOT 25 µM, TBAP 0.5 µM (MeCN). Assembly: 5 trains of square pulses, each composed of 5 wave-cycles at 2.5 Hz, 3 V_{pp}, 0 V_{offset}. The signals applied to the even number electrodes had 180° phase shift, so that odd and even number electrodes were used alternately as the anodes. Testing: + 1 V DC (the first electrode in the sets always the source). Electrodes: Pt, area 6 x 6 μm^2 ca.

For comparison, a conductive PEDOT network with predominance of serial connections was easily obtained using the MMA (Figure 51) and the pulsed DC method. The evident lack of directional / parallel polymer paths in the optical image was reflected in the electrical data, where a general decrease of the measured current at increasing interelectrode gaps was observed. It is worth highlighting that even in this experiment, simply aimed at connecting all the electrodes via the shortest path, the measured currents vary over a range of almost three orders of magnitude. No trend was evident and again no attempt to fit the experimental data to a model was made; indeed it could be noticed that higher polymer load (left-hand side in Figure 51) corresponded to higher currents, and that these were showing a roughly exponential decay with increasing interelectrode gap (broken frame in Figure 51; apparently linear in the $\log_{10}$ current plot).

The signal generator alone (Velleman PCG10/8016) was also used to attempt the directional assembly on the working MMEA. In the next experiment (Figure 52), two initial attempts using signals with 10 Hz frequency failed (sets 3-13 and 8-18; first electrode in the set addressed as the source), and only radial bulk polymerization could be observed at the electrodes. The frequency was then reduced to 1 Hz and set 1-10 was addressed. Directional growth started at electrode 2 (shorted to 1, see arrow in Figure 52), but was found to direct off-platform (over the Si_3N_4): video recording showed that the highly directional polymeric branch pointed toward a 'pin-hole' (in the resist over track 1) and the unwanted polymer aggregate it produced (Figure 53a). As soon as the off-platform growth stopped (spontaneously), highly directional polymerization was observed on-platform, which resulted in the formation of an evident connection between the electrodes addressed. Although no explanation could be given for this phenomenon, some important effects were observed.

Small imperfections in the insulating resist, such as pin-holes, can support electro-polymerization, and produce polymeric aggregates that distort the electric field and yield unexpected results (such as the off-platform growth); unluckily such imperfections cannot be detected until after the experiment, when they are coated with polymer. The off-platform branch, imaged under intense illumination, revealed a micro-scale wave front-like structure analogous to that discussed earlier (Figure 53b; compare with Figure 37 in sub-Section 4.2.1); no information of this kind could be inferred from the optical images of other directional aggregates (i.e. the interconnect between 1-10 in Figure 52, the polymer branches in Figure 43, sub-Section 4.2.2), but

it could be assumed a similar structure would be characteristic of any polymeric film assembled in a directional fashion using low frequency AC potential.

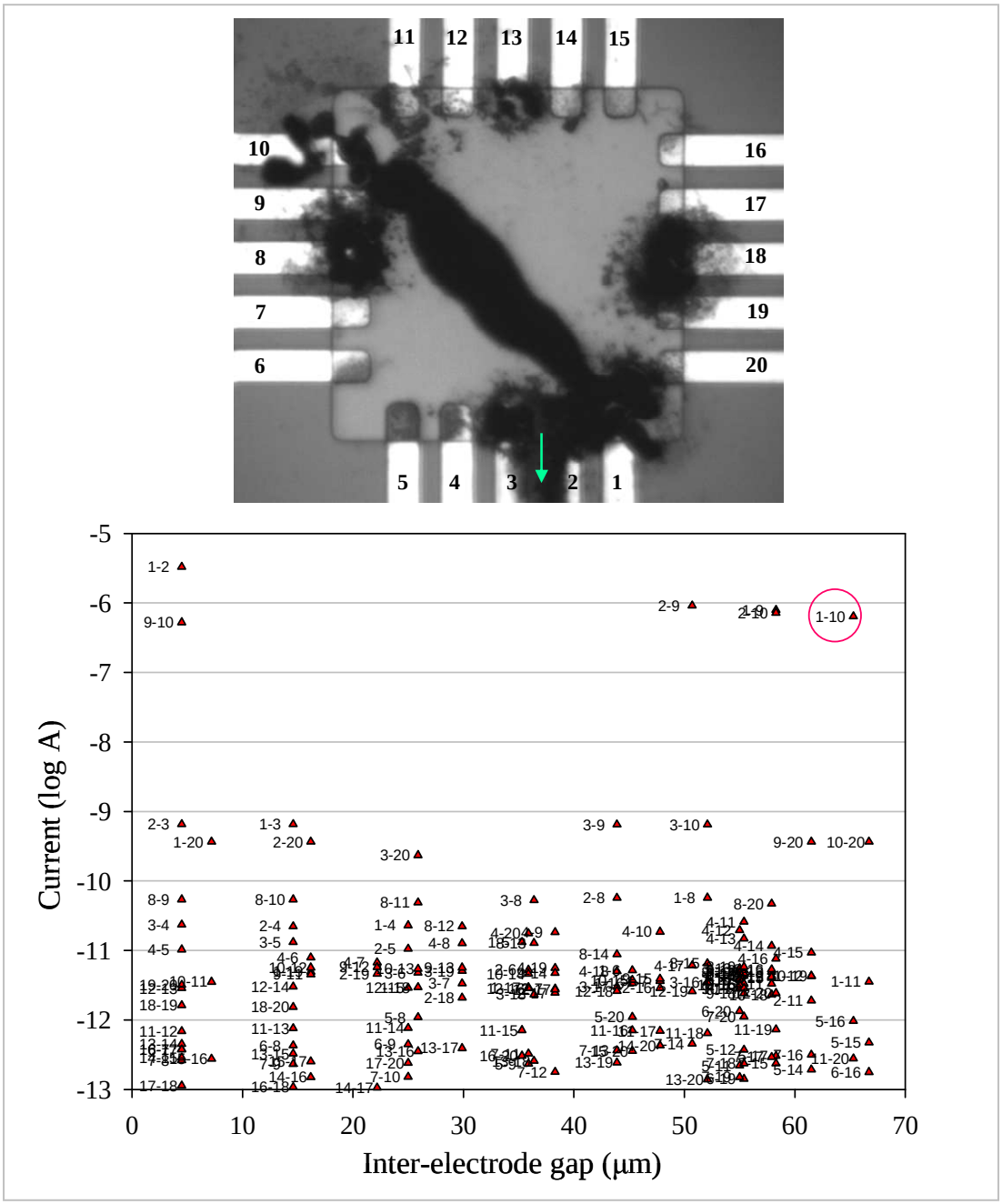

Figure 52. Conductive PEDOT network electrochemically generated on a MMEA. **Conditions.** Solution: EDOT 50 mM, TBAP 0.5 µM (MeCN). Assembly (sequence): sine wave 10 Hz, 7 V_{pp}, 0 V_{offset} on set 3-13, followed by square wave 10 Hz (same voltage) on set 8-18, only produced radial polymerization at the electrodes addressed; sine wave 1 Hz, 6 V_{pp}, 0 V_{off} on set 1-10 produced directional polymerization, first off-platform (arrow; see main text and Figure 53), and then between the electrodes addressed. Testing: + 0.1 V DC (the first electrode in the sets always the source). Note: the plot has been cut at the lower limit of 100 fA (-13 logA); the standard deviation for the measurements below 100 pA (-10 logA) was typically about 0.5 pA. Electrodes: Au, area 6 x 6 μm^2 ca.

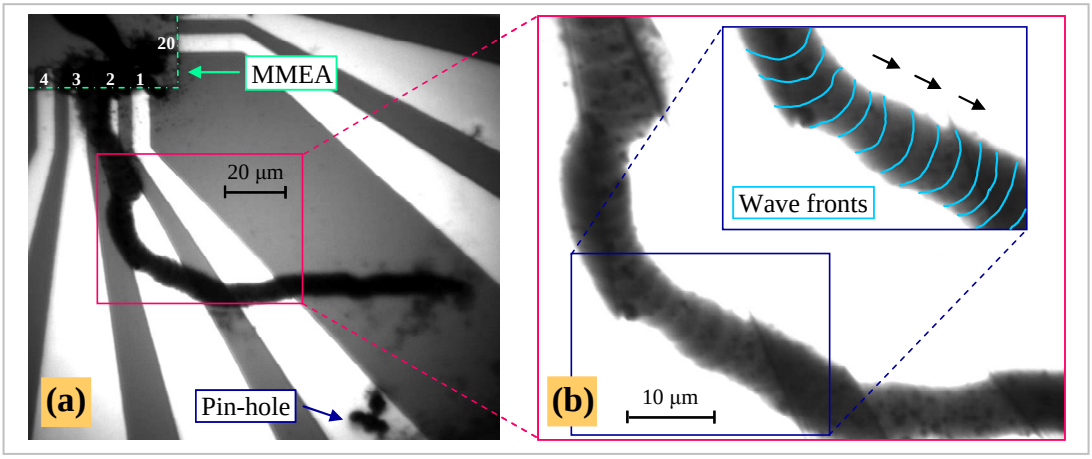

Figure 53. Directional polymerization of PEDOT on a MMEA (off-platform). **Conditions.** Solution: EDOT 50 mM, TBAP 0.5 µM (MeCN). Assembly: sine wave 1 Hz, 6 V_{pp}, 0 V_{off} on set 1-10. **(a)** A directional polymer branch longer than 100 µm accidentally formed off-platform; **(b)** under high intensity illumination the wave front-like structure could be discerned (inset: arrows indicate the direction of growth; the wave fronts have been highlighted).

In this respect it was noticed that the forward speed of about 3 µm / wave cycle (1 Hz signal; distance between wave fronts in Figure 53b) was pointing to a linear relation between the speed of growth and the polymerization (time) window: in fact a speed of 30 µm / wave cycle was previously reported for the mm-scale experiments, run at 0.1 Hz (sub-Section 4.2.1); the speed of growth for the experiments presented in sub-Section 4.2.2 could be inferred from the video information and found close to 3 µm / second, that is 0.3 µm / wave cycle at the frequency employed (10 Hz). These data suggest that a constant forward polymerization speed of about 3 µm / second was typical of such directional growth events. It should be noticed that at 10 Hz the 0.3 µm increments corresponding to each wave cycle could not be possibly discerned, being well below the optical resolution limit. Interestingly a comparable speed of growth can be discerned in the video presented by Thapa[100(a)] as supplementary information[103] (assuming a interelectrode gap of 30 µm in the video, based on the scale bar provided in Figure 1b of the cited document, and real time recording).

Despite the fact that the experiments presented here and the recently reported methodology[100] both aimed at controlling the direction of assembly of a conducting material by means of an electric field, and under AC conditions, a significant difference could be observed in the resulting interconnects. While the use of high frequency and electrolyte concentration favoured bulk aggregation, resulting in a quasi-cylindrical wire connected only to the electrodes, our method, employing low frequency and electrolyte concentration, appeared to produce prevalently surface

aggregation, resulting in a low dimensional polymer film tightly bound to the platform surface (SiO_2). Although this typology of aggregate would be inherently more resistant to washing / drying and successive assembly steps, its production was mainly limited by parasitic polymerization.

In the attempt to limit the extent of polymerization, a very low concentration of electrolyte was used for a set of experiments. Identical polymerizing signals (sine wave 4 Hz, 1 V_{pp}) were applied to electrodes 3, 8, 13 and 18; a continuous but not constant potential difference between the electrodes was obtained by imposing a 90° phase shift between the applied AC signals. These were generated using the NI PCI-6229 DAQ card and a LabVIEW interface, which also allowed time control of the experiment. Even though identical conditions were applied using automated control, the resulting networks (Figure 54) presented significant differences, both in the range of measured currents (not shown for all the experiments) and in the extent of polymerization. The lowered concentration of electrolyte seemed to reduce the extent of parasitic polymerization, so that most of the non-addressed electrodes appeared free from polymer, but indeed all the electrodes were found to be interconnected by electrical analysis.

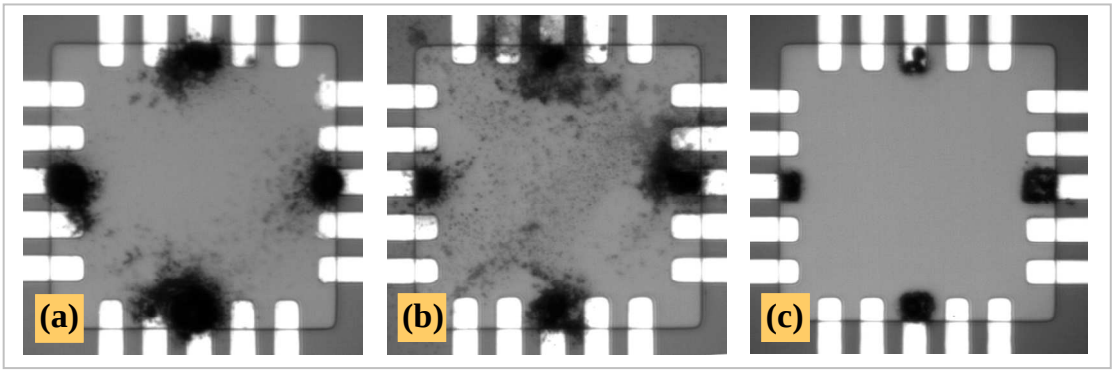

Figure 54. Conductive PEDOT networks produced with nM concentration of electrolyte. **Conditions.** Solution: EDOT 50 mM, $LiClO_4$ 5 nM (MeCN). Assembly: sine wave 4 Hz, 1 V_{pp}, 0 V_{off} on electrodes (phase) 3 (0°), 8 (90°), 13 (180°) and 18 (270°). Electrical testing showed that all electrodes were interconnected, despite the evident lack of polymer on most of the non-addressed ones. Electrodes: Au, area 6 x 6 μm^2 ca.

These results support the hypothesis that nano-scale polymeric interconnects with high conductivity may be formed under certain conditions (see also Figure 47 and 49 in this sub-section), and impose that the video information alone, without electrical monitoring of the experiment, would be insufficient for properly characterizing (and attempt the optimization of) the processes involved. Interestingly, the network with

the most consistent relationship between the morphology and the measured current was the one were only sub-µm-scale connections were formed (Figure 54c and Figure 55). While the currents in the networks showing aggregation spread across ranges of several orders of magnitude (10 pA to 100 nA for that in Figure 54a; 1 pA to 1 nA for that in Figure 54b), those measured on the nano-scale network were mostly centred around 100 pA, and spread across a range of just one-and-half order of magnitude (Figure 55).

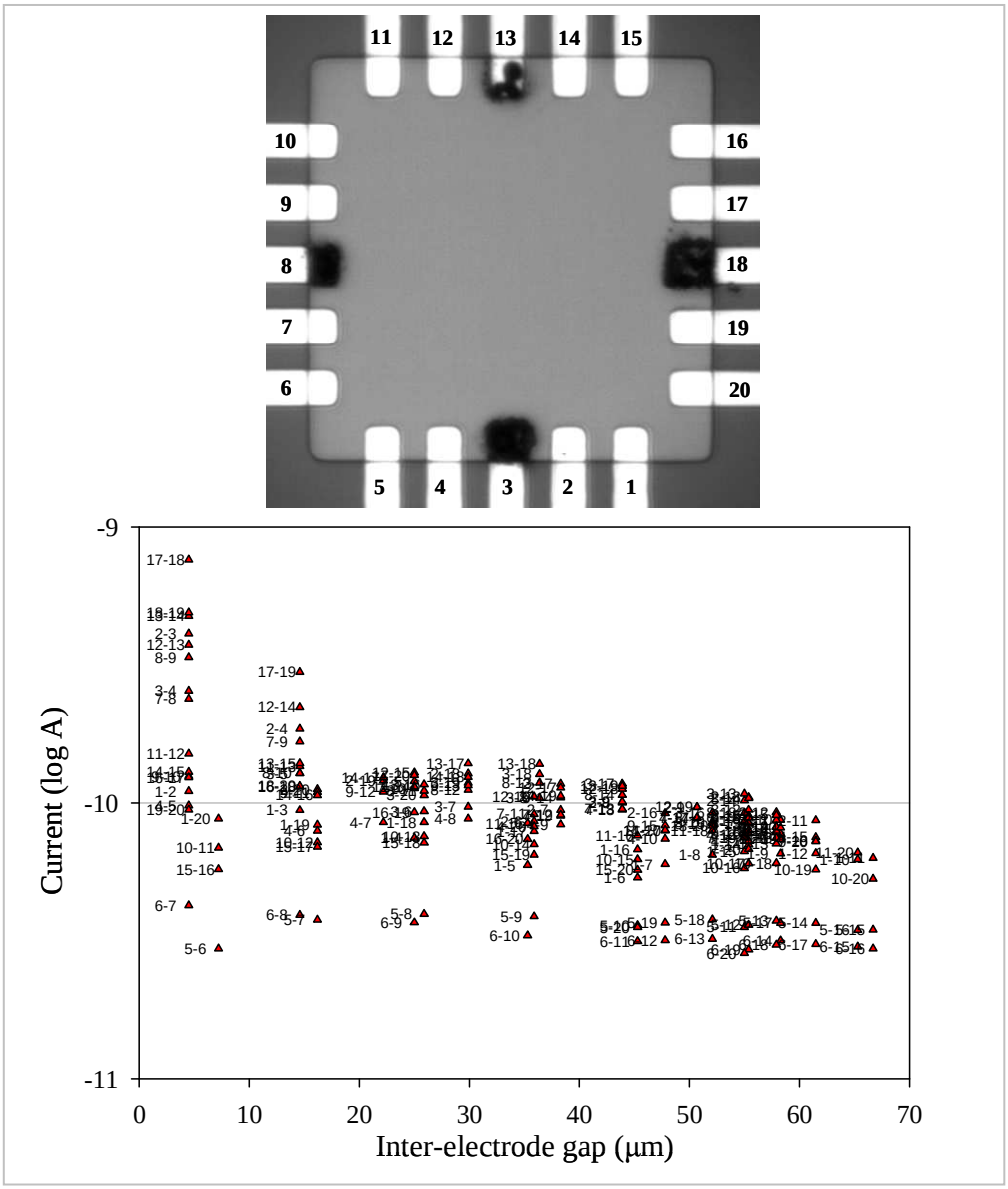

Figure 55. Conductive PEDOT network of sub-µm-scale interconnects (below the optical resolution limit). **Conditions.** Solution: EDOT 50 mM, $LiClO_4$ 5 nM (MeCN). Assembly: sine wave 4 Hz, 1 V_{pp}, 0 V_{off} on electrodes (phase) 3 (0°), 8 (90°), 13 (180°) and 18 (270°). Testing: + 0.1 V DC (the first electrode in the sets always the source). Note that all the electrodes were interconnected, with the measured currents spreading across a limited range (50 pA to 1 nA, -10.5 to -9 logA in the plot; well above the background current of the system, typically less than 1 pA), but no polymer interconnects could be resolved in the optical image. Electrodes: Au, area 6 x 6 μm^2 ca.

Surface probe microscopy (SPM) and electron microscopy (EM) techniques would be needed to correlate the electrical information with the actual morphology of the assemblies (not entirely or not at all resolvable by optical microscopy); it should be also noticed that the measured resistances compare well with those reported by Samitsu[104] for PEDOT nanowires produced by a different method.

Having established that nano-scale PEDOT interconnects with resistance in the GΩ range may also result from parasitic polymerization, it would be interesting to test the conditions reported by Thapa[100] on our system and electrically characterize the networks produced. A combination of the two methods may lead to further optimization and enable the production of highly conductive, surface-bound, nanowire networks under total directional control.

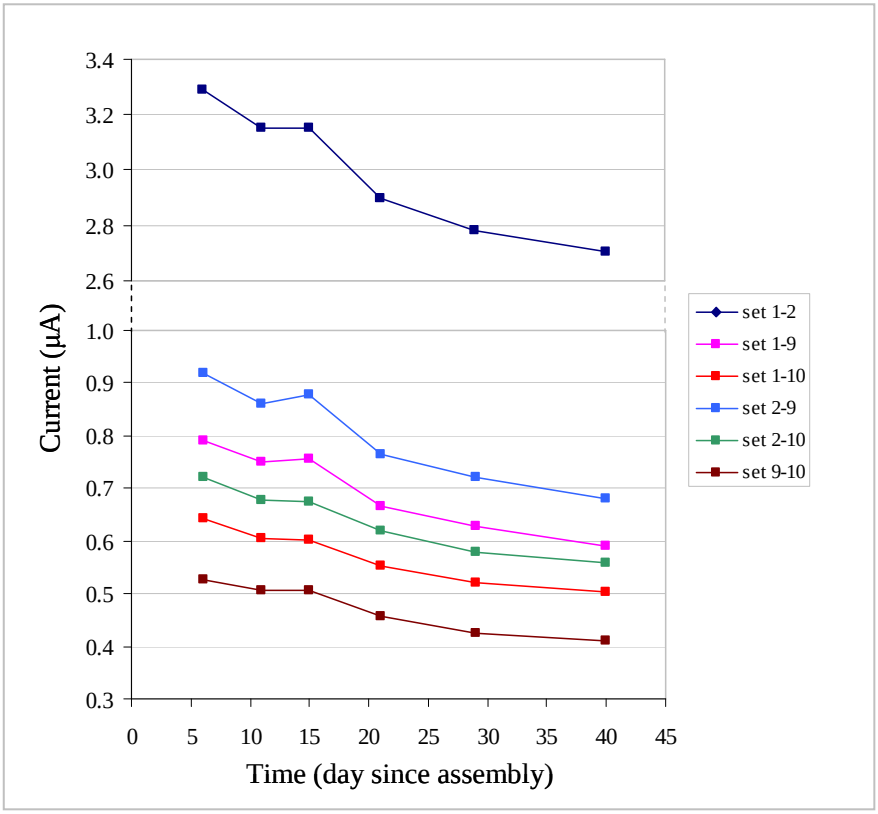

Figure 56. Decay of conductivity over time in a PEDOT network. Each series represent consecutive current measurements on the electrode sets in the legend, the highest conductive in the assembly shown in Figure 52. Testing: + 0.1 V DC, in air, at room temperature. All data series, excluding some in the lower pA range, were showing similar trends in the decay.

A final remark can be made about the stability of the assemblies produced. The post-assembly electrical testing always took place in air and at room temperature, and the samples were typically stored in the same conditions (sealed vials, away from light). Repeated testing of some of the assemblies over a time period of 40 days (6

testing sessions) showed that the patterns of conductivities were varying over time, with a general decrease of the conductivity of the whole network, possibly a consequence of the exposition to oxygen and atmospheric water and / or the dielectric heating. Although for simplicity only data for the most conductive sets of a single network are shown (Figure 56; assembly shown in Figure 52), a similar trend was often observed across the range of conductivity: all the measured currents (down to the lower pA range) were found to decrease over time, pointing to a loss of performance of the material; it should also be noticed that the consistency in the decay observed on different electrode sets served as further proof of the reliability of the test system, as allowed to ascribe the changes observed during repeated testing to an intrinsic property of the material (i.e. its degradability).

4.3 – Assembly of PEDOT / MWNTs networks on the 20-electrode MMEA.

As mentioned earlier, some precedents exist for the assembly of MWNTs under AC potential control[45] (or assembly by dielectrophoresis). The same approach was attempted in order to produce CNTs network on our MMEA. Apart than for their excellent conductivity and other interesting properties, CNTs were chosen principally because of the scale match between their typical length (up to several μm) and the size of the MMEA platform. Although the MWNTs employed here were too small to be optically resolved, a significant number of rod-like bundles were visible: these were found to readily assemble at the electrodes under AC conditions (both at the source and drain electrode), often in a radial fashion; some networks were obtained, but they could not be electrically tested in the dry state because of the fragility of the resulting material. Major changes in the network structure typically occurred during the removal of the solvent and the washing / drying procedure, leading us to dismiss this approach. To overcome such fragility, the assembly of MWNTs was attempted in the presence of EDOT monomer; initial attempts using also electrolyte were found to produce excessive polymerization, so the electrolyte was subsequently omitted: surprisingly, the network resulting from the dielectrophoretic assembly of NTs in the presence of only EDOT were found significantly more robust, suggesting that PEDOT was produced during the process and bound the NTs together; in this context PEDOT would serve as a in-situ polymerized conductive ‘glue’. Several reports appeared on the production of NT/CP hybrid materials[105], but none of these involved the directed

assembly of conducting connections between microelectrodes under AC potential control.

A PEDOT / MWNTs network was assembled on the MMEA by using the signal generator in series with the Keithley instruments (Figure 57). Under such conditions, severely limiting the amount of PEDOT produced (no electrolyte), the aggregation occurred mostly at the active electrodes, and involved prevalently the formation of connections to the adjacent electrodes: the currents measured at these electrode sets were two orders of magnitude higher than the rest, centred mainly around 1 pA (DC testing at + 0.1 V, dry state).

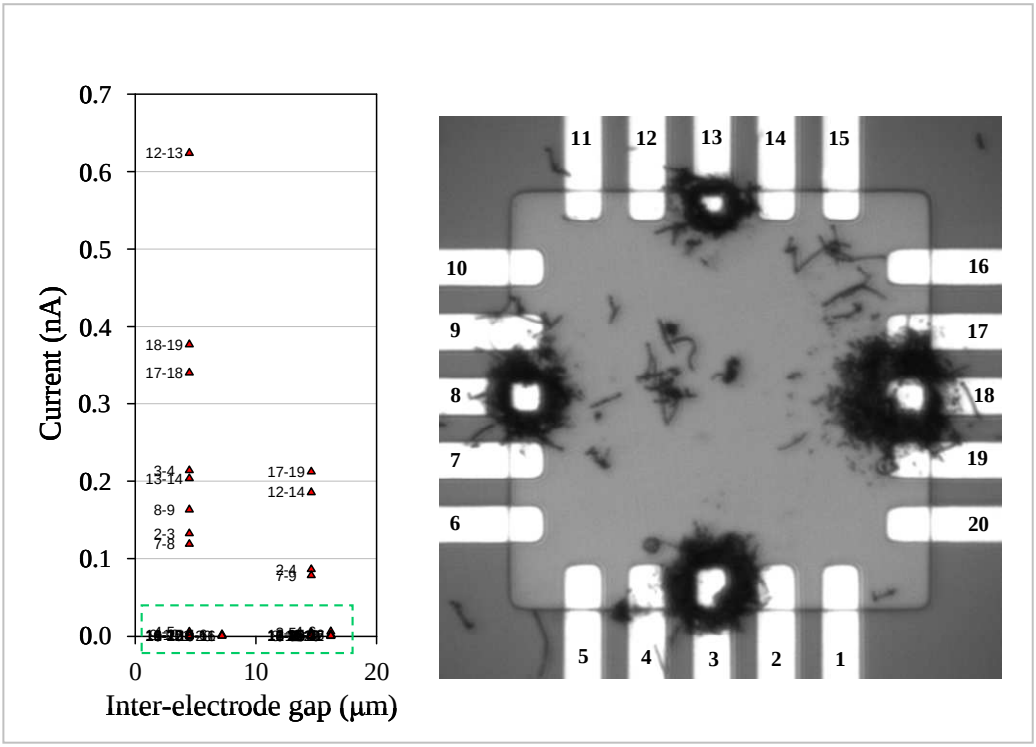

Figure 57. Conductive PEDOT / MWNTs composite network on a MMEA. **Conditions.** Solution: EDOT 50 mM, MWNTs 25 µg / mL (MeCN); CNTs (source, product code, dimensions): MER, MRCSD, diameter 140 +/- 30 nm, length 7 +/- 2 µm. Assembly: square wave 1 Hz, 4 V_{pp}, 0 V_{off} on electrodes 3 and 8; electrodes 13 and 18 were used as drain (at ground potential); the electrodes were automatically exposed to the assembly signal for 10 iterations of a 20 s switching routine (totally 200 s or 200 wave cycles), inter-loop delay 1 s. Testing: + 0.1 V DC (the first electrode in the sets always the source). Electrodes: Au, area 6 x 6 μm^2 ca. The data points out of scale (broken frame) were spread between 0.5 and 10 pA.

Stability testing of the assembly revealed the expected time-dependant degradation of conductivity (Figure 58) for the most conductive electrode sets (current data in Figure 57). The lower conductivity sets, with the measured currents in the lower pA range, showed instead various trends, some of which cannot be explained if we consider the

degradation of the CP as the only process involved. Although a similar decaying trend could be observed for some of these series, others were showing instead an increase of conductivity, suggesting the occurrence of some reconfiguration process over time. Even though these data were very close to the resolution limit of the system, some could be unmistakably considered as true currents (i.e. not due to the background noise) because of evident trends in the time series (Figure 58): notice as an example how the current on set 3-20, after an initial decrease over the first week, was found to increase almost linearly during a period of 20 days, and that a almost identical trend could be observed for set 4-20. For simplicity only the data relative to the connections to electrode 20 were shown, but similar observations could be made for many of the other low conductivity sets; the fact that no optically resolvable aggregation occurred at some of the electrodes would suggest the presence of nano-scale interconnects.

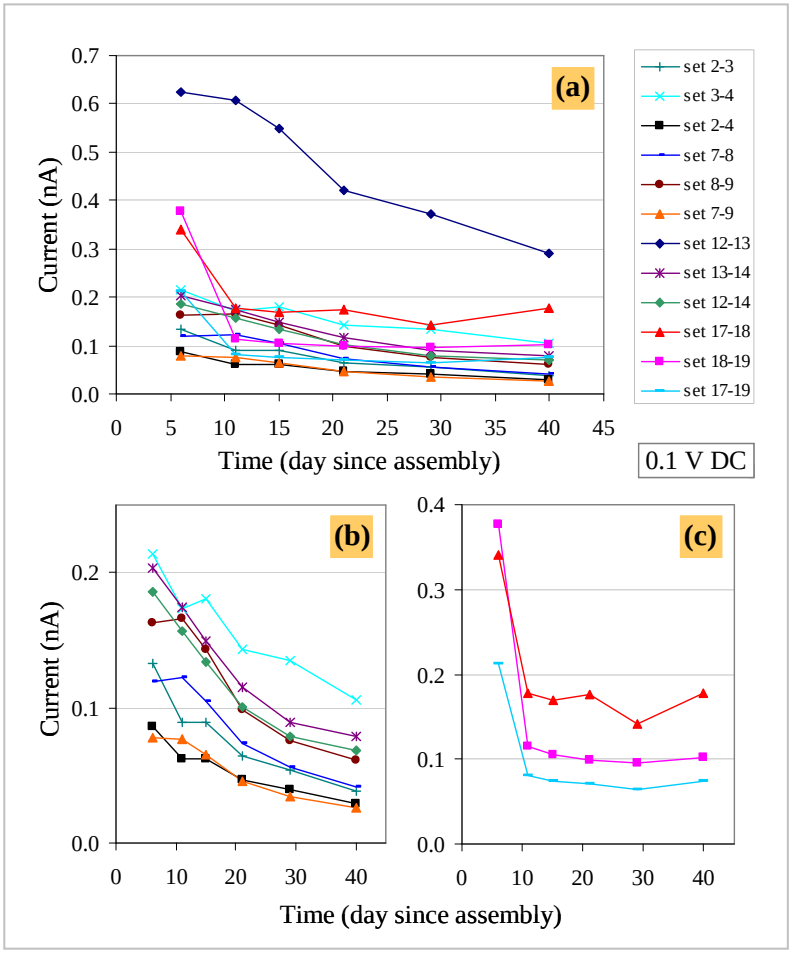

Figure 58. Decay of conductivity over time in a PEDOT / MWNTs network. **(a)** Each series represent consecutive current measurements on the electrode sets in the legend, the highest conductive in the assembly shown in Figure 57. **(b)** and **(c)** show groups of series with similar trends in the decay (same data set, with the exclusion of set 12-13). Testing: + 0.1 V DC, in air, at room temperature; the standard deviation of the data (current averages) in the hundreds of pA range was typically less than 1 pA.

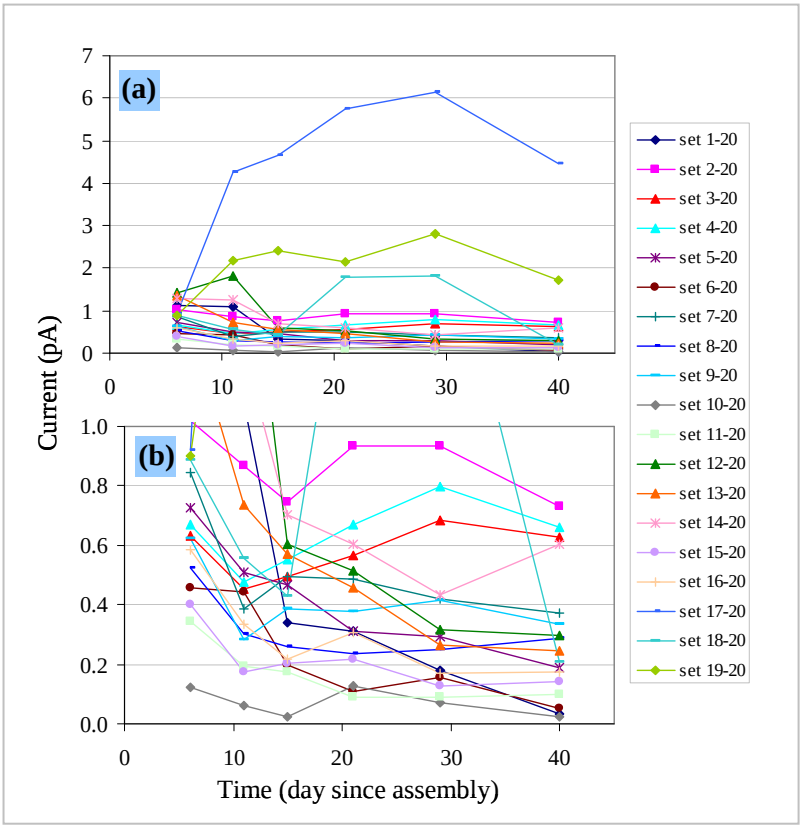

Figure 59. Change of conductivity over time in a PEDOT / MWNTs network. **(a)** Each series represent consecutive current measurements on the sets involving electrode 20: notice the lack of visible aggregation at this electrode (see Figure 57; not addressed during the experiment); **(b)** shows the 0-1 pA range of the same data set. The increase in conductivity was ascribed to rearrangement in the CP / NTs hybrid network; its decrease to the degradation of the PEDOT connections. Testing: + 0.1 V DC, in air, at room temperature; the standard deviation of the data (current averages) in the lower pA range was typically less than 0.5 pA.

Although the MWNTs (length 7 +/- 2 μm, diameter 140 +/- 30 nm) were dispersed using ultrasonication just before the experiment, clusters and bundles were often observed (and assembled at the electrodes); the vast majority of NTs was however suspended in the solvent mixture and available to assemble under the conditions applied. As the assembly extended to the adjacent electrodes part of the potential would have been transferred across the connection to non-addressed electrodes, leading to further assembly: the reduced intensity of the field at these electrodes could have been insufficient to attract the μm-scale particles, and attract instead preferentially single NTs. Poor contact to the electrodes and between NTs would then justify the very high resistances observed (in the tens of GΩ range).

A similar experiment was repeated using slightly longer and thinner MWNTs (length ~ 30 μm, diameter 35 +/- 10 nm). This resulted in a PEDOT / MWNTs

network with overall higher conductance than the one described above: most of the measured currents were close to 50 pA, and high currents (hundreds of nA range) could be detected up to interelectrode distances of 25 μm (Figure 60).

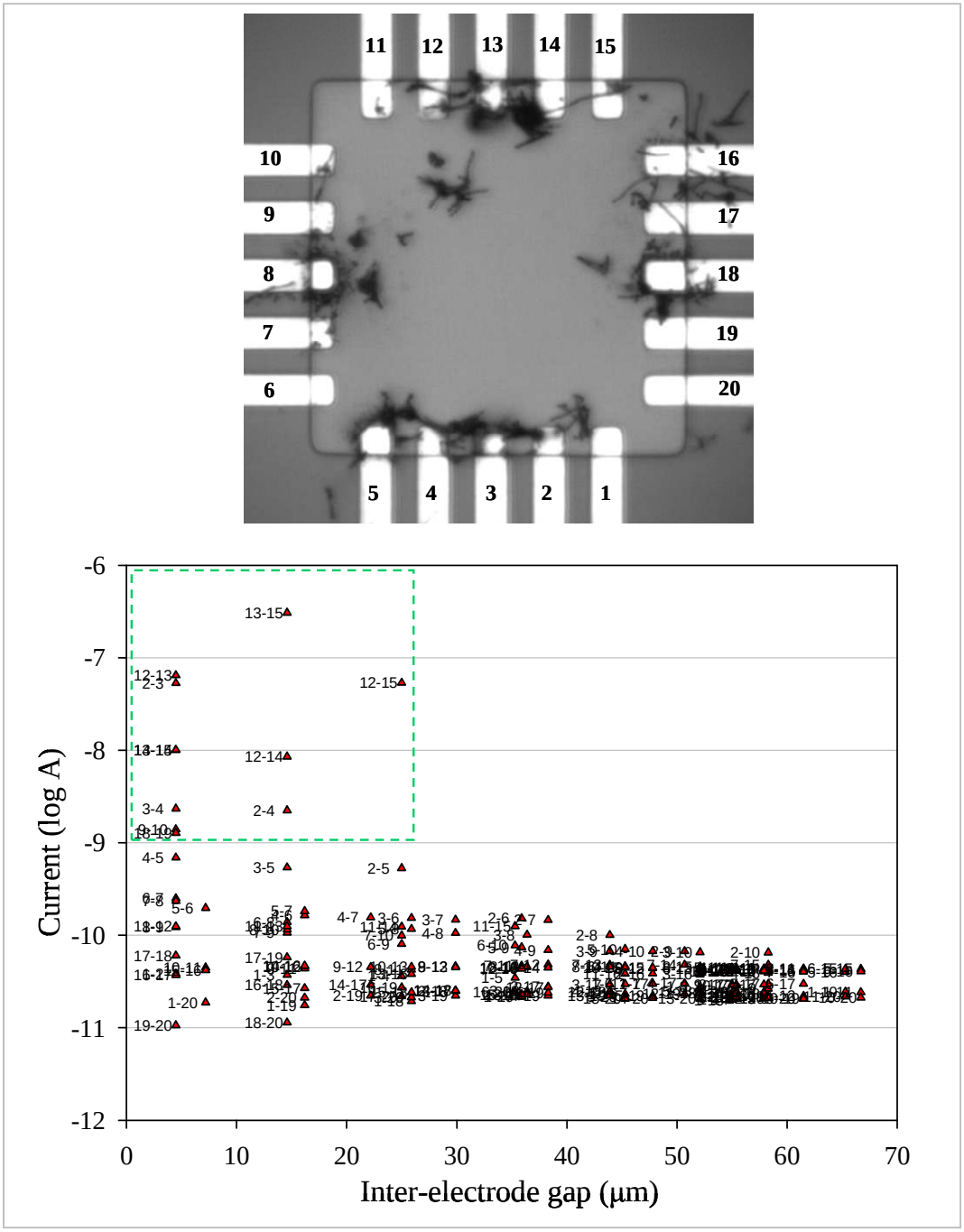

Figure 60. Conductive PEDOT / MWNTs composite network on a MMEA. **Conditions.** Solution: EDOT 50 mM, MWNTs 25 μg / mL (MeCN); CNTs (source, product code, dimensions): MER, MRCMW, diameter 35 +/- 10 nm, length ~ 30 μm. Assembly (sequence): (always sine wave, 0 V_{off}) 1 Hz, 3 V_{pp} on set 3-13; 5 Hz, 4 V_{pp} on set 8-18; 2 Hz, 4 V_{pp} on set 8-18; 2 Hz, 4 V_{pp} on set 5-16; each set of conditions was applied to the electrodes for 5 iterations of a 20 s exposition routine (totally 100 s), inter-loop delay 1 s. Testing: + 0.1 V DC (the first electrode in the sets always the source). Electrodes: Au, area 6 x 6 μm^2 ca.

Stability testing of the assembly revealed the expected time-dependant degradation of conductivity for the most conductive electrode sets (Figure 61; currents above 1 nA in Figure 60, broken frame) and for most of the other connections; some rearrangement was also observed, as many sets were showing a temporary increase of conductivity around day 20 (one evident example set 9-10 in Figure 61).

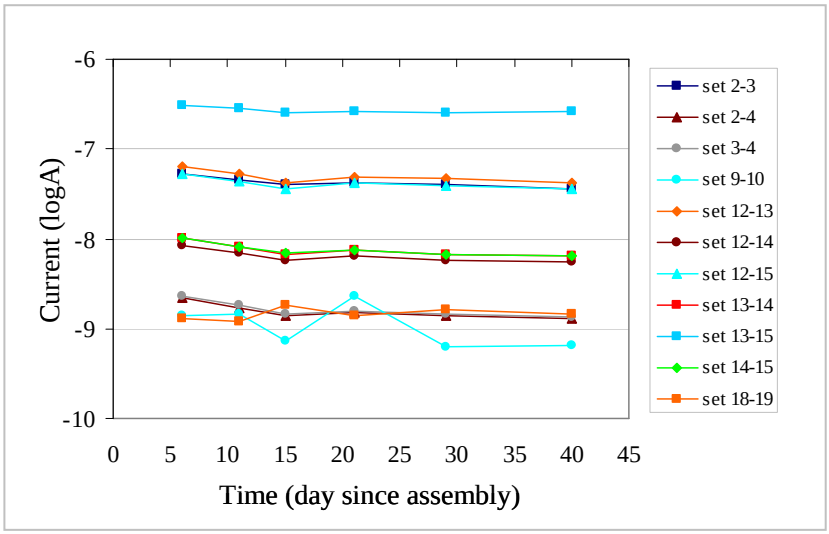

Figure 61. Decay of conductivity over time in a PEDOT / MWNTs network. Each series represent consecutive current measurements on the electrode sets in the legend, the highest conductive in the assembly shown in Figure 60 (broken frame). Testing: + 0.1 V DC, in air, at room temperature; the standard deviation of the data (current averages) was typically less than 1 pA.

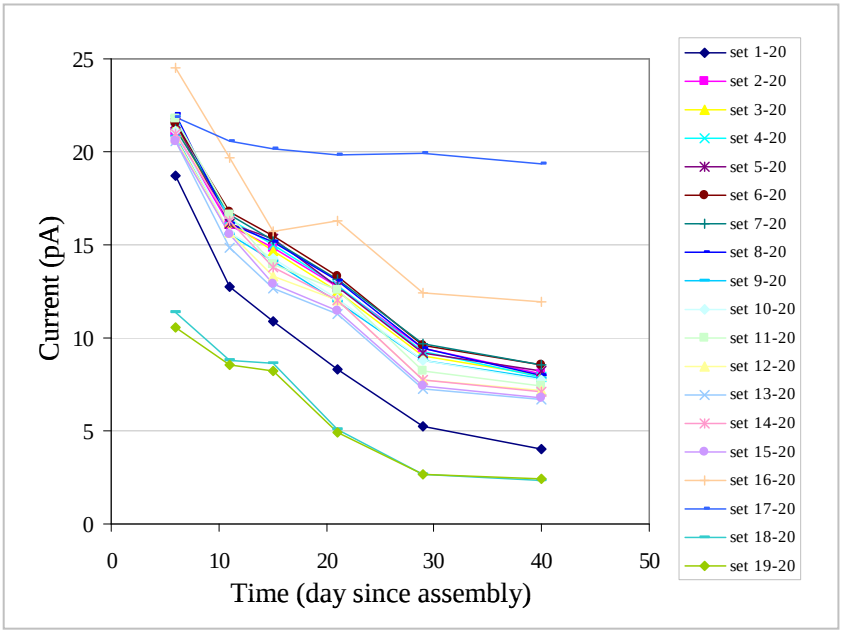

Figure 62. Decay of conductivity over time in a PEDOT / MWNTs network. Each series represent consecutive current measurements on the sets involving electrode 20: notice the lack of visible aggregation at this electrode (see Figure 60; not addressed during the experiment). The decrease in conductivity was ascribed to the degradation of the PEDOT connections. Testing: + 0.1 V DC, in air, at room temperature; the standard deviation of the data (current averages) was typically less than 1 pA.

The sets involving electrode 20 were used as a representative sample to illustrate the trend of decay in conductivity on the least conductive sets (Figure 62): notice that no apparent aggregation occurred at this electrode (see Figure 60) again suggesting the presence of nano-scale interconnects.

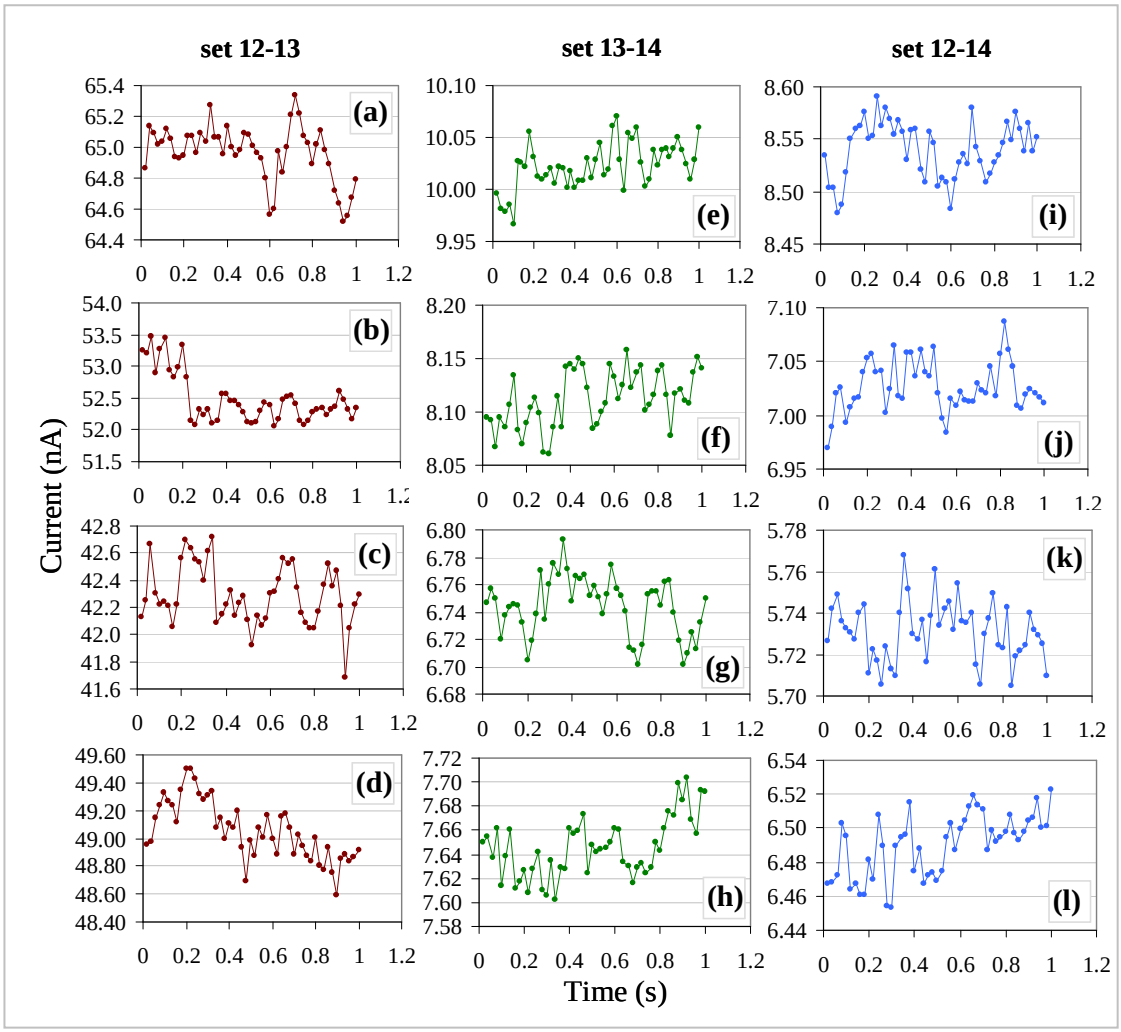

Figure 63. Unstable conductivity in a PEDOT / MWNTs network. Each series represent a raw current measurement (averages of these series were used for the stability test in Figure 61): set 12-13 **(a)** day 6, **(b)** day 11, **(c)** day 15, **(d)** day 21; the same time series applies to set 13-14 **(e-h)** and set 12-14 **(i-l)**. Testing: + 0.1 V DC, in air, at room temperature; the standard deviation of the current averages above 1 nA was found to scale up with the current in a linear fashion as the result of the observed instability.

Further evidence for instability in the networks could be found by analyzing the raw current signals from which the data sets presented so far derive (see Section 3.1 and sub-Section 3.4.1 for details on the measurement protocol). While most of the measurements on CP networks yielded a (quasi) steady state current (usually after the initial capacitive discharge), in the NTs networks a characteristic instability in the measured current was typically observed (Figure 63); in the absence of any trend in

the raw data set (i.e. initial capacitive response) the whole measurement (50 samples in this case, apparent sampling rate 50 Hz) was averaged to yield a representative value for the current. Although the standard deviations were typically in the order of few picoamps for currents up to about 1 nA, these were found to scale up almost linearly with the current for values above 1 nA: such trend, opposite to what would be expected if the measurement was affected by noise, could only be attributed to the observed instability. Thorough analysis of the data may reveal a correlation between the amount of current carried through a connection and its degree of instability. As a representative sample, only raw data relative to three sets of electrodes were shown (Figure 63); indeed similar effects were common in many of the measurements on networks containing NTs. Occasionally a similar instability was observed also in CP-only networks, suggesting a particular mechanism of conduction through the network as the possible cause; such mechanism would predominate on the steady state conduction when many contacts between the conducting elements are present, such as in the NTs-CPs networks. Statistical analysis of the raw data will be needed in order to elucidate the factors underlying such instability.

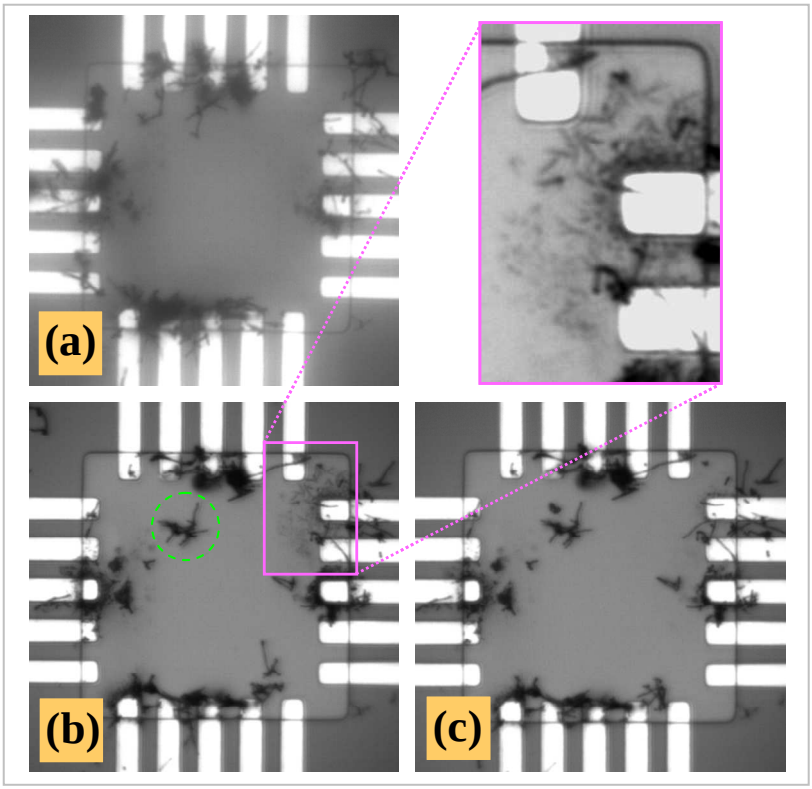

Figure 64. Structural changes during the washing process in a PEDOT / MWNTs network (same as in Figure 60). **(a)** structure at the end of the experiment, with the assembly solution still present; **(b)** after removal of the solvent, notice the collapse of many bulk structures assembled at the electrodes and the repositioning of some clusters (an example in the broken circle); **(c)** after washing with MeCN most of the material is retained; however most of the radial assembly at electrode 16 (inset) was lost.

Although a promising approach toward the production of conductive NTs networks, the directed assembly in solution did present some limitations. As mentioned earlier NTs- only networks were too weak to resist the washing / drying procedure, with the result that the vast majority of the (visible) material was washed away during the process. The concomitant use of CP significantly enhanced the robustness of the network, but in some cases structural changes were observed during the washing process (Figure 64). These were mainly attributed to the collapse of the (3D) structures produced during the in-situ assembly procedure, pointing to the lack of selectivity for the 2D assembly as one of the main limitations of such method. Alternative methods were investigated in order to identify procedures that would allow higher control on the dimensionality of the assemblies produced; the assembly of PEDOT-MWNTs structures by DEP was not studied further.

4.4 – Self-assembly at the interface between immiscible solvents.

In recent years several reports appeared regarding a novel interfacial assembly technique for the production of 2D films of nanomaterials. Although mainly applied to NPs (nanoparticles)[106], such technique was also used for the production of NPs-NTs (nanotubes)[94, 107] and NPs-MWs (molecular wires) composites. In the context of the production of reconfigurable networks of conductive organic materials, the main focus was put on the production of NTs films using a combination of the interfacial assembly method reported by Reincke[106b] with the polyelectrolyte wrapping strategy[108]. The films were transferred onto the MMEA and electrically characterized; strengthening of the con-nections could be achieved by cyclical potential scanning. Directed assembly of PEDOT onto the as-produced NTs films was also attempted, and some evidence for the EDOT polymerization taking part in the strengthening process could be found in cracked/sparse NTs networks.

Some NPs and NPs-MWs composite films were also produced using the same method[106b]: electrical testing highlighted an increase in conduction with increasing MW/NP ratio.

4.4.1 – Interfacial assembly of PSS/MWNTs networks.

In order to produce MWNTs films via the interfacial assembly technique, NTs that could be efficiently dispersed in water were employed. Shortened MWNTs (length ~ 2 μm, diameter ~ 10 nm), produced by D. Marsh[93], were dispersed in water

by ultrasonication; Na PSS was used as the surfactant, so to improve the stability of the dispersion and provide a negatively charged coating. The aqueous solution was covered with a layer of hexane and an aliquot of ethanol was injected into it, causing the immediate destabilization of the solution and the formation of a dark film at the interface between the two immiscible solvents. After the evaporation of the organic layer, circular portions of the film were hand-picked using a metal loop (Pt wire), deposited onto the MMEAs, rinsed and dried in air, and electrically characterized (DC + 0.1 V and cyclic voltammetry). Although such method consistently yielded the desired films, intrinsic variability in the process arose from the film transfer procedure (that should be automated in order to eliminate the human factor). Although some continuous films were successfully transferred onto the devices (Figures 65b, 66 and 67), some were found to crack during the process yielding incomplete coverage of the SiO_2 platform (and the electrodes array; Figures 65a, 68 and 70). Both kinds of films have been reported in order to highlight some differences in the effect of directed assembly conditions on the as-deposited films.

In one case incomplete deposition and electrical characterization (in air) were followed by a second deposition step that successfully covered the whole platform (Figure 65a, first layer; 65b, second layer). By plotting the current before and after the second deposition step it was noticed that very little change occurred on the electrode sets already coated during the first deposition (the black line in the current vs current plot shows the hypothetical 1:1 correlation if no change had occurred); on the contrary the rest of the electrode sets changed from a non-conductive state (all below 1 pA) to a very conductive one, with an increase of 5 orders of magnitude in the measured current. By plotting the current after the second deposition vs. the interelectrode gap (Figure 65) it could be noticed that the set of lower conductivity data spreads almost uniformly around 10 nA irrespectively of the gap size, suggesting the contribution of a large number of parallel connections to the conductivity.

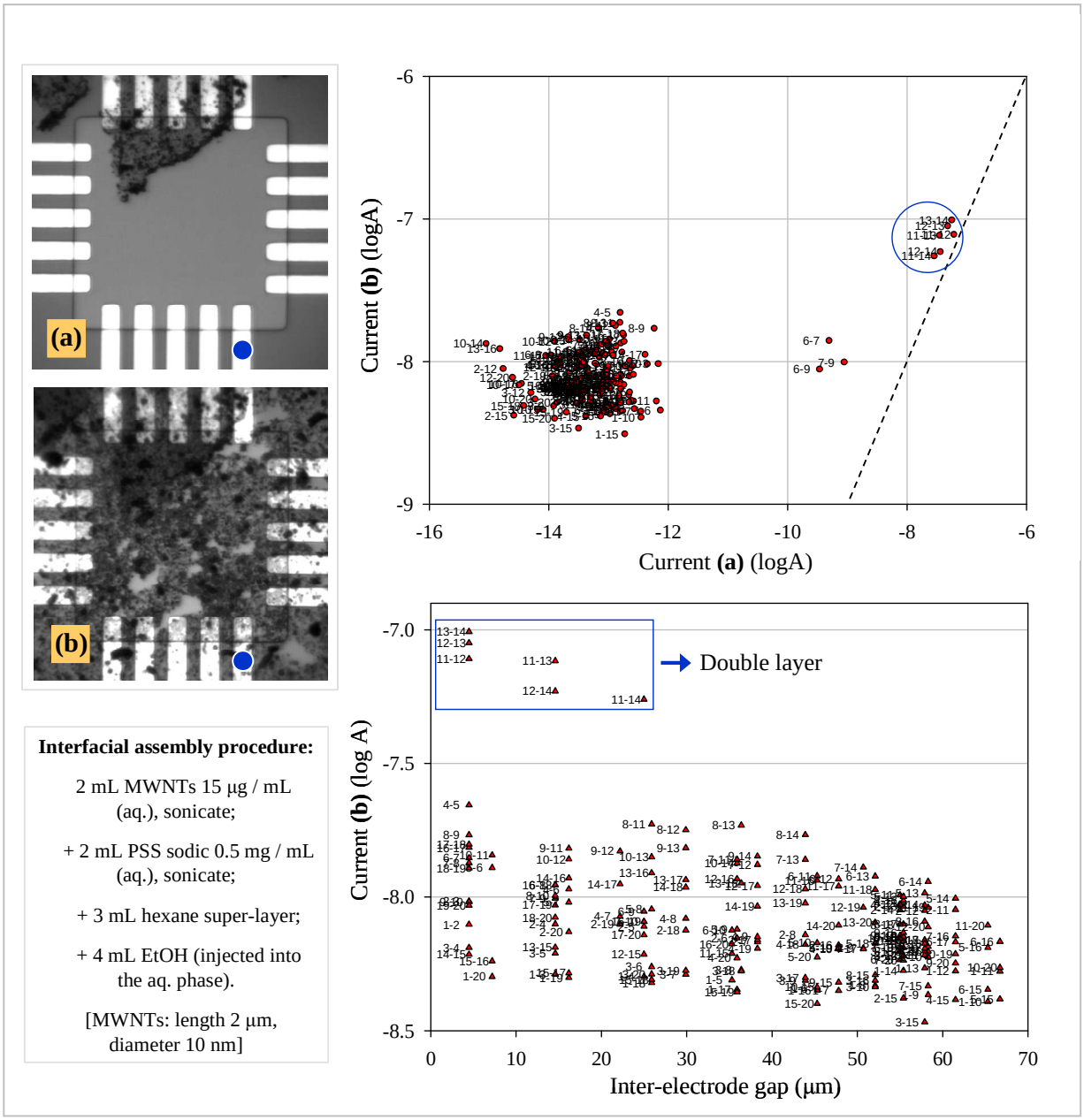

Figure 65. MWNTs-PSS films produced by interfacial assembly and transferred onto a MMEA. **(a)** First transfer attempt, resulting in incomplete coverage; **(b)** second attempt, resulting in complete coverage. After each deposition step the assembly was tested (+ 0.1 V DC, in air), allowing to compare the current before and after the second deposition step. Electrode 1 is marked by the blue dot in the Figure, the electrode count proceeds clock-wise.

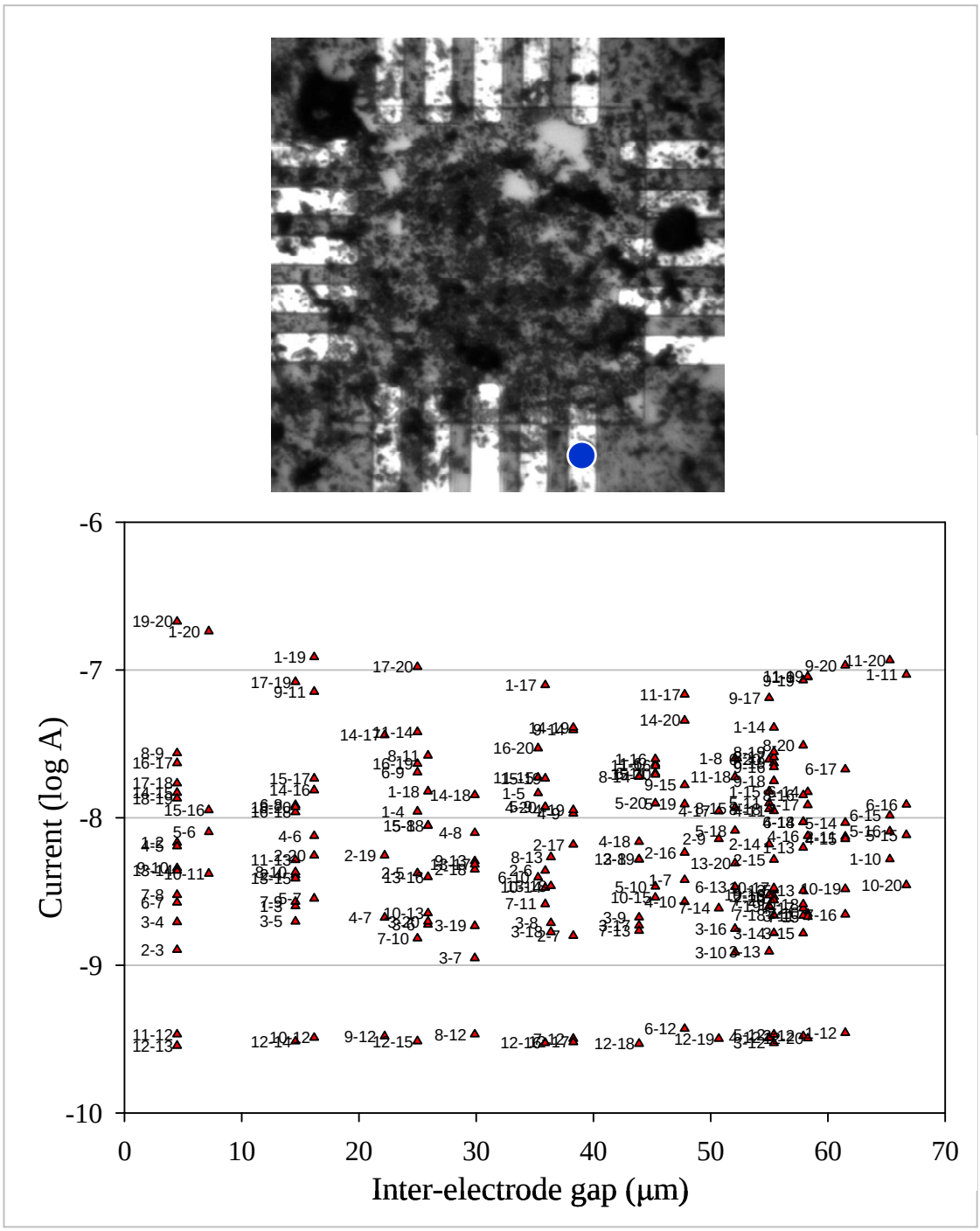

Figure 66. A MWNTs-PSS film produced by interfacial assembly and transferred onto a MMEA. Interfacial assembly: see Figure 65. The resistance of the film was found to vary over 2.5 orders of magnitude, centred at ~ 10 MΩ. Electrode 1 is marked by the dot in the Figure, the electrode count proceeds clock-wise. Testing: + 0.1 V DC, in air (the first electrode in the sets always the source). Electrodes: Pt, area 6 x 6 μm^2 ca.

This was also the case when continuous films were successfully deposited in a single step: current data spread over 2.5 orders of magnitude around 10 nA (Figure 66) and over 2 orders around 100 nA (Figure 67), without any apparent dependence

on the gap size, proved the validity of this approach in the production of highly interconnected, highly parallel, MWNTs networks.

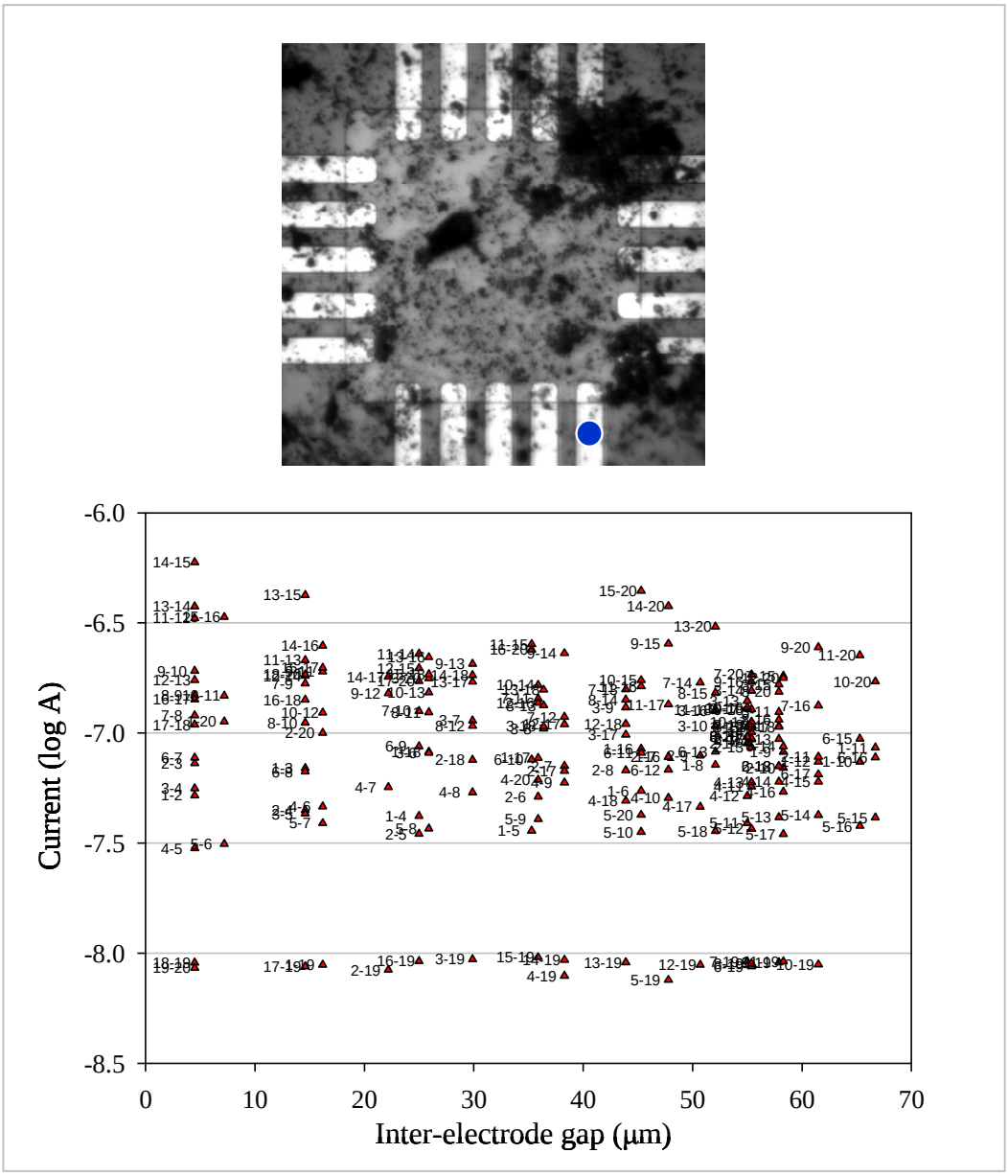

Figure 67. A MWNTs-PSS film produced by interfacial assembly and transferred onto a MMEA. Interfacial assembly: see Figure 65. The resistance of the film was found to vary over 2 orders of magnitude, centred at ~ 1 MΩ. Electrode 1 is marked by the dot in the Figure, the electrode count proceeds clock-wise. Testing: + 0.1 V DC, in air (the first electrode in the sets always the source). Electrodes: Pt, area 6 x 6 μm^2 ca.

In the case of cracked / inhomogeneous films the current data were more spread, as expected (Figures 68 and 70). Although some electrodes were evidently lacking material (by optical imaging), some evidence for nano-scale connections could again be found: conductivity in sets involving electrode 18 was observed for the network in Figure 68, and the same was true for electrode 11 in Figure 71; notice that

also three electrode sets (sets 6-7, 6-9, 7-9) in the network in Figure 65a resulted electrically connected in the absence of any visible aggregate.

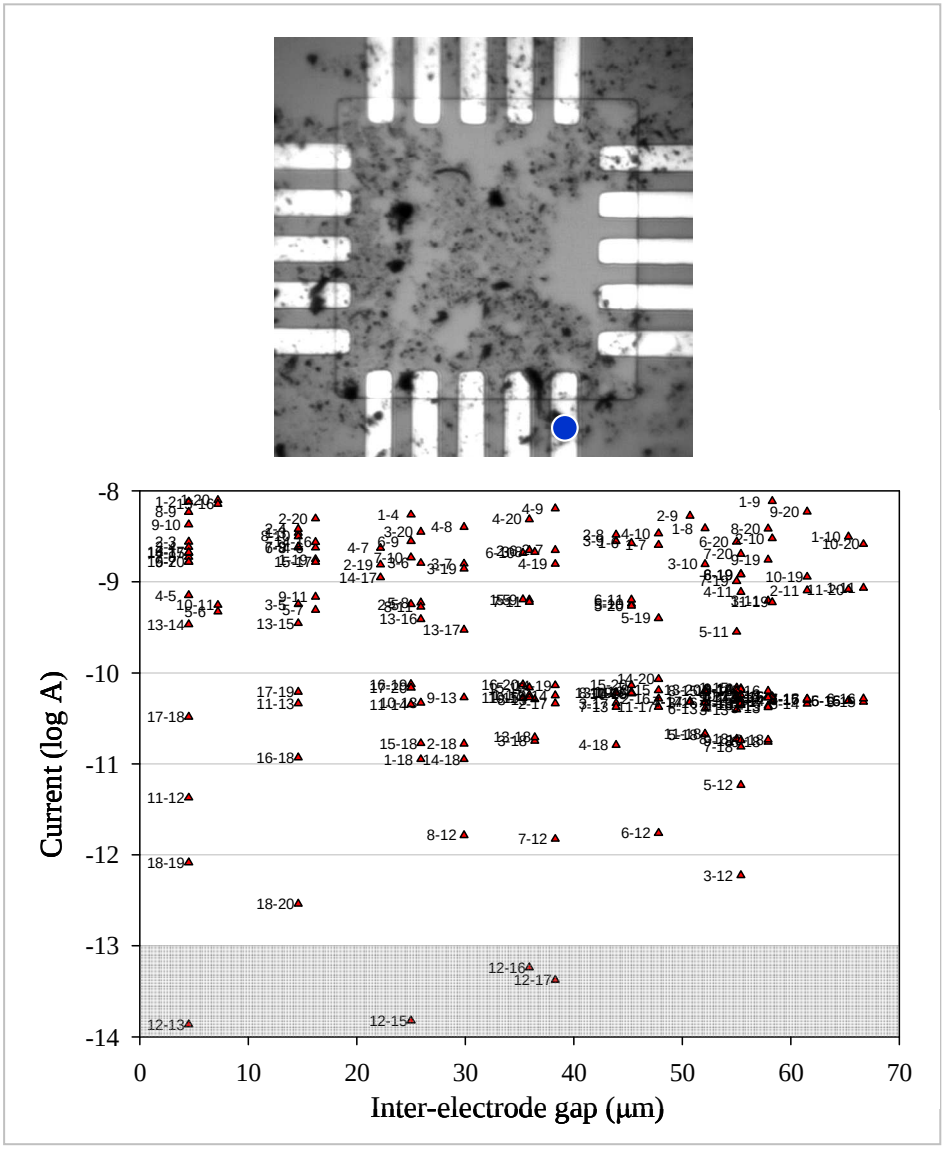

Figure 68. A MWNTs-PSS film produced by interfacial assembly and transferred onto a MMEA. Interfacial assembly: see Figure 65. The data were spread across 5 orders of magnitude; the most conductive sets were centred at about 1 nA (~ 100 MΩ). Electrode 1 is marked by the dot in the Figure, the electrode count proceeds clock-wise. Testing: + 0.1 V DC, in air (the first electrode in the sets always the source). Electrodes: Pt, area 6 x 6 μm^2 ca.

Stability tests were not carried out on these networks; their reconfiguration by electrical method was attempted instead. Cyclic scanning of the potential between 0 and + 5 V DC was performed sequentially on all the electrode sets (190), while measuring the current; the scan was executed three times on each set, for a total of 570 IV scans / experiment. The conductivity pattern in the networks was recorded before and after the potential scan by testing at low voltage (+ 0.1 V DC); all tests were

performed in air, on samples dried in air. This method, applied to the network shown in Figure 68, resulted in increase in conductivity for all the connections present in the network prior to the scan; the currents at baseline level were less affected, but indeed showed a general decrease after the scan (Figure 69). By plotting the currents before vs. those after the scan, the evolution of the conductivity pattern in the system could be visually estimated; evident clustering in the data set could be observed, and no attempt at correlating the whole data set with a theoretical model was made.

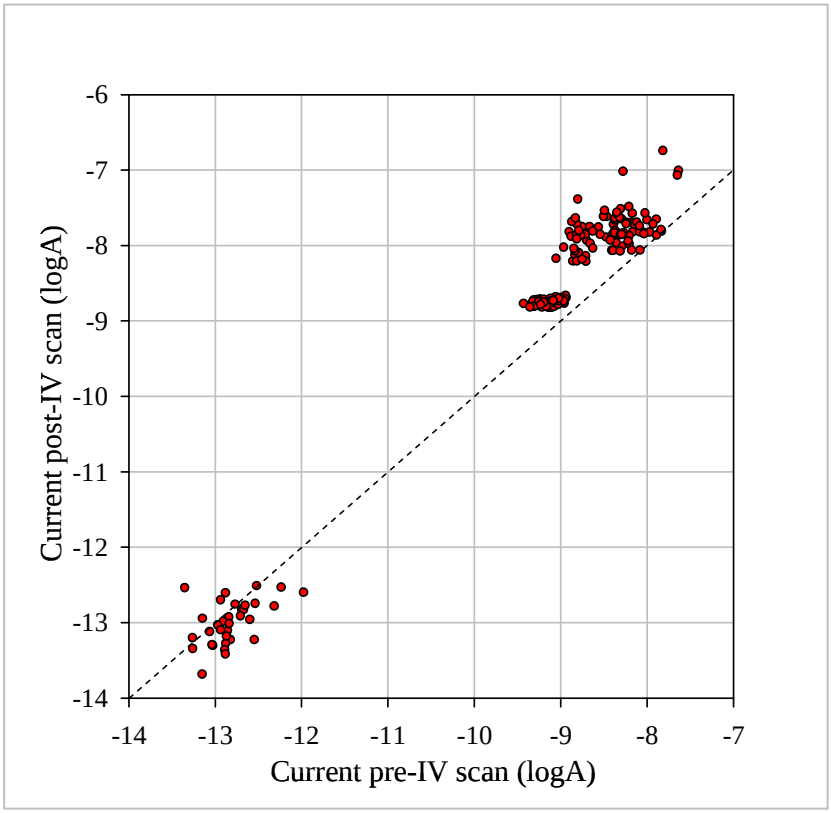

Figure 69. Currents before vs. currents after the IV scan (0 to 5 V, cyclic, performed three times on each set of electrodes) in the network shown in Figure 68. Notice the evident clustering and the general increase in conductivity on the sets already conductive prior to the scan (the broken line shows the expected trend if no change had occurred).

In order to derive a numerical value representative of the change in conductivity for the whole system, the ratios of the current before / current after were used instead; since the same electrical method was applied to all the possible connections, the average of such ratios was used to provide a single number representative of the change in the whole network. Ratios between 0 and 1 would point to a decrease in conductivity, above 1 to an increase; the ratios obtained from the experiments reported here were always higher than 1, confirming that the potential scanning method reproducibly increases the conductivity of the network. Later the

average ratios will be used to compare the effects of the potential scan method on different networks / experiments.

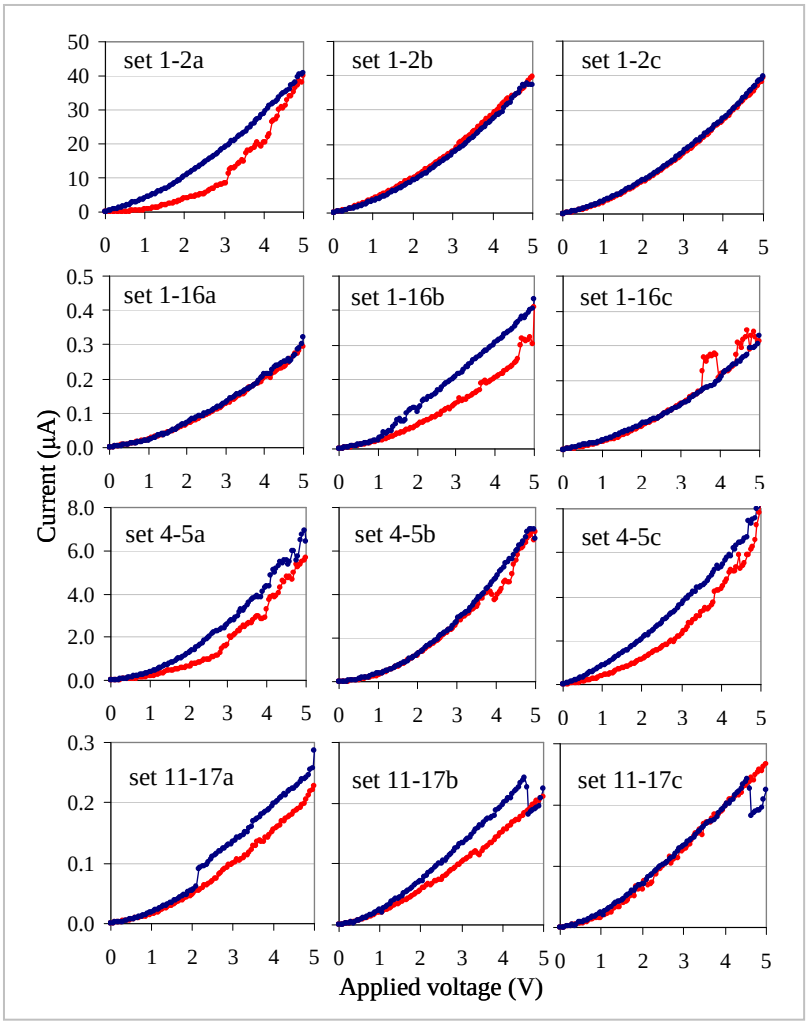

Figure 70. Cyclic potential scanning of some electrodes sets on the MWNTs film shown in Figure 68. The potential on each set was scanned three times consecutively (red trace, forward; blue trace, backward; scan rate ~ 600 mV / s). The strengthening of the connections, often observed, was attributed to the recruitment of conductive elements under potential control.

Interestingly, when monitoring the current during the sequence of three IV scans / electrode set, hysteresis was often observed: the fact that the return scan trace was often on the top of the forward trace provided further evidence for the role of the potential scan in increasing the conductivity of the connections; several current jumps could also be observed, and were attributed to the recruitment of NTs under potential control (Figure 70). The same experiment was repeated on another cracked / inhomogeneous film: while the network in Figure 68 had only been soaked in MeCN prior to the IV scans, the network in Figure 71 was also subject to the drop-cast deposition of EDOT monomer (2 µL EDOT 50 µM in MeCN).

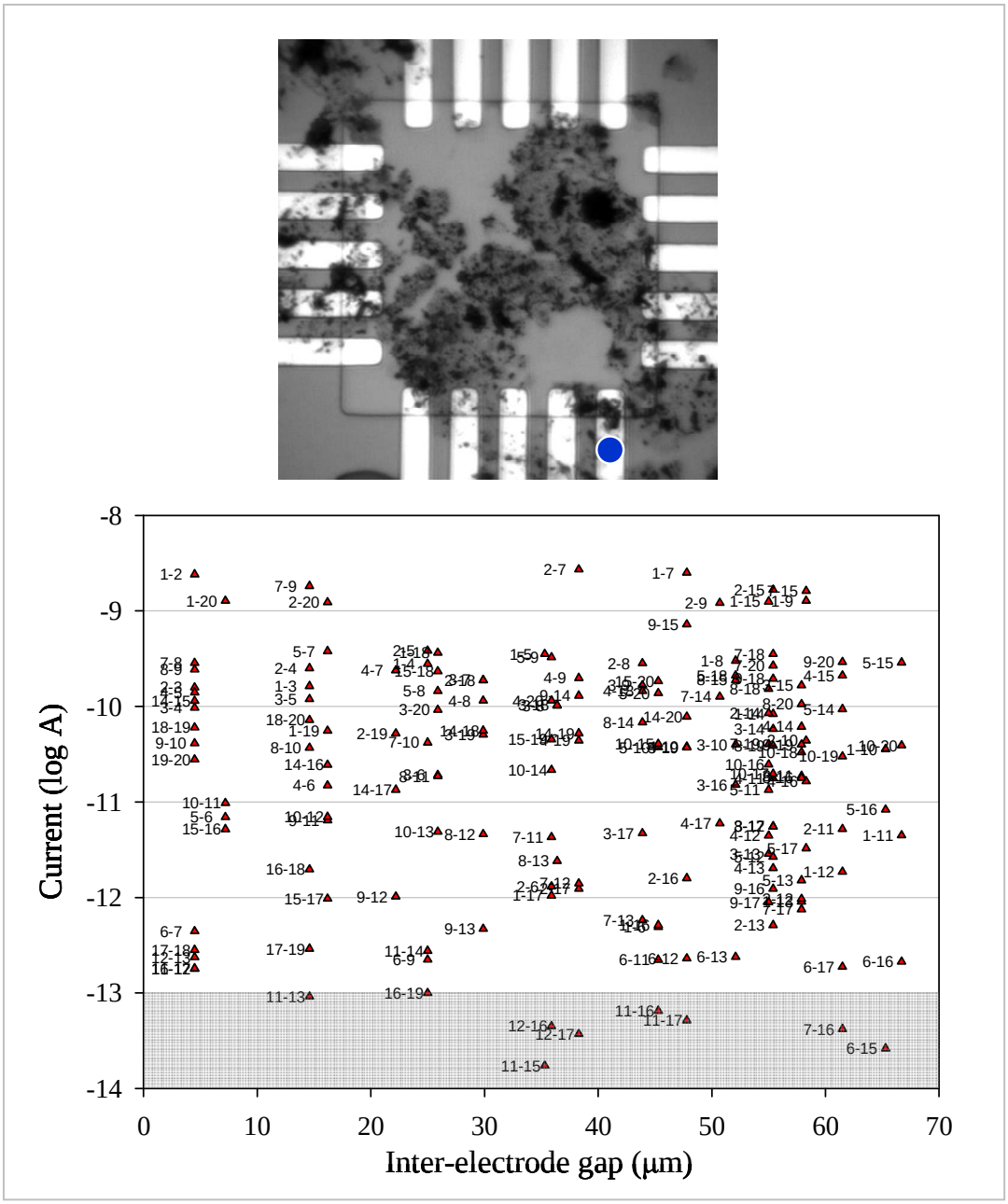

Figure 71. A MWNTs-PSS film produced by interfacial assembly and transferred onto a MMEA. Interfacial assembly: see Figure 65. The data were widely spread across 5 orders of magnitude. Electrode 1 is marked by the dot in the Figure, the electrode count proceeds clock-wise. Testing: + 0.1 V DC, in air (the first electrode in the sets always the source). Electrodes: Pt, area 6 x 6 μm^2 ca.

A general increase in conductivity was again the result (current vs. current plot not shown). Differently from the previous case, a change in slope occurring at about + 2.5 V was often observed: since such change occurred at a potential close to the oxidation potential of EDOT (in solution, ~ 2 V vs. SCE) it was attributed to the formation of PEDOT under electrochemical control. Notice however how current jumps ascribable to the recruitment of NTs could still be observed (Figure 72).

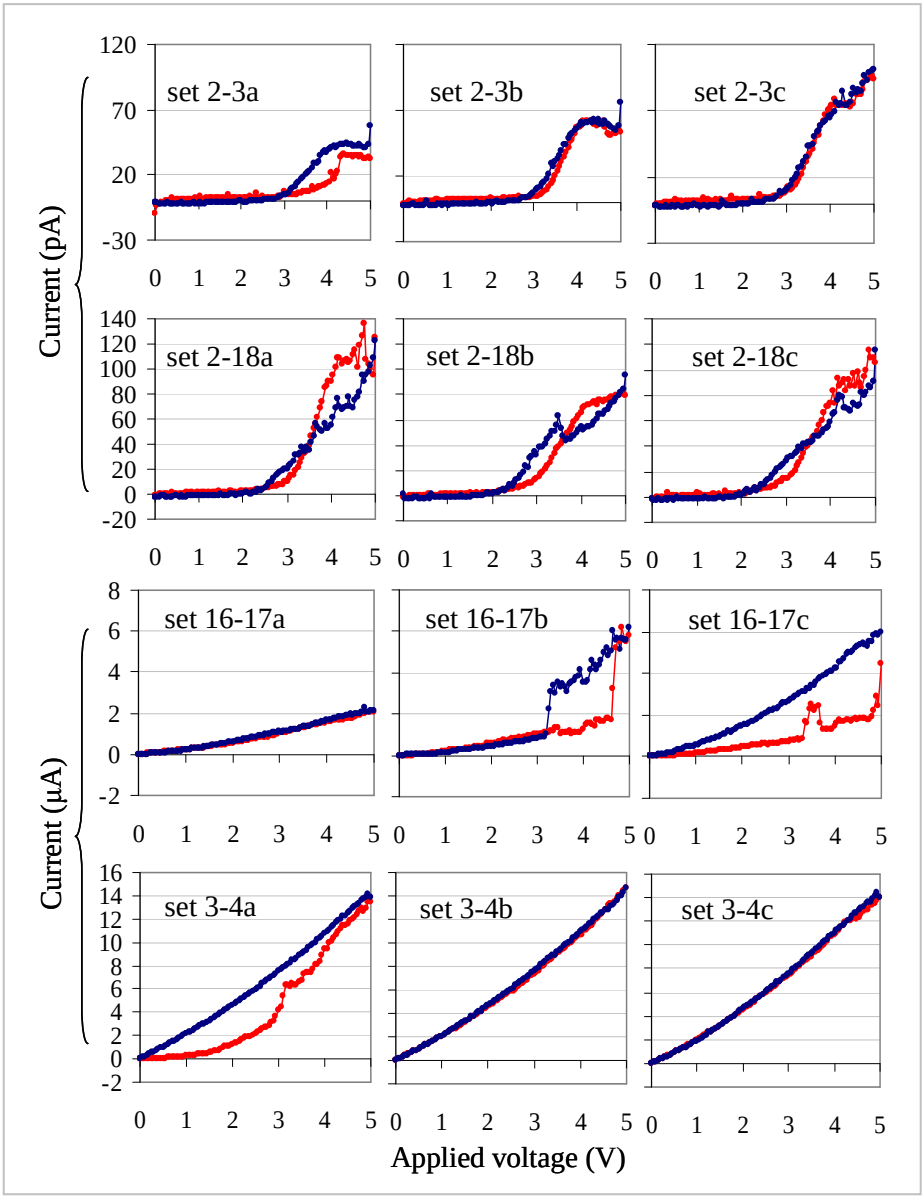

Figure 72. Cyclic potential scanning of some electrodes sets on the MWNTs film shown in Figure 71. The potential on each set was scanned three times consecutively (red trace, forward; blue trace, backward; scan rate ~ 40 mV / s). The strengthening of the connections, often observed, was attributed both to the recruitment of conductive elements and to PEDOT in-situ electropolymerization.

When the same experiment was repeated on a well conductive, homogeneous, network (i.e. that in Figure 66) strengthening of the connections was again the result. This time however no evidence for PEDOT electropolymerization was found in the IV scans; when the average ratios from the three experiments were compared (Table 4) it was evident that the effect of drop-casting EDOT prior to the scan was major only on the cracked / inhomogeneous network; the larger increase in conductivity in the homogeneous film (Figure 66), when compared to the no-EDOT case, was mainly ascribed to the larger amount of NTs available to reinforce the connections. A more detailed

analysis and further experiments are required in order to specify the role of EDOT in strengthening the connections in cracked / inhomogeneous / poorly conductive CNTs networks.

Network (Figure number)	Pre-IV treatment	Post-IV average ratio
68	MeCN dip, Ar dry	3
66	MeCN dip, then drop-cast 2 μL EDOT 50 μM (MeCN)	91
71	MeCN dip, then drop-cast 2 μL EDOT 50 μM (MeCN)	381

Table 4. Averages of the pre-IV / post-IV current ratios for three different MWNTs networks produced via the same interfacial assembly process (see Figure 65 for details on the assembly method). The largest increase in conductivity consequent to IV scanning (cyclic, 0 to + 5 V, three times / electrodes set) was found in the cracked / inhomogeneous network shown in Figure 71 (pre-treated with a solution of EDOT monomer).

It should be noticed that, although not reported for the films produced via the interfacial assembly strategy, unstable conductivity was very common in all the NTs networks. As explained before the raw data were not adequately analyzed to assess the frequency and extent of the current jumps / fluctuations observed; nonetheless this kind of analysis may provide valuable information on the effect of the potential scan technique on the stability of the connections. The selectivity of the method was also not explored: the ability to choose the connections to strengthen, and execute potential scans with little or no effect on non-addressed connections, would classify the reported method as a novel directed assembly strategy.

4.4.2 – Interfacial assembly of NTs / NPs networks.

Some work on the production of hybrid NTs - NPs films via the interfacial assembly technique was done in collaboration with Prof. A. Khlobystov and Dr. D. Marsh (BrainCHELL, University of Nottingham). Since at the time the measurement apparatus here reported had not yet been completed, and only the faulty MMEA was available (see Figure 19 in Section 3.2), the assemblies were transferred on commercial multi-band MEAs (Windsor Scientific) and electrically characterized using the departmental probe station (Rapid Prototyping Facility, School of Physics). The electrodes were addressed using single-probe micromanipulators with coaxial

shielding, placed in a Faraday cage; testing using DC or cyclic potential scans was performed using the Agilent 4155C Parameter Analyzer: the resolution of this system was comparable to that of the system later developed by us.

Since no further work using this composite was done after completion of the experimental system no pertinent data could be reported: refer to the reported document[94] for more details regarding the production of thiol-MWNTs / Au@citrate NPs hybrid conductive networks via the interfacial assembly technique, and their characterization by electrical methods; the same material / method had been previously reported[107], but lacked electrical characterization. Preliminary results suggest the incorporation of NPs into the NTs networks as having little effect on the conductivity at the macro-level; such effect, more pronounced when μm-scale inter-electrode separations are taken into account, has yet to be studied on a MMEA with the size and geometry as that employed in this project.

4.4.3 – Interfacial assembly of MWs / NPs networks.

Some work done in collaboration with Prof. A. Khlobystov and G. Rance (BrainCHELL, University of Nottingham) involved the testing of NPs and MWs/NPs films produced via the interfacial assembly technique, following a procedure similar to that reported by Reincke[106b]. An ethanol-soluble OPE MW (Figure 73) and Au@citrate NPs (average diameter 18.5 nm by TEM, 20.5 by DLS) were produced and assembled into films by G. Rance[95]. Ethanol, needed to destabilise the Au colloid and produce NPs-only films, was also used as solvent for the MW, so to produce composite MWs / NPs films with different MWs /NPs ratios (1/1, 10/1, 100/1); no super-phase was used, yet the assembly quickly occurred at the air-water interface upon mixing the aqueous colloid and the MWs solution (within 5 minutes). The dark-blue films were hand-transferred onto the MMEA devices by using a metal loop (Pt wire), rinsed with water, dried and imaged under the optical microscope, revealing a highly homogeneous structure (Figure 74).

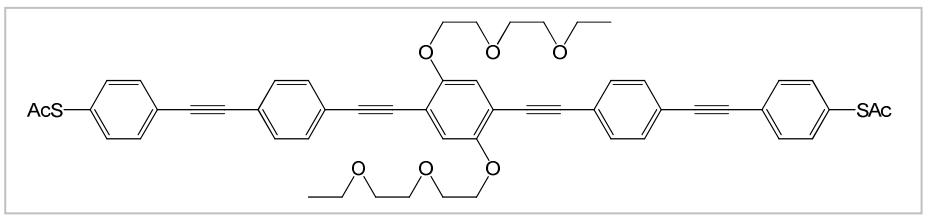

Figure 73. Structure of the thioacetyl-MW used for the assembly of MWs / Au NPs networks. The polyether-chains confer solubility in EtOH, the solvent of choice for the induction of interfacial assembly in aqueous gold colloids. Refer to the reported document[95] for the synthetic procedure.

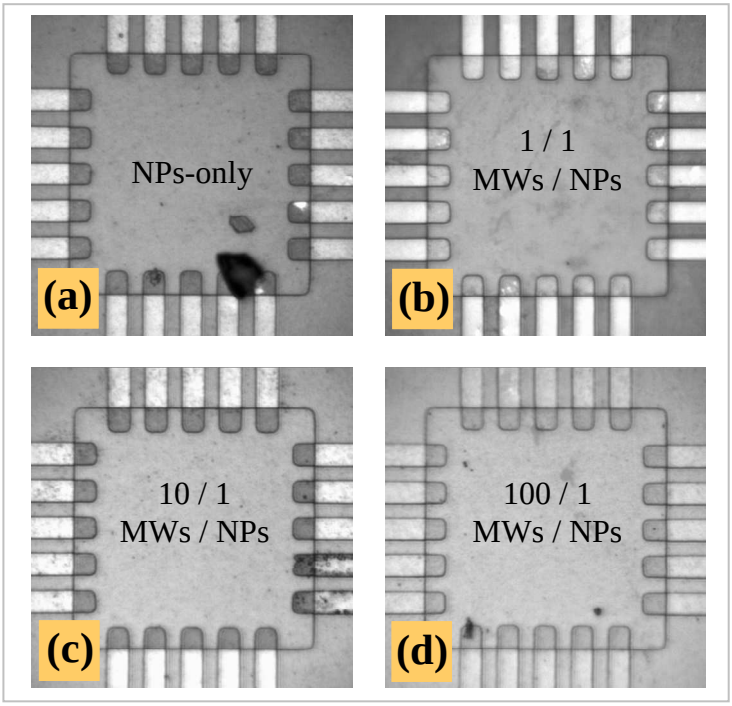

Figure 74. MWs / Au NPs films produced by interfacial assembly and transferred onto MMEAs. **(a)-(d)**: optical images of 4 films with different MWs / NPs ratios, 0/1, 1/1, 10/1, 100/1 respectively. Interfacial assembly: 2 mL Au@citrate NPs, 1.8 x 10^{12} NPs/mL (aq.) + 4 mL neat EtOH (a) or + 4 mL OPE MW (see Figure 73), 1.8 x 10^{12} (b), x 10^{13} (c), x 10^{14} (d) molecules/mL (EtOH; respective solutions 3, 30, 300 pM). NPs average diameter: 18.5 nm (TEM). Hand-transferred onto the MMEA using a Pt loop. Electrodes: Pt, area 6 x 6 μm^2 ca.

All of the assemblies produced were found fairly conductive when electrically tested (+ 0.1 V DC, in air; Figure 75a-d). The homogeneous network morphology was reflected in the relatively narrow interval over which the data were spread, which in turn allowed the use of a general average current value for each of the networks. Not much difference was observed between the NPs-only and the 1/1 MWs / NPs ratio samples, with average currents of 0.94 and 0.46 nA respectively; notice that the incorporation of MWs in 1/1 ratio resulted in a slight decrease in conductivity, probably the consequence of increasing the inter-NP separation without providing a sufficient number of alternative conductive paths. When comparing the three MWs-containing samples, the conductivity was found to increase linearly with the MWs / NPs ratio along the series 1/1, 10/1, 100/1 (Figure 75e).

Another interesting feature could be observed in the current vs. interelectrode gap graphs (Figure 75a-d; one current data point per set of electrodes). While the low conductivity networks were showing a pattern typical of the predominance of series connections (i.e. no high currents at large gaps), the data for the 10/1 MWs / NPs ratio

assembly were spread over the current range irrespectively of the interelectrode gap, suggesting a significantly higher number of parallel conductive paths in the network. Recovery of the trend (current decreasing at larger gaps) was instead observed for the 100/1 MWs / NPs assembly: notice however the (relative) narrowing of the current range in which the data were spread, which would suggest that the system was close to saturation (in term of the maximum number of MW-based connections that could be formed in the network). Further experiments and attempts to fit the data to theoretical models are needed to better define the mechanism of conduction through the networks.

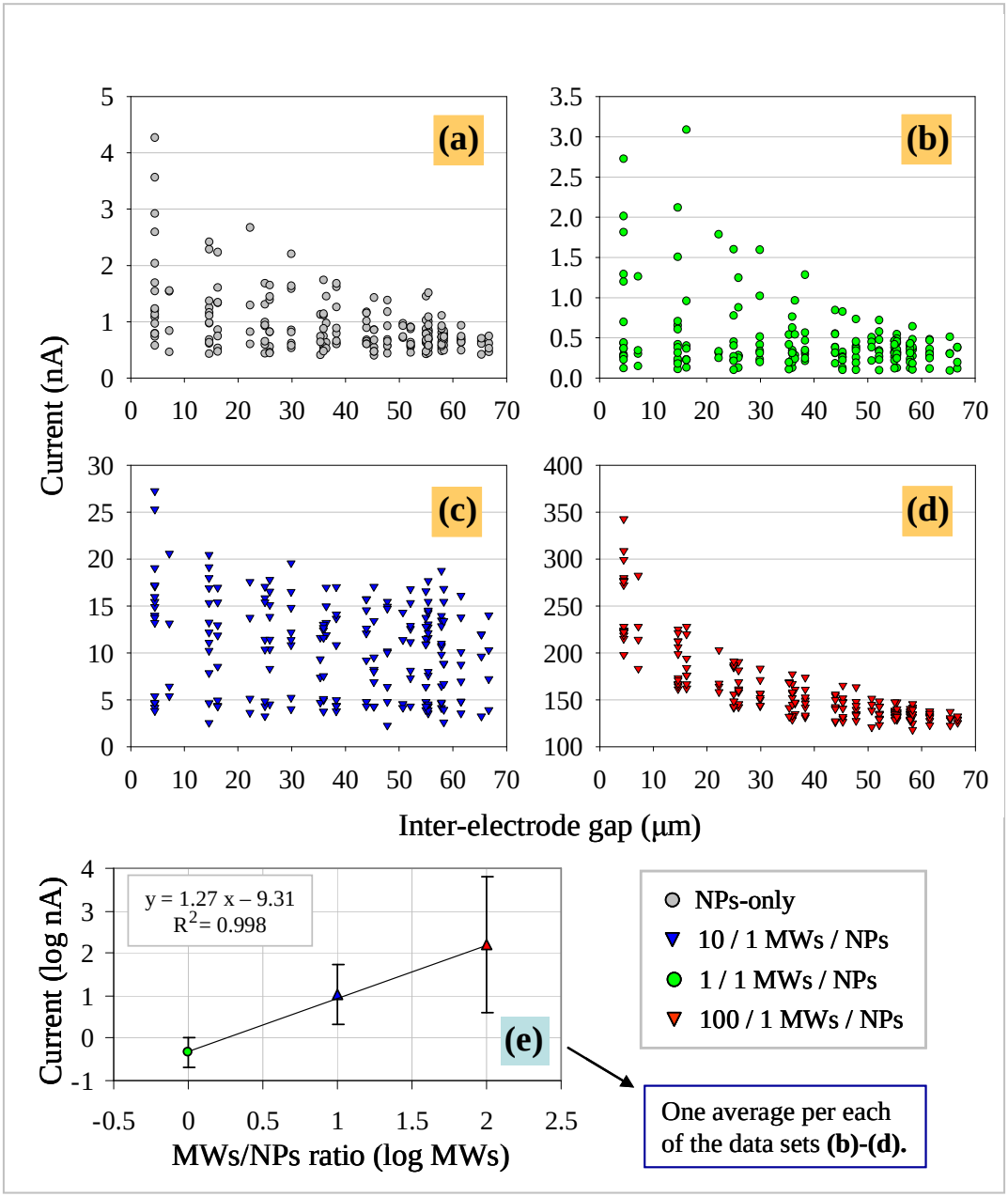

Figure 75. Electrical testing of MWs / Au NPs films deposited onto MMEAs. **(a)-(d)**: Currents at each set of electrodes vs. the inter-electrode gap for the respective assemblies shown in Figure 74; **(e)** a linear correlation was found between the average current on each network and the MWs / NPs ratio. Testing: + 0.1 V DC, in air.

A different approach toward the production of MWs / NPs 2D networks was also attempted. NPs-only films were transferred onto the MMEAs and characterized prior to soaking in a solution containing the MWs. Although an increase in conductivity was often observed, the control experiments did not provide evidence for the role of the MWs in such change: exposition of the NPs films to neat solvents also produced a general increase in conduction, typically accompanied by an increase in reflectivity. Such effect made it impossible to assess the contribution of the MWs to the increase in conductivity, and the approach was discarded.

4.5 – Conclusions.

Using several techniques, conductive micro-networks of organic and hybrid materials were produced and electrically characterized.

Although lacking selectivity (on this scale and under the conditions employed), the directional PEDOT polymerization approach represents a novel and interesting method for the bottom-up assembly of conductive micro- and nano- structures; optimization of the experimental conditions may provide a valuable alternative to the high-frequency method[100], with increased selectivity for the formation of surface-bound structures.

The in-situ directed assembly of NTs appeared mainly limited by the fragility of the aggregates; nonetheless the co-assembly of PEDOT connections provided enough structural strength to allow the electrical characterization in the dry state.

An alternative combined technique has been proposed, that would allow the materials of interest to be assembled into 2D films by a self-assembly procedure (bottom-up), and transferred to the MMEA via a top-down process; post-transfer reconfiguration was shown to take place in these films as the result of cyclically scanning the electric potential across the connections.

A novel MWs / NPs hybrid material in which the conductivity can be modulated by varying the ratio of components has also been presented.

The multichannel apparatus implemented for this project and its built-in automation capabilities (Chapter 3) enabled us to perform a large number of high-sensitivity measurements and assembly protocols on all of the materials presented above: the results presented, although needing further validation, confirm the versatility of the proposed methodology for the efficient screening of the electrical properties of any material of interest in nanoelectronics.

Chapter 5 – General Conclusions and Future Work.

During this project essential preliminary steps have been taken in the study of the assembly of electrically anisotropic 2D networks of organic and hybrid materials.

A silicon-based MEA was produced and served as the experimental platform: it was mainly employed to test different directed assembly techniques, all requiring solution environment, and to electrically characterize the resulting assemblies (in the dry state); alternatively some of the devices served as the substrates for the deposition of films produced via the interfacial assembly technique (and their electrical testing).
Even though some limitations in the directed assembly experiments resulted from the lack of a purpose-designed solvent chamber, it was possible to produce low-dimensional assemblies from solutions of CP monomer or from suspensions of CNTs. The devices then allowed us to wash and dry the as-produced assemblies and electrically characterize them in air.
Testing in air was also performed when the material was produced elsewhere and deposited onto the MEA post-assembly. However relatively few interfacial films were successfully transferred on the devices, mainly as the result of the poor transfer technique (by hand in the preliminary experiments reported here): in order to implement a reproducible transfer routine, a micro-motion automated device should be employed for the film pick-up and transfer; the device should be vibration-isolated and operated so to minimize disturbance to the film during the process; optical observation during the development phase may greatly help in assessing the extent of fracturing and island formation, reassembling and drying effects (after pick-up). A more easily solvable but not less crucial issue would be the screening of various loop materials and wire sizes aimed at optimizing the loop design (in absolute or even for each particular film composition). Using the MEAs produced during this project as substrates for 2D assemblies produced via the interfacial techniques represents at the moment the easiest and most efficient way of employing the large number of MEA devices (> 1000) still available.

Even though inconvenient for some studies (i.e. topographical and spectroscopic analysis of the assemblies), a purpose-designed solvent chamber would surely improve the reproducibility of the directed assembly experiments, which were generally difficult to implement on the available MEA; chemically resistant devices were recently reported using thiolene[109]. MEAs equipped with a microfluidic chamber would permit longer experimental times and, other than being used to control the

solution environment over the array, it would also allow measurements under inert atmosphere and electrosynthesis in gas phase (by feeding the monomer as a diluted aerosol).

In addition to controlling the gas- or liquid-phase environment over the MEA, the use of a thermo-cryostat to control the temperature of the array would also represent an essential step toward the minimization of uncontrolled experimental variables.

If the MEA was to be redesigned the disc electrode geometry would be preferred; larger interelectrode gaps / smaller electrodes would also be a benefit, as they would increase the selectivity of the assembly method (by reducing the extent of the field-induced parasitic assembly on non-addressed electrodes). REs could be included in appropriate locations so to provide a common reference potential for all the active electrodes. Micro- or nano-electrodes electroplated to level the insulating platform would enable a whole new series of experiments where the network could be produced by spin-coating[110] or drop-casting[111] techniques.

A commercial system for the semiautomated characterization of the networks by electrical methods was implemented. State-of-the-art instruments from Keithley (2636, 3706, 3721), together with the use of high performance cabling, connectors and probes, and a Faraday cage, allowed for the measurement of current in the lower pA range; further improvement may come from the optimization of the shielding conditions throughout the system. Additionally, up to six plug-in switching cards could be used simultaneously in the 3706, leaving ample choice in defining the connections and the scan protocols. The two SMU channels on the 2636, capable of parallel operation, could be used for proof-of-principle testing of various electronic devices; ‘daisy-chaining’ of multiple 2636 instruments by using the TSP-link protocol would allow for more than two electrodes to be simultaneously addressed. The automation capability of the system could be conveniently extended by using dedicated LabVIEW software.

A custom-designed electrical analyzer (MMA), which allows the quasi-simultaneous control of the potential and the measurement of the current flow at each of the 20 electrodes, was also developed: further testing and optimization are still needed to fully exploit the operational range of the instrument. The LabVIEW software used to operate the device has been significantly improved; nonetheless extended functionality may be desirable, particularly for directed assembly experiments: as an example, feedback control on the measured current could be used

to automatically interrupt the assembly conditions when a specified threshold is reached; access to input files, operation modes, testing and calibration routines, and preliminary data analysis protocols, could also be included to render the interface more user-friendly. Ultimately, the implementation of protocols for remotely controlling the interface via the internet would allow the CHELLware group in Nottingham to perform evolutionary studies of the assembly and reconfiguration routines: the initial data from a pristine network could be used to generate a virtual model for the simulated evolutionary training; after a number of generations, testing of the 'most fit' conditions on the real system would allow to assess the fidelity of the simulation; iteration of this cross-validation routine will hopefully lead to reliable virtual models of the individual networks, opening the way to the design of nanoelectronic circuits by computational methods and their implementation by directed- and mixed- assembly techniques (all bottom-up).

An important point to be noticed is that we refer to the networks produced as 2D structures mainly on the basis of the particular geometry of the MMEA used, which was specifically designed to detect in-plane conduction. However such assemblies are effectively 3D structures and at least one of their dimensions (i.e. that normal-to-plane) lies in the nanometer range: the information provided by extensive topographic characterization using EM and SPM techniques is considered essential for the study of the assembly procedures and electronic properties of the networks of interest. Although some of this work was originally planned (in collaboration with Prof. A. Khlobystov, University of Nottingham), it was generally difficult to manage the exchange of materials and expertise between the groups in a sufficiently frequent and timely manner: as a result of the short amount of time available the topographic characterization of the assemblies was not accomplished.

Although a preliminary effort has been made to analyze and report the data so to highlight the achievement of the desired network-like structures, the work reported here only constitutes an initial proof-of-principle study. Solid theoretical bases and statistical methods for the interpretation of the data were not provided; further work needs to be planned taking into account the large amount of data accessible via this method.

EXPERIMENTAL SECTION (1): ORGANIC SYNTHESIS.

Organic Syntheses of compounds 1-52 (Chapter 2).

General. ^{1}H and ^{13}C NMR spectra were obtained respectively at 300 and 75 MHz on a Bruker AM-300, and at 400 and 100 MHz on a Bruker Z-400. Chemical shifts (δ) are given in ppm and referenced to the solvent signals ($CHCl_3$ for ^{1}H and $CDCl_3$ for ^{13}C NMR). Coupling constants (J) are given in Hz; when not specified the D1 parameter is always 1 s; the number of scans (NS) is 16, 512 and 256 for ^{1}H, ^{13}C and DEPT respectively, unless differently stated. The $CDCl_3$ was stored over molecular sieves and anhydrous K_2CO_3; when different solvents were needed these were always obtained from ampules or small volume bottles. GCMS (EI) and (CI) (NH_3 reagent gas) were recorded on a ThermoQuest TraceMS. Electrospray mass spectra were recorded using either positive (ES^+) or negative (ES^-) mode on a VG platform quadrupole spectrometer. Values of m/z are reported in atomic mass units and the peak intensity relative to the base peak is reported in parenthesis. Infrared spectra were run as neat films or solids on a Thermo Mattson FTIR Golden Gate spectrometer. Ultraviolet spectra were run in $CHCl_3$ on a Shimadzu UV-1601 spectrophotometer. The GC data reported were obtained using a HP-5 column (crosslinked (5%-phenyl)-methylpolysiloxane; film thickness 0.25 μm, column ID 0.32 mm, length 30 m); the temperature program always started at 80 °C and stopped at 275 °C (hold for 4 minutes), with ramp 25 °C / minute.

Starting materials were purchased from Acros, Aldrich, Alfa Aesar, Fisher and Strem; [60]fullerene from MER; deuterated solvents from C.I.L. and Aldrich. TEA was distilled at ambient pressure and stored over KOH flakes, DMF was distilled under vacuum and stored over CaH_2; DBU and pyridine were distilled under Ar. Analytical grade acetone was used. THF was distilled from Na using benzophenone as indicator; benzene was distilled from Na. When required the solvents and liquid reagents were transferred from the stills/flasks to the reaction vessels using glass syringes, oven-dried overnight at 130 °C, and under Ar atmosphere. All the Schlenk flasks were two-neck, oven-dried. Stirring was achieved by mean of a magnetic stirrer bar. The HV pump employed established a pressure of 0.3 mm/Hg; the evacuation/refilling (with Ar) cycle was always repeated twice.

Several of the following compounds are NCEs. Elemental microanalysis was obtained for four of these, the final compounds **25**, **28**, **33** and **52**. The others were not extensively characterized either because intermediate products (**10**, **15**, **23**, **24**, **35**, **38**, **50**, **51**), or because of the quantity of final compound being insufficient for further purification and analysis (**17**, **36**, **42**, **43**). Microanalysis was attempted on compound **16** without satisfactory results. HRMS was obtained for NCE **42**.

O-4-Iodophenyl-N,N-dimethylthiocarbamate (**1**). To a stirred solution of 4-iodophenol (7.70 g, 35.0 mmol) in DMF (35 mL), in a 100 mL rbf, was added NaH (1.40 g of a 60% dispersion in mineral oil, 35.0 mmol, 1.00 eq.) in small portions, at r.t. After 10 minutes the reaction vessel was heated to 80 ºC over a period of 45 minutes, and then allowed to cool to r.t. before adding dimethylthiocarbamoyl chloride (5.20 g, 42.1 mmol, 1.20 eq.) in small portions. The reaction mixture was stirred for 20 h at r.t., monitoring the disappearance of starting materials by TLC. Once most of the DMF had been vacuum evaporated with a water bath at 60 ºC, the mixture was poured into DCM and washed with water; the water was extracted with DCM, and the combined organic phases were dried over anhydrous $MgSO_4$; evaporation of the solvent afforded the crude title compound (11.42 g). The pure product, a white solid (6.93 g, 22.6 mmol, yield 64%), was obtained by column chromatography on silica gel, using as eluent (8/1) hexane/DCM (R_f 0.5). **M_p** 106-108 °C (lit.[112] 109.5-110.5 °C, from EtOH). **^{1}H NMR** (300 MHz, $CDCl_3$): 7.69 (2H, d, *J* = 8.8, **Ar**), 6.83 (2H, d, *J* = 8.8, **Ar**), 3.44 (3H, s, N**CH_3**), 3.33 (3H, s, N**CH_3**); data consistent with those previously reported[59].

S-4-Iodothiophenyl-N,N-dimethylcarbamate (**2**). Compound **1** (6.29 g, 20.5 mmol) was placed in a Kugelrohr apparatus, at the temperature of 235 ºC for 2 h, with spinning. The resulting brownish oil was eluted with DCM (R_f 0.34; st. mat.: R_f 0.68) on silica gel to afford the title compound, a white solid (2.73 g, 8.89 mmol), and recovered starting material (3.28 g, 10.7 mmol). The product was then recrystallized from cyclohexane as white needles (2.45 g, 7.98 mmol, yield 39%). **M_p** 78-83 °C, from cyclohexane (lit.[112] 87.5-88.8 °C, vacuum sublimed at 106 °C, 0.7 mm Hg).

^{1}H NMR (300 MHz, $CDCl_3$): δ 7.70 (2H, d, *J* = 8.3, **Ar**), 7.21 (2H, d, *J* = 8.3, **Ar**), 3.04 (6H, s, N(**CH_3**)**$_2$**). Data consistent with those previously reported[59]; in the cited ref. the peak at 3.04 ppm is split into two singlets with relative integration 3H.

4-Iodothiophenol (**3**). A stirred solution of **2** (5.3 g, 17.2 mmol) and KOH (2.9 g, 51.7 mmol, 3.00 eq.) in degassed MeOH (100 mL), in a 250 mL rbf, was heated to reflux (80 ºC) for 1 h. The reaction vessel was then cooled in an ice bath and a solution of 2 M HCl (aq.) was added dropwise until the pH of the reaction mixture was approx. 1, followed by the addition of water (60 mL). The resulting suspension was suction-filtered through filter paper and washed with a large amount of water, which was then extracted three times with Et_2O. The combined organic phases were dried over anhydrous $MgSO_4$ and vacuum evaporated to afford a mixture of product (4.0 g, 16.9 mmol, yield 98%) (R_f 0.66) and a small amount of dimerization by-product (trace on TLC; R_f 0.78, (1/1) hexane/DCM). The mixture was used in the next step without further purification. **^{1}H NMR** (300 MHz, $CDCl_3$): 7.53 (2H, d, *J* = 8.4, **Ar**), 7.01 (2H, d, *J* = 8.4, **Ar**), 3.42 (1H, s, **SH**) data consistent with those previously reported[61].

1-Acetylthio-4-iodobenzene (**4**). To a vigorously stirred solution of **3** (2.36 g, 10.0 mmol) in pyridine (30 mL), in a 50 mL Schlenk flask and under Ar atmosphere, was added acetyl chloride (distilled under Ar; 1.42 mL, 1.57 g, 20.0 mmol, 2.00 eq.) dropwise over 15 minutes. The mixture was quenched with crushed ice and water to obtain a suspension that was vac-filtered. The white solid was washed with water, dissolved in Et_2O and dried over anhydrous $MgSO_4$, to afford after evaporation of the solvent the crude title compound (2.30 g). The product (2.21 g) was column chromatographed on silica gel using as eluent (1/1) hexane/DCM; after recrystallization from (1/1) MeOH/water it was washed with water, dissolved in Et_2O and dried over anhydrous $MgSO_4$; after vacuum evaporation the pure product was obtained as white microcrystalline powder (2.03 g, 7.30 mmol, yield 73%) that was stored under Ar. **M_p** 53-58 °C (lit.[64] 54-55 °C). **^{1}H NMR** (300 MHz, $CDCl_3$): δ 7.73 (2H, d, J = 8.3, **Ar**), 7.13 (2H, d, *J* = 8.3, **Ar**), 2.42 (3H, s, **Me**CO). **^{13}C NMR** (75 MHz, $CDCl_3$): δ 193.13 (C, **CO**), 138.44, 136.03 (2CH, **Ar**), 127.90 (C, **Ar**S), 96.02 (C, **Ar**I), 30.35 (CH_3, **Me**CO); data consistent with those reported[61].

In the NMR assignment of all compounds with aliphatic chains these are numbered starting at the methylene unit directly linked to the aromatic portion of the molecule.

1,4-Didodecylbenzene (**5**). Following the procedure described by Maillard[113], in a 250 mL Schlenk flask, fitted with a reflux condenser, dodecylmagnesium bromide (formed from Mg 2.91 g and 1-dodecylbromide 29.9 g, 120 mmol, 1.00 eq.) was diluted in Et_2O (120 mL) to obtain a 1 M solution. This was added dropwise by cannula to a 250 mL Schlenk flask, fitted with a reflux condenser, containing 1,4-dichlorobenzene (7.35 g, 50.0 mmol; recrystallized from EtOH) and $NiCl_2$-dppp (68 mg, 25 mol%), previously evacuated and refilled with Ar, and cooled in a ice bath under positive pressure of Ar. The ice bath was removed and when the mixture was at r.t. the reaction was initiated by heating the flask for few seconds with a heat-gun. After 4 h the mixture was heated to reflux (50 ºC) and stirred overnight. The unreacted alkylmagnesium bromide was then quenched with a solution of HCl 2N (aq. 70 mL), while cooling the flask in an ice bath. The two layers were separated and the aqueous phase was extracted three times with Et_2O; the combined organic phases were washed with water, $NaHCO_3$ (sat.), again water and dried over anhydrous $MgSO_4$. Evaporation of the solvent afforded the crude product as white solid (23.79 g). The by-products of the reaction, mostly dodecane, were removed by distillation in a Kugelrohr apparatus, at 200 ºC, over 3.5 h. The resulting pure product (18.09 g) was recrystallized overnight from MeOH as white microcrystalline powder (17.81 g, 42.9 mmol, yield 86%). **M_p** not available. **^{1}H NMR** (400 MHz, $CDCl_3$): 7.09 (4H, s, **Ar**), 2.58 (4H, t, *J* = 7.8, **C1**), 1.61 (4H, pent, *J* = 7.4, **C2**), 1.35-1.27 (36H, m, **C3-C11**), 0.90 (6H, t, *J* = 6.9, **C12**); data consistent with those previously reported[114].

1,4-Didodecyl-2,5-diiodobenzene (**6**). To a stirred solution of **5** (11.18 g, 26.95 mmol) in DCM (68 mL), in a 500 mL rbf, were added I_2 (27.36 g, 107.8 mmol, 4.00 eq.), H_5IO_6 (18.43 g, 80.85 mmol, 3.00 eq.), CH_3COOH (80 mL) and concentrated H_2SO_4 (11 mL); the mixture was heated to 95 ºC and stirred in the darkness for 20 h, and the disappearance of starting material was monitored by TLC, using as eluent (20/1) hexane/DCM . The reaction mixture was then poured in water and extracted twice with Et_2O; the combined organic phases were washed with $Na_2S_2O_3$ (aqueous, 10% w/v) until there had been complete disappearance of the pink colour, and three times with water, and dried over anhydrous $MgSO_4$. Evaporation of the solvent afforded the crude title compound (16.695 g); the product, as recrystallized from (6/1) EtOH/ethylacetate (tiny white needles, 13.61 g, 20.42 mmol, yield 76%), still contained about 16% trisiodination by product (as estimated by NMR). **M_p** 59-

62 °C (lit.[115] 65-66°C). **^{1}H NMR** (300 MHz, $CDCl_3$): δ 7.59 (2H, s, **Ar**), 2.59 (4H, t, *J* = 7.9, **C1**), 1.55 (4H, pent, *J* = 6.9, **C2**), 1.38-1.26 (36H, m, **C3-C11**), 0.89 (6H, t, *J* = 6.7, **C12**); data consistent with the reported[115]. Trisiodide impurity: 7.68 (1H, s, **Ar**), 3.28 (2H, t, *J* = 8.1, **C1$_a$**), 2.77 (2H, t, *J* = 8.0, **C1$_b$**). **^{13}C NMR** (75 MHz, $CDCl_3$): δ 145.02 (C, **Ar**R), 139.47 (CH, **Ar**), 100.49 (C, **Ar**I), 40.00 (CH_2, **C1**), 32.09 (CH_2, **C10**), 30.36 (CH_2, **C2**), 29.86, 29.84, 29.81, 29.72, 29.56, 29.51, 29.47 (CH_2, **C3-C9**), 22.85 (CH_2, **C11**), 14.28 (CH_3, **C12**). **LRMS**: tried EI and ES techniques but no good ions. **IR** (film): 2950 (w), 2909 (s), 2848 (s) (CH stretch).

1,4-Didodecyl-2,5-bis(2-(trimethylsilyl)ethynyl)benzene (**7**). A 250 mL Schlenk flask containing **6** (6.665 g, 10.00 mmol), $PdCl_2$ (177 mg, 1.00 mmol, 10 mol%), PPh_3 (525 mg, 2.00 mmol, 20 mol%) and CuI (381 mg, 1.00 mmol, 10 mol%), with stirring, was evacuated under HV and refilled with Ar before adding distilled benzene (100 mL). TEA (8.36 mL, 6.071 g, 60.00 mmol, 6.00 eq.) was then added, followed by TMSA (3.39 mL, 2.357 g, 24.00 mmol, 2.40 eq.) dropwise. The reaction mixture was heated to 70 ºC and stirred in the darkness for 20 h, the disappearance of starting material was monitored by TLC. The solvent was vacuum evaporated and the solid was dissolved in DCM, the solution was washed with water twice and dried over anhydrous $MgSO_4$. Evaporation of the solvent afforded the crude title compound (7.298 g) which was column chromatographed on silica gel, using as eluent (20/1) hexane/DCM (R_f 0.5), to obtain the pure product (yellowish solid, 3.524 g, 5.80 mmol, yield 58%). **M$_p$** 41-43 °C (lit.[57] 37-39 °C). **^{1}H NMR** (400 MHz, $CDCl_3$): 7.24 (2H, s, **Ar**), 2.68 (4H, t, *J* = 7.9, **C1**), 1.60 (4H, pent, *J* = 7.3, **C2**), 1.34-1.26 (36H, m, **C3-C11**), 0.89 (6H, t, *J* = 6.8, **C12**), 0.25 (18H, s, **TMS**); data consistent with those previously reported[57].

In the assignment of all the symmetrical OPE compounds the phenyl rings are numbered starting at the central ring; while the area of the ^{1}H signals reflects the presence of symmetry, the carbons reported refer only to the number of signals in the ^{13}C spectra.

1-Bromo-4-(2-(4-(2-(4-bromophenyl)ethynyl)-2,5-didodecylphenyl)-ethynyl)benzene (**8**). A 100 mL Schlenk flask containing **7** (3.524 g, 5.80 mmol), 1-bromo-4-iodobenzene (3.282 g, 11.60 mmol, 2.00 eq.), $PdCl_2$ (247 mg, 1.39 mmol,

24 mol%), PPh_3 (730 mg, 2.78 mmol, 48 mol%) and CuI (221 mg, 1.16 mmol, 20 mol%), with stirring, was evacuated under HV and refilled with Ar before adding distilled benzene (50 mL). DBU (20.8 mL, 21.19 g, 139.2 mmol, 24.00 eq.) was then added dropwise, followed by distilled water (0.17 mL, 167 mg, 9.28 mmol, 1.60 eq.). The reaction mixture was heated to 70 ºC and stirred in the darkness for 17 h, the disappearance of the starting material was monitored by TLC. The solvent was evaporated and the solid was dissolved in DCM, the solution was washed with water twice and dried over anhydrous $MgSO_4$. Evaporation of the solvent afforded the crude title compound, a dark-brown oil (10.124 g), which was column chromatographed on silica gel, using as eluent (7/1) hexane/DCM (R_f 0.57), to obtain the pure product (yellow solid, 2.342 g, 3.03 mmol, yield 52%). **M_p** 65-67 °C (lit.[57] 63-65 °C). **^{1}H NMR** (300 MHz, $CDCl_3$): 7.49 (4H, d, *J* = 8.4, **Ar2**), 7.37 (4H, d, *J* = 8.4, **Ar2**), 7.35 (2H, s, **Ar1**), 2.78 (4H, t, *J* = 7.9, **C1**), 1.69 (4H, pent, *J* = 7.2, **C2**), 1.39-1.24 (36H, m, **C3-C11**), 0.88 (6H, t, *J* = 6.6, **C12**); data consistent with those previously reported[62].

1,4-Didodecyl-2,5-bis(2-(4-(2-(trimethylsilyl)ethynyl)phenyl)-ethynyl) benzene (**9**). A 50 mL Schlenk flask containing **8** (2.275 g, 2.94 mmol), $PdCl_2$ (51 mg, 0.29 mmol, 10 mol%), PPh_3 (155 mg, 0.59 mmol, 20 mol%) and CuI (112 mg, 0.59 mmol, 20 mol%), with stirring, was evacuated under HV and refilled with Ar before adding distilled benzene (30 mL). TEA (2.46 mL, 1.785 g, 17.64 mmol, 6.00 eq.) was then added, followed by TMSA (1.00 mL, 693 mg, 7.05 mmol, 2.40 eq.) dropwise. The reaction mixture was heated to 70 ºC and stirred in the darkness for 20 h, the disappearance of starting material was monitored by TLC. The solvent was evaporated and the solid was dissolved in DCM, the solution was filtered through Celite 521, washed with water twice and dried over anhydrous $MgSO_4$. Evaporation of the solvent afforded the crude product (2.472 g). This was column chromatographed on silica gel, using as eluent (20/1) hexane/DCM (R_f 0.19), to obtain the pure title compound (1.613 g, 2.00 mmol, yield 68%). **M_p** not available. **^{1}H NMR** (300 MHz, $CDCl_3$): 7.44 (8H, m, Ar2), 7.35 (2H, s, Ar1), 2.79 (4H, t, *J* = 7.8, **C1**), 1.69 (4H, pent, *J* = 7.4, **C2**), 1.43-1.25 (36H, m, **C3-C11**), 0.88 (6H, t, *J* = 6.8, **C12**), 0.26 (18H, s, **TMS**); data consistent with those previously reported[57].

1-(2-(2,5-Didodecyl-4-(2-(4-ethynylphenyl)ethynyl)phenyl)ethynyl)-4-ethynylbenzene (**10**). In a 100 mL rbf a solution of **9** (772 mg, 0.95 mmol) in (3/1) DCM/methanol (40 mL) was stirred in presence of K_2CO_3 (1.313 g, 9.50 mmol, 10.00 eq.) for 1.5 h. Water was poured in the flask to dissolve the carbonate, then the solution was extracted twice with DCM; the combined organic phases were dried over anhydrous $MgSO_4$ and vacuum evaporated to afford the crude product (pale yellow solid, 635 mg, 0.86 mmol, yield 90%). By NMR the material was assumed to be pure enough for the next step and only a small amount (52 mg) was recrystallized from MeOH yielding a white solid (36 mg) (R_f 0.42, (8/1) hexane/DCM). **M_p** 69-70 °C.

^{1}H NMR (300 MHz, $CDCl_3$): δ 7.47 (8H, m, **Ar2**), 7.36 (2H, s, **Ar1**), 3.18 (2H, s, C**CH**), 2.80 (4H, t, *J* = 7.9, **C1**), 1.69 (4H, p, *J* = 7.3, **C2**), 1.37-1.25 (36H, m, **C3-C9**), 0.88 (6H, t, *J* = 6.6, **C12**). **^{13}C NMR** (75 MHz, $CDCl_3$): δ 142.54 (C, **Ar1**R), 132.55-131.47 (3CH, **Ar1-Ar2**), 124.09, 122.65 (2C, CC**Ar2**CC), 122.07 (C, **Ar1**CC), 93.64, 90.59 (2C, Ar2**CC**Ar1), 83.43 (C, HC**C**Ar2), 79.08 (CH, Ar2C**CH**; not visible in DEPT), 34.28 (CH_2, **C1**), 32.08 (CH_2, **C10**) 30.82 (CH_2, **C2**), 29.89-29.53 ($7CH_2$, **C3-C9**), 22.85 (CH_2, **C11**), 14.27 (CH_3, **C12**). **LRMS** (EI+): *m*/*z* 663 ($[M+H]^+$, 58%), 662 ($[M^+]$, 100). **IR** (film): 3280 (w, CH stretch, alkyne), 2954 (w), 2917, 2849 (s, CH stretch). **UV**: λ_{max} ($CHCl_3$) 343 nm (ε 74700).

1,4-Didodecyl-2,5-bis(2-(4-(2-(4-cyanophenyl)ethynyl)phenyl)ethynyl) benzene (**11**). A 50 mL Schlenk flask containing **10** (687 mg, 1.03 mmol), 4-bromobenzonitrile (415 mg, 2.28 mmol, 2.21 eq.), $PdCl_2$ (18 mg, 0.10 mmol, 10 mol%), PPh_3 (54 mg, 0.21 mmol, 20 mol%) and CuI (39 mg, 0.21 mmol, 20 mol%), with stirring, was evacuated under HV and refilled with Ar before adding distilled THF (15 mL). TEA (0.86 mL, 625 mg, 6.18 mmol, 6.00 eq.) was then added dropwise and the reaction mixture was stirred at r.t. for 22 h; the disappearance of starting material (R_f 0.12, hexane) was monitored by TLC. The solvent was evaporated and the residue was dissolved in DCM; the solution was filtered through Celite521, washed with water and brine then dried over anhydrous $MgSO_4$. After evaporation of the solvent, the crude title compound (1.063 g) was column chromatographed on silica gel, using as eluent (2/1) DCM/hexane (R_f 0.36), to afford the product (yellow solid, 367 mg, 0.42 mmol, yield 41%). **M_p** 125-127 °C. **^{1}H NMR** (400 MHz, $CDCl_3$): δ 7.65 (4H, d, *J* = 8.5, **Ar3**), 7.61 (4H, d, *J* = 8.5, **Ar3**), 7.53 (8H, m, **Ar2**), 7.38 (2H, s, **Ar1**), 2.81 (4H, t, *J* = 7.8, **C1**), 1.71 (4H, p, *J* = 7.5, **C2**), 1.41-1.25 (36H, m, **C3-**

C11), 0.87 (6H, t, *J* = 6.9, **C12**). Data consistent with those previously reported[62]. **^{13}C NMR** (100 MHz, $CDCl_3$, NS 4096): δ 142.58 (C, **Ar1**R), 133.53, 132.58, 132.22, 131.92, 131.64 (5CH, **Ar1**-**Ar2**-**Ar3**), 128.12 (C, **Ar3**CC), 124.38, 122.67, 122.13 (3C, **Ar1**CC**Ar2**CC), 118.58 (C, **CN**), 111.87 (C, **Ar3**CN), 93.75, 93.55, 91.04, 89.66 (4C, Ar1**CC**Ar2**CC**Ar3), 34.27 (CH_2, **C1**), 32.08 (CH_2, **C10**), 30.81 (CH_2, **C2**), 29.84-29.51 ($7CH_2$, **C3-C9**), 22.83 (CH_2, **C11**), 14.25 (CH_3, **C12**). **LRMS** (MALDI-TOF): *m*/*z* 865 ([M^+], 100). **IR** (film): 2918, 2852 (m, CH stretch), 2227 (w, CN stretch). **UV**: λ_{max} ($CHCl_3$) 364 nm (ε 93000). **Anal**. Calcd. For $C_{64}H_{68}N_2$: C: 88.8; H: 7.9; N: 3.2 %. Found: C: 87.8; H: 7.8; N: 3.0 %.

1,4-Didodecyl-2,5-(2-(4-(2-(4-thioacetylphenyl)ethynyl)phenyl)- ethynyl) benzene (**12**). A 25 mL Schlenk flask containing **10** (580 mg, 0.79 mmol), **4** (484 mg, 1.74 mmol, 2.20 eq.), $PdCl_2$ (14 mg, 0.08 mmol, 10 mol%), PPh_3 (41 mg, 0.16 mmol, 20 mol%) and CuI (30 mg, 0.16 mmol, 2 mol%), with stirring, was evacuated under HV and refilled with Ar before adding distilled THF (10 mL) and EDIA (0.82 mL, 613 mg, 4.74 mmol, 6.00 eq.) dropwise. The reaction mixture was stirred at r.t. for 4 h, the disappearance of starting material was monitored by TLC. The solvent was evaporated and the solid was dissolved in DCM and washed with water, the water was extracted three times with DCM and the organic phases were joined, dried over anhydrous $MgSO_4$ and vacuum evaporated. The crude product (975 mg) was column chromatographed on silica gel, using as eluent (1/1) hexane/DCM (R_f 0.31), to afford the pure product (yellowish solid, 549 mg, 0.53 mmol, yield 67%). **M_p** 128-129 °C.

^{1}H NMR (300 MHz, $CDCl_3$): 7.56 (4H, d, *J* = 8.4, **Ar3**), 7.51 (8H, m, **Ar2**), 7.41 (4H, d, *J* = 8.4, **Ar3**), 7.37 (2H, s, **Ar1**), 2.81 (4H, t, *J* = 7.7, **C1**), 2.44 (6H, s, **Me**CO), 1.71 (4H, pent, *J* = 7.2, **C2**), 1.40-1.25 (36H, m, **C3-C11**), 0.87 (6H, t, *J* = 6.6, **C12**); data consistent with those previously reported[62]. **UV**: λ_{max} ($CHCl_3$) 360 nm (ε 125000).

1,4-Didodecyl-2,5-bis(2-(4-(2-(4-bromophenyl)ethynyl)phenyl)ethynyl)-benzene (**13**). A 25 mL Schlenk flask containing **10** (624 mg, 0.94 mmol), 1-bromo-4-iodobenzene (585 mg, 2.07 mmol, 2.20 eq.), $PdCl_2$ (33 mg, 0.19 mmol, 20 mol%), PPh_3 (99 mg, 0.38 mmol, 40 mol%) and CuI (36 mg, 0.19 mmol, 20 mol%), with stirring, was evacuated under HV and refilled with Ar before adding distilled benzene (15 mL). TEA (0.79 mL, 571 mg, 5.64 mmol, 6.00 eq.) was then added dropwise and

the reaction mixture was heated to 70 ºC and stirred in the darkness for 12 h; the disappearance of starting material (R_f 0.10, hexane) was monitored by TLC. The solvent was evaporated and the residue dissolved in DCM, the solution was washed with water and brine and dried over anhydrous $MgSO_4$. Evaporation of the solvent afforded the crude title compound (1.125 g). The pure product (white solid, presence of bright yellow imp.; 191 mg, 0.19 mmol, yield 21%) was obtained by column chromatography on silica gel [first column: eluent (20/1) hexane/DCM (R_f 0.13), then (1/1) hexane/DCM (R_f 0.86); second column (3/1) hexane/DCM (R_f 0.58)]. The purification was found difficult and it is likely that part of the product has been lost. **M_p** 134-137 °C (precipitated from hexane; not reported in literature[57]). **^{1}H NMR** (400 MHz, $CDCl_3$, D1 5 s): δ 7.50-7.38 (16H, m, **Ar2-Ar3**), 7.37 (2H, s, **Ar1**), 2.81 (4H, t, *J* = 7.7, **C1**), 1.71 (4H, pent, *J* = 7.4, **C2**), 1.42-1.25 (36H, m, **C3-C11**), 0.88 (6H, t, *J* = 6.6, **C12**). **^{13}C NMR** (100 MHz, $CDCl_3$, NS 3072): δ 142.53 (C, **Ar1**R), 133.18, 132.55, 131.84, 131.72, 131.58 (5CH, **Ar1-Ar2-Ar3**), 123.72, 122.90 (double intensity), 122.69, 122.19 (5C, **Ar1**CC**Ar2**CC**Ar3**Br), 93.88, 90.69, 90.40, 90.37 (4C, Ar3**CC**Ar2**CC**Ar1), 34.29 (CH_2, **C1**), 32.10 (CH_2, **C10**), 30.82 (CH_2, **C2**), 29.86-29.53 ($7CH_2$, **C3-C9**), 22.85 (CH_2, **C11**), 14.27 (CH_3, **C12**). **LRMS** (MALDI-TOF, DHB): *m*/*z* 973 ([M^+], 100), 895 (22), 401 (18). **IR** (film): 2918, 2852 (m, CH stretch), 2360, 2341 (w, CC stretch, alkyne).

1,4-Didodecyl-2,5-bis(2-(4-(2-(4-(2-(trimethylsilyl)ethynyl)phenyl)ethynyl) phenyl)ethynyl)benzene (**14**). A 25 mL Schlenk flask containing **13** (191 mg, 0.20 mmol), $PdCl_2$ (4 mg, 0.02 mmol, 10 mol%), PPh_3 (11 mg, 0.04 mmol, 20 mol%) and CuI (8 mg, 0.04 mmol, 20 mol%), with stirring, was evacuated under HV and refilled with Ar before adding distilled benzene (10 mL: five time excess than in the usual procedure). TEA (0.16 mL, 122 mg, 1.20 mmol, 6.00 eq.) was then added, followed by TMSA (0.06 mL, 47 mg, 0.48 mmol, 2.40 eq.) dropwise. The reaction mixture was heated to 70 °C and stirred for 17 h; the disappearance of starting material (R_f 0.05, hexane) was monitored by TLC. The solvent was evaporated, the residue was dissolved in DCM and filtered through Celite521; the solution was then washed with water and brine and dried over $MgSO_4$, to afford, after evaporation of the solvent, the crude title compound (250 mg). The pure product (white solid, 61 mg, 0.06 mmol, yield 30%) was obtained by column chromatography on silica gel, with eluent (6/1) hexane/DCM (R_f 0.33). **M_p** 168-171 °C (not reported in ref.[57]). **^{1}H NMR** (400 MHz,

$CDCl_3$, D1 5 s): δ 7.50 (8H, m, **Ar3**), 7.45 (8H, m, **Ar2**), 7.37 (2H, s, **Ar1**), 2.81 (4H, t, *J* = 7.8, **C1**), 1.70 (4H, pent, *J* = 7.5, **C2**), 1.43-1.25 (36H, m, **C3**-**C11**), 0.87 (6H, t, *J* = 6.9, **C12**), 0.26 (18H, s, **TMS**). **^{13}C NMR** (100 MHz, $CDCl_3$, NS 3072): δ 142.54 (C, **Ar1**R), 132.55, 132.09, 131.75, 131.58, 131.56 (5CH, **Ar1**-**Ar2**-**Ar3**), 123.68, 123.32, 123.25, 123.00, 122.70 (5C, **Ar1**CC**Ar2**CC**Ar3**CC), 104.75 (C, TMSC**C**Ar3), 96.62 (C, TMS**C**C), 93.90, 91.18, 91.11, 90.67 (4C, Ar3**CC**Ar2**CC**Ar1), 34.29 (CH_2, **C1**), 32.09 (CH_2, **C10**), 30.83 (CH_2, **C2**), 29.85-29.53 ($7CH_2$, **C3**-**C9**), 22.85 (CH_2, C11; not visible in DEPT), 14.26 (CH_3, **C12**), 0.07 (CH_3, **TMS**). **LRMS** (MALDI-TOF, alpha): *m*/*z* 1008 ($[M+H]^+$, 100), 885 (13), 699 (16). **IR** (film): 2950 (w), 2919 (m), 2851 (w, CH stretch), 2154 (w, CC stretch, alkyne).

1,4-Didodecyl-2,5-bis(2-(4-(2-(4-ethynylphenyl)ethynyl)phenyl)ethynyl) benzene (**15**). In a 50 mL rbf a solution of **14** (58 mg, 0.06 mmol) in THF (10 mL: large excess) was stirred for 15 min, at r.t., in presence of TBAF (0.84 mL of a solution 1 M in THF; 14.00 eq.); the disappearance of starting material (R_f 0.00, (20/1) hexane/DCM) was monitored by TLC. The solvent was evaporated and the residue was dissolved in DCM; the solution was washed with water and brine, dried over anhydrous $MgSO_4$ and evaporated, to afford the crude product (bright yellow solid, 56 mg, 0.06 mmol, yield 93%). No further purification was carried out. The deprotection with K_2CO_3 and methanol/DCM was not viable because of the too low solubility of the starting material in methanol/DCM. **M_p** 115-120 °C. **^{1}H NMR** (400 MHz, $CDCl_3$, D1 5 s): δ 7.51 (8H, m, **Ar3**), 7.48 (8H, m, **Ar2**), 7.37 (2H, s, **Ar1**), 3.18 (2H, s, C**CH**), 2.81 (4H, t, *J* = 7.8, **C1**), 1.70 (4H, pent, *J* = 7.5, **C2**), 1.42-1.23 (36H, m, **C3**-**C11**), 0.87 (6H, t, *J* = 6.8, **C12**). **^{13}C NMR** (100 MHz, $CDCl_3$, NS 3072): δ 142.54 (C, **Ar1**R), 132.56, 132.27, 131.78, 131.64, 131.59 (5CH, **Ar3**-**Ar2**-**Ar1**), 123.75, 123.70, 122.92, 122.70, 122.28 (5C, **Ar1**CC**Ar2**CC**Ar3**CCH), 93.89, 91.25, 90.89, 90.70 (4C, Ar3**CC**Ar2**CC**Ar1), 83.39 (C, Ar3**C**CH), 79.18 (CH, Ar3C**CH**; low intensity in DEPT), 34.29 (CH_2, **C1**), 32.10 (CH_2, **C10**), 30.83 (CH_2, **C2**), 29.86-29.52 ($7CH_2$, **C3-C9**), 22.85 (CH_2, **C11**), 14.26 (CH_3, **C12**). **LRMS** (MALDI-TOF, DHB): *m*/*z* 862 ($[M^+]$, 100). **IR** (film): 3290 (w, CH stretch, alkyne), 2958 (w), 2918, 2853 (m, CH stretch). **UV**: λ_{max} ($CHCl_3$) 361 nm (ε 70600).

1,4-Didodecyl-2,5-bis(2-(4-(2-(4-(2-(p-benzonitril)ethynyl)phenyl)ethynyl) phenyl)ethynyl)benzene (**16**). A small Schlenk tube containing **15** (40 mg, 46 μmol), 4-bromobenzonitrile (20 mg, 0.11 mmol, 2.40 eq.), $PdCl_2$ (1 mg, 5.00 μmol, 10 mol%), PPh_3 (3 mg, 0.01 mmol, 20 mol%) and CuI (2 mg, 0.01 mmol, 20 mol%), with stirring, was evacuated under HV and refilled with Ar before adding benzene (1.0 mL: ~ 20 mL/mmol) and TEA (0.04 mL, 28 mg, 0.28 mmol, 6.00 eq.) dropwise. The reaction mixture was heated to 70 °C and stirred for 22 h. The solvent was evaporated and the residue was dissolved in DCM; the solution was washed with water and brine and dried over $MgSO_4$, to afford, after evaporation of the solvent, the crude product (mostly yellow solid, 91 mg). The pure title compound (R_f 0.36; yellow solid, 18 mg, 17 μmol, yield 37%) was obtained by column chromatography on silica gel using as eluent (2/1) DCM/hexane. **M_p** 168 °C dec. **^{1}H NMR** (400 MHz, $CDCl_3$, D1 5 s): δ 7.63 (8H, m, **Ar4**), 7.54-7.52 (16H, m, **Ar3**-**Ar2**), 7.37 (2H, s, **Ar1**), 2.81 (4H, t, *J* = 7.8, **C1**), 1.71 (4H, pent *J* = 7.4, **C2**), 1.43-1.25 (36H, m, **C3**-**C11**), 0.87 (6H, t, *J* = 6.9, **C12**). **^{13}C NMR** (100 MHz, $CDCl_3$, NS 6144): δ 142.75 (C, **Ar1**R), 132.77, 132.45 (double intensity), 132.12, 132.02, 131.99, 131.81 (7CH, **Ar1**-**Ar2**-**Ar3**-**Ar4**), 128.32 (C, **Ar4**CC), 124.21, 124.04, 123.05, 122.90, 122.53 (5C, CC**Ar3**CC**Ar2**-CC**Ar1**), 118.80 (C, Ar4**C**N), 112.11 (C, **Ar4**CN), 94.09, 93.71, 91.90, 91.12, 90.97, 89.93 (6C, Ar4**CC**Ar3**CC**Ar2**CC**Ar1), 34.49 (CH_2, **C1**), 32.29 (CH_2, **C10**), 31.03 (CH_2, **C2**), 30.06-29.71 (7CH_2, **C3**-**C9**), 23.05 (CH_2, **C11**), 14.46 (CH_3, **C12**).

LRMS (MALDI-TOF): *m/z* 1065 ([M^+], 100 %). **IR** (film): 2921, 2848 (m, CH stretch), 2357, 2337 (m, CC stretch, alkyne). **UV**: λ_{max} ($CHCl_3$) 373 nm (ε 61000).

1,4-Didodecyl-2,5-bis(2-(4-(2-(4-(2-(4-thioacetylphenyl)ethynyl)phenyl) ethynyl)phenyl)ethynyl)benzene (**17**). A small Schlenk tube containing **15** (47 mg, 54 μmol), **4** (33 mg, 0.12 mmol, 2.20 eq.), $PdCl_2$ (1 mg, 5 μmol, 10 mol%), PPh_3 (3 mg, 0.01 mmol, 20 mol%) and CuI (2 mg, 0.01 mmol, 20 mol%), with stirring, was evacuated under HV and refilled with Ar before adding THF (2.0 mL: approx. 40 mL/mmol). EDIA (0.06 mL, 42 mg, 0.32 mmol, 6.00 eq.) was then added dropwise. The reaction mixture was stirred at r.t. for 14 h; the disappearance of starting material (R_f 0.02, (20/1) hexane/DCM) was monitored by TLC. The solvent was evaporated and the residue was dissolved in DCM; the solution was washed with water and brine and dried over $MgSO_4$, to afford, after evaporation of the solvent, the crude product (86 mg). The solid (orangish, 41 mg) obtained by column chromatography on silica

gel, with eluent (3/1) DCM/hexane, was found to be a mixture of product and unreacted **4** (both R_f 0.56): further chromatographic purification was not attempted because of evidence (by 2D- TLC) of decomposition of the product on silica. The pure product (26 mg, 22 μmol, yield 41%) was obtained as orangish solid by precipitation from hexane/DCM. **M_p** 146-149 °C (hexane/DCM). **^{1}H NMR** (400 MHz, $CDCl_3$, D1 5 s): δ 7.56 (4H, d, *J* = 8.6, **Ar4**), 7.52-7.51 (16H, m, **Ar2**-**Ar3**), 7.41 (4H, d, *J* = 8.3, **Ar4**), 7.37 (2H, s, **Ar1**), 2.81 (4H, t, *J* = 7.8, **C1**), 2.44 (6H, s, **Me**CO), 1.71 (4H, pent, *J* = 7.4, **C2**), 1.43-1.25 (36H, m, **C3**-**C11**), 0.87 (6H, t, *J* = 6.9, **C12**). **^{13}C NMR** (100 MHz, $CDCl_3$, NS 4096): δ 193.47 (C, **CO**Me), 142.54 (C, **Ar1**R), 134.39, 132.56, 132.34, 131.81, 131.77, 131.74, 131.59 (7CH, **Ar1**-**Ar2**-**Ar3**-**Ar4**), 128.54 (C, **Ar4**S), 124.42, 123.71, 123.34, 123.11, 122.99, 122.70 (6C, **Ar4**CC**Ar3**CC**Ar2**CC-**Ar1**), 93.91, 91.32, 91.13, 90.86, 90.76, 90.70 (6C, Ar4**CC**Ar3**CC**Ar2**CC**Ar1), 34.30 (CH_2, **C1**), 32.09 (CH_2, **C10**), 30.83 (CH_2, **C2**), 30.44 (CH_3, **Me**CO), 29.86-29.53 (7CH_2, **C3**-**C9**), 22.85 (CH_2, **C11**), 14.26 (CH_3, **C12**). **LRMS** (MALDI-TOF, DHB): *m*/*z* 1164 ([M^+], 54), 1140 (50), 1121 ([M-Ac]$^+$, 65), 1094 (38), 1080 (37), 381 (70), 365 (87), 340 (65), 320 (84), 279 (95), 277 (47), 270 (46), 260 (44), 155 (46), 137 (100), 39 (61). **IR** (film): 2918, 2850 (m, CH stretch), 2357 (w, CC stretch, alkyne), 1699 (m, CO stretch). **UV**: λ_{max} ($CHCl_3$) 368 nm (ε 137000).

4-(2-(Trimethylsilyl)ethynyl)benzonitrile (**18**). A 100 mL Schlenk flask containing 4-bromobenzonitrile (1.456 g, 8.00 mmol), $PdCl_2$ (71 mg, 0.40 mmol, 5 mol%), PPh_3 (210 mg, 0.80 mmol, 10 mol%) and CuI (76 mg, 0.40 mmol, 5 mol%) was evacuated and refilled with argon before adding distilled THF (60 mL), TEA (3.34 mL, 2.428 g, 24.00 mmol, 3.00 eq.) and TMSA (1.70 mL, 1.178 g, 12.00 mmol, 1.50 eq.) dropwise. The reaction mixture was stirred at r.t. for 3 h and the disappearance of starting material monitored by TLC. The solvent was evaporated and the solid was dissolved in DCM; filtration through silica and evaporation of the solvent afforded the crude title compound (1.820 g) as black oil. The pure product (1.410 g, 7.07 mmol, yield 88%) was obtained by column chromatography on silica gel using (4/1) hexane/DCM as eluent (R_f 0.15). **M_p** not available. **^{1}H NMR** (300 MHz, $CDCl_3$): 7.58 (2H, d, *J* = 8.7, **Ar**), 7.51 (2H, d, *J* = 8.7, **Ar**), 0.25 (9H, s, **TMS**); consistent with those previously reported[63].

4-Ethynylbenzonitrile (**19**). In a 500 mL rbf a solution of **18** (1.49 g, 7.47 mmol) in MeOH (200 mL) was stirred for 3 h in presence of K_2CO_3 (10.32 g, 74.67 mmol, 10.00 eq.), the disappearance of starting material was monitored by TLC. Water was poured in the flask until all the carbonate was dissolved, and the solution was extracted with DCM three times; the combined organic phases were washed with brine, and dried over anhydrous $MgSO_4$. Evaporation of the solvent afforded the crude product (1.02 g) that was column chromatographed on silica gel, using DCM as eluent (R_f 0.57), to obtain the pure title compound (0.74 g, 5.82 mmol, yield 78%). **M_p** not available. **^{1}H NMR** (300 MHz, $CDCl_3$): δ 7.62 (2H, d, *J* = 8.7, **Ar**), 7.56 (2H, d, *J* = 8.7, **Ar**), 3.30 (1H, s, C**CH**). Data consistent with those previously reported[63].

1,4-Didodecyl-2,5-bis-(2-(4-cyanobenzil)ethynyl)benzene (**20**). A 25 mL Schlenk flask containing **6** (133 mg, 0.20 mmol), **19** (51 mg, 0.40 mmol, 2.00 eq.), $PdCl_2$ (7 mg, 40 μmol, 20 mol%), PPh_3 (21 mg, 80 μmol, 40 mol%) and CuI (8 mg, 40 μmol, 20 mol%), with stirring, was evacuated under HV and refilled with Ar before adding distilled benzene (5.0 mL) and TEA (0.17 mL, 121 mg, 1.20 mmol, 6.00 eq.). The reaction mixture was heated to 80 ºC and stirred in the darkness for 4.5 h, the disappearance of starting material was monitored by TLC. The solvent was evaporated and the solid was dissolved in DCM and washed with water, the water was extracted three times with DCM, and the combined organic phases were washed again with water before being dried over anhydrous $MgSO_4$ and evaporated. The crude product (180 mg) was column chromatographed on silica gel, using as eluent (1/1) hexane/DCM, to afford the pure title compound (58 mg, 0.09 mmol, yield 43%), of which a small fraction (10 mg) was recrystallized from EtOH as tiny white needles. **M_p** 119-121 °C. **^{1}H NMR** (300 MHz, $CDCl_3$): 7.65 (4H, d, *J* = 8.4, **Ar2**), 7.59 (4H, d, *J* = 8.4, **Ar2**), 7.39 (2H, s, **Ar1**), 2.80 (4H, t, *J* = 7.7, **C1**), 1.69 (4H, pent, *J* = 7.5, **C2**), 1.35-1.24 (36H, m, **C3-C11**), 0.88 (6H, t, *J* = 6.8, **C12**); data consistent with those previously reported[62]. **UV**: λ_{max} ($CHCl_3$) 346 nm (ε 66000).

Trimethyl(2-(4-(methylthio)phenyl)ethynyl)silane (**21**). A 250 mL Schlenk flask containing 4-bromothioanisole (2.031 g, 10.00 mmol), $PdCl_2$ (89 mg, 0.50 mmol, 5 mol%), PPh_3 (262 mg, 1.00 mmol, 10 mol%) and CuI (190 mg, 1.00 mmol, 10 mol%) was evacuated and refilled with argon before adding distilled MeCN (100 mL). Distilled iPr_2NH (4.22 mL, 3.036 g, 30.00 mmol, 3.00 eq.) was then added,

followed by TMSA (1.70 mL, 1.179 g, 12.00 mmol, 1.20 eq.) dropwise. The reaction mixture was heated to 70 °C and stirred for 25 h; the conversion was estimated to be almost quantitative by GC (SD_FASTD, product RT 5.2 minutes). The solvent was evaporated, the residue was dissolved in DCM (250 mL), washed with water and brine, dried over anhydrous $MgSO_4$. Evaporation of the solvent afforded the crude product (2.616 g); this was adsorbed on a small amount of silica gel and column chromatographed using (20/1) hexane/DCM as eluent, followed by (3/1) hexane/DCM. A fraction of title compound containing starting material (higher R_f) was columned again using hexane as eluent, and then changing to (5/1) hexane/DCM gradually. The pure product (orange oil, R_f 0.14 in (20/1) hexane/DCM; 1.689 g, 7.66 mmol, yield 77 %) was found to be unstable on silica when exposed to light (2D TLC). **^{1}H NMR** (300 MHz, $CDCl_3$): δ 7.37 (2H, d, *J* = 8.6, **Ar**), 7.15 (2H, d, *J* = 8.6, **Ar**), 2.47 (3H, s, S**Me**), 0.24 (9H, s, **TMS**). **^{13}C NMR** (75 MHz, $CDCl_3$): δ 139.75 (C, **Ar**S), 132.38, 125.88 (2CH, **Ar**), 119.61 (C, **Ar**CC), 105.04 (C, Ar**C**C), 94.32 (C, C**C**Si), 15.52 (CH_3, **Me**S), 0.17 (CH_3, **TMS**). **LRMS** (EI): *m*/*z* 220 ([M^+], 56%), 205 ([M-CH_3]$^-$, 58), 190 ([205-CH_3]$^-$, 58), 103 ([$PhCH_2CH_2$]$^+$, 58). **IR** (film): 2958, 2921, 2897 (w, CH stretch), 2155 (m, CC stretch, alkyne). Data not reported in literature[64].

In the following two-ring compounds the sulfur-terminated aromatic ring has been named Ar1 and the other ring Ar2; however in the symmetrical MWs Ar1 is still the central ring.

2-(4-(2-(4-Bromophenyl)ethynyl)phenyl)methylthioether (**22**). A 50 mL Schlenk flask containing impure **21** (541 mg; at least 2.45 mmol of the title compound), 1-bromo-4-iodobenzene (764 mg, 2.70 mmol, 1.10 eq.), $PdCl_2$ (43 mg, 0.24 mmol, 10 mol%), PPh_3 (126 mg, 0.48 mmol, 20 mol%) and CuI (46 mg, 0.24 mmol, 10 mol%), with stirring, was evacuated under HV and refilled with Ar before adding distilled benzene (25 mL). DBU (4.40 mL, 4.48 g, 29.4 mmol, 12.00 eq.) was then added dropwise, followed by distilled water (~ 0.04 mL, 35 mg, 1.96 mmol, 0.80 eq.). The reaction mixture was heated to 70 ºC and stirred for 1 d, the disappearance of starting material was monitored by TLC (R_f 0.28, (6/1) hexane/DCM). The solvent was evaporated and the solid was dissolved in DCM, the solution was washed with water and brine and dried over anhydrous $MgSO_4$. Evaporation of the solvent afforded

the crude product (2.137 g) that was column chromatographed on silica gel, using as eluent (3/1) hexane/DCM (R_f 0.31), to obtain the pure product (yellowish flakes (558 mg, 1.84 mmol, yield 75%). **M_p** 148-153 °C. **^{1}H NMR** (300 MHz, $CDCl_3$): δ 7.48 (2H, d, *J* = 8.8, **Ar2**), 7.43 (2H, d, *J* = 8.8, **Ar2**), 7.37 (2H, d, *J* = 8.8, **Ar1**), 7.21 (2H, d, *J* = 8.8, **Ar1**), 2.50 (3H, s, S**Me**). **^{13}C NMR** (75 MHz, $CDCl_3$): δ 139.89 (C, **Ar1**S), 133.07, 132.00, 131.77, 131.75 (4CH, **Ar1**-**Ar2**), 122.53, 122.47 (2C, Br**Ar2**CC), 119.33 (C, **Ar1**CC), 90.51, 88.57 (2C, Ar2**CC**Ar1), 15.51 (CH_3, **Me**S). **LRMS** (EI): *m*/*z* 304-302 ([M^+], 100), 289-287 ([M-CH_3]$^-$, 44), 208 ([288-Br]$^+$, 35), 176 ([208-S]$^+$, 37), 163 ([208-CH]$^+$, 66), 152 (36). **IR** (film): 2917 (w, CH stretch), 2210 (w, CC stretch, alkyne). Data not reported in literature[64].

Trimethyl(2-(4-(2-(4-(methylthio)phenyl)ethynyl)phenyl)ethynyl)silane (**23**).

A 100 mL Schlenk flask containing **22** (547 mg, 1.80 mmol), $PdCl_2$ (16 mg, 0.09 mmol, 5 mol%), PPh_3 (47 mg, 0.18 mmol, 10 mol%) and CuI (17 mg, 0.09 mmol, 5 mol%), with stirring, was evacuated under HV and refilled with Ar before adding distilled benzene (18 mL). TEA (0.75 mL, 546 mg, 5.40 mmol, 3.00 eq.) was then added, followed by TMSA (0.30 mL, 212 mg, 2.16 mmol, 1.20 eq.) dropwise. The reaction mixture was heated to 70 °C and stirred for 21 h; the disappearance of starting material (R_f 0.31, (3/1) hexane/DCM) was monitored by TLC. The solvent was evaporated and the residual dissolved in DCM; the solution was filtered through Celite521, washed with water and brine and dried over $MgSO_4$, to afford, after evaporation of the solvent, the crude title compound (640 mg). The pure product (yellowish solid, 418 mg, 1.30 mmol, yield 72%) was obtained by column chromatography on silica gel, with eluent (10/1) hexane/DCM (R_f 0.16). **M_p** 137-140 °C. **^{1}H NMR** (400 MHz, $CDCl_3$): δ 7.44 (4H, m, **Ar2**), 7.42 (2H, d, *J* = 8.5, **Ar1**), 7.21 (2H, d, *J* = 8.5, **Ar1**), 2.50 (3H, s, S**Me**), 0.26 (9H, s, **TMS**). **^{13}C NMR** (100 MHz, $CDCl_3$, NS 1024): δ 139.83 (C, **Ar1**S), 132.00, 131.43, 126.05, 126.01 (4CH, **Ar2**-**Ar1**), 123.55, 122.98 (2C, CC**Ar2**CC), 119.41 (C, CC**Ar1**), 104.82 (C, TMSC**C**Ar2), 96.38 (C, TMS**C**CAr2), 91.31, 89.30 (2C, Ar2**CC**Ar1), 15.49 (CH_3, **Me**S), 0.06 (CH_3, **Me_3**Si). **LRMS** (EI): *m*/*z* 320 ([M^+], 90%), 305 ([M-CH_3]$^-$, 90), 290 ([305-CH_3]$^-$, 52), 153 ([SiCCPhCCH]$^-$, 100). **IR** (film): 2958, 2897 (w, CH stretch), 2214, 2154 (w, CC stretch, alkyne).

2-(4-(2-(4-(Methylthio)phenyl)ethynyl)phenyl)ethynylene (**24**). In a 50 mL rbf a solution of **23** (96 mg, 0.30 mmol) in 15 mL of (2/1) MeOH/DCM was stirred for 1.5 h, at r.t., in presence of K_2CO_3 (415 mg, 3.00 mmol, 10.00 eq.). The disappearance of starting material (R_f 0.16, (10/1) hexane/DCM) was monitored by TLC. The reaction mixture was diluted with water and extracted twice with DCM; the solution was dried over $MgSO_4$ and evaporated to afford the pure product (74 mg, 0.30 mmol, yield 99%; R_f 0.12 in (10/1) hexane/DCM). **M_p** 151-152 °C. **^{1}H NMR** (300 MHz, $CDCl_3$): δ 7.46 (4H, m, **Ar2**), 7.43 (2H, d, *J* = 8.6, **Ar1**), 7.21 (2H, d, *J* = 8.6, **Ar1**), 3.17 (1H, s, C**CH**), 2.50 (3H, s, S**Me**). **^{13}C NMR** (75 MHz, $CDCl_3$): δ 139.92 (C, **Ar1**S), 132.21, 132.04, 131.53, 126.03 (4CH, **Ar2**-**Ar1**), 123.99, 121.93 (2C, HCC**Ar2**CC), 119.33 (C, CC**Ar1**), 91.39, 89.10 (2C, Ar2**CC**Ar1), 83.45 (C, HC**C**Ar2), 79.00 (CH, **HC**C), 15.50 (CH_3, **Me**S). **LRMS** (EI): *m*/*z* 248 ([M^+], 100%), 233 ([M-CH_3]$^-$, 43), 124 ([CCPhCC]$^-$, 26). **IR** (film): 3270 (w, CH stretch, alkyne), 2962 (w, CH stretch), 2212 (w, CC stretch, alkyne).

1,4-Didodecyl-2,5-bis(2-(4-(2-(4-methylthio)phenyl)ethynyl)phenyl)-ethynyl-benzene (**25**). A small Schlenk tube containing **6** (173 mg, 0.26 mmol), **24** (144 mg, 0.57 mmol, 2.20 eq.), $PdCl_2$ (5 mg, 26 μmol, 10 mol%), PPh_3 (14 mg, 0.05 mmol, 20 mol%) and CuI (10 mg, 0.05 mmol, 20 mol%) was evacuated and refilled with Ar before adding distilled benzene (5.0 mL) and TEA (0.20 mL, 158 mg, 1.56 mmol, 6.00 eq.). The reaction mixture was heated to 70 °C and stirred in the darkness for 16 h; the disappearance of starting materials (**R_f**s 0.88 and 0.59 respec., (1/1) hexane/DCM) as monitored by TLC was not complete after 13 h: the reaction was not monitored again and assumed stationary because of the presence of at least seven byproducts absorbing light at 365 nm. The solvent was vacuum evaporated, the residue dissolved in DCM, washed with water and brine and dried over $MgSO_4$, to afford, after evaporation of the solvent, the crude title compound (282 mg). The pure product (110 mg, 0.12 mmol, yield 47%) was obtained by column chromatography on silica gel, using as eluent (2/1) hexane/DCM (R_f 0.50). **M_p** 133-135 °C. **^{1}H NMR** (400 MHz, $CDCl_3$, D1 5 s): δ 7.50 (8H, m, **Ar2**), 7.45 (4H, d, *J* = 8.8, **Ar3**), 7.37 (2H, s, **Ar1**), 7.22 (4H, d, *J* = 8.8, **Ar3**), 2.81 (4H, t, *J* = 7.8, **C1**), 2.51 (6H, s, **Me**S), 1.70 (4H, pent, *J* = 7.4, **C2**), 1.45-1.25 (36H, m, **C3**-**C11**), 0.87 (6H, t, *J* = 6.9, **C12**). **^{13}C NMR** (100 MHz, $CDCl_3$, NS 3072): δ 142.50 (C, **Ar1**R), 139.84 (C, **Ar3**S), 132.53 (CH, **Ar3**), 132.05, 131.65, 131.54 (3CH, **Ar1**-**Ar2**), 126.05 (CH, **Ar3**), 123.35,

123.34, 122.70, 119.48 (4C, **Ar3**CC**Ar2**CC**Ar1**), 93.96, 91.34, 90.52, 89.42 (4C, Ar3**CC**Ar2**CC**Ar1), 34.29 (CH_2, **C1**), 32.09 (CH_2, **C10**), 30.82 (CH_2, **C2**), 29.86, 29.85, 29.82, 29.78, 29.72, 29.70, 29.52 ($7CH_2$, **C3-C9**), 22.85 (CH_2, **C11**), 15.53 (CH_3, S**Me**), 14.26 (CH_3, **C12**). **LRMS** (MALDI-TOF, DHB): *m/z* 907 ([M^+], 100%), 339 ([M-2SMe-$C_{10}H_{14}$]$^+$, 31). **IR** (film): 2951(w), 2918 (s), 2851 (m, CH stretch), 2210 (w, CC stretch, alkyne). **UV**: λ_{max} ($CHCl_3$) 362 nm (ε 88600).
Anal. Calcd. For $C_{64}H_{74}S_2$: C: 84.7; H: 8.2 %. Found: C: 83.7; H: 7.3 %.

1,4-bis(Octyloxy)benzene (**26**). Repeating the procedure described by Loupy[116], in a sealed Schlenk tube hydroquinone (0.55 g, 4.99 mmol), TBAB (63 mg, 9% w/w KOH) and KOH powder (0.7 g, 12.47 mmol, 2.50 eq.) were stirred for 10 minutes before adding octylbromide (2.16 mL, 2.42 g, 12.53 mmol, 2.51 eq.) and heating to 80 ºC for 17 h. The reaction mixture was then dissolved in Et_2O and washed with water, the organic phase was dried over anhydrous $MgSO_4$ and the solvent evaporated to afford the crude title compound (1.87 g). The pure product (1.03 g, 3.08 mmol) was obtained by column chromatography on silica gel, using as eluent (5/1) hexane/DCM (R_f 0.15); this was then recrystallized from EtOH as white thin flakes (0.77 mg, 2.30 mmol, yield 46%). **M_p** 54-57 °C (lit.[117] 55.0-58.5 °C, from EtOH).
^{1}H NMR (300 MHz, $CDCl_3$): δ 6.82 (4H, s, **Ar**), 3.90 (4H, t, *J* = 6.6, O**C1**), 1.75 (4H, pent, *J* = 7.0, **C2**), 1.48-1.29 (20H, m, **C3**-**C7**), 0.89 (6H, t, *J* = 6.8, **C8**).

1,4-Diiodo-2,5-bis(octyloxy)benzene (**27**). Repeating the procedure described by Shirai[65], in a 250 mL rbf a solution of **26** (2.04 g, 6.10 mmol), $Hg(OAc)_2$ (4.84 g, 15.19 mmol, 2.49 eq.) and I_2 (3.85 g, 15.17 mmol, 2.49 eq.) in DCM (60 mL) was stirred at r.t. for 19 h. The reaction mixture was filtered through Celite 521 with DCM and the organic phase was washed with $Na_2S_2O_3$ (aqueous, 10% w/v), to the complete disappearance of the pink colour, then with $NaHCO_3$ (saturated), water and brine, and dried over anhydrous $MgSO_4$. Evaporation of the solvent and recrystallization from EtOH afforded the pure product (3.15 g, 5.37 mmol, yield 88%). **M_p** 50-51 °C (lit.[65] 52-53 °C). **^{1}H NMR** (300 MHz, $CDCl_3$): δ 7.17 (2H, s, **Ar**), 3.92 (4H, t, *J* = 6.5, O**C1**), 1.80 (4H, pent, *J* = 6.6, **C2**), 1.50 (4H, pent, *J* = 7.3, **C3**), 1.33-1.30 (16H, m, **C4**-**C7**), 0.89 (6H, t, *J* = 6.6, **C8**). **^{13}C NMR** (75 MHz, $CDCl_3$): δ 153.05 (C, **Ar**O), 123.00 (CH, **Ar**), 86.48 (C, **Ar**I), 70.55 (CH_2, O**C1**), 31.95 (CH_2, **C2**), 29.40-29.31 ($3CH_2$, **C2**, **C4**, **C5**), 26.19 (CH_2, **C3**), 22.82 (CH_2, **C7**),

14.26 (CH_3, **C8**). **LRMS**: tried EI and ES techniques but no good ions. **IR** (film): 2940, 2916, 2849 (m, CH stretch).

1,4-bis(2-(4-(2-(4-Methylthio)phenyl)ethynyl)phenyl)ethynyl-2,5-bis(octyl-oxy)-benzene (**28**). A 25 mL Schlenk flask containing **27** (152 mg, 0.26 mmol), **24** (144 mg, 0.58 mmol, 2.23 eq.), $PdCl_2$ (5 mg, 26 μmol, 10 mol%), PPh_3 (14 mg, 0.05 mmol, 20 mol%) and CuI (10 mg, 0.05 mmol, 20 mol%) was evacuated and refilled with Ar before adding distilled benzene (5.0 mL). TEA (0.20 mL, 158 mg, 1.56 mmol, 6.00 eq.) was then added dropwise; the reaction mixture was heated to 70 °C and stirred, in the darkness, for 13 h. The disappearance of starting materials (**R_f**s 0.65 and 0.42 respec., (2/1) hexane/DCM) was monitored by TLC. The solvent was evaporated, the residue was dissolved in DCM, washed with water and brine and dried over anhydrous $MgSO_4$. After evaporation of the solvent, the crude title compound (261 mg) was column chromatographed on silica gel, using as eluent (5/4) DCM/hexane (R_f 0.46), yielding a mixture of product and impurities with similar R_fs (113 mg); further purification using as eluent (3/2) hexane/DCM (R_f 0.14) afforded the pure product (yellow solid, 86 mg, 104 μmol, yield 40%). **M_p** 160-163 °C. **^{1}H NMR** (400 MHz, $CDCl_3$, D1 5 s): δ 7.50 (4H, m, **Ar2**), 7.49 (4H, m, **Ar2**), 7.44 (4H, d, *J* = 8.6, **Ar3**), 7.22 (4H, d, *J* = 8.6, **Ar3**), 7.01 (2H, s, **Ar1**), 4.04 (4H, t, *J* = 6.5, O**C1**), 2.51 (6H, s, **Me**S), 1.86 (4H, pent, *J* = 7.0, **C2**), 1.55 (4H, pent, *J* = 7.3, **C3**), 1.42-1.29 (16H, m, **C4**-**C7**), 0.88 (6H, t, *J* = 6.9, **C8**). **^{13}C NMR** (100 MHz, $CDCl_3$, NS 2048): δ 153.89 (C, **Ar1**OR), 139.83 (C, **Ar3**S), 132.05, 131.65, 131.59, 126.08 (4CH, **Ar3**-**Ar2**), 123.37, 123.32 (2C, CC**Ar2**CC), 119.50 (C, CC**Ar3**), 117.12 (CH, **Ar1**), 114.20 (C, **Ar1**CC), 94.89, 91.33, 89.46, 88.09 (4C, Ar3**CC**Ar2**CC**Ar1), 69.86 (CH_2, O**C1**), 31.98 (CH_2, **C6**), 29.55, 29.53, 29.47, 26.26 ($4CH_2$, **C2-C5**), 22.83 (CH_2, **C7**), 15.54 (CH_3, S**Me**), 14.24 (CH_3, **C8**). **LRMS** (MALDI-TOF, alpha matrix): *m*/*z* 827 ([M^+], 100), 335 ([M-2SMe-$C_{10}H_{18}$]$^+$, 53). **IR** (film): 2919, 2851 (m, CH stretch), 2210 (w, CC stretch, alkyne). **UV**: λ_{max1} ($CHCl_3$) 388 nm (ε 130400); λ_{max2} ($CHCl_3$) 339 nm (ε 108600). **Anal**. Calcd. For $C_{56}H_{58}O_2S_2$: C: 81.3; H: 7.1 %. Found: C: 79.9; H: 6.3 %.

Methyl(4-(2-phenylethynyl)phenyl)sulfane (**29**). A 250 mL Schlenk flask containing 4-bromothioanisole (2.03 g, 10.0 mmol), $PdCl_2$ (89 mg, 0.5 mmol, 5 mol%), PPh_3 (262 mg, 1.0 mmol, 10 mol%) and CuI (95 mg, 0.5 mmol, 5 mol%),

with stirring, was evacuated under HV and refilled with Ar before adding distilled benzene (80 mL). TEA (4.18 mL, 3.04 g, 30.0 mmol, 3.00 eq.) was then added, followed by phenylacetylene (1.21 mL, 1.12 g, 11.0 mmol, 1.10 eq.) dropwise. The reaction mixture was heated to 70 °C, stirred for 23 h and then stopped before the disappearance of starting material (4-bromothioanisole R_f 0.32, (6/1) hexane/DCM). The solvent was evaporated, the residue was dissolved in DCM and filtered through Celite521; the solution was then washed with water and brine and dried over $MgSO_4$, to afford, after evaporation of the solvent, a mixture of crude title compound and unreacted starting material (3.118 g). The pure product (white solid, 947 mg, 4.22 mmol, yield 42%) was obtained by column chromatography on silica gel using as eluent (6/1) hexane/DCM (R_f 0.17). **M_p** 88-90 °C (lit.[64] 83-84 °C). **^{1}H NMR** (300 MHz, $CDCl_3$): 7.55-7.51 (2H, m, **Ar**), 7.45 (2H, d, *J* = 8.6, **Ar**), 7.37-7.33 (3H, m, **Ar**), 7.22 (2H, d, *J* = 8.6, **Ar**), 2.50 (3H, s, S**Me**); consistent with those previously reported[64]. **^{13}C NMR** (75 MHz, $CDCl_3$): 139.66 (1C, **Ar**S), 132.22 (2CH, **Ar**), 131.88 (2CH, **Ar**), 128.64 (3CH, **Ar**), 126.30 (2CH, **Ar**), 123.68, 120.00 (2C, **Ar**CC**Ar**), 89.82, 89.54 (2C, **CC**), 15.76 ($1CH_3$, S**Me**).

(2-(4-Bromophenylthio)ethyl)trimethylsilane (**30**). A Schlenk tube containing 4-bromothiophenol (756 mg, 4.00 mmol) was evacuated and refilled with argon before adding vinyltrimethylsilane (0.67 mL, 461 mg, 4.60 mmol, 1.15 eq.) and tertbutylperoxide (0.11 mL, 88 mg, 0.60 mmol, 0.15 eq.); the mixture was stirred at 100 °C for 3 hours and the disappearance of starting material monitored by GC. Hexane was poured in the flask and the solution was extracted once with NaOH (5% aq.); after drying over $MgSO_4$ and evaporation of the solvent a mixture of crude title compound and disulfide byproduct was obtained (yellow oil, 814 mg). This was column chromatographed on silica gel using hexane as eluent; once the disulfide (R_f 0.34; white solid) had been separated the pure product (clear oil, 534 mg, 1.85 mmol, yield 46%; R_f 0.26 in hexane) was recovered eluting with (2/1) hexane/ethylacetate. **^{1}H NMR** (300 MHz, $CDCl_3$): 7.39 (2H, d, *J* = 8.8, **Ar**), 7.16 (2H, d, *J* = 8.8, **Ar**), 2.96-2.90 (2H, m, S**CH_2**), 0.94-0.88 (2H, m, **CH_2**Si), 0.04 (9H, s, **TM**S); consistent with those previously reported[67]. **^{13}C NMR** (75 MHz, $CDCl_3$): 136.84 (1C, **Ar**S), 132.19 (2CH, **1**), 130.84 (2CH, **2**), 119.78 (1C, **Ar**Br), 30.09 ($1CH_2$, S**CH_2**), 17.16 ($1CH_2$, **CH_2**Si), -1.42 ($3CH_3$, **TM**S).

(2-(Trimethylsilyl)ethyl)(4-(2-(trimethylsilyl)ethynyl)phenyl)sulfane (**31**). A 50 mL Schlenk flask containing **30** (534 mg, 1.84 mmol), $PdCl_2$ (16 mg, 0.09 mmol, 5 mol%), PPh_3 (48 mg, 0.18 mmol, 10 mol%) and CuI (35 mg, 0.18 mmol, 10 mol%), with stirring, was evacuated under HV and refilled with Ar before adding distilled benzene (20 mL). TEA (0.77 mL, 559 mg, 5.52 mmol, 3.00 eq.) was then added, followed by TMSA (0.31 mL, 217 mg, 2.21 mmol, 1.20 eq.) dropwise. The reaction mixture was heated to 70 °C and stirred for 22 h; it was stopped before the disappearance of starting material (R_f 0.25, hexane) because the yield of product was not increasing and a byproduct was forming (GC). The solvent was evaporated, the residue was dissolved in DCM and filtered through Celite 521; the solution was then washed with water and brine and dried over $MgSO_4$, to afford, after evaporation of the solvent, the crude title compound (628 mg). The pure product (164 mg, 0.53 mmol, yield 29%) was obtained by column chromatography on silica gel using as eluent first hexane and then (20/1) hexane/DCM (R_f 0.12 in hexane). **M_p** 44-47 °C (not reported in ref.[67]). **^{1}H NMR** (300 MHz, $CDCl_3$). 7.37 (2H, d, *J* = 8.7, **Ar**), 7.19 (2H, d, *J* = 8.7, **Ar**), 2.99-2.93 (2H, m, S**CH_2**), 0.96-0.90 (2H, m, **CH_2**Si), 0.25 (9H, s, **TMS**), 0.05 (9H, s, alkyl**TM**S); consistent with those previously reported[67]. **^{13}C NMR** (75 MHz, $CDCl_3$): 138.90 (1C, **Ar**S), 132.54 (2CH, **1**), 128.10 (2CH, **2**), 120.30 (1C, **Ar**CC), 105.25 (1C, Ar**C**C), 94.63 (1C, C**C**Si), 29.27 ($1CH_2$, S**CH_2**), 17.00 ($1CH_2$, **CH_2**Si), 0.33 ($3CH_3$, CC**TMS**), -1.43 ($3CH_3$, alkyl**TMS**).

(2-(4-Ethynylphenylthio)ethyl)trimethylsilane (**32**). In a 250 mL rbf a solution of **31** (565 mg, 1.84 mmol) in (5/1) MeOH/DCM (84 mL) was stirred in presence of K_2CO_3 (2.54 g, 18.4 mmol, 10.0 eq.) for 3 h at r.t. Water was poured in the flask to dissolve the carbonate, then the mixture was extracted with DCM and dried over $MgSO_4$. Evaporation of the solvent afforded the title compound (yellow oil, 380 mg, 1.62 mmol, yield 88%; R_f 0.10 in (10/1) hexane/DCM). **^{1}H NMR** (300 MHz): 7.39 (2H, d, *J* = 8.6, **Ar**), 7.21 (2H, d, *J* = 8.6, **Ar**), 3.07 (1H, s, C**CH**), 3.00-2.94 (2H, m, S**CH_2**), 0.97-0.91 (2H, m, **CH_2**Si), 0.05 (9H, s, **TMS**); consistent with those previously reported[67]. **^{13}C NMR** (75 MHz, $CDCl_3$): 139.42 (1C, **Ar**S), 132.73 (2CH, **Ar**), 128.07 (2CH, **Ar**), 119.20 (1C, **Ar**CC), 83.80 (1C, Ar**C**C), 77.62 (1CH, C**CH**), 29.23 ($1CH_2$, S**CH_2**), 17.00 ($1CH_2$, **CH_2**Si), -1.43 ($3CH_3$, **TMS**).

1-(2-(Trimethylsilyl)ethylthio)-4-(2-(4-(2-(4-(2-(trimethylsilyl)ethylthio) phenyl)ethynyl)-3-nitrophenyl)ethynyl)benzene (**33**). A 25 mL Schlenk flask containing 1,4-dibromonitrobenzene (228 mg, 0.81 mmol), **32** (418 mg, 1.78 mmol, 2.20 eq.), $PdCl_2$ (7 mg, 0.04 mmol, 5 mol%), PPh_3 (21 mg, 0.08 mmol, 10 mol%) and CuI (15 mg, 0.08 mmol, 10 mol%), with stirring, was evacuated under HV and refilled with Ar before adding distilled benzene (10 mL). TEA (0.68 mL, 492 mg, 4.86 mmol, 6.00 eq.) was then added dropwise, and the reaction mixture was stirred at 70 °C for 5 h; the disappearance of starting materials was monitored by TLC. The solvent was evaporated, the residue was dissolved in DCM and the solution was washed with water and brine and dried over $MgSO_4$; evaporation of the solvent afforded the crude product (637 mg), dark oil containing bright yellow solid. This was column chromatographed on silica gel using as eluent (4/1) hexane/DCM, yielding the pure title compound (orangish solid, 194 mg, 0.33 mmol, yield 41%; R_f 0.08), the homocoupling dimer **34** (yellow solid, 81 mg, 0.17 mmol, yield 21%; R_f 0.33) and the monocoupling byproduct **35** (dark-red solid, 127 mg, 0.29 mmol, yield 36%; R_f 0.17); data for the byproducts are reported separately. **M_p** 105-109 °C.

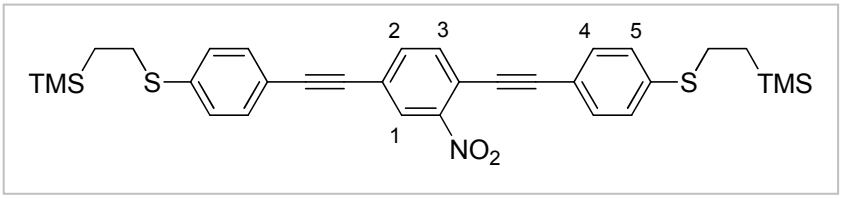

^{1}H NMR (300 MHz, $CDCl_3$): 8.16 (1H, s, **1**), 7.62-7.61 (2H, m, **2**-**3**), 7.48-7.40 (4H, m, **4**), 7.24-7.21 (4H, m, **5**), 3.01-2.95 (4H, m, S**CH_2**), 0.97-0.91 (4H, m, **CH_2**Si), 0.05 (18H, s, **TMS**). **^{13}C NMR** (75 MHz, $CDCl_3$): 149.62 (1C, **Ar**NO_2), 140.62, 140.27 (2C, **Ar**S), 135.36, 134.61 (2CH, **2**-**3**), 132.62 (2CH, **4**/**5**), 132.33 (2CH, **4**/**5**), 127.81 (1CH, **1**), 124.25, 119.06, 118.90, 118.30 (4C, **Ar**CC**Ar**CC**Ar**), 99.28, 93.84, 87.52, 85.59 (4C, Ar**CC**Ar**CC**Ar), 28.99, 28.94 ($2CH_2$, S**CH_2**), 16.89 ($2CH_2$, **CH_2**Si), -1.43 ($6CH_3$, **TMS**). **LRMS** (MALDI-TOF, DHB): *m*/*z* 1160 (7%), 660 (48), 588 ($[M+H]^+$, 100). **IR** (film): 2950 (w, CH stretch), 2210 (w, CC stretch, alkyne). **UV**: λ_{max} ($CHCl_3$) 345 nm (ε 56700). **Anal**. Calcd. For $C_{32}H_{37}NO_2S_2Si_2$: C: 65.4; H: 6.3; N: 2.4 %. Found: C: 64.4; H: 5.8; N: 2.2 %.

1,4-bis(4-(2-(Trimethylsilyl)ethylthio)phenyl)buta-1,3-diyne (**34**). See reaction to compound **33**. **M_p** 100-103 °C (not reported in ref.[67]). **^{1}H NMR** (300

MHz, $CDCl_3$): 7.43-7.40 (4H, m, **Ar**), 7.22-7.19 (4H, m, **Ar**), 3.01-2.95 (4H, m, S**CH$_2$**), 0.98-0.92 (4H, m, **CH$_2$**Si), 0.06 (18H, s, **TMS**). Data consistent with those previously reported[67]. **^{13}C NMR** (75 MHz, $CDCl_3$): 140.35 (2C, **Ar**S), 133.01, 132.98 (4CH, **Ar**), 127.72, 127.69 (4CH, **Ar**), 118.60 (2C, **Ar**CC), 82.01 (2C, Ar**C**C), 74.59 (2C, ArC**C**), 28.98 ($2CH_2$, S**CH$_2$**), 16.89 ($2CH_2$, **CH$_2$**Si), -1.43 ($6CH_3$, **TMS**).

(2-(4-(2-(4-Bromo-2-nitrophenyl)ethynyl)phenylthio)ethyl)trimethylsilane (**35**). See reaction to compound **33**. **M$_p$** 77-79 °C.

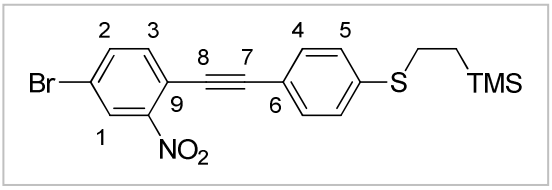

^{1}H NMR (300 MHz, $CDCl_3$): 8.20 (1H, d, *J* = 1.9, **1**), 7.68 (1H, dd, *J* = 8.3, 1.9, **2**), 7.53 (1H, d, *J* = 8.3, **3**), 7.47-7.45 (2H, m, **4**/**5**), 7.24-7.21 (2H, m, **4**/**5**), 3.01-2.95 (2H, m, S**CH$_2$**), 0.97-0.91 (2H, m, **CH$_2$**Si), 0.05 (9H, s, **TMS**). **^{13}C NMR** (75 MHz, $CDCl_3$): 150.00 (1C, **Ar**NO_2), 140.77 (1C, **Ar**S), 136.24, 135.70 (2CH, **2**-**3**), 132.61 (2CH, **4**/**5**), 128.16 (1CH, **1**), 127.75 (2CH, **4**/**5**), 121.93 (**Ar**Br), 118.87, 118.18 (2C, **6**-**9**), 98.90 (1C, **7**), 84.73 (1C, **8**), 28.96 ($1CH_2$, S**CH$_2$**), 16.92 ($1CH_2$, **CH$_2$**Si), -1.43 ($3CH_3$, **TM**S). **LRMS** (EI): *m*/*z* 433-435 ([M^+], 2%), 405-407 (10), 73 (100). **IR** (film): 2954 (w, CH stretch), 2210, 1928 (m, CC stretch, alkyne).

2'-(R and **S)-Hexyl-N-methylpyrrolidino[3',4' : 1,2][60]fullerene (36).** A 100 mL Schlenk flask equipped with a condenser and containing [60]fullerene (25 mg, 35 μmol) and N-methylglycine (sarcosine; 6 mg, 70 μmol, 2.00 eq.) was evacuated under HV and refilled with Ar before adding distilled toluene (35 mL). The reaction mixture was heated to 120 ºC (reflux) and heptanal (24.5 μL, 175 μmol, 5.00 eq.) was added dropwise, with the colour of the solution changing from purple to dark-brown within few minutes. After stirring for 2 h hexane (20 mL) was poured in the flask; the organic phase was washed with water (2 x 60 mL) and dried over anhydrous $MgSO_4$. Evaporation of the solvent afforded the crude product (50 mg). This was column chromatographed on silica gel, using toluene as eluent, to obtain the partially pure product and recovered fullerene starting material (~ 20 mg); the pure title compound (dark-brown solid, R_f 0.52; 6 mg, 7 μmol, yield 20%; mixture of two

enantiomers) was obtained by centrifugation in hexane. $\mathbf{M_p}$ > 350 °C (likely decomposition to solid residue).

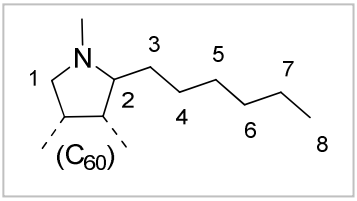

Position 2 is a stereocentre. The hydrogen atoms in positions 1 and 3 are diastereotopic.

^{1}H NMR (400 MHz, $CDCl_3$): δ 4.82 (1H, d, *J* = 9.8, **1a**/**1b**), 4.16 (1H, d, *J* = 9.8, **1a**/**1b**), 3.90 (1H, t, *J* = 5.4, **2**), 2.99 (3H, s, N**Me**), 2.58-2.49 (2H, m, **3a/b**), 2.42-2.33 (2H, m, **3a/b**), 1.96-1.84 (2H, m, **4**), 1.48 (2H, p, *J* = 7.2, **5**), 1.37-1.27 (4H, m, **6-7**), 0.89 (3H, t, *J* = 7.0, **8**). **^{13}C NMR** (100 MHz, $CDCl_3$): δ 156.73, 154.75, 154.67, 153.71, 146.58, 146.37, 146.35, 146.29, 146.24, 145.59, 145.58, 145.52, 145.49, 145.43, 144.94, 144.79, 144.56, 142.88, 142.82, 142.80, 142.41, 142.36, 142.27 (double intensity), 141.87, 139.94, 139.79, 136.45, 136.00, 135.70 (30 C, **C_{60}**), 78.46 (CH, **2**), 70.66 (CH_2, **1**), 40.20 (CH_3, N**Me**), 31.82 (CH_2, **6**), 31.74 (CH_2, **6**), 31.30, 30.13, 27.68 (3 CH_2, **3-4-5**), 22.80 (CH_2, **7**), 22.75 (CH_2, **7**), 14.25 (CH_3, **8**), 14.20 (CH_3, **8**). **LRMS** (MALDI): *m*/*z* 862 ([M^+], 100 %). **IR** (film): 2913, 2848, 2770 (s, CH stretch), 2353, 2325 (m, CC stretch, C_{60}), 2124 (w). ^{1}H NMR and IR data consistent with those reported[118] for the nonyl- analogue (^{13}C NMR data not reported).

(R)-4-((3R,10S,13R,17R)-Hexadecahydro-3-hydroxy-10,13-dimethyl-1H-cyclopenta[α]phenanthren-17-yl)pentanal (37). A 50 mL Schlenk flask containing lithocholic acid (1.88 g, 4.99 mmol) was evacuated and refilled with argon; a solution of isopropylmagnesium bromide 2 M in Et_2O (6.25 mL, 12.50 mmol, 2.50 eq.) was then added, yielding a white suspension that was cooled to 0 °C. To a small Schlenk tube containing bis[π-cyclopentadienyl]titanium dichloride (12 mg, 0.05 mmol, 1 mol%), previously evacuated and refilled with argon, was added a solution of isopropylmagnesium bromide 2 M in Et_2O (3.75 mL, 7.50 mmol, 1.50 eq.); the resulting blue solution was cooled at 0 °C for 5 minutes and then added to the flask containing the lithocholic acid suspension. The reaction mixture was let warming to r.t. and stirred for 5 hours. Then the excess Grignard reagent was quenched with HCl 2 N; after most of the solvent had been removed in a rotating evaporator, the mixture was diluted with DCM and washed with water and brine. Drying over $MgSO_4$ and evaporation of the solvent yielded the pure title compound (white solid; 239 mg, 0.66

mmol, yield 13 %). **M_p** not available (sample stored for further characterization decomposed to a semisolid).

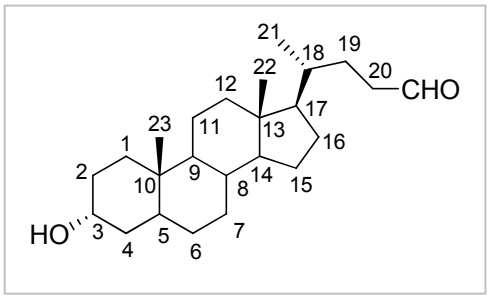

^{1}H NMR (400 MHz, $CDCl_3$): δ 9.77 (1H, s, C**H**O), 3.62 (2H, ept, *J* = 5.1, **20**), 2.49-2.41 (2H, m, **2/4**), 2.38-2.30 (2H, m, **2/4**), 1.98-0.91 (27H, m, **1**, **3**, **5-19**, **21**), 0.65 (6H, s, **22-23**). **^{13}C NMR** (100 MHz, $CDCl_3$): δ 203.11 (CH, **CHO**), 71.78 (CH, **3**), 56.48, 55.98 (2 CH, **17-18**), 42.74 (C, **10/13**), 42.08 (CH), 40.90 (CH_2), 40.42 (CH), 40.15, 36.44 (2 CH_2), 35.84 (CH), 35.31 (CH_2), 34.56 (CH), 30.53 (CH_2), 29.66 (C, **10/13**), 28.22, 27.95, 27.17, 26.40, 24.18 (5 CH_2), 23.35 (CH_3, **21**), 20.81 (CH_2), 18.35, 12.04 (2 CH_3, **22-23**). **LRMS** (ES^+): *m*/*z* 378 ([oxidation to carboxylic acid starting material], 100 %). **IR** (film): 3363 (w broad, OH stretch), 2921, 2860 (s, CH stretch), 1720 (s, C=O stretch).

2'-(R and **S)-[(R)-3-((3R,10S,13R,17R)-Hexadecahydro-3-hydroxy-10,13-dimethyl-1H-cyclopenta[α]phenanthren-17-yl)butyl]-N-methylpyrrolidino[3',4' : 1,2]-[60]fullerene (38).** A 250 mL Schlenk flask equipped with a condenser and containing [60]fullerene (94 mg, 0.13 mmol) and N-methylglycine (sarcosine; 23 mg, 0.26 mmol, 2.00 eq.) was evacuated under HV and refilled with Ar before adding distilled toluene (115 mL). The reaction mixture was heated to 120 ºC (reflux) and a degassed solution of lithocholic aldehyde **37** (71 mg, 0.20 mmol, 1.54 eq.) in distilled toluene (15 mL) was added dropwise. The colour of the solution gradually changed from purple to dark-brown. After stirring for 2.5 h the mixture was let cooling to r.t. and DCM (150 mL) was poured in the flask; the organic phase was washed with water and brine, and dried over anhydrous $MgSO_4$. Evaporation of the solvent afforded the crude product (177 mg). This was column chromatographed on silica gel, using (4/1) DCM/Et_2O as eluent, to obtain the partially pure (aliphatic impurities) product (dark-brown solid, R_f 0.49; 68 mg, 61 μmol, yield 5 %), recovered fullerene starting material (R_f 0.78, 32 mg) and a non-identified byproduct (dark solid, striking from R_f 0 to 0.22;

25 mg). Title compound with higher purity was obtained, for characterization purpose, by centrifugation in hexane. $\mathbf{M_p}$ > 350 °C (likely decomposition to solid residue).

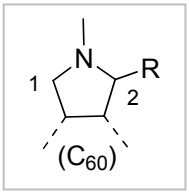

Position 2 is a stereocentre. The presence of other four chiral centers on the steroidic fragment results in a mixture of two diastereomers, as evidenced by ^{1}H NMR (presence of two NMe signals and two additional signals for the diastereotopic hydrogens in position 1).

^{1}H NMR (400 MHz, $CDCl_3$): δ 4.83 (1H, d, *J* = 9.6, **1a/1b**), 4.82 (1H, d, *J* = 9.8, **1a/1b**), 4.17 (1H, d, *J* = 9.8, **1a/1b**), 4.14 (1H, d, *J* = 9.8, **1a/1b**), 3.90-3.85 (1H, m, **2**), 3.59-3.65 (1H, m, **CH**OH), 3.00 (3H, s, N**Me**), 2.97 (3H, N**Me**), 2.63-0.65 (37H, m, **aliphatic fragment**). **^{13}C NMR** (100 MHz, $CDCl_3$, NS 5120): δ 145.53-139.71 (58C, **C_{60}**), 78.82, 78.56 (CH), 76.17 (C), 71.88 (CH, **CH**OH), 70.49 (CH_2, **1**), 70.21, 70.07 (C, **Ar**C), 56.53, 56.22 (CH), 53.40 (CH_2), 42.79 (C), 42.12 (CH), 40.47 (CH_3, N**Me**), 40.21 (CH_2), 39.98, 36.80, 36.69 (CH), 36.50 (CH_2), 35.87 (CH), 35.37, 34.59 (CH_2), 33.86 (C), 32.91, 30.59, [28.40, 28.09, 27.50], 27.21, 26.44, 24.29 (CH_2), 23.38 (CH_3), 20.85 (CH_2), 18.82, 12.08 (CH_3). **LRMS** (MALDI): *m*/*z* 1110 ($[M+H]^+$, 100 %). **IR** (film): 2921, 2852, 2774 (s, CH stretch), 2357, 2329 (s, CC stretch, C_{60}). **UV**: λ_{max} ($CHCl_3$) 256 nm (ε 192000), shoulder λ 300-325 nm (ε 62000).

(4-Ethynylphenyl)(methyl)sulfane (39).[80] In a 1 L rbf, compound **21** (2.11 g, 9.57 mmol) was dissolved in MeOH (300 mL) and stirred for 0.5 h in presence of K_2CO_3 (13.21 g, 95.58 mmol, 9.99 eq.). Water (300 mL) was poured in the flask and the mixture was extracted with DCM (2 x 250 mL); the combined organic phase was washed with water and brine, and dried over $MgSO_4$. Evaporation of the solvent afforded the pure title compound (GC, SD_FASTD, RT 3.6 minutes; R_f 0.20 in (20/1) hexane/DCM) as a brownish oil (1.375 g, 9.28 mmol, yield 97 %) with a characteristic scent of mushroom. **^{1}H NMR** (400 MHz, $CDCl_3$): δ 7.40 (2H, d, *J* = 8.0, **Ar**), 7.21 (2H, d, *J* = 8.3, **Ar**), 3.07 (1H, s, C**CH**), 2.48 (3H, s, S**Me**). **^{13}C NMR** (100 MHz, $CDCl_3$): δ 140.29 (C, **Ar**S), 132.60, 126.00 (2 CH, **Ar**), 118.56 (C, **Ar**CC), 83.67 (C, Ar**C**C; present in DEPT), 77.41 (CH, C**CH**), 15.52 (CH_3, S**Me**). **LRMS** (EI): *m*/*z* 148 ($[M^+]$, 100 %), 133 ($[M-Me]^+$, 60), 89 ($[C_6H_5C^+]$, 45). **IR** (film): 3281 (s broad, CH stretch, alkyne), 2917 (m, CH stretch), 2104 (m, CC stretch, alkyne). Data not reported in [80].

2,5-dibromoacetophenone (40). Repeating the standard Friedel-Crafts acylation procedure, 2,5-dibromobenzene (7.08 g, 30.0 mmol) and $AlCl_3$ (4.00 g, 30.0 mmol, 1.00 eq.) were ground and placed in a 50 mL Schlenk flask fitted with a condenser; after the evacuation/refill with Ar cycle, the top Schlenk arm was replaced with an oil bubbler. AcCl (2.13 mL, 30.0 mmol, 1.00 eq.) was then added, and the mixture was heated to 120 °C; before all of the solid had been washed down by the refluxing AcCl (B_p 52 °C), the solution turned dark-green (after 10 minutes). After 2 hours the reaction, containing both unreacted starting material (as monitored by GC, SD_FASTD, RT 3.0 min) and product (RT 4.7 min), was let cooling to r.t. and HCl (2N) was added slowly (with shaking) until the evolution of gas stopped. The aqueous phase was extracted with Et_2O (3 x 50 mL), the combined organic phases where washed again with HCl (2N, 50 mL) and dried over $MgSO_4$. Evaporation of the solvent afforded the crude product (brown oil, 7.070 g) that was column chromatographed on silica gel using (10/1) hexane/Et_2O to yield the partially pure title compound (brownish solid, R_f 0.26; 1.694 g). This was dissolved in hot hexane, let cool to r.t. and then in ice, to obtain, after filtration and evaporation, the pure product (white flakes, 1.35 g, 4.86 mmol, yield 16 %). **M_p** 58-60 °C (hexane; consistent with the reported[119]). **^{1}H NMR** (300 MHz, $CDCl_3$): δ 7.80 (1H, d, *J* = 1.8, **6**), 7.51 (1H, dd, *J* = 8.4, 1.5, **4**), 7.36 (1H, d, *J* = 8.1, **3**), 2.61 (3H, s, **Me**CO). **^{13}C NMR** (75 MHz, $CDCl_3$): δ 200.11 (C, **CO**Me), 140.13 (C, **1**, **Ar**CO), 136.45 (CH, **6**), 130.86 (CH, **3/4**), 130.36 (CH, **3/4**), 125.54 (C, **2**, **C**Br), 120.03 (C, **5**, **C**Br), 30.33 (CH_3, **Me**CO). **LRMS** (GC-EI, RT 13.2 min.): *m/z* 278 ([M^+], 70 %), 263 ([M-Me]$^+$,100 %), 235 ([M-MeCO]$^+$, 20 %); two-Br patterns.

2,5-Dibromobenzoic acid (41). Following a procedure reported by Vogel[81], ketone **40** (1.35 g, 4.86 mmol) was dissolved in dioxane (7 mL, ~ 5 mL/g) and added dropwise to a NaClO solution ('bleach') pre-heated to 50 °C. The mixture was then heated to 75 °C and let stirring for ½ h, time sufficient for the complete disappearance of starting material to occur (R_f 0.50 in 1/1 hexane/Et_2O). After cooling to r.t., water (50 mL) was added, followed by $Na_2S_2O_3$ (20% aq., 25 mL) to quench the excess oxidizer (confirmed by negative reaction on starch/I^- paper). The mixture, strongly basic, was washed with Et_2O (50 mL), then acidified until pH 1 with HCl (2N, 100 mL), resulting in the formation of a white flocculate. This was separated by vacuum filtration, washed with iced water and dried; the solid was dissolved in a small volume

of Et_2O and loaded onto silica gel, then column chromatographed through a short silica plug using 1/1 hexane/Et_2O as eluent (product R_f 0.75). Evaporation of the solvent afforded the title compound (white solid, 1.116 g, 3.99 mmol, yield 82 %) that was not purified further. **M_p** 158-160 °C (lit.[120] 156-157 °C). **^{1}H NMR** (300 MHz, $CDCl_3$): δ 7.92 (1H, d, *J* = 1.8, **6**), 7.90 (1H, d, *J* = 8.4, **3**), 7.57 (1H, dd, *J* = 8.4, 1.8, **4**). **^{13}C NMR** (75 MHz, $CDCl_3$): δ 221.10 (C, **CO**OH), 164.25 (C, **1**, **Ar**CO), 137.63 (CH, **6**), 133.67 (CH, **3/4**), 130.84 (CH, **3/4**), 127.97 (C, **2**, **C**Br), 123.78 (C, **5**, **C**Br). **LRMS** (ES^-): *m*/*z* 279 ([M^-], 100 %; two-Br pattern), 559 ([2M]$^-$, 20 %). **IR** (film): 3085, 2933, 2850, 2627, 2537 (m, CH stretch), 1675 (s, C=O stretch), 1028 (s, C-O stretch), 556 (s, C-Br stretch).

2,5-bis(2-(4-(Methylthio)phenyl)ethynyl)benzoic acid (42). A 25 mL Schlenk flask containing **41** (128 mg, 0.46 mmol), **39** (150 mg, 1.01 mmol, 2.20 eq.), $PdCl_2$ (8 mg, 46 μmol, 10 mol%), PPh_3 (24 mg, 0.09 mmol, 20 mol%), CuI (17 mg, 0.09 mmol, 20 mol%) and DABCO (310 mg, 2.76 mmol, 6.00 eq.) was evacuated and refilled with argon before adding distilled DMF (10 mL). The reaction mixture was then heated to 60 °C; after 2 h it was interrupted because of the presence of at least 4 fluorescent compounds (as monitored by TLC and UV lamp at 365 nm; two of these were probably originating from decomposition on silica, see next). After most of the solvent was evaporated (rotating evaporator at 60 °C) the residue was dissolved in DCM, washed with water (the pH was found to be ~ 5 and was not corrected) and brine and dried over anhydrous $MgSO_4$. Evaporation of the solvent afforded the crude product (226 mg) that was column chromatographed on silica gel using (3/1) hexane/DCM; the eluent composition was gradually changed to (3/1) DCM/hexane during the elution. The main fraction containing product (bright yellow solid, R_f 0.54 in DCM; green fluorescence at 365 nm, UV longwave) and impurities (totally 47 mg) was purified again by Chromatotron (eluent DCM) followed by precipitation from DCM/hexane. The product (19 mg, 46 μmol, yield 10 %) was found to decompose on silica, originating two fluorescent byproducts with **R_f**s 0.00 (green fluorescence) and 0.43 (cyan fluorescence) in DCM. The purity could only be assessed by ^{1}H NMR analysis. **M_p** 206-208 °C (likely decomposition).

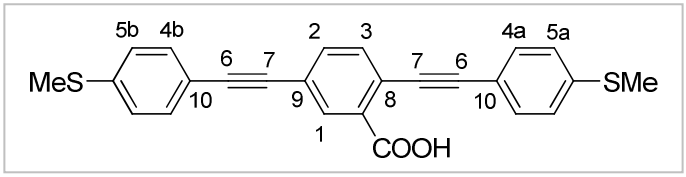

^{1}H NMR (400 MHz, $CDCl_3$): δ 8.06 (1H, s, **1**), 7.82 (1H, d, *J* = 8.0, **2**), 7.78 (2H, d, *J* = 8.3, **4a/4b**), 7.72 (2H, d, *J* = 8.0, **3**), 7.47 (2H, d, *J* = 8.3, **4a/4b**), 7.28 (2H, d, *J* = 8.3, **5a/5b**), 7.24 (2H, d, *J* = 8.3, **5a/5b**), 6.40 (1H, broad s, COO**H**), 2.53 (3H, s, S**Me a/b**), 2.52 (3H, s, S**Me a/b**). **^{13}C NMR** (100 MHz, $CDCl_3$): δ 166.20 (C, **C**O), 143.87 (C, **Ar**COOH), 140.41, 139.93, 139.39 (3 C, 2x **Ar**S + **8**), 137.24 (CH, **2**), 131.99, 130.49 (2 CH, **4a-4b**), 129.63 (C, **9**), 128.46 (CH, **1**), 126.18, 125.85 (2 CH, **5a-5b**), 125.09, 123.60 (2 C, **10**), 119.70 (CH, **3**), 118.58 (C, ?), 107.57 (CH, ?), 92.24, 88.08 (2 C, **6-7**), 15.30 (CH_3, S**Me**). **LRMS** (MALDI): *m/z* 851 ($[2M+Na]^+$, 58 %), 469 ($[M+Na+MeOH]^+$, 90), 437 ($[M+Na]^+$, 50), 415 ($[M+H]^+$, 100). **IR** (film): 3064, 2909, 2848 (w, CH stretch), 2210 (w, CN stretch), 1781, 1777 (s, C=O stretch). **UV**: λ_{max} ($CHCl_3$) 391 nm (ε 62100). **HRMS** (ES) for $C_{25}H_{18}Na_1O_2S_2$ $[M+Na]^+$: *m/z* calcd. 437.0640, found 437.0636.

(3'''R,10'''S,13'''R,17'''R)-hexadecahydro-10''',13'''-dimethyl-17'''-((R)-4''-((R and **S)-1''-methylpyrrolidin-([3',4':1,2]-[60]fulleren-yl)-2'-yl)-butan-2''-yl)-1H-cyclopenta[α]phenanthren-3'''-yl 2,5-dibromobenzoate (43)**. The acid **41**[121,122] (14 mg, 0.05 mmol) was placed in a 50 mL Schlenk flask fitted with a condenser and under inert atmosphere. After adding $SOCl_2$ (4 mL, 80 mL / mmol of acid) the reaction was heated to 90 °C and stirred for 1.5 h. Vacuum evaporation of the unreacted thionyl chloride was followed by cooling to r.t. and further evaporation (2 h). Compound **38** (50 mg, 45 μmol, 0.90 eq.) and DMAP (6 mg, 0.05 mmol, 1.00 eq.) were dissolved in dry DCM (10 mL) under inert atmosphere and ultrasonic conditions; TEA (0.02 mL, 0.15 mmol, 3.00 eq.) was added, and the solution was transferred to the flask containing the 2,5-dibromobenzoyl chloride. After the immediate evolution of HCl the reaction was left stirring at r.t. for 22 h. DCM (10 mL) was added, and the mixture was washed twice with HCl (2 N, 5 mL aliquots) and crushed ice, then with brine. The aqueous phase was extracted with small aliquots of DCM until cleared, and the joined organic phases were dried over $MgSO_4$ and vacuum evaporated to yield the crude product (dark-brown solid, 73 mg). This was purified by column chromatography on silica gel, using as eluent DCM, to give the title compound **43** (R_f 0.63, brown stain and UV absorbing; dark-brown solid, 19 mg, 14 μmol, yield 28 %). A significant amount of unidentified aliphatic compound (17 mg) eluted first (R_f 0.80, visible after PMA staining). The starting material **38** was recovered by changing the

eluent to 1 / 1 DCM / Et_2O (R_f 0.66 in this solvent system, 0.07 in neat DCM; dark-brown solid, 17 mg, recovery yield 34 %). **M_p** > 250 °C (likely decomposition).

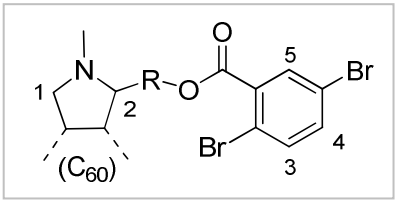

Mixture of diastereomers (see comment to compound **38**).
R = steroidic fragment

^{1}H NMR (400 MHz, $CDCl_3$): δ 7.83 (1H, m, **5**), 7.63 (1H, d, *J* = 8.8, **3**), 7.49 (1H, d, *J* = 9.2, **4**), 5.04-4.94 (2H, m, **CH**OCO), 4.83 (1H, d, *J* = 9.6, **1a/1b**), 4.82 (1H, d, *J* = 10.0, **1a/1b**), 4.17 (1H, d, *J* = 9.6, **1a/1b**), 4.13 (1H, d, *J* = 9.6, **1a/1b**), 3.89-3.85 (2H, m, **2**), 2.99 (3H, s, N**Me**), 2.96 (3H, N**Me**), 2.64-0.66 (74H, m, **aliphatic fragment**). **^{13}C NMR** (100 MHz, $CDCl_3$, NS 6K): δ 165.28 (C, **CO**), 162.70, 156.67, 156.60, 154.79, 154.72, 154.64, 153.73, 153.67, 147.41, 147.37, 147.01, 146.99, 146.77, 146.66, 146.54, 146.45, 146.42, 146.34, 146.31, 146.26, 146.24, 146.21, 146.14, 146.11, 146.00, 145.97, 145.73, 145.68, 145.57, 145.50, 145.47, 145.44, 145.40, 145.35, 144.91, 144.78, 144.75, 144.57, 144.52, 143.50, 143.20, 142.80, 142.32, 142.26, 142.00, 141.90, 141.82, 140.43, 140.34, 139.90, 139.71, 137.33 (C, **C_{60}** arom.), 136.84 (CH), 136.40, 135.95 (C), 135.64 (C, **Ar**CO), 132.31 (CH), 132.00 (C), 130.57 (CH), 126.12, 122.53 (C, **C**Br), 78.91, 78.73 (CH), 76.58 (CH, **CH**OCO), 76.27, 70.32 (C), 70.61 (CH_2), 70.32, 70.17 (C, **C_{60}** sp^3), 56.66, 56.24 (CH), 42.93 (C), 42.17 (CH), 40.66 (CH_3, N**Me**), 40.29 (CH_2), 40.23, 40.14, 36.88, 36.73, 35.96 (CH), 35.19 (CH_2), 34.80 (C), 33.91, 33.05, 32.36, 29.85 (CH_2), 28.59 (C), 28.54, 28.04, 27.40, 27.18, 26.82, 26.50, 24.42 (CH_2), 23.50 (CH_3), 21.04 (CH_2), 19.01, 12.25 (CH_3). **LRMS** (MALDI): *m/z* 1370 ($[M+H]^+$, 100 %). **IR** (film): 2922, 2854, 2775 (m, CH stretch), 2359, 2336 (m, CC stretch, C_{60}), 1720 (m, C=O stretch), 1032 (s, C-O stretch), 525 (s, C-Br stretch). **UV**: λ_{max} ($CHCl_3$) 254 nm (ε 169000), shoulder λ 300-314 nm (ε 55000).

cis- and trans-O,O'-Cyclohexane-1,4-diylbis(methylene)toluensulfonate (44 and **45).** Following a procedure reported by Swepston[83], a 50 mL Schlenk flask containing 1,4-cyclohexanedimethanol (1/1 cis-/trans-; 2.88 g, 20.0 mmol) was evacuated and refilled with argon. Pyridine (20 mL) was added, and the mixture was stirred at r.t. for 10 minutes. After cooling to 0 °C, p-toluenesulfonylchloride (8.39 g, 44.0 mmol, 2.20 eq.) was added, under argon. Stirring at low temperature for further

10 minutes yielded a thick suspension that was then kept in the fridge (1 °C) for 65 hours (over the weekend). After warming to r.t. the mixture was diluted with water (50 mL) and its pH (slightly acidic) was neutralized with diluted NaOH. The resulting suspension was vacuum filtered; the solid was dissolved in MeOH (50 mL), precipitated with H_2O and filtered again. Washing the solid with MeOH (2 x 20 mL) and evaporation of the filtrate yielded respectively 6.14 g (trans-enriched) and 2.43 g (cis-enriched) of crude product, with a reaction yield > 95%. Higher purity was achieved by crystallization in the case of the trans-isomer (**45**: recrystallized three times from boiling EtOH, purification yield 50%; white needles, purity > 95%, 1.77 g, 3.91 mmol, yield 20%). The cis-enriched fraction was refluxed in MeOH (2 h; slightly saturated), then let cooling slowly to r.t. under stirring (kept in the oil bath). The solution was filtered to remove the trans-containing solid and concentrated. Iteration of the procedure yielded a reasonably pure cis-isomer (**44**: purification yield 93%; white solid, purity ~ 90%, 187 mg, 0.41 mmol, yield 2 %). Both isomers were used in the next step without further purification.

cis-O,O'-Cyclohexane-1,4-diylbis(methylene)toluensulfonate (44).

TLC: R_f 0.55 (4/1 Et_20/hexane). **GC**: not applicable. **M_p** 81-86 °C (lit.[84] 95 °C). **^{1}H NMR** (300 MHz, $CDCl_3$): δ 7.77 (4H, d, *J* = 8.4, **Ar**), 7.35 (4H, d, *J* = 7.9, **Ar**), 3.87 (4H, d, *J* = 7.1, **CH_2**O), 2.46 (6H, s, **Me**), 1.75-1.90 (2H, m, cHex **CH**), 1.35-1.50 (4H, m, cHex **CH_2 ax/eq**), 1.15-1.30 (4H, m, cHex **CH_2 ax/eq**). **^{13}C NMR** (75 MHz, $CDCl_3$): δ 144.86 (2C, **Ar**SO_2), 133.19 (2C, **Ar**Me), 129.96 (4 CH, **Ar**), 128.01 (4CH, **Ar**), 72.87 (2CH_2, **CH_2**O), 34.57 (2CH, **cHex**), 24.69 (4CH_2, **cHex**), 21.80 (2 CH_3, **Me**). **IR** (film): 2830 (w, br), 2858 (w) (CH stretch), 1591 (w), 1349 (s), 1293 (m), 1172, 1092, 945, 813, 779, 665, 552 (s) cm^{-1}.

trans-O,O'-Cyclohexane-1,4-diylbis(methylene)toluensulfonate (45).

TLC: R_f 0.55 (4/1 Et_20/hexane). **GC**: not applicable. **M_p** 164-168 °C, recrystallized from EtOH as white needles (lit.[84] 162-163 °C). **^{1}H NMR** (300 MHz, $CDCl_3$): δ 7.77 (4H, d, *J* = 8.2, **Ar**), 7.35 (4H, d, *J* = 7.9, **Ar**), 3.81 (4H, d, *J* = 6.4, **CH_2**O), 2.46 (6H, s, **Me**), 1.70-1.80 (4H, m, cHex **CH_2 ax/eq**), 1.50-1.70 (2H, m, cHex **CH**), 0.80-1.00 (4H, m, cHex **CH_2 ax/eq**). **^{13}C NMR** (75 MHz, $CDCl_3$): δ 144.86 (2C, **Ar**SO_2), 133.19 (2C, **Ar**Me), 129.96 (4CH, **Ar**), 128.01 (4CH, **Ar**), 74.95 (2CH_2, **CH_2**O), 37.12 (2CH, **cHex**), 28.19 (4CH_2, **cHex**), 21.80 (2CH_3, **Me**). **IR** (film): 2941, 2865

(w, CH stretch), 1595 (w), 1342, 1168 (s), 1096 (m), 941, 809, 790, 665, 548 (s) cm^{-1}. **XR**: the structure was confirmed by X-ray crystallography[123].

cis-S,S'-Cyclohexane-1,4-diylbis(methylene)diethanetioate (46). Following the procedure reported by Whistler[85] the bis-tosylate **44** (93 mg, 0.20 mmol) was dissolved in 1 mL of acetone in a 10 mL rbf. Potassium thiolacetate (59 mg, 0.52 mmol, 2.60 eq.) was added, and after stirring for 10 min at r.t. the suspension was heated to reflux temperature (65 °C) and left overnight. After cooling to r.t. the reaction mixture was filtered, and the inorganic residue was washed with Et_2O once. The organic phase was washed with brine, dried over $MgSO_4$, and evaporated to yield the crude brown oil (59 mg). This was dissolved in DCM and shaken with decolourizing charcoal; filtration and evaporation of the solvent afforded a yellow oil (37 mg, 0.14 mmol, reaction yield 71%; purity: 87% cis-isomer, the rest of the mass is mostly trans-isomer and by-products; the pure product is supposedly a clear oil or low M_p white solid). R_f 0.69 (UV 254 nm; 4/1 Et_20/hexane). **GC**: retention time 6.57 min (SD_FASTD). **^{1}H NMR** (300 MHz, $CDCl_3$): δ 2.88 (4H, d, *J* = 7.1, **CH_2**S), 2.33 (6H, s, **Me**CO), 1.60-1.70 (4H, m, cHex **CH_2 ax/eq**), 1.50-1.60 (2H, m, cHex **CH**), 1.35-1.50 (4H, m, cHex **CH_2 ax/eq**). **^{13}C NMR** (75 MHz, $CDCl_3$): δ 196.06 (2C, **CO**Me), 35.57 (2CH, **cHex**), 33.53 ($2CH_2$, **CH_2**S), 30.79 ($2CH_3$, **Me**CO), 27.97 ($4CH_2$, **cHex**). **LRMS** (EI; GC-MS retention time 9.4 min): *m*/*z* 261 ($[M+H]^+$, 5%), 217 ($[M-Ac]^+$, 64), 185 ($[M-AcS]^+$, 14), 175 ($[M-2Ac]^+$, 32), 167 (12), 141 ($[M-Ac-AcS]^+$, 98), 43 ($[Ac^+]$, 100). **IR** (film): 2960, 2922, 2854 (w, CH stretch), 1697 (w), 1259 (s), 1081, 1009 (s, br), 790 (s, br) cm^{-1}.

trans-S,S'-Cyclohexane-1,4-diylbis(methylene)diethanethioate (47). As reported for **46**, the bis-tosylate **45** (905 mg, 2.00 mmol) and potassium thiolacetate (594 mg, 5.20 mmol, 2.60 eq) were reacted in 4 mL of acetone. Work-up and evaporation of the solvent yielded the crude product (brownish solid, 485 mg, purity 95% including the cis-contaminant, reaction yield 79%); this was dissolved in Et_2O and treated with decolourizing charcoal. The yellow solid obtained (396 mg) was recrystallized twice in cold EtOH/H_2O (flakes) to yield the pure product (white waxy solid, 52 mg, 0.20 mmol, yield 10%; purity > 95% trans-isomer). R_f 0.69 (UV 254 nm; 4/1 Et_20/hexane). **GC**: retention time 6.63 min (SD_FASTD). **M_p** 48-51 °C

(from EtOH; lit.[124] 51-52 °C). **^{1}H NMR** (300 MHz, $CDCl_3$): δ 2.78 (4H, d, *J* = 7.3, **CH_2**S), 2.32 (6H, s, **Me**CO), 1.75-1.90 (4H, m, cHex **CH_2 ax/eq**), 1.32-1.48 (2H, m, cHex **CH**), 0.86-1.06 (4H, m, cHex **CH_2 ax/eq**). **^{13}C NMR** (75 MHz, $CDCl_3$): δ 195.97 (2C, **CO**Me), 37.87 (2CH, **cHex**), 35.76 ($2CH_2$, **CH_2**S), 32.01 ($4CH_2$, **cHex**), 30.78 ($2CH_3$, **Me**CO). **LRMS** (EI; GC-MS retention time 9.5 min): *m*/*z* 261 ($[M+H]^+$, 27%), 219 ($[(M-Ac)+H]^+$, 35), 185 ($[M-AcS]^+$, 82), 174 ($[M-2Ac]^+$, 21), 167 (54), 141 ($[M-Ac-AcS]^+$, 98), 43 ($[Ac^+]$, 100). **IR** (film): 3353 (w), 2964 (w), 2926 (s), 2850 (m) (CH stretch), 1682 (s), 1436, 1414 (s), 1130, 1100, 1066, 949, 620 (s) cm^{-1}. **Anal.** Calcd. for $C_{12}H_{20}O_2S_2$: C, 55.3; H 7.7 %. Found: C, 54.9; H, 7.8 %.

Dimethylbi(cyclohexane)-4,4'-dicarboxylate (48). Following a procedure reported by Cannon[86], a glass vessel was loaded with methyl ester biphenyl-dicarboxylate (2.0 g, 7.4 mmol), PtO_2 (33 mg, 20 mol%), Pd/C (5% Pd, 66 mg, 0.4 mol%) and AcOH (50 mL), and the mixture was sonicated shortly. The vessel was fitted in a steel high pressure apparatus that was vented and then filled with H_2 until a pressure of 350 psi was established. The reaction was heated to 50 °C and stirred for several days: addition of more gas was needed to keep the pressure at the set-point. Monitoring by GC (SD_FASTD) was carried on by letting cooling the reaction and releasing the pressure prior to sampling: after 2 d this showed 3 main peaks at 7.13, 7.29 and 7.46 min, 2 minor peaks at 7.59 and 7.74 min, and starting material as a trace at 8.56 min; after further 2 d only the three main peaks were left, and these were assigned to the three possible diastereomeric products. The mixture was filtered through filter paper (double layer), taken up in DCM (50 mL), washed with water (2 x 100 mL) and dried over $MgSO_4$. The crude product (white solid, 1.97 g, 6.98 mmol, yield 94%) was used in the next step without further purification; the completeness of the reduction was assessed by ^{1}H NMR from the disappearance of the aromatic signals. **GC** (SD_FASTD): 7.13 min (40%), 7.29 (48), 7.46 (12). **^{1}H NMR** (300 MHz, $CDCl_3$): δ 3.53-3.51 (m, **Me**), 2.45-2.38 (m, **CH**CO), 2.12-0.74 (m, all the rest). **^{13}C NMR** (75 MHz, $CDCl_3$): δ 176.32, 176.27, 175.58, 175.50 (C, **CO**), 51.19, 43.22, 42.12, 41.54, 40.48, 39.93, 39.81 (CH_3 and CH), 29.10, 29.04, 29.02, 28.91, 28.76, 26.66, 26.50, 26.42, 26.31 (CH_2). **LRMS** (EI; GC-MS): *m*/*z* 282 ($[M^+]$, 3%) was observed in both fractions at 9.50 and 9.71 min, not in that at 9.96 min.

trans,trans-Bi(cyclohexane)-4,4'-dicarboxylic acid (49). As reported by Cannon[86], the ester **48** (1.61 g, 5.70 mmol) was hydrolized by refluxing for 4 h in presence of NaOH (0.72 g, 18.0 mmol, 3.16 eq.), in a mixture of EtOH (13 mL) and water (3.5 mL) at 75° C. After cooling, most of the EtOH was vacuum evaporated; water was added (25 mL), followed by concentrated HCl (7 mL) which caused the precipitation of the title compound. This was filtered, washed with water and dried, initially in air and then in high vacuum (at least 10 h to ensure dryness), yielding the mixture of acid diastereomers (white solid, 1.29 g, 5.07 mmol, hydrolysis yield 89%) . The solid was ground and tightly packed in a small reaction tube; this was placed in a sand bath inside an aluminium block preheated to 275° C. After 3 h the material was left cooling then dissolved by sonication in Na_2CO_3 (sat.); after adding of decolourizing coal the suspension was filtered. Addition of HCl (10% w/v, 20 mL) caused the precipitation of the title compound that was filtered, washed with water and dried in air for several days. The product (white solid, 1.01 g, 3.97 mmol, yield 70%), as analyzed by NMR, was found to be 90% single diastereomer: the assignment to the trans,trans- geometry was supported by the comparison of the M_p with that reported in literature. **M_p** 351-353 °C with darkening (lit.[86] 351-353° C). **GC** (not applicable). **^{1}H NMR** (300 MHz, DMSO): δ 11.97 (2H, br s, **COOH**), 2.08 (2H, tt, *J* = 12.0, 3.4, **CH**CO), 1.89 (4H, dq, *J* = 11.1, **CH_2**CHCO eq.), 1.70 (4H, dq, *J* = 10.2, **CH_2**CHCO ax.), 1.50-1.37 (2H, m, **CH**CH), 1.31 (4H, q, *J* = 12.0, CH_2**CH_2**CH eq.), 1.01-0.92 (4H, m, CH_2**CH_2**CH ax.). **^{13}C NMR** (75 MHz, DMSO): δ 176.78 (2C, **CO**), 42.72 (2CH, **CH**CO), 42.70 (2CH, CH_2**CH**CH), 28.96 (4CH_2), 28.61 (CH_2); quantity of material with cis- configuration can be estimated from the intensity of the CH_2 signals at 26.50 and 26.12 ppm. **LRMS** (ZMD ESI$^-$): *m*/*z* 253 ([M-H$^+$]$^-$, 100%). **IR** (film): 3300-2400 (very br, OH stretch), 2926, 2858 (m, CH stretch), 2661, 2563 (w), 1690 (very s, CO stretch), 1448, 1419 (m, CH bend), 1304, 1259, 1206, 945, 922, 896, 537 (m) cm^{-1}.

trans,trans-Bi(cyclohexane)-4,4'-diyldimethanol (50). Following a standard procedure, a 50 mL Schlenk flask was loaded with the acid **49** (50 mg, 0.20 mmol), then evacuated and refilled with argon before adding distilled THF (10 mL). A condenser was fitted onto the flask and $LiAlH_4$ (60 mg, 1.58 mmol, 7.90 eq.) was added at once. The reaction was heated to 60° C for 1.5 h; after cooling the excess hydride was quenched with HCl 2 N (2 mL, dropwise). The suspension was diluted

with Et_2O (20 mL) and washed with water (3 x 20 mL); this was extracted with Et_2O (2 x 15 mL) and the organic fractions were joined and dried over $MgSO_4$. Evaporation of the solvent yielded the crude product (49 mg) that was column chromatographed over silica gel, using EtOAc as eluent (R_f 0.5), to obtain the title compound (29 mg, 0.13 mmol, yield 64%). This was analyzed by NMR and found to contain about 10% cis- contaminant, yet it was used in the next step without further purification. **^{1}H NMR** (300 MHz, CD_3OD): δ 4.85 (2H, s, **OH**; over-integrated), 3.33 (4H, d, *J* = 6.3, **CH_2**OH), 1.85-1.77 (8H, m), 1.52-1.29 (4H, m), 1.04-0.85 (8H, m); the amount of cis-contaminant can be estimated from the intensity of the **CH_2**OH signal at 3.47 ppm. **^{13}C NMR** (75 MHz, CD_3OD): δ 68.88 ($2CH_2$, **CH_2**OH), 44.87 (2CH, **CH**CH_2OH), 42.02 (2CH, CH_2**CH**CH), 31.08 ($4CH_2$, cHex), 30.75 ($4CH_2$, cHex); cis- impurity, **CH_2** signals at 27.21 and 26.86 ppm. **LRMS** (CI; GC-MS): *m*/*z* 225 ([M^+], 1.5%) at retention time 9.49 min.

Trans,trans-bi(cyclohexane)-4,4'-diylbis(methylene)bis(4-methylbenzene-sulfonate) (51). Following a procedure reported by Swepston[83], a 25 mL Schlenk flask containing compound **50** (212 mg, 0.94 mmol) was evacuated and refilled with argon before adding pyridine (2 mL). The resulting suspension was stirred at r.t. for 10 minutes; after cooling to 0 °C p-toluenesulfonylchloride (448 mg, 2.35 mmol, 2.50 eq.) was added, under argon, and the reaction mixture was kept in the fridge (1 °C) overnight. After warming to r.t. the mixture was diluted with water (5 mL) and filtered; the solid was washed with water and then dissolved using a mixture of MeOH/DCM. Evaporation of the solvent yielded the crude product (white solid, 473 mg) that was column chromatographed using DCM as eluent (R_f 0.35). NMR analysis on the purified compound (417 mg) showed about 10% of cis- signal. Recrystallization from boiling EtOH (45 mL) yielded the title compound with 97% purity, as estimated by ^{1}H NMR (white needles, 279 mg, 0.52 mmol, yield 55%). **M_p** 148-150° C (from EtOH). **GC**: not applicable.

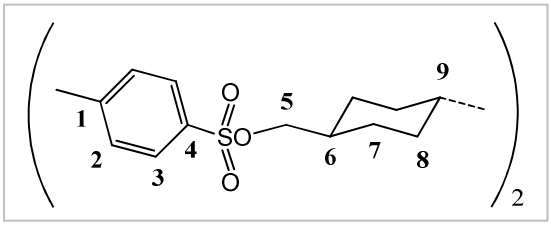

^{1}H NMR (300 MHz, $CDCl_3$): δ 7.77 (4H, d, *J* = 8.4, **c**), 7.33 (4H, d, *J* = 7.8, **2**), 3.79 (4H, d, *J* = 6.6, **5**), 2.44 (6H, s, **Me**), 1.74-1.67 (8H, m, **7/8**), 1.60-1.50 (2H, m, **6**), 0.99-0.80 (10H, m, **7/8** and **9**). **^{13}C NMR** (75 MHz, $CDCl_3$): δ 144.72 (2C, **4**), 133.31 (2C, **1**), 129.91 (4CH, **2/3**), 128.01 (4CH, **2/3**), 75.49 ($2CH_2$, **5**), 42.89 (2CH, **6**), 37.56 (2CH, **9**), 29.37 ($4CH_2$, **7/8**), 29.12 ($4CH_2$, **7/8**), 21.80 ($2CH_3$, **Me**). **LRMS** (ZMD ESI$^+$): *m*/*z* 557 ([M+Na]$^+$, 100%). **IR** (film): 2429 (w), 2911, 2847 (m, CH stretch), 1599, 1448 (w), 1338 (s), 1308, 1187 (m), 1172 (s), 1096 (m), 949 (s), 832, 813, 775 (s), 707 (w), 665 (s), 548 (s) cm^{-1}.

Trans,trans-S,S'-bi(cyclohexane)-4,4'-diylbis(methylene)diethanethioate (52). Following a procedure reported by Whistler[85], the bis-tosylate **51** (279 mg, 0.52 mmol) was dissolved in 6 mL of acetone. Potassium thiolacetate (154 mg, 1.35 mmol, 2.60 eq.) was added, and the suspension was heated to reflux temperature (70 °C) and stirred overnight. The resulting orange suspension was let cooling to r.t. and filtered; the white residue (TosK) was washed with Et_2O (25 mL); the joined organic phases were washed with brine twice (25 mL) and dried over $MgSO_4$. Evaporation of the solvent yielded the crude title compound (yellow solid, 161 mg, 0.47 mmol, yield 90%) that showed satisfactory purity by TLC (R_f 0.62 in 2/1 Et_2O/hexane, UV 254 nm), GC (SD_FASTD, retention time 7.75 min) and NMR analysis. This was dissolved in a small volume of DCM, treated with decolourizing charcoal and filtered; after evaporation a light yellow colour still persisted. Part of the material (74 mg) was recrys-tallized from hot EtOH (5 mL) yielding the pure title compound (white needles, 45 mg, rcr yield 60%). **M_p** 110-112° C (from EtOH). **^{1}H NMR** (300 MHz, $CDCl_3$): δ 2.76 (4H, d, *J* = 6.6, **CH_2**S), 2.31 (6H, s, **Me**CO), 1.82-1.78 (4H, m, **CH_2**$CHCH_2$ eq.), 1.71-1.68 (4H, m, **CH_2**$CHCH_2$ ax.), 1.42-1.30 (2H, m,**CHCH**), 0.99-0.85 (8H+2H, m, **CH_2**CHCH eq. + ax. and CH_2**CH**CH_2). **^{13}C NMR** (75 MHz, $CDCl_3$): δ 196.15 (2C, **CO**), 42.95 (2CH, **CHCH**), 38.28 (2CH, CH_2**CH**CH_2), 36.04 ($2CH_2$, **CH_2**S), 32.77 ($4CH_2$, **cHex**), 30.79 ($2CH_3$, **Me**), 29.71 ($4CH_2$, **cHex**). **LRMS** (GCEI): *m*/*z* 342.8 ([M$^+$], 14%). **IR** (film): 3357 (w), 2956, 2915, 2843 (m, CH stretch), 1682 (very s, C=O stretch), 1652, 1433, 1353, 1262 (m), 1130, 1100, 971 (s), 801, 745 (m), 624 (s) cm^{-1}. **Anal**. Calcd. For $C_{18}H_{30}O_2S_2$: C: 63.1; H: 8.8; S: 18.7 %. Found: C: 63.1; H: 8.8; S: 18.5 %. **XR**: the structure was confirmed by X-ray crystallography[125].

EXPERIMENTAL SECTION (2): DAFP.

Directed Assembly of Functional Patterns: supplementary informations on materials, instruments and apparatus described in Chapters 3 and 4.

Materials.

EDOT and TTF, Na p-toluensulfonate, $LiClO_4$ and TBAB were purchased from Aldrich. Solvents were purchased from Fisher: analytical grade MeCN and IPA were employed. Materials and solvents were used without further purification, exception made for DMF that was distilled (and deaerated). Water was microfiltered and deionized. MWNTs were purchased from MER (two types: MRCSD, diameter 140 +/- 30 nm, length 7 +/- 2 μm; MRCMW, diameter 35 +/- 10 nm, length ~ 30 μm; dimensions as reported by the producer) and employed without further purification; they were suspended in the solvent of choice (neat MeCN or MeCN/ H_2O) by ultrasonication.

Microelectrode arrays.

MEAs with mm-scale interelectrode separation were produced by embedding Pt wires (from Aldrich) in different substrates and consecutively grounding / polishing the exposed cross-sections of the wires to produce disc microelectrodes. Two arrays were produced as single units and repeatedly used for different experiments; after each experiment the electrodes and the substrate surface where washed with IPA, polished with sanding paper (2000), washed with IPA again. Two of these MEAs have been reported here: **A**, substrate Teflon, Pt wire diameter 250 μm, 2-electrode array with ~ 2 mm separation; **B**, substrate glass, Pt wire diameter 127 μm, 4-electrodes square-array with ~ 1 mm gaps (produced in collaboration with the Glassblowing Workshop of the University of Southampton).

MEAs with μm-scale interelectrode gaps were produced in collaboration with external contractors; conventional optical lithography techniques were employed for the deposition of the metal structures and the insulating resist on SiO_2/Si substrates.
The 40-electrode array produced by Innos Ltd. featured 4 line-arrays (10 electrodes each, Au on Ti) along the sides of a ~ 100 x 100 μm^2 square platform defined by the overlaying resist (SU8, organic resist); square microelectrodes with 5 μm side and 10 μm pitch formed the line-arrays. The whole device measured 1 cm^2.

The 20-electrode arrays produced by J. Gardner (Warwick) featured 4 line arrays (5 electrodes each, Au or Pt) along the sides of a 67 x 67 μm^2 square platform defined by the overlaying resist (Si_3N_4, inorganic resist); square electrodes with 6 μm side and 9 μm pitch formed the line arrays. The whole device measured 0.25 cm^2.

Solvent chambers.

When using the mm-scale MEA (A or B) a solvent chamber was obtained by clamping the device against a glass microscope slide (well-type) with the concavity pre-filled with ~ 0.2 mL of solution (excess solution was used to prevent the trapping of air bubbles); by de-centering the electrodes array with respect to the center of the well (during the mounting procedure) the bubbles produced during the experiment were allowed to drift away from the optical path (sometimes tapping was employed to speed up the process).

When using the μm-scale MEA a solvent chamber was obtained by depositing a square-ring (silicone) onto the device and filling its bore with (excess) solution; a decent seal was obtained by lightly pressing a fragment of glass cover slide (thickness ~ 0.1 mm) onto the gasket. While the maximum thickness of the ring was fixed at 0.5 mm (maximum height of the column of solvent allowing microscopic observation), its maximum diameter and bore size where determined by the overall size of the MEA device: on the 0.25 cm^2 devices (20-electrode) gaskets with 3 mm OD and 1 mm ID were used, resulting in a maximum volume of ~ 0.4 μL (1 μL was the minimum volume deliverable by micropipette, which resulted in an hemispherical droplet protruding out of the ring; the excess solvent was flushed out during the deposition of the cover slip); different size gaskets, allowing to employ larger volumes (up to 5 μL), were used on the 1 cm^2 device (40-electrode).

One essential requirement of this method of creating a temporary solvent chamber is to use completely grease- and dust-free components: both the devices and the gaskets where ultrasonicated in acetone prior to the assembly (the silicone gaskets for about 1 s) and dried using filtered compressed air; the seal usually held for a time varying from few minutes to half an hour, and when it failed the leaking typically occurred at the cover slip-gasket junction.

The siliconic gaskets were produced via a two step method using Sylgard 184 silicone elastomer kit: (1) the base elastomer and the curing agent were mixed in ratio 10/1, sandwiched between two polished (μm-sized alumina powder) Teflon slabs, and

left curing for 3 days at r.t.; the use of Teflon spacers (0.53 mm thick) allowed for the production of a smooth silicone sheet with reproducible thickness; (2) metal tubes of two different diameters (from a radio antenna) were used to pierce the silicone sheet (against a glass slide), producing the required square-ring gaskets.

Microscopes.

Videos and snapshots were acquired using different optical microscopes for the two types of MEA employed (mm- and μm-scale gaps).

For the mm-scale MEA an IntelPlayQX3 computer microscope (magnification 10, 60 or 200X) was used. The assembled solvent chamber was mounted onto the stage by using a pressure-sensitive polymer (Blu-Tack type); this also allowed adjusting the position of the MEA during the observation.

When the probe station was produced, a zoom microscope with long working distance objective was used for optical observation of the μm-scale MEA while this was connected to the electrical instrumentation. The microscope was mounted on the probe station via three stacked micro-positioning stages that allowed full spatial control: x- and y-stages with 15 mm travel (0.5 mm per knob rotation) and a z-stage with 10 mm travel (0.5 mm per knob rotation, 5 Kg load capacity) were used. The microscope was composed of a Mitutoyo objective M Plan Apo (0.55 NA, 50X PMAG, 13 mm WD), a Mitutoyo coaxial focusable objective adapter, and pre-assembled precision zoom lenses (25-170 μm FOV range when assembled in this system; maximum zoom 7X); a TV tube (2X) and a ½ inch progressive scan CMOS monochrome camera (1280 x 1024 pixels, sensor size 6.6 x 5.3 mm^2, pixel depth 8-bit, max acquisition rate 25 fps, video output USB 2.0) were employed for digital acquisition of the visual data; an optical fiber illuminator (Dolan-Jenner MI-150) and a coaxial adaptor (mounted between the objective adapter and the zoom tube) provided coaxial illumination. Tremble-free videos and images were obtained by placing the whole probe station on a vibration isolation platform (50BM-6 from Minus K Technology); a further reduction in vibrational noise resulted from placing the (fan-cooled) illuminator onto a wall-mounted shelf.

Probe station.

Two Aluminium breadboards (15 mm thick) were mounted in a two-level assembly by using four steel posts; post holders were used to secure the posts, which

were leveled by resting on four identical steel balls placed inside the holders. The top breadboard was adapted to mount the probe cards, which were fitted on its lower face. Four stacked micro-positioning stages were mounted onto the bottom breadboard and used to align the MEA device with the probe card and electrically connect the two: a x-stage with 125 mm travel (18 mm per knob rotation), a y-stage with 15 mm travel (0.5 mm per knob rotation) and a θ-stage (total fine rotation 10°) were used for alignment, with the help of a monocular microscope (25X PMAG, 63 mm WD, 10 mm FOV); a z-stage with 5 mm travel (0.5 mm per knob rotation, 3 Kg load capacity) was used to create electrical contact between the probes and the pads on the MEA device.

The whole system (probe station, microscopes and anti-vibration platform) was placed inside a welded Aluminium Faraday cage (sheet thickness 3 mm; earthed) to effectively shield the probe card from EMI interferences; a removable panel (3 mm thick Al) fitted with handles and four latches allowed access to the system; electrical continuity in the enclosure was ensured by fitting a conductive gasket seal onto the access panel. The microscope camera was typically unplugged when performing low-noise electrical measurement.

NOTE: Micro-positioning stages, microscopes (except the IntelQX3), illuminator and structural components (breadboards, posts, holders, etc.) were purchased from Edmund Optics. Some of the components (top breadboard, z-stage mounting plate, microscope mount) were adapted in the Mechanical Workshop (Dept. of Chemistry, University of Southampton).

Probe cards and connectors.

Two custom-made probe cards were acquired from SV Probe, Inc. and used for connecting the differently sized MEA devices.

To connect the 40-electrodes MEA (device size 1 cm^2), a card with the following characteristics was used: 40 probes (Be/Cu, epoxy-fixed), flat tip; probe force 1.5 g/mil overdrive; PCB electrical characteristics: allowable leakage 10 nA, contact resistance 4 Ohm, forcing voltage 5 V, forcing current 20 mA. The simple cables used initially were subsequently shielded to reduce EMI-induced noise (using tin foil as a common shield; see Chapter 3, Figure 28). Automatic switching was not available at the time this card was employed: a breadboard for circuit testing (spring

clips 2.54 mm pitch, Au plated Ag-Ni alloy, R < 1 mΩ) and manual switching of short, rigid, jumper wires (Cu) allowed to address different electrodes (or sets of) without disturbing the cables connected to the card or the instruments. The Faraday cage had not yet been produced when this card was used; still a p-p noise of only 0.25 nA (open circuit) was achieved by shielding / grounding the cables and the probe station.

Successively the 40-electrodes device was dismissed and only the 20-electrodes MEA (device size 0.25 cm^2) was employed; this was connected using a 'LLPC blade card' with the following characteristics: 20 probes (Be/Cu, flat tip), mounted on shielded ceramic blades; coaxial cables soldered directly onto the blades; electrical characteristics: contact resistance, forcing voltage, forcing current and probe force were not provided; the producer could not guarantee for the absence of leaking current smaller than 10 nA at 10 V DC. Electrical testing (source to line, drain to PCB backplane) highlighted the presence of short circuits on some lines: some of these could be located and mechanically broken; the rest (very low leaking, few pA at 1 V DC) was found to degrade spontaneously during repeated use, until no difference could be observed in the insulation resistance on different lines (typically higher than 1 TΩ).

A spring-socket connector (custom-made by Aries Electronics) was also used as an alternative method of connecting the 20-electrode MEA (see Chapter 3, Figure 24). The socket was made in chemically resistant material (Ultem) and mounted twenty spring-loaded crown tips (Au-plated Be-Cu). A PCB, custom-designed by P. Kapetanopoulos, was used to increase the separation between the lines and provide soldering points for the coaxial cables; the connector was mounted onto the PCB by mean of 4 nylon screws (and bolts). The connector alone was sufficient to address the device, resulting in a much more practical method of connection (no need for probe station and micro-positioning); when needed, a mounting plate could be used to fix the socket onto the station so to reduce vibration-induced noise (triboelectric effects). Despite the fact that microscopic observation was in principle possible (long WD objective with coaxial illumination), this kind of connector allowed only the assembly of larger capacity solvent chambers: a piece of Teflon tubing (2 cm long and 3 mm OD) served as the chamber, which could accommodate a wire electrode, and a silicone gasket similar to that previously described served as the seal; other than being used for some experiments in solution (as an example see Chapter 3, Figure 30), this

connector served mostly to allow higher throughput during the electrical testing of conductive networks in air.

Both 20-pin cards mounted 50 cm long coaxial cables (RG174) fitted with SMB connectors. Identical wires (with oppositely mating connector) extended these to the Keithley system or to the breadboard; in the case of the MMA oppositely mating connectors were mounted directly onto the instrument, resulting in shorter connections (most of which inside the Faraday cage).

Electrical instrumentation.

Preliminary testing of the MEA devices (from Innos) was carried out using a Semiconductor Parameter Analyzer (Agilent 4155C), a probe station and a Faraday cage in the Rapid Prototyping Facility of the Dept. of Physics (University of Southampton).

A signal generator (PCG10/8016 from Velleman) and a digital multimeter (UT70B from UNI-T; max. current 400 μA on the most sensitive range, resolution 0.1 μA) were used respectively as the source of potential and the current measuring device in some experiments. Both instruments were PC-controlled using the software provided by the producers.

The experiments on the 20-electrode MEA were run using prevalently automated switching, as provided by the Keithley 3706 System Switch Multimeter: this was equipped with a 3721 dual 1 x 20 multiplexer card and could be PC-controlled using tsp code and a GPIB interface. When this system was not connected to other sources of potential, the Keithley 2636 dual Source Monitor Unit was used to apply / measure voltage or current: this configuration (Keithley-only instruments connected in series) was the most used for the electrical characterization of the materials produced (see sub-Section 3.4.1 for details and performance). The wiring configuration of the Keithley 2636-3706-3721 system and scripts (.tsp) for automatic scanning routines are reported at the end of this section.

The home-built MMAs, controlled using hardware from National Instruments (DAQ PCI 6229 and 6703; see sub-Section 3.4.2), were designed in collaboration with and assembled by P. Kapetanopoulos. The DAQ cards were operated using a LabVIEW software interface, initially developed by P. Kapetanopoulos and later optimized by us; LabVIEW code and interface for controlling the MMA are reported

at the end of this section; code for experiments run using only the NI DAQ 6229 card is also reported.

Wiring configuration of the 3721 connectors (a) and circuit diagram of the 2636-3721 testing apparatus with individually addressable channels (b).

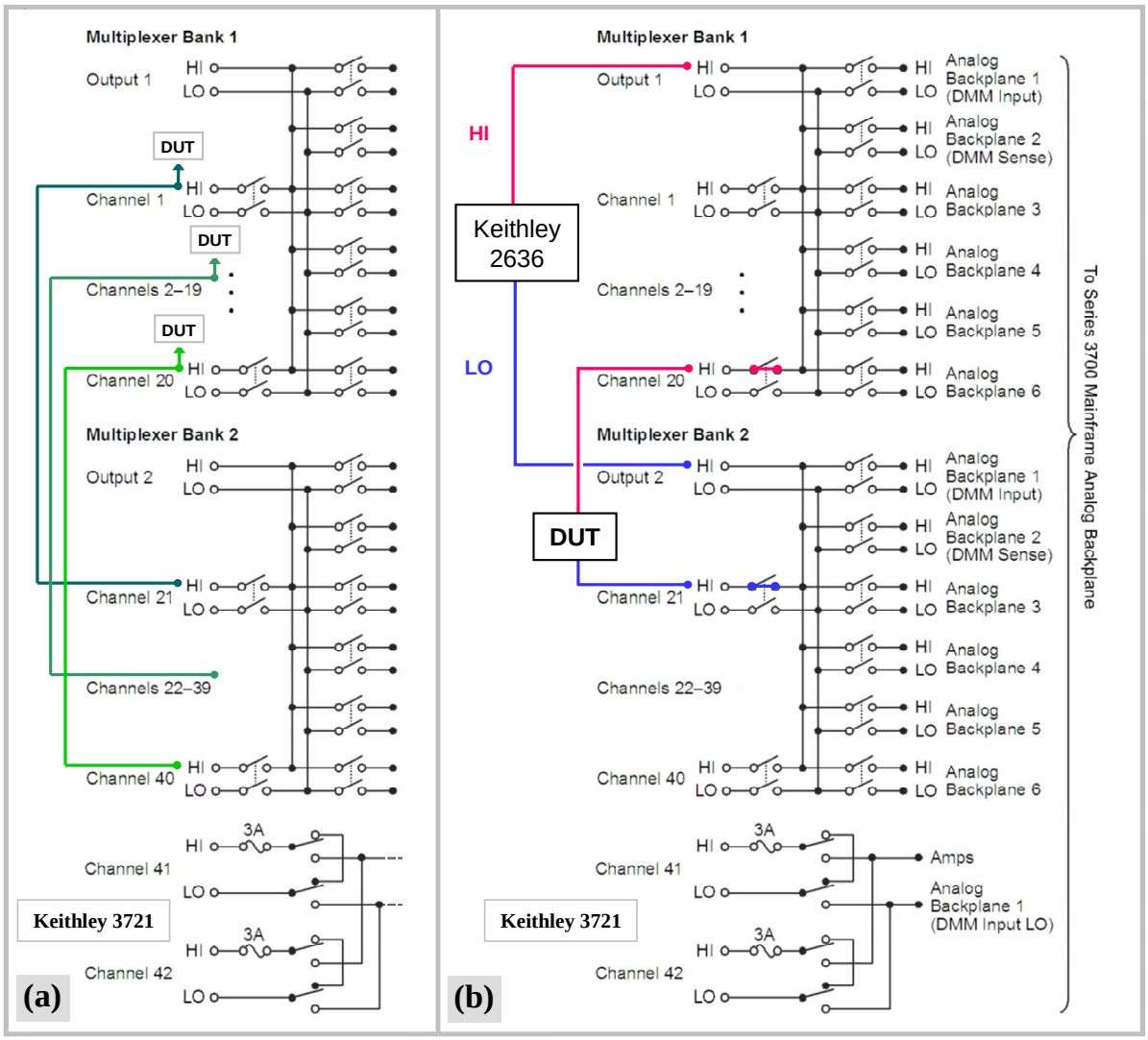

(a) The Keithley 3721 is a dual 20-channel multiplexer card controlled via the Keithley 3706 System Switch. Channels 1-20 on Bank 1 are connected to the 20 measurement lines (DUT, i.e. the MEA) and to the correspondent channels on Bank 2.

(b) One SMU channel on the Keithley 2636 (HI and LO) is used for measuring across any combination of two electrodes or electrode arrays (max. array size 19 electrodes). Measurements are only possible between Bank 1 and Bank 2 channels

(examples: with the switching configuration in the diagram MEA set 20-1 is under test; to measure MEA set 1-2, channels 1 and 22 are switched closed).

General DC scan routine (node[1], Keithley 2636; node[2], Keithley 3706 with a 3721 card; 'DCall_switch.tsp': it scans the 190 combinations of 2-electrode sets in a 20-electrode system).

```
--tsplink.reset() initializes the 2636-3706 connection
smua.reset()
smua.nvbuffer1.clear()
readingbuffer=smua.nvbuffer1
smua.source.func=smua.OUTPUT_DCVOLTS
smua.source.levelv=0.1
smua.measure.nplc=1
--smua.measure.rangei=1e-9
smua.measure.autorangei=smua.AUTORANGE_ON
smua.source.limiti=1e-3
smua.source.output=smua.OUTPUT_ON
smua.nvbuffer1.appendmode = 1
smua.measure.count=50
--smua.measure.autozero=smua.AUTOZERO_ONCE
--smua.measure.rel.enablei=smua.REL_ON
for e1 = 1,19 do
relay1 = 1000+e1
relay1txt=tostring(relay1)
node[2].channel.close(relay1txt)
for e2 = e1+1,20 do
relay2 = 1020 + e2
relay2txt = tostring(relay2)
node[2].channel.close(relay2txt)
smua.measure.i(smua.nvbuffer1)
print(relay1txt,  relay2txt, "&&")
printbuffer(1,50,readingbuffer)
smua.nvbuffer1.clear()
node[2].channel.open(relay2txt)
end
node[2].channel.open(relay1txt)
end
smua.source.output=smua.OUTPUT_OFF
```

Assembly routine used for the experiment in Figure 45 (Keithley 2636-3706-3721; ‘PulseTestSwitch3.tsp’, here configured for addressing set 1-2).

```
--tsplink.reset() initializes the 2636-3706 connection
--timer.reset() to be given manually when the video starts
smua.reset()
smua.measure.nplc=1
smua.measure.autozero=smua.AUTOZERO_ONCE
smua.nvbuffer1.appendmode=1
smua.source.limiti=1e-3
smua.measure.rangei=1e-8
--
node[2].channel.exclusiveclose("1001,1022")
smua.source.output=smua.OUTPUT_ON --this not in the loop as the output stays on after the second DC cycle
print(timer.measure.t())
for n=1,5 do
smua.nvbuffer1.clear()
smua.source.levelv=1
smua.measure.count=10
smua.measure.i(smua.nvbuffer1)
printbuffer(1,10,smua.nvbuffer1)
--
smua.nvbuffer1.clear()
PulseVMeasureI(smua, -3, 3, 0.05,0.05, 5)
printbuffer(1,5,smua.nvbuffer1)
--
smua.nvbuffer1.clear()
smua.source.output=smua.OUTPUT_ON --this needs to be here because the PulseVMeasureI function switches the output off on completion
smua.source.levelv=1
smua.measure.count=10
smua.measure.i(smua.nvbuffer1)
printbuffer(1,10,smua.nvbuffer1)
end
--
node[2].channel.open("1001,1022")
smua.source.output=smua.OUTPUT_OFF
smua.nvbuffer1.clear()
```

Switching routine used for the experiments in Figures 57 and 60 (Keithley 3706-3721 and Velleman signal generator; ‘DC single_switch_tstamped_Measure I only.tsp’, here configured for ten assembly loops).

```
--tsplink.reset() initializes the 2636-3706 connection
smua.reset()
smua.nvbuffer1.clear()
smua.measure.nplc=1
smua.measure.autorangei=smua.AUTORANGE_ON
--smua.measure.rangei=10e-6
smua.source.limiti=1e-3
smua.nvbuffer1.appendmode=1
smua.nvbuffer1.collecttimestamps=1 --tstamps are relative to the basetimestamp, in seconds since the unit is powered up
smua.nvbuffer1.timestampresolution=0.0001 --0.1 ms resolution adequate because at 1PLC each reading should take ~ 20 ms
smua.measure.count=1000
--
for n= 1,10 do
node[2].channel.exclusiveclose("1003,1008,1033,1038")
--
--delay(20)
smua.measure.i(smua.nvbuffer1)
--
node[2].channel.open("1003,1008,1033,1038")
printbuffer(1,1000,smua.nvbuffer1)
printbuffer(1,1000,smua.nvbuffer1.timestamps)
smua.nvbuffer1.clear()
delay (1)
end
smua.nvbuffer1.clear()
```

Assembly routine used for the experiment in Figures 70 and 72 (Keithley 2636-3706-3721; ‘Sweep test_switch_3.tsp’).

```
--tsplink.reset() initializes the 2636-3706 connection
smua.reset()
smua.nvbuffer1.clear()
smua.source.func=smua.OUTPUT_DCVOLTS
smua.measure.nplc=1
--smua.measure.rangei=100e-9
smua.measure.autorangei=smua.AUTORANGE_ON
smua.source.limiti=1e-3
smua.nvbuffer1.appendmode = 1
smua.source.output=smua.OUTPUT_ON
--smua.measure.autozero=smua.AUTOZERO_ONCE
--smua.measure.rel.enablei=smua.REL_ON
for e1 = 1,19 do
relay1 = 1000+e1
relay1txt=tostring(relay1)
node[2].channel.close(relay1txt)
for e2 = e1+1,20 do
relay2 = 1020 + e2
relay2txt = tostring(relay2)
node[2].channel.close(relay2txt)
print(relay1txt,  relay2txt, "&&")
for n=1,3 do
timer.reset()
SweepVLinMeasureI(smua, 0,5, 0.01, 101)
printbuffer(1,101,smua.nvbuffer1)
print(timer.measure.t())
timer.reset()
SweepVLinMeasureI(smua, 5,0, 0.01, 101)
printbuffer(1,101,smua.nvbuffer1)
print(timer.measure.t())
end
smua.nvbuffer1.clear()
node[2].channel.open(relay2txt)
end
node[2].channel.open(relay1txt)
end
smua.source.output=smua.OUTPUT_OFF
```

MMA software interface: LabVIEW Front Panel for ‘BOXSW_15.1.09_fra12B.vi’. It allows control of the 16 ao (NI 6703 DAQ) and 4 ao (NI 6229 DAQ) channels with a seamless interface; 20 ai channels (NI 6229 DAQ) are used to monitor the potential. It controls relays for channel(s) and measurement range selection. It was employed to acquire the data shown in Figures 30, 31, 33.

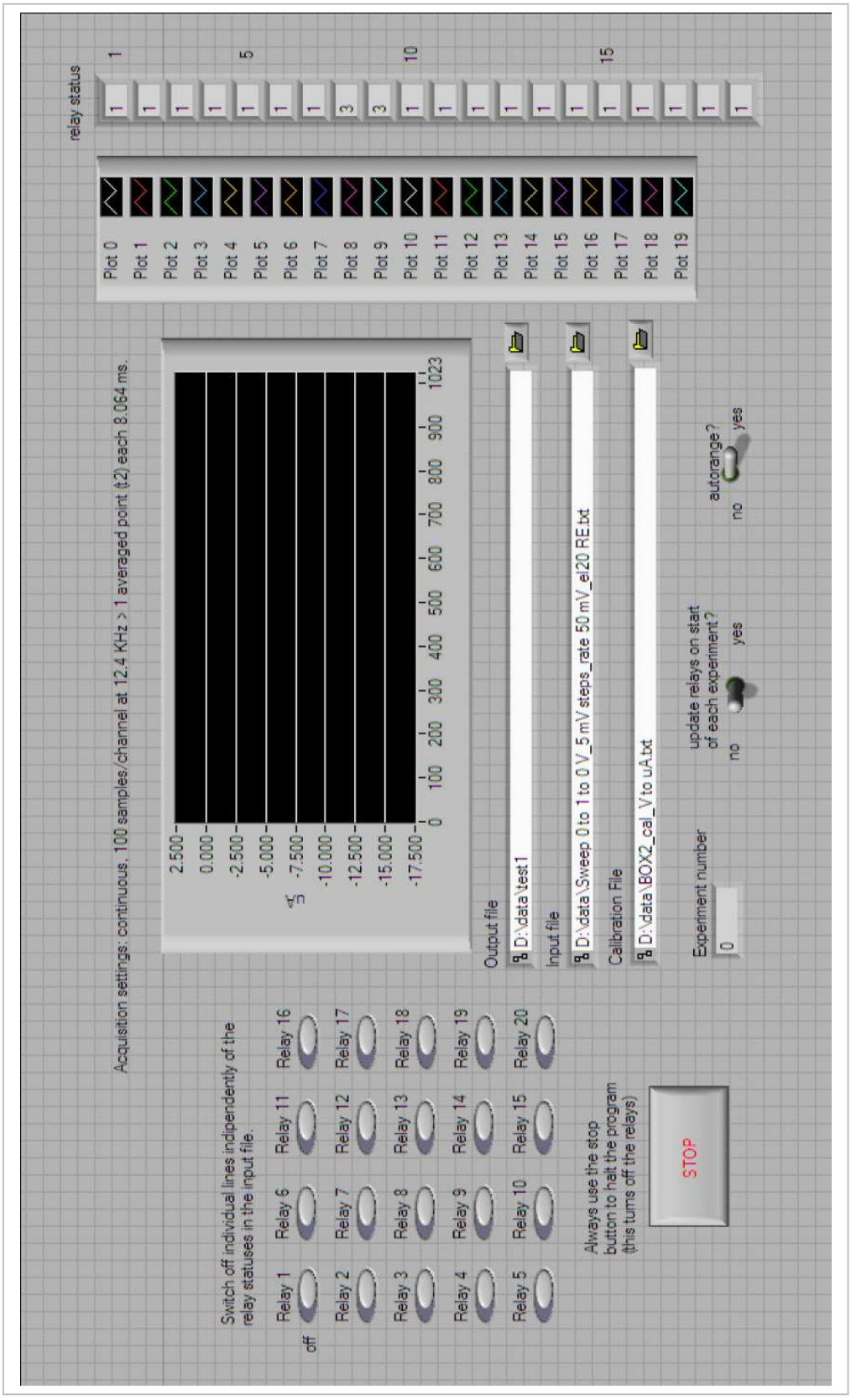

LabVIEW code: Block Diagram (left) for ‘BOXSW_15.1.09_fra12B.vi’.

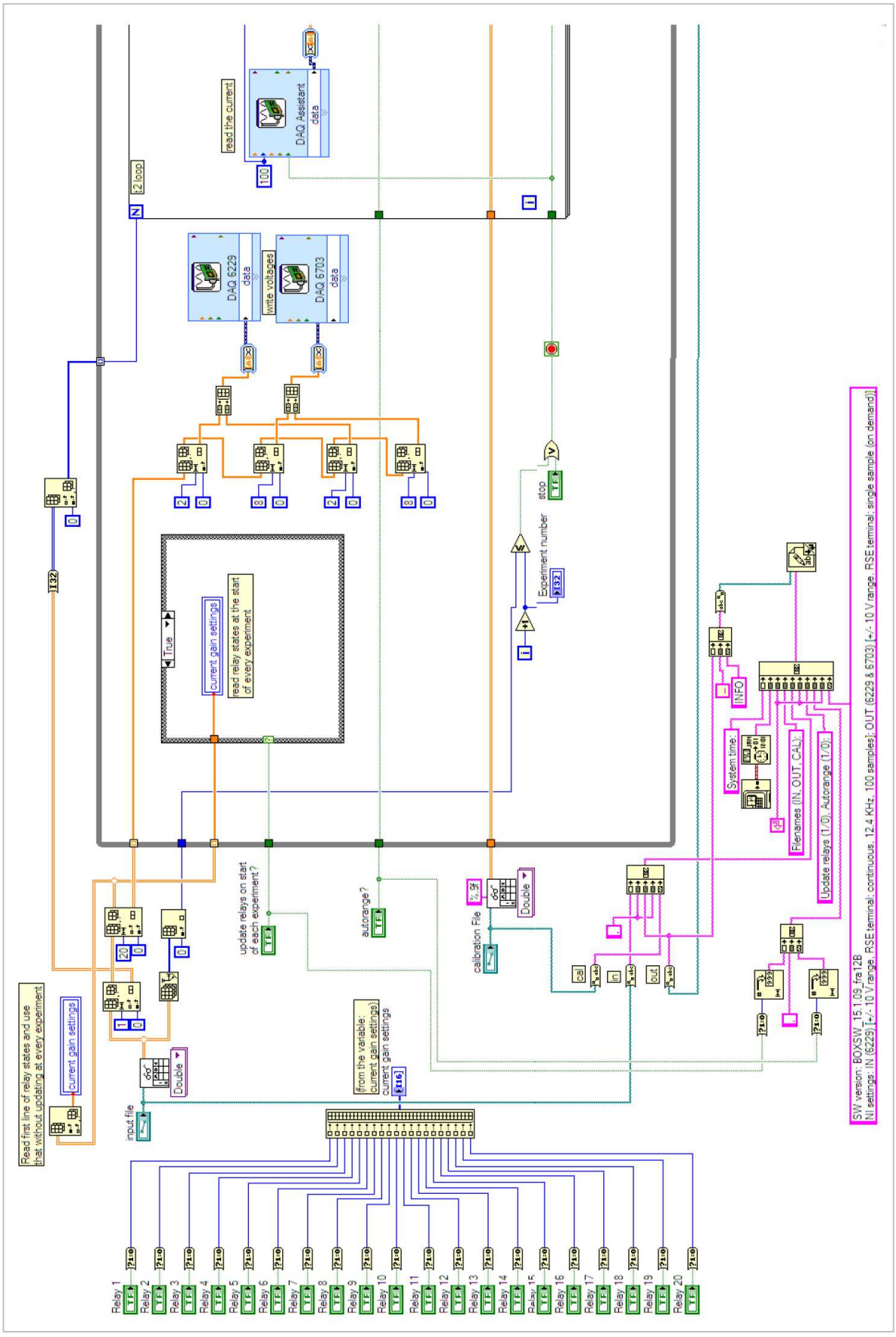

LabVIEW code: Block Diagram (right) for ‘BOXSW_15.1.09_fra12B.vi’.

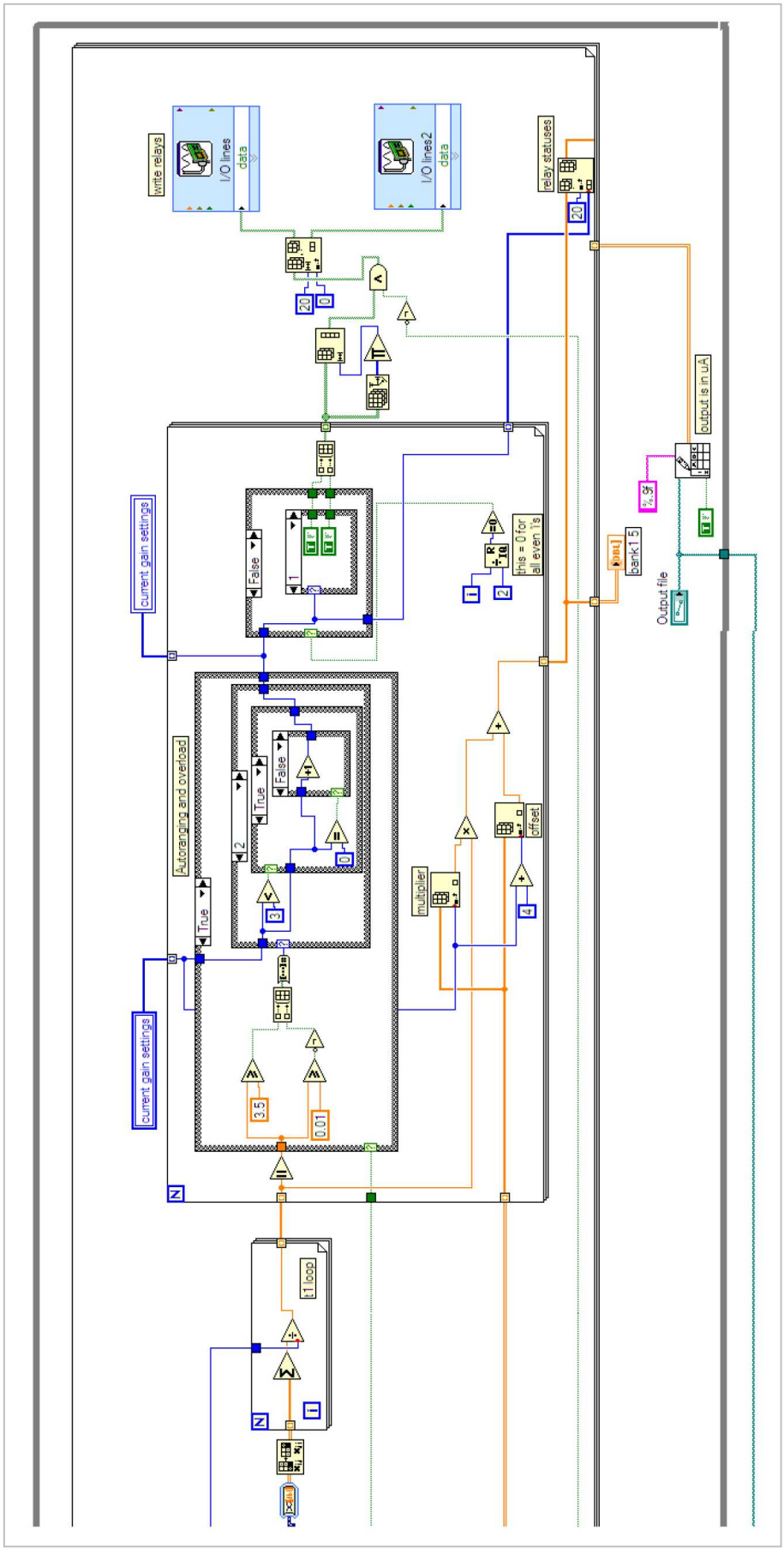

MMA software interface and code: LabVIEW Front Panel and Block Diagram for '4 channels sine generator 6229_A2_timed.vi'. It allows to use the signal generator capabilities of the NI 6229 DAQ card (4 ao channels); when the max run time (ms) is reached or the STOP button is hit the signals are automatically zeroed.

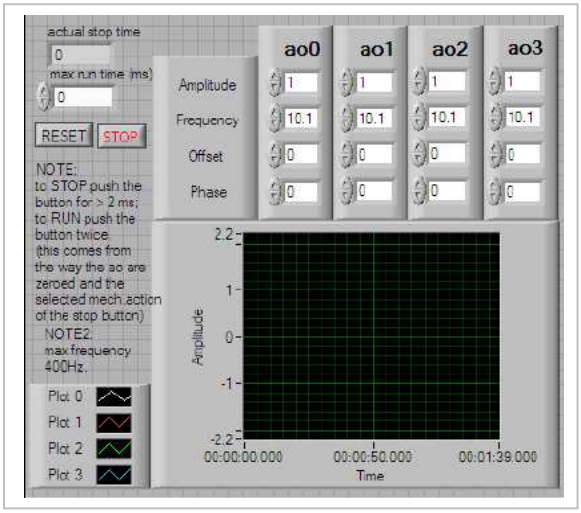

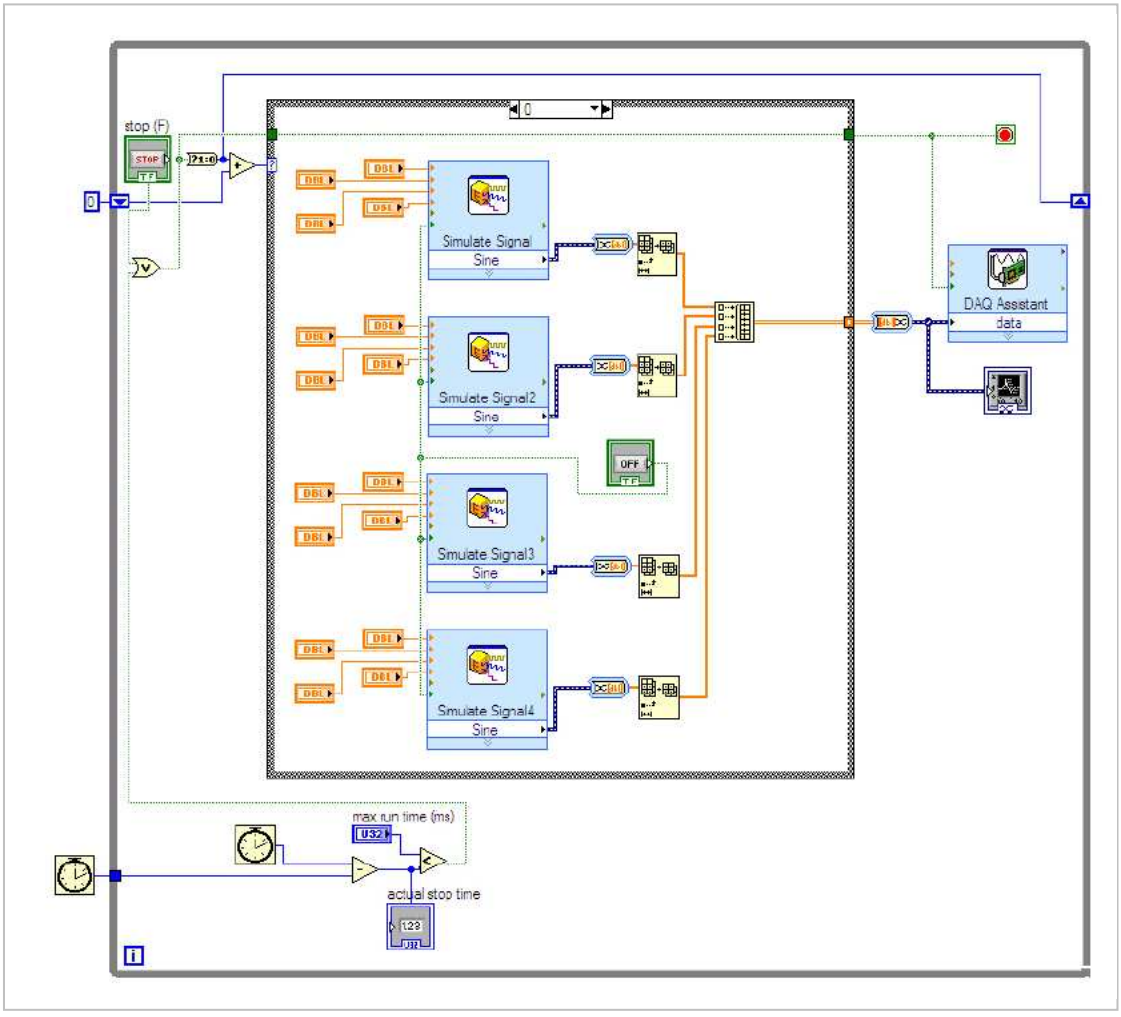

REFERENCES.

Chapter 1 – Introduction.

[1] : Feynman, R. P. *'There's plenty of room at the bottom'*. First published in *Engineering and Science* **1960**, 23, 13 pp.

[2] : Taniguchi, N. *Proc. Intl. Conf. Prod. London, part II, British Society of Precision Engineering* **1974**. *'On the Basic Concept of Nano-Technology'*.

[3] : Drexler, K. E. *'Nanosystems: Molecular Machinery, Manufacturing, and Computation'*. **1992**, John Wiley & Sons.

[4] : Aviram, A.; Ratner, M.A. *Chem. Phys. Lett*. **1974**, 29, 277-283.

[5] : (a) Shirakawa, H. *Synth. Met.* **2002**, 125, 3-10; (b) MacDiarmid, A. G. *Synth. Met.* **2002**, 125, 11-22; (c) Heeger, A. J. *Synth. Met.* **2002**, 125, 23-42.

[6] : Moriarty, P. *Rep. Prog. Phys.* **2001**, 64, 297-381.

[7] : Swalen, J. D.; Allara, D. L.; Andrade, J. D.; Chandross, E. A.; Garoff, S.; Israelachvili, J.; McCarthy, T. J.; Murray, R. ; Pease, R. F.; Rabolt, J. F.; Wynne, K. J.; Yu, H. *Langmuir* **1987**, 3, 932-950.

[8] : Chidsey, C. E. D.; Murray, R. W. *Science* **1986**, 231, 25-31.

[9] : Collier, C. P.; Wong, E. W.; Belohradsky, M.; Raymo, F. M.; Stoddart, J. F.; Kuekes, P. J.; Williams, R. S.; Heath, J. R. *Science* **1999**, 285, 391-394.

[10] : Sirringhaus, H.; Kawase, T.; Friend, R. H.; Shimoda, T.; Inbasekaran, M.; Wu, W.; Woo, E. P. *Science* **2000**, 290, 2123-2126.

[11] : Ashwell, G. J. ; Wierzchowiec, P. ; Bartlett, C. J.; Buckle, P. D. *Chem. Comm.* **2007**, (12), 1254-1256.

[12] : Liu, K.; Avouris, P.; Bucchignano, J. ; Martel, R. ; Sun, S. ; Michl, J. *Appl. Phys. Lett.* **2002**, 80, 865-867.

[13] : Kashimura, Y.; Nakashima, H.; Furukawa, K.; Torimitsu, K. *Thin Solid Films* **2003**, 438, 317-321.

[14] : Mahapatro, A. K.; Ghosh, S.; Janes, D. B. *IEEE Trans. Nanotechnol.* **2006**, 5, 232-235.

[15] : Park, H.; Lim, A. K.; Alivisatos, A. P.; Park, J.; McEuen, P. L. *Appl. Phys. Lett.* **1999**, 75, 301-303.

[16] : Khondaker, S. I.; Yao, Z. *Appl. Phys. Lett.* **2002**, 81, 4613-4615.

[17] : Gardner, C. E. ; Ghanem, M. A.; Wilson, J. W.; Smith, D. C. *Anal. Chem.* **2006**, 78, 951-955.

[18] : Lortscher, E ; Ciszek, J. W. ; Tour, J. ; Riel, H. *Small* **2006**, 2, 973-977.

[19] : Amlani, I.; Rawlett, A. M.; Nagahara, L. A.; Tsui, R. K. *Appl. Phys. Lett.* **2002**, 80, 2761-2763.

[20] : Xu, C.; van Zalinge, H.; Pearson, J. L.; Glidle, A.; Cooper, J. M.; Cumming, D. R. S.; Haiss, W.; Yao, J.; Schiffrin, D. J.; Proupin-Perez, M.; Cosstick, R.; Nichols, R. J. *Nanotech.* **2006**, 17, 3333-3339.

[21] : (a) Cui, X. D.; Primak, A.; Zarate, X. ; Tomfohr, J. ; Sankey, O. F. ; Moore, A. L.; Moore, T. A.; Gust, D.; Harris, G.; Lindsay, S. M. *Science* **2001**, 294, 571-574; (b) Morita, T.; Lindsay, S. *J. Am. Chem. Soc.* **2007**, 129, 7262-7263.

[22] : (a) Gittins, G. I.; Bethell, D.; Schiffrin, D. J.; Nichols, R. J. *Nature* **2000**, 408, 67-69; (b) Haiss, W.; Nichols, R. J.; Higgins, S. J.; Bethell, D.; Hobenreich, H.; Schiffrin, D. J. *Faraday Discuss.* **2004**,

125, 179-194; (c) Haiss, W.; Martin, S.; Leary, E.; van Zalinge, H.; Higgins, S. J.; Bouffier, L.; Nichols, R. J. *J. Phys. Chem. C* **2009**, 113, 5823-5833.

[23] : (a) Haiss, W.; van Zalinge, H.; Higgins, S. J.; Bethell, D.; Hobenreich, H.; Schiffrin, D. J.; Nichols, R. J. *J. Am. Chem. Soc.* **2003**, 125, 15294-15295; (b) Haiss, W.; Nichols, R. J.; van Zalinge, H.; Higgins, S. J.; Bethell, D.; Schiffrin, D. J. *Phys. Chem. Chem. Phys.* **2004**, 6, 4330-4337; (c) Haiss, W.; van Zalinge, H.; Hobenreich, H.; Bethell, D.; Schiffrin, D. J.; Higgins, S. J.; Nichols, R. J. *Langmuir* **2004**, 20, 7694-7702.

[24] : Haiss, W.; van Zalinge, H.; Bethell, D.; Ulstrup, J.; Schiffrin, D. J.; Nichols, R. J. *Faraday Disc.* **2006**, 131, 253-264.

[25] : Ashwell, G. J.; Urasinska, B.; Wang, C.; Bryce, M. R.; Grace, I.; Lambert, C. J. *Chem. Comm.* **2006**, (45), 4706-4708.

[26] : James, D. K.; Tour, J. M. *Chem. Mater.* **2004**, 16, 4423-4435.

[27] : (a) Tseng, G. Y. ; Ellenbogen, J. C. *Science* **2001**, 294, 1293-1294; (b) Ashwell, G. J.; Wierzchowiec, P.; Phillips, L. J.; Collins, C. J.; Gigon, J.; Robinson, B. J.; Finch, C. M.; Grace, I. R.; Lambert, C. J.; Buckle, P. D.; Ford, K.; Wood, B. J.; Gentle, I. R. *Phys. Chem. Chem. Phys.* **2008**, 10, 1859-1866.

[28] : (a) Slot, J. W.; Geuze, H. J. *Eur. J. Cell Bio.* **1985**, 38, 87-93; (b) Brust, M.; Walker, M.; Bethell, D.; Schiffrin, D. J.; Whyman, R. *J. Chem. Soc., Chem. Commun.* **1994**, (7), 801-802.

[29] : (a) Grabar, K. C.; Freeman, R. G.; Hommer, M. B.; Natan, M. J. *Anal. Chem.* **1995**, 67, 735-743; (b) Liu, S.; Maoz, R.; Schmid, G.; Sagiv, J. *Nano Lett.* **2002**, 2, 1055-1060; (c) Zhao, S.-Y.; Wang, S.; Kimura, K. *Langmuir* **2004**, 20, 1977-1979; (d) Schmid, G.; Simon, U. *Chem. Comm.* **2005**, (6), 697-710; (e) Bigioni,T. P.; Lin, X.-M.; Nguyen, T. T.; Corwin, E. I.; Witten, T. A.; Jaeger, H. M. *Nature Mater.* **2006**, 5, 265-270.

[30] : (a) Simard, J.; Briggs, C.; Boal, A. K.; Rotello, V. M. *Chem. Comm.* **2000**, (19), 1943-1944; (b) Galow, T. H.; Boal, A. K.; Rotello, V. M. *Adv. Mater.* **2000**, 12, 576-579; (c) Boal, A. K.; Ilhan, F.; DeRouchey, J. E.; Thurn-Albrecht, T.; Russel, T. P.; Rotello, V. M. *Nature* **2000**, 404, 746-748.

[31] : (a) Lindsey, J. S. *New J. Chem.* **1991**, 15, 153-180; (b) Huie, J. C. *Smart Mater. Struct.* **2003**, 12, 264-271; (c) Kovtyukhova, N.I.; Mallouk, T. E. *Chem. Eur. J.* **2002**, 8, 4355-4363.

[32] : (a) Jérôme, C.; Labaye, D.; Bodart, I.; Jérôme, R. *Synth. Met.* **1999**, 101, 3-4 ; (b) Demoustier-Champagne, S.; Ferain, E.; Jérôme, C.; Jérôme, R.; Legras, R. *Eur. Polym. J.* **1998**, 12, 1767-1774; (c) Choi, S.-J.; Park, S.-M. *Adv. Mater.* **2000**, 20, 1547-1549; (d) Hernández, R. M.; Richter, L. Semancik, S.; Stranick, S.; Mallouk, T. E. *Chem. Mater.* **2004**, 16, 3431-3438.

[33] : (a) Messmore, B. W.; Hulvat, J. F.; Sone, E. D.; Stupp, S. I. *J. Am. Chem. Soc.* **2004**, 126, 14452-14458; (b) Schenning, A. P. H. J.; Meijer, E. W. *Chem. Comm.* **2005**, 3245-3258 ; (c) Tang, Z.; Kotov, N. A.; Giersig, M. *Science* **2002**, 297, 237-240 ; (d) Tang, Z.; Kotov, N. A. *Adv. Mater.* **2005**, 17, 951-962.

[34] : (a) Huang, Y.; Duan, X.; Wei, Q.; Lieber, C. M. *Science* **2001**, 291, 630-633; (b) Huang, Y.; Duan, X.; Cui, Y.; Lauhon, L. J.; Kim, K.-H.; Lieber, C. M. *Science* **2001**, 294, 1313-1317; (c) Cui, Y.; Lieber, C. M. *Science* **2001**, 291, 851-853.

[35] : He, H.; Zhu, J.; Tao, N. J.; Nagahara, L. A.; Amlani, I.; Tsui, R. *J. Am. Chem. Soc.* **2001**, 123, 7730-7731.

[36] : Ramanathan, K.; Bangar, M. A.; Yun, M.; Chen, W.; Mulchandani, A.; Myung, N. V. *Nano Lett.* **2004**, 7, 1237-1239.

[37] : Shan, J.; Yuan, C.; Zhang, H. *Thin Solid Films* **1997**, 301, 23-27.

[38] : Curtis, C. L.; Ritchie, J. E.; Sailor, M. J. *Science* **1993**, 262, 2014-2016.

[39] : (a) Fujii, M.; Arii, K.; Yoshino, K. *Synth. Met.* **1995**, 71, 2223-2224; (b) Fujii, M.; Izawa, T.; Ohnishi, H.; Arii, K.; Yoshino, K. *Jpn. J. Appl. Phys.* **1996**, 35, 290-293; (c) Fujii, M.; Takahashi, N.; Ohnishi, H.; Yoshino, K. *Synth. Met.* **1997**, 85, 1409-1410; (d) Fujii, M.; Takahashi, N.; Ihori, H.; Arii, K.; Yoshino, K. *Synth. Met.* **1999**, 101, 397-398 ; (e) Fujii, M.; Ihori, H.; Arii, K.; Onoda, M. *Synth. Met.* **2001**, 119, 483-484 ; (f) Fujii, M.; Ihori, H.; Arii, K. *Thin Solid Films* **2001**, 393, 393-398; (g) Fujii, M.; Kushida, K.; Ihori, H.; Arii, K. *Thin Solid Films* **2003**, 438 - 439, 356-359; (h) Fujii, M.; Abe, S.; Ihori, H. *Synth. Met.* **2005**, 152, 41-44.

[40] : Hibbert, D. B.; Melrose, J. R. *Proc. R. Soc. Lond. A* **1989**, 423, 149-158.

[41] : Mogi, I.; Kamiko, M.; Okubo, S. *Phys. B* **1995**, 211, 319-322.

[42] : Bradley, J.-C.; Chen, H.-M.; Crawford, J.; Eckert, J.; Ernazarova, C.; Kurzeja, T.; Lin, M.; McGee, M.; Nadler, W.; Stephens, S. G. *Nature* **1997**, 389, 268-271.

[43] : Ural, A.; Li, Y.; Dai, H. *Appl. Phys. Lett.* **2002**, 81, 3464-3466.

[44] : (a) Hermanson, K. D.; Lumsdon, S. O.; Williams, J. P. ; Kaler, E. W.; Velev, O. D. *Science* **2001**, 294, 1082-1086; (b) Bhatt, K. H.; Velev, O. D. *Langmuir* **2004**, 20, 467-476; (c) Kretschmer, R.; Fritzsche, W. *Langmuir* **2004**, 20, 11797-11801; (d) Bernard, L.; Calame, M.; van der Molen, S. J.; Liao, J.; Schonenberger, C. *Nanotech.* **2007**, 18, 235202 (6pp).

[45] : Lumsdon, S. O.; Scott, D. M. *Langmuir* **2005**, 21, 4874-4880.

[46] : Chen, J.; Reed, M. A.; Asplund, C. L.; Cassell, A. M.; Myrick, M. L.; Rawlett, A. M.; Tour, J. M.; Van Patten, P. G. *Appl. Phys. Lett.* **1999**, 75, 624-626.

[47] : (a) Tour, J. M. *'Molecular Electronics: Commercial Insights, Chemistry, Devices, Architecture and Programming'* **2003**, World Scientific Publishing Co; (b) Tour, J. M.; van Zandt, W. L.; Husband, C. P.; Husband, S. M.; Wilson, L. S.; Franzon, P. D.; Nackashi, D. P. *IEEE Trans. Nanotech.* **2002**, 1, 100-109; (c) Husband, C. P.; Husband, S. M.; Daniels, J. S.; J. M. Tour *IEEE Trans. Electron Devices* **2003**, 50, 1865-1875; (d) Tour, J. M.; Cheng, L.; Nackashi, D. P.; Yao, Y.; Flatt, A. K.; St. Angelo S. K.; Mallouk, T. E.; Franzon, P. D. *J. Am. Chem. Soc.* **2003**, 125, 13279-13283; (e) Nackashi, D. P.; Di Spigna, N. H.; Winick, D. A.; Amsinck, C. J.; Cheng, L.; Tour, J. M.; Franzon, P. D. *NSTI Nanotech.* **2004**, 3, 45-48; (f) Seminario, J. M.; Ma, Y.; Agapito, L. A.; Yan, L.; Araujo, R. A.; Bingi, S.; Vadlamani, N. S.; Chagarlamudi, K.; Sudarshan, T. S.; Myrick, M. L.; Colavita, P. E.; Franzon, P. D.; Nackashi, P. D.; Cheng, L.; Yao, Y.; Tour, J. M. *J. Nanosc. Nanotech.* **2004**, 4, 907-917.

[48] : (a) Tour, J. M.; Jones, L. II, Pearson, D. L. ; Lamba, J. J. S. ; Burgin, T. P. ; Whitesides, G. M.; Allara, D. L.; Parikh, A. N.; Atre, S. V. *J. Am. Chem. Soc.* **1995**, 117, 9529-9534; (b) Andres, R. P.; Bein, T.; Dorogi, M.; Feng, S.; Henderson, J. I.; Kubiak, C. P.; Mahoney, W.; Osifchin, R. G.; Reifenberger, R. *Science* **1996**, 272, 1323-1325; (c) Andres, R. P.; Bielefeld, J. D.; Henderson, J. I.;

Janes, D. B.; Kolagunta, V. R.; Kubiak, C. P.; Mahoney, W. J.; Osifchin, R. G. *Science* **1996**, 273, 1690-1693; (d) McConnell, W. P.; Novak, J. P.; Brousseau, L. C. III ; Fuierer, R. R.; Tenent, R. C.; Feldheim, D. L. *J. Phys. Chem. B* **2000**, 104, 8925-8930; (e) Liao, J.; Bernard, L.; Langer, M.; Schonenberger, C.; Calame, M. *Adv. Mater.* **2006**, 18, 2444-2447.

[49] : (a) Hopfield, J. J. *Proc. Natl. Acad. Sci.* **1982**, 79, 2554-2558; (b) Hopfield, J. J. *IEEE Circuits Devices Mag.* **1988**, 4, 3-10.

[50] : Haddon, R. C.; Lamola, A. A. *Proc. Natl. Acad. Sci.* **1985**, 82, 1874-1878.

[51] : (a) Chen, J.; Reed, M. A.; Rawlett, A. M.; Tour, J. M. *Science* **1999**, 286, 1550-1552; (b) Yu, C. J.; Chong, Y.: Kayyem, J. F.; Gozin, M. *J. Org. Chem.* **1999**, 64, 2070-2079; (c) Chen, J.; Wang, W.; Reed, M. A.; Rawlett, A. M. Price, D. W.; Tour, J. M. *Appl. Phys. Lett.* **2000**, 77, 1224-1226; (d) Tour, J. M. *Acc. Chem. Res.* **2000**, 33, 791-804; (e) Tour, J. M.; Rawlett, A. M.; Kozaki, M.; Yao, Y.; Jagessar, R. C.; Dirk, S. M.; Price, D. W.; Reed, A. M.; Zhou, C.-W.; Chen, J.; Wang, W.; Campbell, I. *Chem. Eur. J.* **2001**, 7, 5118-5134; (f) Donhauser, Z. J.; Mantooth, B. A.; Kelly, K. F.; Bumm, L. A.; Monnell, J. D.; Stapleton, J. J.; Price, D. W. Jr.; Rawlett, A. M.; Allara, D. L.; Tour, J. M.; Weiss, P. S. *Science* **2001**, 292, 2303-2307; (g) Reed, M. A.; Chen, J.; Rawlett, A. M.; Price, D. W.; Tour, J. M. *Appl. Phys. Lett.* **2001**, 78, 3735-3737; (h) Park, J.; Pasupathy, A. N.; Goldsmith, J. I.; Chang, C.; Yaish, Y.; Petta, J. R.; Rinkoski, M.; Sethna, J. P.; Abruna, H. D.; McEuen, P. L.; Ralph, D. C. *Nature* **2002**, 417, 722-725; (i) Wang, C.; Batsanov, A. S.; Bryce, M. R.; Sage, I. *Org. Lett.* **2004**, 6, 13, 2181-2184.

[52] : (a) Bahr, J. L.; Yang, J.; Kosynkin, D. V.; Bronikowski, M. J. ; Smalley, R. E.; Tour, J. M. *J. Am. Chem. Soc.* **2001**, 123, 6536-6542; (b) Bahr, J. L.; Tour, J. M. *Chem. Mater.* **2001**, 13, 3823-3824; (c) Steuerman, D. W.; Star, A.; Narizzano, R.; Choi, H.; Ries, R. S.; Nicolini, C.; Stoddart, J. F.; Heath, J. R. *J. Phys. Chem. B* **2002**, 106, 3124-3130; (d) Ma, Y.; Cheung, W.; Wei, D.; Bogozi, A.; Chiu, P. L. ; Wang, L. ; Pontoriero, F. ; Mendelsohn, R. ; He, H. *ACS Nano* **2008**, 2, 1197-1204.

[53] : Lee, I. Y.; Liu, X.; Kosko, B.; Zhou, C. *Nano Letters* **2003**, 3, 1683-1686.

[54] : Cronin, L.; Krasnogor, N.; Davis, B. G.; Alexander, C.; Robertson, N.; Steinke, J. H. G.; Schroeder, S. L. M.; Khlobystov, A. N.; Cooper, G.; Gardner, P. M.; Siepmann, P.; Whitaker, B. J.; Marsh, D. *Nature Biotech.* **2006**, 24, 1203-1206.

[55] : Siepmann, P.; Martin, C. P.; Vancea, I.; Moriarty, P. J.; Krasnogor, N. *Nano Lett.* **2007**, 7, 1985-1990.

Chapter 2 – Organic Synthesis.

[56] : Sonogashira, K.; Tohda, Y.; Hagihara, N. *Tetrahedron Lett.* **1975**, 4467-4470.

[57] : Huang, S.; Tour, J. M. *Tetrahedron Lett.* **1999**, 40, 3347-3350.

[58] : James, D. K.; Tour, J. M. *Aldrichimica Acta* **2006**, 39, 2, 47-56.

[59] : Wang, C.; Batsanov, A. S.; Bryce, M. R.; Sage, I. *Synthesis* **2003**, 13, 2089-2095.

[60] : Mio, M. J.; Kopel, L. C.; Braun, J. B.; Gadzikwa, T. L.; Hull, K. L.; Brisbois, R. G.; Markworth, C. J.; Grieco, P. A. *Org. Lett.* **2002**, 4, 19, 3199-3202.

[61] : Wang, C.; Batsanov, A. S.; Bryce, M. R.; Sage, I. *Org. Lett.* **2004**, 6, 13, 2181-2184.

[62] : Dixon, S. University of Southampton, UK (unpublished work).

[63] : McIlroy, S. P.; Clo, E.; Nikolajsen, L.; Frederiksen, P. K.; Nielsen, C. B.; Mikkelsen, K. V.; Gothelf, K. V.; Ogilby, P. R. *J. Org. Chem.* **2005**, 4, 1134-1146.

[64] : Hsung, R. P.; Babcock, J. R.; Chidsey, C. E. B.; Sita, L. R. *Tetrahedron Lett.* **1995**, 36, 26, 4525-4528.

[65] : Shirai, Y.; Zhao, Y. M.; Cheng, L.; Tour, J. M. *Org. Lett.* **2004**, 6, 13, 2129-2132.

[66] : Pinchart, A.; Dallaire, C.; Van Bierbeek, A.; Gingras, M. *Tetrahedron Lett.* **1999**, 40, 5479-5482.

[67] : Chan, Y.-H.; Lin, J.-T.; Chen, I.-W. P.; Chen, C.-H. *J. Phys. Chem. B* **2005**, 109, 19161-19168.

[68] : Yu, C. J.; Chong, Y.: Kayyem, J. F.; Gozin, M. *J. Org. Chem.* **1999**, 64, 2070-2079.

[69] : Prato, M; Maggini, M. *Acc. Chem. Res.* **1998**, 31, 519-526.

[70] : Echegoyen, L.; Echegoyen, L. E. *Acc. Chem. Res.* **1998**, 31, 593-601.

[71] : Sariciftci, N. S.; Wudl, F.; Heeger, A. J.; Maggini, M.; Scorrano, G.; Prato, M.; Bourassa, J.; Ford, P. C. *Chem. Phys. Lett.* **1995**, 247, 510-514.

[72] : Williams, R. M.; Zwier, J. M.; Verhoeven, J. W. *J. Am. Chem. Soc.* **1995**, 117, 4093-4099.

[73] : Prato, M. *J. Mater. Chem.* **1997**, 7, 1097-1109.

[74] : Guldi, D. M. *Chem. Comm.* **2000**, (5), 321-327.

[75] : Langa, F.; de la Cruz, P.; Delgado, J. L.; Gomez-Escalonilla, M.; Gonzalez-Cortes, A.; de la Hoz, A.; Lopez-Arza, V. *New J. Chem.* **2002**, 26, 76-80.

[76] : Guldi, D. M.; Prato, M. *Acc. Chem. Res.* **2000**, 33, 695-703.

[77] : Maggini, M.; Guldi, D. M.; Mondini, S.; Scorrano, G.; Paolucci, F.; Ceroni, P.; Roffia, S. *Chem. Eur. J.* **1998**, 4, 1992-2000.

[78] : Maggini, M.; Scorrano, G. *J. Am. Chem. Soc.* **1993**, 115, 9798-9799.

[79] : Sato, F.; Jinbo, T.; Sato, M. *Communications* (Stuttgart) **1981**, 871 (1 page).

[80] : Stiegman, A. E.; Graham, E.; Perry, K. J.; Khundkar, L. R.; Cheng, L.-T.; Perry, J. W. *J. Am. Chem. Soc.* **1991**, 113, 7658-7666.

[81] : *"Vogel's Textbookof Practical Organic Chemistry"* Furniss, B. S.; Hannaford, A. J.; Smith, P. W. G.; Tatchell, A.R. (Longman Scientific and Technical, UK, 5th edition).

[82] : Hale, J. J. et al. (18), *Bioorg. Med. Chem. Lett.* **2002**, 12, 2997-3000.

[83] : Swepston, P. N.; Lin, S.-T.; Hawkins, A.; Humphrey, S.; Siegel, S.; Cordes, A. W. *J. Org. Chem.* **1981**, 46, 3754-3756.

[84] : Haggis, G. A.; Owen, L. N. *J. Chem. Soc.* **1953**, paper 81, 404-407 (Alicyclic glycols, part X).

[85] : Whistler, R. L.; Campbell, C. S. *J. Org. Chem.* **1966**, 31, 816-818.

[86] : Cannon, J. G.; Liang, C.-Y. *Synth. Comm.* **1995**, 25, 14, 2079-2089.

[87] : (a) Light, M. E.; Giustiniano, F.; Whitby, R. J. *Private communication to the Cambridge Structural Database, deposition number CCDC 737126* **2009**; (b) Light, M. E.; Giustiniano, F.; Whitby, R. J. *Private communication to the Cambridge Structural Database, deposition number CCDC 737127* **2009**.

[88] : Santiago, M.; Giustiniano, F.; Haiss, W.; Higgins, S. J.; Whitby, R. J.; Nichols, R. J. *J. Phys. Chem. C* **2009**, 113, 18884-18890.

[89] : Haiss, W.; Martin, S.; Leary, E.; van Zalinge H.; Higgins, S. J.; Bouffier, L.; Nichols, R. J. *J. Phys. Chem. C* **2009**, 113, 5823-5833.

Chapter 3 – Electrical characterization: Methods and Apparatus.

[90] : D. Marsh, University of Nottingham, Dept. of Chemistry; unpublished material.

[91] : P. Kapetanopoulos, University of Leeds, Dept. of Chemistry: unpublished material.

[92] : P. Kapetanopoulos, University of Leeds, Dept. of Chemistry: *PhD Thesis "Feedback and Control of Coupled Chemical Oscillators"*.

Chapter 4 – Methods for the production of μm-scale 'physical' Neural Networks.

[93] : Marsh, D. H.; Rance, G. A.; Zaka, M. H.; Whitby, R. J.; Khlobystov, A. N. *Phys. Chem. Chem. Phys.* **2007**, 9, 5490-5496.

[94] : Marsh, D. H.; Rance, G. A.; Whitby, R. J.; Giustiniano, F.; Khlobystov, A. N. *J. Mat. Chem.* **2008**, 18, 2249-2256.

[95] : Rance, G. A., University of Nottingham, Dept. of Chemistry: *PhD Thesis "Interactions in self-assembled nanoparticle superstructures"*.

[96] : Groenendaal, L.; Jonas, F.; Freitag, D.; Pielartzik, H.; Reynolds, J. R. *Adv. Mat.* **2000**, 12, 481-494.

[97] : Pei, Q.; Zuccarello, G.; Ahlskog, M.; Inganas, O. *Polymer* **1994**, 35, 1347-1351.

[98] : Kawai, T.; Motobayashi, H.; Kuwabara, T.; Yoshino, K. *Jpn. J. Appl. Phys.* **1991**, 30, L622-L623.

[99] : (a) Baba, A.; Knoll, W. *Adv. Mat.* **2003**, 15, 1015-1019; (b) Lu, G.; Qu, L.; Shi, G. *Electrochimica Acta* **2005**, 51, 340-346.

[100] : (a) Thapa, P. S.; Yu, D. J.; Wicksted, J. P.; Hadwiger, J. A.; Barisci, J. N.; Baughman, R. H.; Flanders, B. N. *Appl. Phys. Lett.* **2009**, 94, 033104 (3 pp.); (b) Thapa, P. S.; Ackerson, B. J.; Grischkowsky, D. R. Flanders, B. N. *Nanotech.* **2009**, 20, 235307 (10 pp.).

[101] : Smith, P. A.; Nordquist, C. D.; Jackson, T. N.; Mayer, T. S. *Appl. Phys. Lett.* **2000**, 77, 1399-1401.

[102] : Gurtner, C.; Sailor, M. J.: Katz, A. S.; Dynes, R. C. *J. Phys. Chem. B* **1998**, 102, 1599-1604.

[103] : EPAPS Document No. E-APPLAB-94-065903 : 'PEDOT_Wire_Growth_Processes.mpeg'.

[104] : Samitsu, S.; Iida, T.; Fujimori, M.; Heike, S.; Hashizume, T.; Shimomura, T.; Ito, K. *Synth. Met.* **2005**, 152, 497-500.

[105] : (a) Chen, G. Z.; Shaffer, M. S. P.; Coleby, D.; Dixon, G.; Zhou, W.; Fray, D. J.; Windle, A. H. *Adv. Mat.* **2000**, 12, 522-526; (b) Hughes, M.; Shaffer, M. S. P.; Renouf, A. C.; Singh, C.; Chen, G. Z.; Fray, D. J.; Windle, A. H. *Adv. Mat.* **2002**, 14, 382-385; (c) Blanchet, G. B.; Subramoney, S.; Bailey, R. K.; Jaycox, G. D. *Appl. Phys. Lett.* **2004**, 85, 828-830; (d) Peng, C.; Snook, G. A.; Fray, D. J.; Shaffer, M. S. P.; Chen, G. Z. *Chem. Comm.* **2006**, 44, 4629-4631.

[106] : (a) Kumar, A.; Mandal, S.; Mathew, S. P.; Selvakannan, P. R.; Mandale, A. B.; Chaudhari, R. V.; Sastry, M. *Langmuir* **2002**, 18, 6478-6483; (b) Reincke, F.; Hickey, S. G.; Kegel, W. K.; Vanmaekelbergh, D. *Angew. Chem., Int. Ed.* **2004**, 43, 458-462; (c) Lee, K. Y.; Han, S. W. *Bull. Korean Chem. Soc.* **2005**, 26, 1306-1308; (d) Lee, K. Y.; Cheong, G. W.; Han, S. W. *Colloids Surf. A* **2006**, 275, 79-82; (e) Wang, J.; Wang, D.; Sobal, N. S.; Giersig, M.; Jiang, M.; Mohwald, H. *Angew. Chem., Int. Ed.* **2006**, 45, 7963-7966.

[107] : Lee, K. Y.; Kim, M.; Hahn, J.; Suh, J. S.; Lee, I.; Kim, K.; Han, S. W. *Langmuir* **2006**, 22, 1817-1821.

[108] : (a) Kim, B.; Sigmund, W. M. *Langmuir* **2004**, 20, 8239-8242; (b) Correa-Duarte, M. A.; Liz-Marzan, L. M. *J. Mater. Chem*. **2006**, 16, 22-25.

Chapter 5 – General Conclusions and Future Work.

[109] : Hung, L.-H.; Lin, R.; Lee, A. P. *Lab on a Chip* **2008**, 8, 983-987.

[110] : (a) Moriarty, P.; Taylor, M. D. R.; Brust, M. *Phys. Rev. Lett.* **2002**, 89, article number 248303 (4 pp.); (b) O'Shea, J. N.; Phillips, M. A.; Taylor, M. D. R.; Moriarty, P.; Brust, M.; Dhanak, V. R. *Appl. Phys. Lett.* **2002**, 81, 5039-5041; (c) Martin, C. P.; Blunt, O. M.; Moriarty, P. *Nano Lett.* **2004**, 4, 2389-2392.

[111] : (a) Ge, G.; Brus, L. *J. Phys. Chem. B* **2000**, 104, 9573-9575; (b) Maillard, M.; Motte, L.; Ngo, A. T.; Pileni, M. P. *J. Phys. Chem. B* **2000**, 104, 11871-11877; (c) Pileni, M. P. *J. Phys. Chem. B* **2001**, 105, 3358-3371; (d) Rabani, E.; Reichman, D. R.; Geissler, P. L.; Brus, L. E. *Nature* **2003**, 426, 271-274.

EXPERIMENTAL SECTION (1): ORGANIC SYNTHESIS.

[112] : Perjessy, A.; Jones, R. G.; McClair, S. L.; Wilkins, J. M. *J. Org. Chem.* **1983**, 48, 1266-1271.

[113] : Maillard, M.; Motte, L.; Ngo, A. T.; Pileni, M. P. *J. Phys. Chem. B* **2000**, 104, 11871-11877.

[114] : Kumada, M.; Tamao, K.; Sumitani, K. *Org. Synth*. **1978**, 58 (annual volume), 127 (4 pp.).

[115] : Shenlin, H.; Tour, J. M. *J. Org. Chem*. **1999**, 64, 8898-8906.

[116] : Loupy, A.; Sansoulet, J.; Diez-Barra, E.; Carrillo, J. R. *Synth. Comm*. **1991**, 21, 1465-1471.

[117] : Aubert, P.-H.; Knipper, M.; Groenendaal, L.; Lutsen, L.; Manca, J.; Vanderzande, D. *Macromolecules* **2004**, 37, 4087-4098.

[118] : Brough, P.; Klumpp, C.; Bianco, A.; Campidelli, S.; Prato, M. *J. Org. Chem.* **2006**, 71, 2014-2020.

[119] : Polivka, Z.; Jilek, J.; Holubek, J.; Svatek, E.; Dlabac, A.; Valchar, M.; Protiva, M. *Coll.Czech.Chem.Comm.* **1984**, 49, 1, 86-109.

[120] : Pearson, D. E.; Pope, H. W.; Hargrove, W. W.; Stamper, W. E. *J. Org. Chem.* **1958**, 23, 1412-1416.

[121] : Douglas, W. E.; Benfield, R. E.; Antipov O. L.; Klapshina, L. G.; Kuzhelev, A. S.; Guy, D. M. H.; Jones, R. G.; Mustafa, A.; Domrachev, G. A. *Physical Chemistry Chemical Physics* **2000**, 14, 3195-3202.

[122] : Bunnet et al. *JACS* **1954**, 76, 5755-5761.

[123] : Light, M. E.; Giustiniano, F.; Whitby, R. J. *Private communication to the Cambridge Structural Database, deposition number CCDC 737126* **2009**.

[124] : Haggis *J. Chem. Soc.* **1953**, paper 80, 399-403 (Alicyclic glycols, part IX).

[125] : Light, M. E.; Giustiniano, F.; Whitby, R. J. *Private communication to the Cambridge Structural Database, deposition number CCDC 737127* **2009**.